

**SYNTHESIS AND TRIBOLOGICAL CHARACTERISATION
OF
Ni-P BASED ELECTROLESS COMPOSITE COATINGS**

A THESIS

*Submitted in fulfillment of the
requirements for the award of the degree*

of

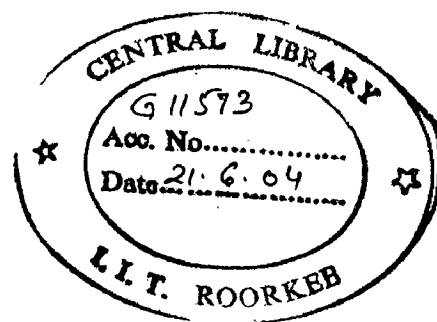
DOCTOR OF PHILOSOPHY

in

METALLURGICAL AND MATERIALS ENGINEERING

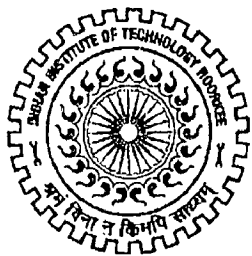
By

SUNIL BANSILAL SHARMA



**DEPARTMENT OF METALLURGICAL AND MATERIALS ENGINEERING
INDIAN INSTITUTE OF TECHNOLOGY ROORKEE
ROORKEE-247 667 (INDIA)**

JULY, 2002



INDIAN INSTITUTE OF TECHNOLOGY
ROORKEE

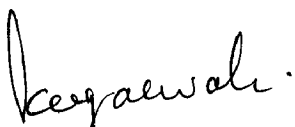
CANDIDATE'S DECLARATION


I hereby certify that the work which is being presented in the thesis, entitled "SYNTHESIS AND TRIBOLOGICAL CHARACTERISATION OF Ni-P BASED ELECTROLESS COMPOSITE COATINGS" in fulfillment of the requirements for the award of the Degree of Doctor of Philosophy and submitted in the Department of Metallurgical and Materials Engineering of the Institute, is an authentic record of my own work carried out during a period from July, 1999 to July, 2002 under the supervision of Dr. R. C. Agarwala and Dr. (Mrs.) V. Agarwala.

The matter presented in this thesis has not been submitted by me for the award of any other degree of this or any other Institute/University.

(SUNIL BANSILAL SHARMA)

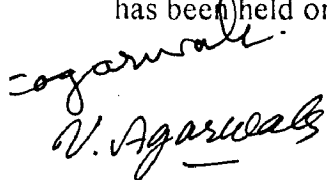
This is to certify that the above statement made by the candidate is correct to the best of our knowledge.

Date: July 1, 2002 
(Dr. R. C. AGARWALA)
Assoc. Professor


(Dr. (Mrs.) V. AGARWALA)
Assoc. Professor

Department of Metallurgical and Materials Engineering
Indian Institute of Technology
Roorkee - 247667, India

The Ph.D. Viva-Voce examination of **Sunil Bansilal Sharma**, Research Scholar, has been held on 15.11.2002



Signature of Supervisor(s)



Signature of H.O.D.



Signature of External Examiner

ABSTRACT

Non-crystalline solids like amorphous metallic alloys have emerged as an important class of novel industrial materials, which has received considerable attention of scientific community in the recent years. Amongst the various techniques used to prepare amorphous solids, electroless deposition is an important method, established over the years. In electroless coating technique, the alloys with or without external reinforcement are deposited in the form of a uniform film on a catalytic surface by a reduction reaction. Since the inception of electroless coating by Brenner and Riddel in 1946, it has become a subject of intensive research and during the past decade, emphasis has shifted to the studies of its properties and applications. The simplicity of the technique has credited many industrial usage of this method. This valuable process can coat not only electrically conductive materials including graphite but also fibers/fabric and insulators like plastics, rubber etc. The co-deposition of externally added particulate matter within the growing film has led to a new generation of electroless composite coatings, many of these coatings possess excellent wear and corrosion resistance. Relatively higher hardness of electroless coatings obtained inherently, could be further enhanced by suitable heat treatment which has made this coating a suitable candidate for many applications involving wear.

Despite the various materials in use - alloys, ceramics and polymeric composites, employed for wear resistant applications, much of the wear research being conducted is directed towards coatings. In the face of development of new wear resistant coatings, electroless coatings have succeeded to retain their place in wide ranging wear resistance applications. It may not be out of place to list a few important industrial applications of electroless nickel based coatings to combat wear as in ball studs, differential pinion ball shafts, disc brake pistons, knuckle pins, piston heads, bearing journals, hydraulic actuator splines, gyro parts, sun gears, loom ratchets, tank turret bearings, rotor blades, stator rings, precision tools etc. Generally, co-depositing particles in electroless nickel and particle concentration in deposits depend on various factors like bath composition, particle

characterisation, operating condition etc. Each combination between a certain type of particles and the Ni-P matrix can lead to a new set of properties, therefore, a multi-criteria decision is involved in the selection of appropriate coating system for a specific substrate. The electroless coatings offer a unique advantage of tailoring the desired properties by selecting the composition of alloy/composite/metallic coating and suitable heat treatment to suit the specific requirement. The electroless composite coatings possess some unique features like uniform deposition, high hardness, amorphous and microcrystalline nature in as-deposited condition, improved hardness and adhesion by suitable heat treatment etc. Also, Ni-P coated graphite provides better wettability characteristics with molten aluminium alloy. The present investigation is aimed to develop an electroless composite coating by in-situ co-precipitation of alumina and zirconia followed by their co-deposition into Ni-P matrix and analyse the friction and wear behaviour of the newly developed electroless Ni-P-X ($X = \text{ZrO}_2\text{-Al}_2\text{O}_3\text{-Al}_3\text{Zr}$) composite coated steel and aluminium under dry sliding condition using a pin-on-disc wear testing machine in the specific context of coating composition and heat treatment. Also the work is aimed to coat the carbon fabric using the electroless technique and assess the feasibility of reinforcement of coated fabric into aluminium alloy.

In the present study, synthesis and characterisation of a new electroless Ni-P based composite coating by in-situ co-precipitation of Al_2O_3 and ZrO_2 followed by their co-deposition along with Al_3Zr on three different substrate materials viz., commercial aluminium, low carbon (0.14%) steel and carbon fabric have been carried out. The coating characterisation in terms of qualitative and quantitative analysis has been dealt with. Steel and aluminium pin wear samples of cylindrical shape, having flat surface with rounded corner have been coated and then subjected to wear study in different conditions, i.e., as-coated and heat treated. Steel substrates were coated with Ni-P-X and Ni-P followed by wear testing in as-coated, heat treated at 400°C for 1 h and 400°C for 2 h conditions whereas aluminum substrates were coated with Ni-P-X followed by wear testing in as-coated, heat treated at 400°C for 1 h and 250°C for 12 h conditions. The friction and wear behaviour of above types of pins has been analysed and compared with those

observed for uncoated substrate material of normalised steel and commercial aluminium. The present work also focuses on electroless Ni-P-X and Ni-P coatings on carbon fabric as substrate and the feasibility of reinforcement of coated carbon fabric into aluminium alloy by use of conventional casting method.

Chapter 1 underscores the salient features of the electroless nickel based coatings in terms of their industrial applications and scientific research.

Chapter 2 is a critical review of literature explaining the different electroless coating systems, bath types, coating mechanism, composition and properties of coatings by various experimental techniques. The effect of different coating parameters like concentration of nickel sulphate, concentration of sodium hypophosphite, bath temperature, pH, bath loading area and time has been summarized. Structure and crystallisation kinetics in electroless Ni-P coatings have been outlined. The present day knowledge of coating tribology and contact mechanisms in general and wear studies on electroless nickel based coatings in particular has been summarized on the basis of available literature. The limited knowledge on the coating composition and wear behaviour of both the electroless alloy and electroless composite coating systems has been highlighted as these variables have the relevance to the present investigation. The knowledge base concerning electroless coated carbon fibers, vitreous carbon and wettability characteristics has been outlined. In the end of this chapter, the formulation of problem is presented.

Chapter 3 deals with the experimental techniques for electroless coatings and their characterisation as adopted in the present investigation. The details of the electroless coating setup, plating bath and co-precipitation reaction used, have been described. The selection of coating parameters has been carried out based on maximum coating weight achieved. Synthesis of electroless Ni-P and Ni-P-X on three different substrate materials such as aluminium, normalised steel and carbon fabric are outlined in respect of pretreatment and surface preparation for coating. The method followed for the chemical analysis of coatings has been discussed. The experimental details for the heat

treatment carried out and the hardness tests performed have been described. The X-ray diffraction analyses of the co-precipitated powder, as-coated and heat treated electroless coatings, uncoated and coated carbon fabric and the wear debris generated during dry sliding wear tests have been carried out to identify the phase constituents following the method described. The procedure used to confirm the phase constituents in coatings by TEM has been outlined. The procedure of sample preparation and make/model of different tools used in metallographic studies conducted have been summarized in respect of the qualitative and quantitative analyses of the coating. The different characterisation tools used in the present investigation viz., Optical microscope, SEM, TEM, X-ray diffraction, EPMA (both qualitative and quantitative), DSC etc., also have been summarised. The principle used for non-isothermal studies by DSC also forms a part of this chapter. Dry sliding wear tests carried out for different loads on electroless coating–substrate systems and the substrate have been elaborated. The details of the pin-on-disc wear testing machine, pin shaped specimen and the counterface of En-32 steel hardened to HRC 62–65 used in the study have been provided. In determination of friction and wear of normalised steel (NS), Ni-P-X as-coated steel (AC₁), Ni-P-X coated and heat treated at 400°C for 1 h (HT₁-A), Ni-P-X coated and heat treated at 400°C for 2 h (HT₂-A), Ni-P as-coated steel (AC₂), Ni-P coated and heat treated at 400°C for 1 h (HT₁-B) and Ni-P coated and heat treated at 400°C for 2 h (HT₂-B) three normal loads viz., 29.4, 34.3 and 39.2 N have been used whereas for commercial aluminium (AL), Ni-P-X as-coated aluminium, Ni-P-X coated and heat treated at 400°C for 1 h (HT₁-C) and Ni-P-X coated and heat treated at 250°C for 12 h (HT₂-C) four normal loads viz., 4.9, 7.4, 9.8 and 12.3 N have been used. All the tests were carried out at constant sliding speed of 0.5 m/s and in the relative humidity range of in-between 75–80 %. Wear surfaces of the pin after dry sliding have been examined under SEM while both the optical microscope and the SEM are used for examination of the wear debris generated during dry sliding wear tests. Procedure used for tensile testing of uncoated carbon fabric, Ni-P-X as-coated and heat treated at 400°C for 1 h, Ni-P as-coated and heat treated at 400°C for 1 h has been described. The method followed for reinforcement of uncoated and Ni-P-X coated carbon fabric in

aluminium by casting and their examination under SEM and EPMA X-ray mapping has been outlined.

Chapter 4 describes the synthesis and characterisation of Ni-P-X and Ni-P based electroless coatings in as-coated and heat treated conditions. In order to optimize the bath parameters for the new composition of the electroless bath used for synthesis of Ni-P-X coatings, selection of electroless bath temperature and pH for coating has been carried out by using an experimental design technique. Further, an attempt has been made to explain the process in terms of selection and optimization of coating condition, including bath loading factor and coating time. With the acquired data, an empirical model for the variation of coating weight, W in mg, with time, t , of Ni-P-X deposition is as given below.

$$W = k_1 t^{n_1} \quad (1)$$

where, k_1 is the coefficient and n_1 is an exponent. The coefficient, k_1 significantly changes with area immersed for the coating but the exponent n_1 does not change much with the area. The average value of n_1 has been found to be 0.73. The coefficient, k_1 as a function of area is given by

$$k_1 = 0.59 A_s^{0.96} \quad (2)$$

where, A_s is the area of the substrate in cm^2 .

The coating weight for composite coating has been experimentally found to be saturating after coating time of about 45 *min* which is irrespective of the surface area immersed in the electroless composite coating bath used in the present work. The reproducibility of the coating has been assessed by the repeated deposition of Ni-P-X and Ni-P on different pin shaped substrates used. The coating rate for composite coating under consideration is about 1.50 times greater than that of Ni-P alloy coatings for similar operating conditions. The co-precipitated powder that settled at the bottom of the electroless bath has been subjected to microscopic examination and X-ray analysis and the results reveal that the powder consists of very fine particles and a few large agglomerates

of oxides of aluminium and zirconium. Characterisation of as-coated Ni-P-X coatings are carried out by metallographic studies of different coatings. The coating mechanism has been studied in terms of globule sizes and its frequency of distribution. The electroless coating has nucleated at several isolated sites and have grown both laterally and vertically to cover the entire surface of the substrate. The deposition of hemispherical islands growing gradually to cover the substrate area by repeated nucleation and lateral growth has been observed. This mechanism has been observed for both the Ni-P alloy and the Ni-P-X composite coating for all three substrate materials under this study. Uniform layer of coating and its thickness obtained have been confirmed by SEM micrographs of the cross section of coating. The results of qualitative and quantitative analyses of the coatings by different analytical tools viz., XRF, X-ray diffraction, SEM-EDX, TEM, EPMA and DSC have been discussed. Qualitative studies depicted the uniform distribution of the second phase particles such as ZrO_2 , Al_2O_3 , and Al_3Zr in the composite coatings. The particles co-deposited in electroless Ni-P-X composite coating by using an in-situ co-precipitation reaction are distributed in nanosized particles and a few regions consisting of relatively coarser agglomerates of these particles. The as-coated deposits show the typically microcrystalline nature of the film. Quantitative study reveals that the presence of second phase particles result in a little decrease in phosphorus content. The electroless Ni-P-X composite coating primarily consists of Ni/Ni_xP_y phases and has the crystallization temperature of around $375^\circ C$. From the DSC studies, the non-isothermal kinetics of transformations in electroless Ni-P and Ni-P-X coatings have been observed for different heating rates of 10, 15, 20 and $25^\circ C/min$ and Avrami exponent (n) and activation energy (E , kJ/mol) are calculated by using Kissinger method. The growth dimension for composite coating is observed to be marginally less than that for the Ni-P coatings. The as-coated specimens with different substrates are subjected to heat treatments. The coated steel samples are heat treated at $400^\circ C$ for 1 h and 2 h whereas coated aluminium samples are heat treated at $400^\circ C$ for 1 h and $250^\circ C$ for 12 h. The micro and macro hardness data for coatings in different conditions: as-coated and heat treated, have been presented. The heat treatment applied to substrate along with coating at $400^\circ C$ for 1 h experienced the

maximum hardness, which is about twice the hardness of as-coated specimens and this is attributed to the formation of Ni₃P phase. The presence of Al₂O₃, Al₃Zr and ZrO₂ particles, which are embedded in the Ni-P matrix, also contributes to improvement in hardness.

The tribological behaviour of electroless Ni-P-X and Ni-P coatings on steel substrate in different conditions, i. e., as-coated, heat treated at 400°C for 1 *h* and heat treated at 400°C for 2 *h* under different normal loads of 29.4, 34.3 and 39.2 *N* are studied in terms of dry sliding friction and wear against counterface of case hardened steel and reported in chapter 5. The primary objective of the study is to understand the effect of the coating and load on the friction and wear behaviour of coated steel substrate in both the as-coated and the heat treated conditions. The results have been discussed to develop a coherent understanding of the tribological behaviour in terms of its correlation with the coating composition and hardness. The cumulative volume loss has been considered as basic data for wear performance of pin type samples. The cumulative volume losses for different types of pins have been observed to increase linearly with increasing sliding distance. The cumulative volume loss has also been observed to increase with increasing applied normal load. The Ni-P-X coating on steel substrate has been found to result in significant improvement in the resistance to wear in terms of cumulative volume loss and wear rate. A further improvement in the resistance to wear is observed after heat treating the coated steel samples. The wear rate increases with increasing load but that decreases with increasing hardness of the pin. Therefore, the wear rate variations are primarily associated with the change in the real area of contact at different normal loads and hardness of the pin. The coefficient of friction is found to fluctuate about its mean value and then stabilizes for almost all types of wear pins used. The average coefficient of friction has been observed to decrease with increasing applied load. The examination of worn surfaces under SEM has been conducted to observe the nature of wear tracks and the formation of transfer layer. The micrographic studies and X-ray diffraction analysis of wear debris collected during wear tests, have been carried out to understand the mechanism of wear. The wear debris particles collected during the test of normalised steel substrate and electroless Ni-P-X and Ni-P as-coated steel pins, are relatively fine but those

for coated and heat treated pin specimens are of coarser flake shapes. Fine debris of oxide contains the oxide agglomerates and the coarse and flaky particles of transfer layer must have resulted due to flaking off the transfer layer.

The tribological behaviour of Ni-P-X coatings on aluminium substrate in different conditions, i. e., as-coated, heat treated at 400°C for 1 *h* and heat treated at 250°C for 12 *h* have been studied in terms of dry sliding friction and wear against counterface of case hardened steel for different normal loads of 4.9, 7.4, 9.8 and 12.3 *N* as reported in chapter 6. An attempt is made to understand the effect of load on the dry sliding wear and friction for electroless coatings in as-coated and heat treated conditions in terms of cumulative volume loss, wear rate and coefficient of friction. The results have been compared with those obtained for the aluminium substrate. The debris particles collected have been studied by micrographs and X-ray diffraction analysis. The tribological behaviour of these systems with aluminium substrate has been explained in the context of coating composition and hardness. The wear rates of uncoated aluminum substrates are significantly higher than that observed for electroless Ni-P-X coated aluminium. The heat treatments to the coated aluminium pins further improved the resistance to wear. Coating composition, normal load applied and hardness of both the coating and substrate influences the wear rate of the coated substrate. In the dry sliding wear of aluminum substrate and as-coated electroless Ni-P-X aluminium, the debris particles are relatively fine which may primarily formed due to the oxide layer formed on the sliding surface. The debris of the latter contains a few particles and larger agglomerates of oxide. The debris from heat treated coatings are coarse and flaky particles of transfer layer which result from the flaking off the transfer layer of oxide on the sliding surface.

Carbon fibers play an indispensable role in the manufacturing of reinforcement metal matrix composite (MMC) and Ni-P-X coatings can facilitate the reinforcement to have better usage in fabric reinforced into aluminium alloys. Therefore, an attempt is made to study the tensile behaviour and feasibility of reinforcement of Ni-P based coated carbon fabric into aluminium matrix and described in chapter 7. The primary objective of this

segment of investigation is to apply electroless Ni-P-X and Ni-P coatings on carbon fabric and their characterisation in terms of uniformity, composition and phase constituents present. The characteristics of the coated fabric have been compared with those of the coatings on metallic substrates of aluminium and steel as explained in chapter 4. The uniformity of the coated fibers with about $0.8 \mu\text{m}$ thickness has been revealed by microscopic studies. The ultimate tensile strength (UTS) of the coated fabric in as-coated and heat treated (400°C for 1 h) conditions have been compared with that of uncoated carbon fabric. A little improvement in UTS on coating has been found but after heat treatment, a significant increase in UTS is observed. The feasibility of reinforcement of aluminium matrix by the coated carbon fabric using conventional casting technique with the help of specially designed carbon cloth holder in the mould is demonstrated. The micrographs of the carbon fabric zone into aluminium matrix from castings with and without coating on the fabric samples have been shown. The X-ray mapping under EPMA has been used for assessing the different elements near the interface that revealed chemical reaction at the interface between coating layer on the fabric and aluminium matrix.

The major conclusions on the basis of above experimental studies have been enumerated in chapter 8. In-situ co-precipitation of alumina–zirconia within the conventional electroless nickel bath can be used for synthesis of electroless Ni-P-X composite coating. This type of coating results in submicron and nanosized islands of the deposits consisting the second phases within the globular structure of Ni-P matrix. In certain regions, clusters of the particles are also observed. The Ni-P-X composite coating is expected to have better consistency in composition and relatively higher coating rate when compared to those in Ni-P coatings carried at the same conditions. Uniform and well adherent electroless Ni-P-X coating can be applied successfully on aluminium, steel and carbon fabric substrates. The Ni-P-X coated steel and aluminium samples exhibit substantially lower cumulative wear volume and wear rates, against hardened steel counterface during dry sliding at 0.5 m/s sliding speed, in the load ranges of $29.4\text{-}39.2 \text{ N}$ and $4.9\text{-}12.3 \text{ N}$ respectively when compared to corresponding substrates. The wear rates further decrease due to the heat treatment of coated samples. Operating wear mechanism is

primarily oxidative under the given conditions during dry sliding in both the as-coated Ni-P-X and the heat treated after coating the samples. Incorporating ceramic particles like X ($ZrO_2-Al_2O_3-Al_3Zr$) in Ni-P coating has the potential of further enhancing wear resistance if it could be incorporated in a relatively larger amounts but the coefficient of friction may increase. The segment of the investigation dealing with the Ni-P-X and Ni-P coatings on carbon fabric reveals that the reinforcement of coated fabric in aluminium melt is feasible.

ACKNOWLEDGEMENTS

The author is pleased to express his immense sense of gratitude to Dr. R. C. Agarwala and Dr. (Mrs.) V. Agarwala, Associate Professor, Department of Metallurgical and Materials Engineering, Indian Institute of Technology, Roorkee for their invaluable guidance, thought provoking discussions and untiring efforts throughout the tenure of this work. Their timely help, constructive criticism and painstaking efforts made the author possible to present the work contained in this thesis in its present form.

The author wishes to record his deep sense of gratitude to Dr. S. Ray, Professor, Metallurgical and Materials Engineering Department (MMED), Indian Institute of Technology, Roorkee for his critical suggestions, advice and time to time invaluable guidance in distressful time during the work.

The author acknowledges his deep sense of gratitude to the Head, MMED and the Director, Institute Instrumentation Centre (IIC), Indian Institute of Technology, Roorkee for providing him the necessary facilities and support during the course of the experimental work.

The author is highly obliged and wishes to owe his sincere thanks to the technical staff of MMED, especially to Mr. S. C. Kaushik, Dr. A. P. Nautiyal, Mr. Ajmer Singh, Mr. Shakti Gupta, Mr. T. K. Sharma, Mr. M. Pandey, Mr. S. N. Kaushik, Mr. Madhu Singh, Mr. N. K. Seth, Mr. Rajendra Sharma, Mr. Shamsher Singh, Mr. Balesh Sharma, Mr. S. P. Sharma, Mr. Dhan Prakash, Mr. Vidya Prakash, Mr. Dharam Pal, Mr. Vaish, Mr. R. K. Sharma, Mr. Ahuja, Mr. Giri, Mr. Ram Kishan, Mr. A. Kush and Mr. Naresh Kumar who have helped him all possible ways during the experimental work. Thanks are due to Mr. S. K. Sharma, Librarian of MMED for providing help at crucial times. The author also acknowledges his sincere thanks to Mrs. Rekha Sharma, Dr. Tamal Ghosh, Mr. Rajiv Jual, Mr. S. K. Saini, Mr. Anil Kumar of IIC. Sincere thanks are also due to Mr. Jagpal Singh of Welding Research Laboratory of Mechanical and Industrial Engineering Department, IIT, Roorkee for his cooperation during the experimental work of the thesis. The author is

indebted to Deptt. of Hydrology for providing the data on relative humidity. The facilities provided by Wadia Institute of Himalyan Geology, Dehradun are also sincerely acknowledged. Thanks are also due to Mr. Puran Sharma for preparing high quality micrographs, Mr. Kameshwar Saini for the tracing of the drawings and Mr. Sandeep Jain for type setting of manuscript of the thesis.

The author acknowledges with deep sense of gratitude, help and moral support rendered by Dr. S. K. Nath and Prof. M. L. Kapoor of MMED during the pungent facet of the work. The author wishes to acknowledge Dr. K. G. Satyanarayana, Senior Deputy Director, Regional Research Laboratory, Thiruvananthapuram for helpful suggestions and providing the carbon fabric used in this work and Dr. S. Seetharaman, Head, Division of Metallurgy, Royal Institute of Technology, Stockholm, Sweden for extending the cooperation in qualitative analysis.

The author express his gratitude to Principal, Shri Guru Gobind Singhji (SGGS) College of Engineering and Technology, Nanded, India and Director of Technical Education, Maharashtra State, Mumbai, India for his deputation for this work. The financial support provided by Quality Improvement Programme of all India Council for Technical Education, Govt. of India, New Delhi is also highly acknowledged.

Author wishes to thank Dr. Rajnesh Tyagi, Research Scientist in MMED for his cooperation during the acute phase of the thesis preparation. Sincere thanks are due to friends and colleagues who helped in alleviating the onus, especially to Dr. Shantanu Bhowmik, Mr. Narendra Kumar, Mr. Buta Singh, Mr. Sumit, Mr. V. K. Giri, Mr. Balaprasad, Mr. Milind Rajurkar, Mrs. Archana Rajurkar, Mrs. Gitangly, Mr. Punit Kumar, Mr. Bhanu Pant, Mr. Kailas Harne, Mr. Pradeep Solankar, Mr. M. D. Patil, Mr. Ambrish Panwar, Mr. Sandeep Bansal, Mr. Sanjay Panwar, Dr. Satish Hamde and Dr. Laxman Waghmare. Author also wishes to thank Dr. S. P. Kallurkar, Dr. S. R. Kajale, Dr. B. M. Dabade, Mr. V. B. Tungikar and his other colleagues from Production Engineering Department, SGGS College of Engineering and Technology, Nanded for reassuring him during this work.

The author would like to mention that his wife, Rekha deserves special acknowledgement, especially at arduous times and the perseverance shown by her to bear

the extra responsibilities at household front throughout the tenure of this course. The author would like to express reverence for his mother Mrs. Chandrakala and father Shri. B. L. Sharma who have always been a guiding force. The author wishes to express his sincere thanks to his sister, brother and other family members who have shown patience during the entire duration of this work. The author can not forget to remember his father in law, late Mr. Rambilasji Bheda who had always been the source of inspiration. Thanks are also due to all near and dear who have helped in various ways during the course of this work.

At the last, thanks to the almighty God who has given the author spiritual support and courage at every step to carry out this work. The author humbly dedicates this work to the almighty God.

Date: July 1, 2002

(Sunil Sharma)

CONTENTS

	Page No.
<i>Candidate's Declaration</i>	<i>i</i>
<i>Abstract</i>	<i>ii</i>
<i>Acknowledgements</i>	<i>xii</i>
<i>Contents</i>	<i>xv</i>
<i>List of Figures</i>	<i>xxi</i>
<i>List of Tables</i>	<i>xxxii</i>
<i>Nomenclature</i>	<i>xxxv</i>
<i>List of Publications</i>	<i>xxxvii</i>
Chapter 1 INTRODUCTION	1
Chapter 2 REVIEW OF LITERATURE	6
2.1 Introduction	6
2.2 Development of Electroless Deposition	6
2.3 Classification of Electroless Coatings	7
2.3.1 Alloy Coatings	7
2.3.1.1 Bath composition and characteristics	8
(a) Reducing Agents	9
(b) Energy	12
(c) Complexing Agents	13
2.3.2 Composite Coating	13
2.3.2.1 Classification of Composite Electroless Coating Systems	14
(a) Co-deposition of hard particles	14
(b) Co-deposition of soft particles	15
2.3.3 Metallic Coatings	16
2.4 Factors Affecting Coating Process	16

2.5	Structure of Electroless Coating	18
2.5.1	As-coated Electroless Nickel Coatings	18
2.5.2	Heat Treated Electroless Nickel Coatings	19
2.6	Crystallisation of Electroless Coatings	21
2.6.1	Sequence of Crystallisation of Ni-P Coatings	21
2.6.2	Kinetics of Crystallisation	22
	2.6.2.1 Application of Non-Isothermal Method to Determine Kinetics of Crystallisation	25
2.7	Alumina-Zirconia Powder Synthesis by Chemical Methods	29
2.7.1	Methods of Fabrication of Alumina-Zirconia Powder	29
	(a) Chemical polymerisation	29
	(b) Destabilisation of mixed sols	30
	(c) Co-precipitation	30
2.8	Properties of Electroless Coatings	31
2.8.1	Hardness of Electroless Nickel Deposits	32
2.8.2	Corrosion Characteristics	33
2.9	Wear and Friction	33
2.9.1	Dry Sliding Wear	35
	a) Types of wear	36
	b) Friction behaviour of materials	39
2.9.2	Coating Tribology and Contact Mechanisms	40
2.9.3	Wear Debris	44
2.9.4	Wear and Friction of Electroless Coatings	45
	2.9.4.1 Electroless Ni-P Alloy Coatings	46
	2.9.4.2 Electroless Ni-P based Composite Coatings	48
	(a) Composite coatings with hard particles	48
	(b) Composite coatings with soft particles	50

2.10	Coatings on Graphite and Carbon Fibers	51
2.10.1	Electroless Coating on Carbon Fibers	53
2.10.2	Wettability and Carbon Fiber/Metal Matrix Interface	54
2.11	Formulation of Problem	57
Chapter 3	EXPERIMENTAL WORK	61
3.1	Substrate Materials	61
3.2	Synthesis of Electroless Coatings	62
3.2.1	Substrate Preparation and Pretreatment	62
3.2.1.1	Steps for surface preparation	62
3.2.1.2	Substrate pretreatment	62
3.2.2	Bath Composition	63
3.2.3	Selection of Operating Parameters	64
3.2.4	Optimum Coating Time and Bath Loading Factor	65
3.2.5	Process Details	65
3.3	Examination of Co-precipitated Powder	67
3.4	Heat Treatment of Coated Samples	68
3.5	X-Ray Diffraction Analysis	68
a)	Co-precipitated powder	70
b)	Ni-P-X and Ni-P coatings in as-coated and heat treated conditions	70
c)	Carbon fabric and coatings on it	70
d)	Wear debris	71
3.6	Transmission Electron Microscopy (TEM) Study	71
3.7	Hardness Measurements	73
3.8	Metallographic Studies of Electroless Coatings	73
3.8.1	Optical and Scanning Electron Microscopic Studies	74
3.8.2	X-Ray Fluorescence Studies	74
3.8.3	Area Analysis by SEM-EDAX	75

3.8.4	Spectrographic Analysis by SEM-EDX	75
3.8.5	Qualitative and Quantitative Analysis by Electron Probe Micro Analyser	75
3.9	Determination of Coating Globule Size and its Distribution	76
3.10	Kinetics Study by Differential Scanning Calorimeter	77
3.11	Tensile Testing of Carbon Fabric Samples	77
3.12	Fractographic Studies	79
3.13	Examination of Fabric Zone into Aluminium Matrix	79
3.14	Dry Sliding Friction and Wear Testing	80
3.15	Microscopic Examinations	84
3.15.1	Worn Surfaces	84
3.15.2	Examination of Wear Debris	85
Chapter 4	SYNTHESIS AND CHARACTERISATION OF ELECTROLESS Ni-P-X AND Ni-P COATINGS ON ALUMINIUM AND STEEL	86
4.1	Results	86
4.1.1	Composition of Substrate Materials	86
4.1.2	Optimum Bath Conditions and Coating Parameters	87
(a)	Temperature, pH and time	87
(b)	Relative concentration of co-precipitation reaction components	89
4.1.3	Empirical Model	91
(a)	Assumptions made for developing the empirical model	91
(b)	Model development	92
4.1.4	In-Situ Co-precipitation	94
(a)	Reaction involved in co-precipitation	94
(b)	Characterisation of co-precipitation reaction product	99
(i)	Examination of co-precipitated powder	99
(ii)	X-ray diffraction analysis of co-precipitated powder	99
4.1.5	Coating Thickness	99
4.1.6	Coating Rate	103

4.1.7	Reproducibility of Electroless Coatings	106
4.1.8	Morphological Studies of Electroless Coatings	106
	(a) Examination of the surface of coatings	106
	(b) Examination of cross section of coatings	109
	(c) Coating globule size and its distribution	114
4.1.9	Composition of Electroless Ni-P-X Coatings	114
	4.1.9.1 Qualitative analysis	117
	(a) X-ray fluorescence	117
	(b) Area analysis	117
	(c) Line analysis	120
	(d) Point analysis	120
	(e) X-ray mapping	120
	4.1.9.2 Quantitative analysis of Ni-P-X coating	125
	(a) EPMA point analysis	125
	(b) SEM-EDAX	126
	(i) Area scanning	126
	(ii) Point scanning	126
4.1.10	Phase Analysis	130
	(a) As-coated films	130
	(b) Heat treated films	137
4.1.11	Non-Isothermal Kinetics of Transformation	137
4.1.12	Hardness	144
4.2	Discussion	147
	(a) Synthesis	147
	(b) Metallographic study	152
Chapter 5	FRICION AND WEAR BEHAVIOUR OF ELECTROLESS Ni-P-X AND Ni-P COATINGS ON STEEL	164
5.1	Results	164
	5.1.1 Dry Sliding Friction and Wear Behaviour	167
	a) Wear Behaviour	167
	b) Friction Behaviour	179
	5.1.2 Examination of Wear Surfaces and Wear Debris	190
	5.1.2 X-Ray Diffraction Analysis	199
5.2	Discussion	209

Chapter 6	FRICITION AND WEAR BEHAVIOUR OF ELCTROLESS Ni-P-X COATINGS ON ALUMINIUM	217
6.1	Results	217
6.1.1	Dry Sliding Friction and Wear Behaviour	217
(a)	Wear behaviour	218
(b)	Friction behaviour	226
6.1.2	Examination of Wear Surfaces and Wear Debris	232
6.1.3	X-Ray Diffraction Analysis	239
6.2	Discussion	245
Chapter 7	ELECTROLESS COATED CARBON FABRIC : A CASE STUDY	251
7.1	Results	251
7.1.1	Specifications of Carbon Fabric	252
7.1.2	Coatings on Carbon Fabric	252
7.1.3	Examination of Carbon Fabric under SEM	254
7.1.4	Phase Analysis	258
7.1.5	Tensile Testing and Fractography	261
7.1.6	Reinforcement Feasibility into Metal Matrix	264
(a)	Examination of fabric zone into aluminium matrix	264
(b)	X-ray mapping	265
7.2	Discussion	270
Chapter 8	CONCLUSIONS	275
8.1	Synthesis and Characterisation of Coatings	275
8.2	Tribological Behaviour of Ni-P-X Coatings on Steel and Aluminium	278
	FUTURE SCOPE	281
	APPENDIX	282
	REFERENCES	293

LIST OF FIGURES

No.	Title	Page No.
Fig. 2.1	Differential scanning calorimetry curves of the crystallisation processes for the electroless nickel deposits obtained from various solutions in terms of phosphorus, P content (a) 6.3 wt.%P, (b) 10.1 wt.%P, (c) 11.5 wt.%P, (d) 12.5 wt.%P and (e) 13.6 wt.%P (Hur <i>et al.</i> , 1990).	23
Fig. 2.2	The temperatures of exothermic peaks in the differential scanning calorimetry curves for electroless and electro Ni-P deposits as a function of phosphorus content for different nickel deposits obtained. □, ∇, • and ■ indicate the results from the work of different researchers (Hur <i>et al.</i> , 1990).	24
Fig. 2.3	Schematic drawing of hypothetical free energy against composition diagram (Hur <i>et al.</i> , 1990).	24
Fig. 2.4	Microhardness of the different electroless coatings and the aluminium substrate for various heat treatments at 200, 250, 300 and 400°C for 1 h (Apachitei <i>et al.</i> , 1998/1).	34
Fig. 2.5	Illustration to show how the parameters of the coating deposition influences the tribological response of the coating composites through the coating characteristics which in turn determines the basic and tribological coating properties (Hogmark <i>et al.</i> , 1997).	37
Fig. 2.6	Schematic drawing of the geometries employed in sliding wear tests: (a) ring-on-ring with line contact, (b) ring-on-ring with face to face contact, (c) pin-on-disc, (d) pin-on-rim, (e) block-on-ring and (f) pin-on-flat (Huchings, 1992).	38
Fig. 2.7	The macromechanical contact conditions for different mechanisms that influence friction when a hard spherical slider moves on a coated flat surface (Holmberg <i>et al.</i> , 1998).	43
Fig. 2.8	Tribological performance of electroless Ni-P and electroless Ni-P-3%MoS ₂ coated blocks running against various coated rings: (a) variation of wear with sliding distance and (b) variation of coefficient of friction with sliding distance (Moonir-Vaghefi <i>et al.</i> , 1997).	53
Fig. 2.9	Wetting behaviour of aluminium: (a) contact angle on nickel and nickel coated graphite as a function of contact time and (b) on various substrates: (i) graphite, (ii) electrolytic nickel and (iii) nickel coated graphite (Ip <i>et al.</i> , 1998).	56

Fig. 3.1	Schematic diagram of the experimental set up used for electroless coating.	66
Fig. 3.2	Schematic diagram of the tube furnace along with argon gas flow arrangement.	69
Fig. 3.3	Schematic of the indexed SAD ring pattern obtained by TEM for nickel.	72
Fig. 3.4	Base line construction method used to measure area under DSC peak (Scott, M. G., 1978).	78
Fig. 3.5	Photograph of the wear pin sample.	81
Fig. 3.6	Photograph of the pin-on-disc wear testing machine.	81
Fig. 3.7	Schematic view of the pin-on-disc wear testing machine.	82
Fig. 4.1	Variation in coating weight for different concentrations of co-precipitation reactants within electroless nickel bath.	90
Fig. 4.2	Variation of (a) coating weight in electroless Ni-P-X composite coating with time for different bath loading areas and (b) logarithmic plot for the coating weight vs. time for different bath loading areas.	93
Fig. 4.3	Variation in (a) logarithmic plot for the coefficient, k_1 vs. bath loading area, A_s in accordance of the Eq. (4.1) and (b) difference between the calculated and experimental coefficients, $k_{\text{calculated}} - k_{\text{experimental}}$, Δk_1 , with bath loading area.	95
Fig. 4.4	Calculated and experimental values of the coating weight in Ni-P-X deposition for different time of coating: (a) 15 min, (b) 30 min, (c) 45 min, (d) 60 min and (e) 75 min.	96
Fig. 4.5	Variation in difference between coating weight calculated and experimental, $W_{\text{calculated}} - W_{\text{experimental}}$ with bath loading area in the Ni-P-X deposition for different time.	97
Fig. 4.6	SEM micrographs of the co-precipitated powder: (a) fine particles and coarser agglomerates at $\times 300$ and (b) Cluster of many particles at $\times 10,000$.	100
Fig. 4.7	X-ray diffraction pattern of the powder obtained by co-precipitation reaction within the electroless bath.	101
Fig. 4.8	Cross section of the electroless coating under SEM showing uniform thickness in (a) Ni-P-X deposition and (b) Ni-P deposition.	102
Fig. 4.9	Variation of (a) coating weight in electroless Ni-P-X and Ni-P coating on aluminium substrate for the specific coating conditions and (b) difference between the coating weight of Ni-P-X and Ni-P deposits, $W_{\text{Ni-P-X}} - W_{\text{Ni-P}}$ with time.	104

Fig. 4.10	Coating rates observed in different types of electroless coatings with bath temperature 90°C and 9.0 pH ($X = \text{ZrO}_2\text{-Al}_2\text{O}_3\text{-Al}_3\text{Zr}$).	105
Fig. 4.11	Scatter observed in weight of electroless Ni-P-X composite coating on aluminium substrates at 9.0 pH and 90°C.	107
Fig. 4.12	Scatter observed in weight of electroless Ni-P-X composite coating on steel substrates at 9.0 pH and 90°C.	107
Fig. 4.13	Scatter observed in weight of electroless Ni-P alloy coating on aluminium substrates at 9.0 pH and 90°C.	107
Fig. 4.14	SEM micrographs of electroless Ni-P-X composite coating in as-coated condition (a) $\times 924$ and (b) back scatter image at $\times 4000$.	108
Fig. 4.15	SEM micrographs of electroless Ni-P alloy coating in as-coated condition (a) $\times 1001$ and (b) coating globule fracture at $\times 2004$.	108
Fig. 4.16	SEM micrograph of electroless Ni-P-Al ₂ O ₃ deposition in as-coated condition.	110
Fig. 4.17	SEM micrograph of electroless Ni-P-ZrO ₂ deposition in as-coated condition.	110
Fig. 4.18	SEM micrographs of electroless Ni-P-X composite coating on aluminium substrate after heat treatment at: (a) 400°C for 1 h, (b) 400°C for 2 h and (c) 250°C for 12 h.	111
Fig. 4.19	SEM micrographs of electroless Ni-P-X composite coating on aluminium substrate after heat treatment at 400°C for 1h (a) showing the precipitation of Ni ₃ P and (b) cracking near grain boundary and (c) back scatter image at $\times 4000$.	112
Fig. 4.20	Cross section of the electroless Ni-P-X coating after developing the deposition layer: (a) $\times 250$, (b) $\times 2000$ and (c) substrate-coating interface, $\times 2004$.	113
Fig. 4.21	Coating globule size distribution in different electroless coating systems: (a) Ni-P, (b) Ni-P-Al ₂ O ₃ , (c) Ni-P-ZrO ₂ , and (d) Ni-P-ZrO ₂ -Al ₂ O ₃ -Al ₃ Zr.	115
Fig. 4.22	Average coating globule size in different electroless coating systems ($X = \text{ZrO}_2\text{-Al}_2\text{O}_3\text{-Al}_3\text{Zr}$).	116
Fig. 4.23	Qualitative analysis of the different elements present in the electroless Ni-P-X composite coating: (a) Ni, (b) P, (c) Zr and (d) Al.	118
Fig. 4.24	Qualitative analysis of different elements present in the electroless Ni-P-X coating by SEM-EDAX area analysis (a) micrograph of the typical area and (b) peaks showing the presence of different elements viz., Ni, P, Zr and Al.	119

Fig. 4.25	SEM spectrographic analysis results in terms of distribution of different elements present (a) micrograph showing the line selected for spectrographic analysis and (b) spectograph along 10.84 μm line for I-profile of coating along the line, II-O K_{α} , III-Al K_{α} , IV-P K_{α} , V-Zr L_{α} , VI-Ni K_{α} and VII-Zr K_{α} .	121
Fig. 4.26	EPMA qualitative analysis of the electroless Ni-P-X coating (a) showing the presence of Ni, P and Al and (b) showing the presence of Zr along with P.	122-123
Fig. 4.27	Micrographs showing the X-Ray mapping of electroless Ni-P-X coating under EPMA (a) area selected for mapping, (b) distribution of nickel, (c) distribution of phosphorus, (d) distribution of zirconium and (e) distribution of aluminium.	124
Fig. 4.28	Micrographs showing three different areas of Electroless Ni-P-X coated sample subjected to quantitative analysis by SEM-EDAX.	127
Fig. 4.29	Point analysis by SEM-EDAX on typically nickel rich points in the electroless Ni-P-X coating (a) micrograph showing different nickel rich points as marked on it and (b) distribution of different elements in wt. % for the points marked in the above micrograph.	128
Fig. 4.30	Point analysis by SEM-EDAX on typically zirconium rich points in the electroless Ni-P-X coating (a) micrograph showing different zirconium rich points as marked on it and (b) distribution of different elements in wt.% for the points marked in the above micrograph.	129
Fig. 4.31	X-ray diffraction pattern of electroless Ni-P-X coating in as-coated condition.	132
Fig. 4.32	X-ray diffraction pattern of electroless Ni-P coating in as-coated condition.	133
Fig. 4.33	Micrograph of electroless Ni-P-X coating film under TEM (a) bright field image, (b) dark field image and (c) SAD pattern.	134
Fig. 4.34	Micrograph of electroless Ni-P-X coating film under TEM (a) bright field image, (b) dark field image of the clustered point and (c) SAD pattern.	135
Fig. 4.35	Micrograph of electroless Ni-P coating film under TEM (a) bright field image, (b) dark field image and (c) SAD pattern.	136
Fig. 4.36	X-ray diffraction pattern of electroless Ni-P-X coating after heat treating at 400°C for 1 h.	138
Fig. 4.37	Differential Scanning Calorimetry response curves for electroless Ni-P-X coating obtained at different heating rates (a) 10 °C/min, (b) 15 °C/min, (c) 20 °C/min and (d) 25 °C/min.	139

Fig. 4.38	Differential Scanning Calorimetry response curves for electroless Ni-P coating obtained at different heating rates (a) 10 °C/min, (b) 15 °C/min, (c) 20 °C/min and (d) 25 °C/min.	139
Fig. 4.39	Kissinger plot of $(-\ln(\beta/T_m^2))$ vs. $(1/T_m)$ for the curves shown in Figs. 4.37 and 4.38.	141
Fig. 4.40	$\ln \ln(1/1-\alpha)$ vs. $(1/T)$ plots for electroless Ni-P-X and Ni-P coatings at different heating rates (a) 10 °C/min, (b) 15 °C/min, (c) 20 °C/min and (d) 25 °C/min.	142
Fig. 4.41	Variation of E/RT with heating rate in electroless Ni-P-X and Ni-P coatings.	143
Fig. 4.42	Hardness observed in different conditions for electroless Ni-P-X and Ni-P coatings (a) microhardness and (b) macrohardness.	146
	Note: HT ₁ – heat treated at 400°C for 1 h for both steel and aluminium substrates and HT ₂ – heat treated at: 400°C for 2 h for steel substrate and 250°C for 12 h for aluminium substrate.	
Fig. 5.1	Cumulative wear volume with sliding distance at 29.4 N load in electroless Ni-P-X coatings on steel for different coating times.	166
Fig. 5.2	Variation of limiting sliding distance with time at 29.4 N load in electroless Ni-P-X coatings on steel.	166
Fig. 5.3	Cumulative wear volume with sliding distance at different loads in normalised steel (NS).	169
Fig. 5.4	Cumulative wear volume with sliding distance at different loads in electroless Ni-P-X as-coated steel (AC ₁).	169
Fig. 5.5	Cumulative wear volume with sliding distance at different loads in electroless Ni-P-X coated and heat treated at 400°C for 1 h specimens (HT ₁ -A).	170
Fig. 5.6	Cumulative wear volume with sliding distance at different loads in electroless Ni-P-X coated and heat treated at 400°C for 2 h specimens (HT ₂ -A).	170
Fig. 5.7	Cumulative wear volume with sliding distance at different loads in electroless Ni-P as-coated steel (AC ₂).	173
Fig. 5.8	Cumulative wear volume with sliding distance at different loads in electroless Ni-P coated and heat treated at 400°C for 1 h specimens (HT ₁ -B).	173
Fig. 5.9	Cumulative wear volume with sliding distance at different loads in electroless Ni-P coated and heat treated at 400°C for 2 h specimens (HT ₂ -B).	174
Fig. 5.10	Wear rate with coating time at 29.4 N load in electroless Ni-P-X as-coated steel (AC ₁) specimens.	174

Fig. 5.11	Variation of wear rate with normal load in normalised steel (NS), electroless Ni-P-X as-coated steel (AC ₁), Ni-P-X coated and heat treated at 400°C for 1 <i>h</i> specimens (HT ₁ -A) and Ni-P-X coated and heat treated at 400°C for 2 <i>h</i> specimens (HT ₂ -A).	177
Fig. 5.12	Variation of wear rate with normal load in normalised steel (NS), electroless Ni-P as-coated steel (AC ₂), Ni-P coated and heat treated at 400°C for 1 <i>h</i> specimens (HT ₁ -B) and Ni-P coated and heat treated at 400°C for 2 <i>h</i> specimens (HT ₂ -B).	177
Fig. 5.13	Comparison of wear rates in Ni-P-X and Ni-P coatings for as-coated and heat treated specimens at different loads.	178
Fig. 5.14	Variation of wear rate with macrohardness of the wear pin specimen in normalised steel (NS), electroless Ni-P-X as-coated steel (AC ₁), Ni-P-X coated and heat treated at 400°C for 1 <i>h</i> specimens (HT ₁ -A) and Ni-P-X coated and heat treated at 400°C for 2 <i>h</i> specimens (HT ₂ -A) at different normal loads.	178
Fig. 5.15	Variation of wear rate with macrohardness of the wear pin specimen in electroless Ni-P as-coated steel (AC ₂), Ni-P coated and heat treated at 400°C for 1 <i>h</i> specimens (HT ₁ -B) and Ni-P coated and heat treated at 400°C for 2 <i>h</i> specimens (HT ₂ -B) at different normal loads.	181
Fig. 5.16	Variation of sliding friction coefficient with distance at different loads in normalised steel (NS).	181
Fig. 5.17	Variation of sliding friction coefficient with distance at different loads in electroless Ni-P-X as-coated steel (AC ₁).	182
Fig. 5.18	Variation of sliding friction coefficient with distance at different loads in electroless Ni-P-X coated and heat treated at 400°C for 1 <i>h</i> specimens (HT ₁ -A).	182
Fig. 5.19	Variation of sliding friction coefficient with distance at different loads in electroless Ni-P-X coated and heat treated at 400°C for 2 <i>h</i> specimens (HT ₂ -A).	185
Fig. 5.20	Variation of coefficient of friction averaged over the distance of sliding during wear in normalised steel (NS), electroless Ni-P-X as-coated steel (AC ₁), Ni-P-X coated and heat treated at 400°C for 1 <i>h</i> specimens (HT ₁ -A) and Ni-P-X coated and heat treated at 400°C for 2 <i>h</i> specimens (HT ₂ -A).	185
Fig. 5.21	Variation of sliding friction coefficient with distance at different loads in electroless Ni-P as-coated steel (AC ₂).	186
Fig. 5.22	Variation of sliding friction coefficient with distance at different loads in electroless Ni-P coated and heat treated at 400°C for 1 <i>h</i> specimens (HT ₁ -B).	186
Fig. 5.23	Variation of sliding friction coefficient with distance at different loads in electroless Ni-P coated and heat treated at 400°C for 2 <i>h</i> specimens (HT ₂ -B).	187

Fig. 5.24	Variation of coefficient of friction averaged over the distance of sliding during wear in normalised steel (NS), electroless Ni-P as-coated steel (AC ₂), Ni-P coated and heat treated at 400°C for 1 <i>h</i> specimens (HT ₁ -B) and Ni-P coated and heat treated at 400°C for 2 <i>h</i> specimens (HT ₂ -B).	187
Fig. 5.25	Comparison of average coefficient of friction in Ni-P-X and Ni-P coatings for as-coated and heat treated specimens at different loads.	189
Fig. 5.26	Variation in average coefficient of friction with hardness during wear in electroless Ni-P-X and Ni-P coated steel specimens at a load of 29.4 <i>N</i> under dry sliding condition.	189
Fig. 5.27	Wear surfaces of the specimens of normalised steel (NS) after sliding through a distance of 480 <i>m</i> at the normal loads of (a) 29.4 <i>N</i> , (b) 34.3 <i>N</i> and (c) 39.2 <i>N</i> .	192
Fig. 5.28	Wear debris of normalised steel (NS) after spreading on white paper (a) optical micrograph at magnification of × 25 and (b) SEM micrograph.	193
Fig. 5.29	Wear surfaces of the specimens of electroless Ni-P-X as-coated steel (AC ₁) after sliding through (a) 300 <i>m</i> at 29.4 <i>N</i> , (b) 300 <i>m</i> at 34.3 <i>N</i> and (c) 150 <i>m</i> at 39.2 <i>N</i> .	194
Fig. 5.30	Wear debris of electroless Ni-P-X as-coated steel (AC ₁) after spreading on white paper (a) optical micrograph at magnification of × 25 and (b) SEM micrograph.	195
Fig. 5.31	Wear surfaces of the specimens of electroless Ni-P-X coated and heat treated at 400°C for 1 <i>h</i> steel specimens (HT ₁ -A) after sliding through (a) 600 <i>m</i> at 29.4 <i>N</i> , (b) 420 <i>m</i> at 34.3 <i>N</i> and (c) 300 <i>m</i> at 39.2 <i>N</i> .	196
Fig. 5.32	Wear debris of electroless Ni-P-X coated and heat treated at 400°C for 1 <i>h</i> steel specimens (HT ₁ -A) after spreading on white paper (a) optical micrograph at magnification of × 25 and (b) SEM micrograph.	197
Fig. 5.33	Wear surfaces of the specimens of electroless Ni-P-X coated and heat treated at 400°C for 2 <i>h</i> steel specimens (HT ₂ -A) after sliding through (a) 600 <i>m</i> at 29.4 <i>N</i> , (b) 300 <i>m</i> at 34.3 <i>N</i> and (c) 150 <i>m</i> at 39.2 <i>N</i> .	200
Fig. 5.34	Wear debris of electroless Ni-P-X coated and heat treated at 400°C for 2 <i>h</i> steel specimens (HT ₂ -A) after spreading on white paper (a) optical micrograph at magnification of × 25 and (b) SEM micrograph.	201
Fig. 5.35	Wear surfaces of the specimens of electroless Ni-P as-coated steel (AC ₂) after sliding through (a) 240 <i>m</i> at 29.4 <i>N</i> , (b) 240 <i>m</i> at 34.3 <i>N</i> and (c) 150 <i>m</i> at 39.2 <i>N</i> .	202

Fig. 5.36	Wear surfaces of the specimens of electroless Ni-P coated and heat treated at 400°C for 1 <i>h</i> steel specimens (HT ₁ -B) after sliding through (a) 540 <i>m</i> at 29.4 <i>N</i> , (b) 420 <i>m</i> at 34.3 <i>N</i> and (c) 300 <i>m</i> at 39.2 <i>N</i> .	203
Fig. 5.37	Wear surfaces of the specimens of electroless Ni-P coated and heat treated at 400°C for 2 <i>h</i> steel specimens (HT ₂ -B) after sliding through (a) 420 <i>m</i> at 29.4 <i>N</i> , (b) 420 <i>m</i> at 34.3 <i>N</i> and (c) 150 <i>m</i> at 39.2 <i>N</i> .	204
Fig. 5.38	The cracks in the transfer layer in electroless Ni-P coated and heat treated at 400°C for 2 <i>h</i> specimens (HT ₂ -B) after sliding through (a) 420 <i>m</i> at 29.4 <i>N</i> and (b) 150 <i>m</i> at 39.2 <i>N</i> .	205
Fig. 5.39	Wear debris of Ni-P coated steel by pooling together for different conditions (i.e., AC ₂ , HT ₁ -B and HT ₂ -B) after spreading on white paper for all the three normal loads, i.e., 29.4 <i>N</i> , 34.3 <i>N</i> and 39.2 <i>N</i> (a) optical micrograph at magnification of × 25 and (b) SEM micrograph.	206
Fig. 5.40	X-ray diffraction pattern of the wear debris of normalised steel (NS) generated at all the three, i.e., 29.4 <i>N</i> , 34.3 <i>N</i> and 39.2 <i>N</i> normal loads and collected from the disc counterface.	207
Fig. 5.41	X-ray diffraction pattern of the wear debris of Ni-P-X as-coated steel specimens (AC ₁) generated at all the three, i.e., 29.4 <i>N</i> , 34.3 <i>N</i> and 39.2 <i>N</i> normal loads and collected from the disc counterface.	208
Fig. 5.42	X-ray diffraction pattern of the wear debris of Ni-P-X coated and heat treated at 400 °C for 1 <i>h</i> , (HT ₁ -A) and heat treated at 400 °C for 2 <i>h</i> , (HT ₂ -A) generated at all the three, i.e., 29.4 <i>N</i> , 34.3 <i>N</i> and 39.2 <i>N</i> normal loads and collected from the disc counterface.	208
Fig. 5.43	Comparison of cumulative volume losses in NS, AC ₁ and AC ₂ type of wear pin samples with sliding distance at (a) 29.4 <i>N</i> , (b) 34.3 <i>N</i> and (c) 39.2 <i>N</i> .	210
Fig. 6.1	Cumulative wear volume with sliding distance at different loads in commercial aluminium (AL).	221
Fig. 6.2	Cumulative wear volume with sliding distance at different loads in electroless Ni-P-X as-coated aluminium (AC ₃).	221
Fig. 6.3	Cumulative wear volume with sliding distance at different loads in electroless Ni-P-X coated and heat treated at 400°C for 1 <i>h</i> specimens (HT ₁ -C).	222
Fig. 6.4	Cumulative wear volume with sliding distance at different loads in electroless Ni-P-X coated and heat treated at 250°C for 12 <i>h</i> specimens (HT ₂ -C).	222
Fig. 6.5	Variation of wear rate with normal load in commercial aluminium (AL), electroless Ni-P-X as-coated aluminium (AC ₃), Ni-P-X coated and heat treated at 400°C for 1 <i>h</i> specimens (HT ₁ -C) and Ni-P-X coated and heat treated at 250°C for 12 <i>h</i> specimens (HT ₂ -C).	224

Fig. 6.6	Variation of wear rate with macrohardness of the wear pin specimen in commercial aluminium (AL), electroless Ni-P-X as-coated aluminium (AC ₃), Ni-P-X coated and heat treated at 400°C for 1 <i>h</i> specimens (HT ₁ -C) and Ni-P-X coated and heat treated at 250°C for 12 <i>h</i> specimens (HT ₂ -C) at different normal loads.	224
Fig. 6.7	Wear rate vs. $(H_{\text{coating}} \times H_{\text{substrate}})^{1/2}$ in commercial aluminium (AL), electroless Ni-P-X as-coated aluminium (AC ₃), Ni-P-X coated and heat treated at 400°C for 1 <i>h</i> specimens (HT ₁ -C) and Ni-P-X coated and heat treated at 250°C for 12 <i>h</i> specimens (HT ₂ -C) at different normal loads.	227
Fig. 6.8	Variation of sliding friction coefficient with distance at different loads in commercial aluminium (AL).	227
Fig. 6.9	Variation of sliding friction coefficient with distance at different loads in electroless Ni-P-X as-coated aluminium (AC ₃).	228
Fig. 6.10	Variation of sliding friction coefficient with distance at different loads in electroless Ni-P-X coated and heat treated at 400°C for 1 <i>h</i> specimens (HT ₁ -C).	228
Fig. 6.11	Variation of sliding friction coefficient with distance at different loads in electroless Ni-P-X coated and heat treated at 250°C for 12 <i>h</i> specimens (HT ₂ -C).	231
Fig. 6.12	Variation of coefficient of friction averaged over the distance of sliding during wear in commercial aluminium (AL), electroless Ni-P-X as-coated aluminium (AC ₃), Ni-P-X coated and heat treated at 400°C for 1 <i>h</i> specimens (HT ₁ -C) and Ni-P-X coated and heat treated at 250°C for 12 <i>h</i> specimens (HT ₂ -C).	231
Fig. 6.13	Variation of average coefficient of friction with hardness during wear in commercial aluminium (AL), electroless Ni-P-X as-coated aluminium (AC ₃), Ni-P-X coated and heat treated at 400°C for 1 <i>h</i> specimens (HT ₁ -C) and Ni-P-X coated and heat treated at 250°C for 12 <i>h</i> specimens (HT ₂ -C).	233
Fig. 6.14	Average coefficient of friction vs. $(H_{\text{coating}} \times H_{\text{substrate}})^{1/2}$ in commercial aluminium (AL), electroless Ni-P-X as-coated aluminium (AC ₃), Ni-P-X coated and heat treated at 400°C for 1 <i>h</i> specimens (HT ₁ -C) and Ni-P-X coated and heat treated at 250°C for 12 <i>h</i> specimens (HT ₂ -C) at different normal loads.	233
Fig. 6.15	Wear surfaces of the specimens of aluminium (AL) after sliding through a distance of 600 <i>m</i> at the normal load of (a) 4.9 <i>N</i> , (b) 7.4 <i>N</i> , (c) 9.8 <i>N</i> and (d) 12.3 <i>N</i> .	235
Fig. 6.16	Wear debris of aluminium substrate (AL) after spreading on white paper (a) optical micrograph at magnification of $\times 25$ and (b) SEM micrograph.	236

Fig. 6.17	Wear surfaces of the specimens of electroless Ni-P-X as-coated aluminium (AC ₃) after sliding through (a) 600 <i>m</i> at 4.9 <i>N</i> , (b) 600 <i>m</i> at 7.4 <i>N</i> , (c) 480 <i>m</i> at 9.8 <i>N</i> and (d) 420 <i>m</i> at 12.3 <i>N</i> .	237
Fig. 6.18	Wear debris of electroless Ni-P-X as-coated aluminium (AC ₃) after spreading on white paper (a) optical micrograph at magnification of × 25 and (b) SEM micrograph.	238
Fig. 6.19	Wear surfaces of the specimens of electroless Ni-P-X coated and heat treated at 400°C for 1 <i>h</i> aluminium (HT ₁ -C) after sliding through (a) 600 <i>m</i> at 4.9 <i>N</i> , (b) 600 <i>m</i> at 7.4 <i>N</i> , (c) 480 <i>m</i> at 9.8 <i>N</i> and (d) 420 <i>m</i> at 12.3 <i>N</i> .	240
Fig. 6.20	Wear debris of electroless Ni-P-X coated and heat treated at 400°C for 1 <i>h</i> aluminium specimens (HT ₁ -C) after spreading on white paper (a) optical micrograph at magnification of × 25 and (b) SEM micrograph.	241
Fig. 6.21	Wear surfaces of the specimens of electroless Ni-P-X coated and heat treated at 250°C for 12 <i>h</i> aluminium (HT ₂ -C) after sliding through 600 <i>m</i> at given normal load of (a) 4.9 <i>N</i> , (b) 7.4 <i>N</i> , (c) 9.8 <i>N</i> and (d) 12.3 <i>N</i> .	242
Fig. 6.22	Wear debris of electroless Ni-P-X coated and heat treated at 250°C for 12 <i>h</i> aluminium specimens (HT ₂ -C) after spreading on white paper (a) optical micrograph at magnification of × 25 and (b) SEM micrograph.	243
Fig. 6.23	X-ray diffraction pattern of the wear debris of Ni-P-X as-coated aluminium specimens (AC ₃) generated at all the four loads applied and collected from the disc counterface.	244
Fig. 6.24	X-ray diffraction pattern of the wear debris of Ni-P-X coated and heat treated at 400°C for 1 <i>h</i> (HT ₁ -C) and heat treated at 250°C for 12 <i>h</i> (HT ₂ -C) generated at all the four loads applied and collected from the disc counterface.	244
Fig. 6.25	Comparison of cumulative volume losses in AL, AC ₃ , HT ₁ -C and HT ₂ -C type of wear pin samples with sliding distance at (a) 4.9 <i>N</i> , (b) 7.4 <i>N</i> , (c) 9.8 <i>N</i> and (d) 12.3 <i>N</i> .	246
Fig. 7.1	Photographs of the carbon fabric specimen (A) uncoated, (B) electroless Ni-P as-coated and (C) electroless Ni-P-X as-coated.	253
Fig. 7.2	SEM micrograph of electroless Ni-P-X coated carbon fabric showing the fibers with uniform coating.	253
Fig. 7.3	SEM micrographs of the uncoated carbon fabric in (a) longitudinal view and (b) cross sectional view.	255
Fig. 7.4	SEM micrographs of the electroless Ni-P-X as-coated carbon fabric in (a) longitudinal view (b) cross sectional view and (c) schematic diagram of coated fiber.	256

Fig. 7.5	SEM micrographs of the electroless Ni-P as-coated carbon fabric in (a) longitudinal view and (b) cross sectional view.	257
Fig. 7.6	SEM-EDAX for a typical point on the electroless Ni-P-X as-coated carbon fabric showing the presence of different elements in the composite coating.	259
Fig. 7.7	X-ray diffraction pattern of uncoated carbon fabric substrate.	259
Fig. 7.8	X-ray diffraction pattern of electroless Ni-P-X coated carbon fabric sample in (a) as-coated and (b) heat treated at 400°C for 1 <i>h</i> conditions.	260
Fig. 7.9	X-ray diffraction pattern of electroless Ni-P coated carbon fabric sample in (a) as-coated and (b) heat treated at 400°C for 1 <i>h</i> conditions.	260
Fig. 7.10	Tensile failure loads for different carbon fabric specimens (a) uncoated, (b) Ni-P-X as-coated, (c) Ni-P-X coated and heat treated at 400°C for 1 <i>h</i> , (d) Ni-P as-coated and (e) Ni-P coated and heat treated at 400°C for 1 <i>h</i> .	262
Fig. 7.11	UTS values for carbon fabric samples in uncoated, Ni-P-X as coated, Ni-P-X coated and heat treated, Ni-P as-coated and Ni-P coated and heat treated conditions.	263
Fig. 7.12	Fractographs of the carbon fabric specimens under SEM (a) uncoated, (b) electroless Ni-P-X as-coated and (c) electroless Ni-P-X coated and heat treated at 400°C for 1 <i>h</i> (d) electroless Ni-P as-coated, (e) electroless Ni-P coated and heat treated at 400°C for 1 <i>h</i> .	266
Fig. 7.13	SEM micrographs showing the uncoated carbon fabric zone into aluminium matrix (a) × 500 and (b) × 1000.	267
Fig. 7.14	SEM micrographs showing the electroless Ni-P-X coated carbon fabric zone into aluminium matrix (a) × 500 and (b) × 1000.	267
Fig. 7.15	Uncoated carbon fabric zone into aluminium matrix under EPMA when subjected to X-ray mapping for aluminium.	268
Fig. 7.16	Electroless Ni-P-X coated carbon fabric zone into aluminium matrix under EPMA when subjected to X-ray mapping (a) area selected for mapping, (b) distribution of nickel, (c) distribution of phosphorus and (d) distribution of aluminium.	269

LIST OF TABLES

No.	Title	Page No.
Table 1.1	Electroless Nickel Based Coating Systems and their Properties Studied in Recent Past.	3
Table 2.1	Different Electroless Alloy Coatings Developed and Primarily Referred in the Literature.	8
Table 2.2	Compositions of the Acid Nickel Solutions (pH: 4-6, Temperature: 90-92°C).	10
Table 2.3	Compositions of Alkaline Ammonical Nickel Solutions (pH: 8-9, Temperature: 90-92°C).	11
Table 2.4	Different Electroless Composite Coatings Developed and Primarily Referred in the Literature.	14
Table 2.5	Value of C_1 , C_2 and the Percentage of Error in the Activation Energy, ϵ , Calculated by the Least Square Method According to Eq. (2.21).	28
Table 2.6	Properties of Electroless Nickel Based Coatings.	32
Table 3.1	Bath Components and Operating Conditions for Electroless Coating.	64
Table 3.2	Composition of Purified Argon Gas used for Heat Treatment.	68
Table 3.3	Chemical Composition of Case Harden EN-32 Steel Disc (wt. %).	80
Table 3.4	Different Wear Pin Samples Subjected to Wear and Friction Testing and their Corresponding Designations.	84
Table 4.1	Composition of the Commercially Pure Aluminium (wt. %).	87
Table 4.2	Composition of Low Carbon Normalised Steel (wt. %).	87
Table 4.3	An Experimental Layout using ' L_4 ' Array and Results of the Responses.	88
Table 4.4	ANOVA Table for Experiments Conducted as per the Array ' L_4 ' as Shown in Table 4.3.	89
Table 4.5	Quantitative Analysis of Electroless Ni-P-X Coating.	125
Table 4.6	Quantitative Analysis of Electroless Ni-P Coating.	125
Table 4.7	Composition of Electroless Ni-P-X Coated Sample as Shown in Figs. 4.27 (a) to (c) by Area Scan under SEM-EDAX.	126

Table 4.8	Kinetics Parameters of Transformation in Electroless Ni-P-X and Ni-P Coatings.	144
Table 5.1	The Sliding Distances Selected for Different Types of Wear Pins (NS, AC ₁ , HT ₁ -A, HT ₂ -A, AC ₂ , HT ₁ -B and HT ₂ -B) for the Tests under Different Loads.	165
Table 5.2	Wear Coefficients for Different Types of Wear Pin Samples (NS, AC ₁ , HT ₁ -A, HT ₂ -A, AC ₂ , HT ₁ -B and HT ₂ -B) during Dry Sliding.	176
Table 5.3	Ranges of Fluctuation of Coefficient of Friction (μ) in Different Types of Pin Samples (NS, AC ₁ , HT ₁ -A, HT ₂ -A, AC ₂ , HT ₁ -B and HT ₂ -B) at Specified Loads.	180
Table 6.1	The Sliding Distances Selected for Different Types of Wear Pins (AL, AC ₃ , HT ₁ -C and HT ₂ -C) for the Tests under Different Loads.	218
Table 6.2	Wear Coefficients for Different Types of Wear Pin Samples (AL, AC ₃ , HT ₁ -C and HT ₂ -C) during Dry Sliding.	225
Table 6.3	Ranges of Fluctuation of Coefficient of Friction (μ) in Different Types of Pin Samples (AL, AC ₃ , HT ₁ -C and HT ₂ -C) at Specified Loads.	229
Table 7.1	Specifications of the Carbon Fabric.	252
Table A.1	The Values of n_1 and k_1 for Different Bath Loading Factors.	282
Table A.2	Correlation Factors for Least Square Fit Lines for the $\ln(W)$ vs. $\ln(t)$ Plots for Different Bath Loading Factors.	282
Table A.3	X-Ray Diffraction Analysis for Co-precipitated Powder Showing Phase Constituents Present and Their Characteristics.	283
Table A.4	Results of XRF Analysis of Ni-P-X Coating Showing the Intensities and Position of Different Peaks.	283
Table A.5	X-Ray Diffraction Analysis for Ni-P-X As-coated Film Showing Phase Constituents Present and Their Characteristics.	284
Table A.6	X-Ray Diffraction Analysis for Ni-P As-coated Film Showing Phase Constituents Present and Their Characteristics.	285
Table A.7	Phases Identified by Indexing the SAD Patterns of Ni-P-X Electroless Composite Coatings.	286
Table A.8	X-Ray Diffraction Analysis for Ni-P-X Coated and Heat Treated at 400°C for 1 h Film Showing Phase Constituents Present and Their Characteristics.	287
Table A.9	The Different Phase Constituents Present in Electroless Ni-P Based Coatings Under This Study.	288
Table A.10	Temperatures Observed for the Peak of DSC Curves for Electroless Ni-P-X and Ni-P Coatings.	289

Table A.11	Microhardness of Electroless Ni-P-X and Ni-P Coatings.	289
Table A.12	Microhardness of Different Phases Present in Different Types of Sample used in Wear Testing.	289
Table A.13	Macrohardness of Electroless Ni-P-X and Ni-P Coatings.	290
Table A.14	Microhardness and Macrohardness of the Substrate Materials in Different Conditions.	290
Table A.15	X-Ray Diffraction Analysis for Wear Debris Showing the Characteristics of Phase Constituents Present in NS, AC ₁ , (HT ₁ -A + HT ₂ -A), AC ₃ and (HT ₁ -C + HT ₂ -C) Samples.	291
Table A.16	X-Ray Diffraction Analysis of Uncoated Carbon (C) Fabric Showing Characteristics.	292
Table A.17	The Different Phase Constituents Present in the Electroless Ni-P-X and Ni-P Coated Carbon Fabric.	292

NOMENCLATURE

α	Fraction Transformed
K	Thermally Activated Rate Constant
T	Temperature
n	Avrami Exponent or Reaction Exponent
K_0	Constant (C_0)
E	Activation Energy
R	Universal Gas Constant
β	Heating Rate
T_m	Peak Temperature
α_m	Reacted Fraction at the Maximum of the Reaction Rate
E_a	Apparent Activation Energy
C_1 and C_2	Constants
ϵ	Percentage of Error in the Activation Energy
Q	Wear Volume
P	Applied Load
HV	Microhardness
H_{coating}	Microhardness of Coating
$H_{\text{substrate}}$	Microhardness of Substrate
l	Sliding Distance
θ_c	Contact Angle
θ	Bragg's Angle
λ	Wavelength
R_i	Radius of the Rings Observed in SAD Pattern, $i = 1, 2, 3, \dots$
L	Camera Constant
F	Degrees of Freedom
s	Sum of Squares
V	Mean Square Variance
F_1	Variance Ratio
P_c	Percent Contribution
r_1	Ratio of Weight of AlCl_3 to that of $\text{ZrOCl}_2 \cdot 8\text{H}_2\text{O}$
W	Coating Weight

7. **S. B. Sharma**, R. C. Agarwala, V. Agarwala and S. Ray, "Wear and Friction Behaviour of Ni-P-ZrO₂-Al₂O₃ Composite Electroless Coatings", Proc. *International Conference in Mechanical Engineering*, Dec. 26-28, 2001, BUIT, Dhaka (2001).
8. R. C. Agarwala, V. Agarwala and **S. B. Sharma**. " A Study on Electroless Ni-P based Composite Coatings by Co-Deposition of Hard Particles", Proc. *National Seminar, Advances in Materials and Processing*, Nov. 9-10, 2001, Metallurgical and Materials Engineering Dept., IIT, Roorkee, Eds. S. Ray *et al.*, pp. 172-179 (2001).
9. Satyanarayana, K. G., Agarwala, R. C., Agarwala, V. and **Sharma, S. B.**, "Ni-P-Al₂O₃-Al₃Zr-ZrO₂: Co-precipitation of Alumina-Zirconia followed by Co-deposition", Indian Patent Application filed through CSIR Lab., India, No. 100/Del/2001, appeared in the *Gazette of India, Part III – Sec. 2*, May 19, 2001.
10. R. C. Agarwala, V. Agarwala and **S. B. Sharma**, "Engineering Surface Preparation by Electroless Nickel based Coating Technology: A Promising Area in Industrial Applications", Proc. *Institute Industry Interaction Meet on Metal Matrix Composites*, Oct 9, 1999, Metallurgical and Materials Engineering Dept., University of Roorkee, (now Indian Institute of Technology), Roorkee, Eds. Agarwala *et al.*, pp. 32-40 (1999).

Chapter 1

INTRODUCTION

The metallic nickel from aqueous solution in presence of hypophosphite was first deposited on steel by Wurtz in 1885. After its illustrious re-discovery by Brenner and Riddell in 1946 interest of the scientific community was aroused, which resulted in a large number of investigations on various aspects of these fascinating novel materials. By the controlled chemical reduction reaction, the electroless coating chemistry has emerged as one of the leading growth areas in surface engineering, metal finishing etc., and is estimated to grow at a rate of beyond fifteen percent per annum. It is one of the most suitable methods to produce amorphous coatings, which is found to be extensively adopted since seventies and is yet to reach its peak potential. The process of electroless deposition is also one of the most elegant methods available for production of alloy coatings (Gillespie, 1996). Electroless nickel is a chemically formed compound or solid solution of nickel and phosphorus. It is metallurgically different from electroplated nickel and even electroplated nickel/phosphorus alloy. The electroplated coatings are chemically crystalline in nature while electroless formed coatings vary from poorly defined crystalline solid to a completely non-crystalline solid, depending on the amount of phosphorus in the coating. Electroless nickel coating can be satisfactory and cost effective, competing with electrolytic nickel plating for brightness and chromium plating for hardness and wear resistance when properly designed for service (Groshart, 1983).

Electroless coatings are being used increasingly because of their unique physicochemical and mechanical properties. The electroless deposition can provide uniform thickness of the coating, ranging from 2.5 to 500 μm , even on the complex geometrical components over the whole area, unlike electroplating which provides uneven thickness of coating at corners and awkwardly located areas (Husheng *et al.*, 1991; Gawne and Ma, 1989). A substantial portion of the increasing usage of electroless nickel is at the

Reliability, efficiency and longer service life are imperative for any engineering system, which entails the use of appropriate engineering materials. One of the basic requirements of the engineering system, the *wear*, is often considered as a criterion for the efficient and the reliable service life of the engineering system. Wear contributes a substantial cost every year in the industries as well as in day to day life. The component replacement/repair resulting due to wear also has an indirect effect on profit ratio of an industry, which includes plant shut down, lead time, efficiency, sustaining the production schedules, extra investments etc. Indeed the friction and wear behaviour of surfaces is often critical to the performance of industrial equipment due to this reason a considerable amount of effort has been expended in developing coating and surface treatments for tribological applications. Therefore, it becomes critically important in the testing of coated components where the presence of the coating can change the operating wear mechanism (Bull, 1997). Electroless composite coatings possess better resistance to wear (Henry, 1985 and Apachitei *et al.*, 1998/1). Therefore the thrust is increasingly being given on the development of new composite coating system and understanding of their tribological behaviour, which may ^{influence} profoundly the field of their applications.

Composite coatings consist of solid particles incorporated in a metallic matrix. This can be obtained by maintaining particles in suspension in the bath either by mechanical or chemical means (Grosjean *et al.*, 1997). Development of new coatings, or selection of coatings for tribological applications, requires knowledge of tribological properties of coating composites, which could be obtained through basic properties. In practice, however, there is as yet no general theory available to link the basic properties with the tribological response. The consolidation of tribological data for coatings is difficult due to vast array of parameters involved and tribologically induced change of the critical material properties, combined with the number of different situations of mechanical, thermal and chemical loads encountered in tribological applications (Hogmark *et al.*, 1997).

2.1 INTRODUCTION

Electroless coating technology is credited mainly to Brenner and Riddell (1946). By the controlled chemical reduction reaction, the electroless coating chemistry has emerged as one of the leading growth areas in surface engineering, metal finishing etc., and is estimated to grow at a rate of beyond fifteen percent per annum, certainly no other chemistry is growing at this rate. Electroless coatings have unique physicochemical and mechanical properties for which they are being used increasingly. Some of the properties which render them usable are: uniformity ($\pm 2.5 \mu m$), excellent corrosion resistance, wear and abrasion resistance, solderability, high hardness, amorphous/microcrystalline deposit, low coefficient of friction, resistivity and magnetic properties. Most applications of the electroless coatings investigated are based on their wear and corrosion resistance.

2.2 DEVELOPMENT OF ELECTROLESS DEPOSITION

The metallic nickel from aqueous solution in presence of hypophosphite was first noted in 1844 as a chemical curiosity by Wurtz. Later, Breteau, in 1911 had almost inevitably precipitated the metal in powder form, which was deposited on the surface of reaction vessels, as bright coatings. A similar work led to further development by Roux in 1946 as proclaimed in the work of Gillespie (1996). However, during the infant stages of this process, further developments were not carried out until its fortuitous re-discovery by Brenner and Riddell (1946). The composite coatings, were first carried out in pursuing for improved corrosion resistance for electrodeposited nickel-chromium by Odekerken (1966), in which an intermediate layer, containing finely divided particles including: aluminum oxide and polyvinyl chloride resin (PVC) distributed within a metallic matrix. Further, electroless nickel coating containing alumina (Al_2O_3) particles was enunciated by Metzger *et al.* in

1966. Also their efforts credited first commercial application of electroless Ni-SiC coating on the Wankel (rotary) internal combustion engine. In the due course of time, in 1981, a commercial composite coating with PTFE was introduced. In contrast to the difficulties encountered with diamond and polytetrafluoroethylene (PTFE) particles, composites incorporating aluminum oxide or silicon carbide were achieved without serious difficulties (Feldstein, *et al.*, 1983).

2.3 CLASSIFICATION OF ELECTROLESS COATINGS

Electroless amorphous binary Ni-P/ (B) and Co-P/ (B) alloy deposits are applied widely in industrial usage owing to their excellent properties. Further exploitation of applications of ternary and quaternary electroless nickel, cobalt-base alloys are also becoming important to work with (Wang *et al.*, 1997). Apart from such alloy coating systems, Ni-P matrix composites with dispersion of fine particles have been a subject of interest since the early eighties. However, the work described in the literature is mainly of technological in nature and no systematic correlation between structure and properties has appeared till date (Bozzini, *et al.*, 1999). Therefore, it is fairly reasonable to classify the electroless coatings as: (i) Alloy coatings, (ii) Composite coatings and (iii) Metallic coatings.

2.3.1 Alloy Coatings

Apart from plating by reduction reaction, two other methods have also been reported, these include immersion plating on steel from solutions of nickel chloride and boric acid, and decomposition of nickel carbonyl vapour on steel substrate (Gaurilow, 1979). However, the latter is hazardous and the former is a poor adherent and non protective. The advantage of using autocatalytic reduction reaction is for maintaining overall uniformity of coating in composition and thickness which is independent of the roughness of the substrate (Agarwala, 1987). Several binary and ternary alloys have been deposited (Table 2.1). Different alloys have been coated for desired physical and mechanical properties. Nickel ^{stands} stems out to be the single widely coated element with phosphorus.

Table 2.1 Different Electroless Alloy Coatings Developed and Primarily Referred in the Literature.

Coating Alloy	Reference and Year
Ni-P	Brenner and Riddell, 1946; Graham <i>et al.</i> , 1962 and 1965; Henry, 1985; Harris <i>et al.</i> , 1985; Bakonyi <i>et al.</i> , 1986; Agarwala, 1987; Husheng <i>et al.</i> , 1991; Andre <i>et al.</i> , 1993; Puchi <i>et al.</i> , 1997; Chitty <i>et al.</i> , 1997; Bozzini and Boniardi, 1997; Bozzini <i>et al.</i> , 1999; Balaraju and Seshadri, 1999; Zhang <i>et al.</i> , 1998/1; and Apachitei and Duszczuk, 2000.
Ni-B	Datta <i>et al.</i> , 1991; Bedingfield <i>et al.</i> , 1991; Srivastava <i>et al.</i> , 1992; Giampaolo <i>et al.</i> , 1997 and Vasudevan <i>et al.</i> , 1998.
Ni-Cu-P,	Gorbunova <i>et al.</i> , 1966.
Ni-Re-P	
Ni-W-P	Pearlstein <i>et al.</i> , 1963 and Li <i>et al.</i> , 1996.
Co-P,	Brenner, 1963.
Co-B	
Ni-Co-P	Wang <i>et al.</i> , 1997 and Kim, <i>et al.</i> , 1995.
Fe-Sn-B,	Wang <i>et al.</i> , 1997 and 1999.
Fe-W-B,	
Fe-Mo -W-B	
Ni-Sn-Cu-P	Bangwei <i>et al.</i> , 1999.
Fe-Mo-W-B	Wang <i>et al.</i> , 1997.

2.3.1.1 Bath Composition and Characteristics

Mainly two types of baths are being used for depositing alloys, viz., acidic and alkaline baths. Electroless alloy coatings are produced by the controlled chemical reduction of metallic ions onto a catalytic surface, the deposit/coating itself is catalytic to reduction reaction and the reaction continues as long as the surface remains in contact with the bath solution or the solution gets depleted of solute metallic ions (Gaurilow, 1979). The coating is uniform throughout the contours of the substrate because no electric current is used. Therefore, all parts of the surface area of substrate, which are equally immersed in the bath, have equal probability of getting an ion deposited.

The electrolytic bath characteristics have been considered by taking nickel as an example. A source of nickel ions, usually nickel sulphate or nickel chloride is used. Besides this, electroless bath solution comprises of different chemicals each performing an

important function as: (a) a reducing agent to supply electrons for the reduction of nickel, (b) energy (heat) and (c) complexing agents to control the free nickel available to the reaction (Agarwala, 1987).

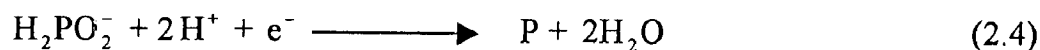
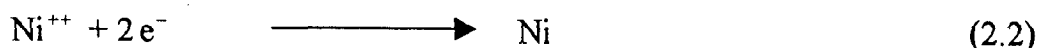
(a) Reducing agents

Four types of reducing agents are mostly used in electroless alloy coatings for electroless nickel bath, such as (i) sodium hypophosphite, (ii) amineboranes, (iii) sodium borohydride and (iv) hydrazine.

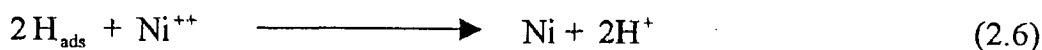
(i) Sodium hypophosphite baths

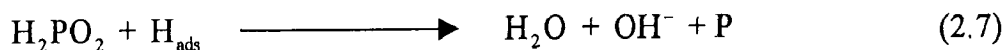
More than 70% electroless nickel is deposited from solutions reduced by sodium hypophosphite. The main advantages of these solutions over the solutions reduced by borohydride or hydrazine include lower costs, greater ease of process control etc. Several mechanisms have been proposed for the chemical reactions that occur in hypophosphite reduced electroless nickel plating solutions. Most widely accepted mechanisms are illustrated by the following equations (Gutzeit, 1959).

Electrochemical mechanism, where catalytic oxidation of the hypophosphite yields electrons at the catalytic surface which in turn reduces nickel and hydrogen ions as is illustrated below:

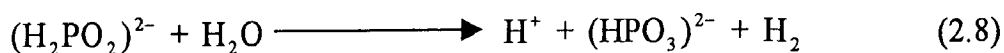


Atomic hydrogen mechanism, where atomic hydrogen is released as a result of the catalytic dehydrogenation of hypophosphite molecule adsorbed at the surface as is illustrated below:





The adsorbed active hydrogen, as illustrated by Eq. (2.5), then reduces nickel at the surface of the catalyst.



Simultaneously, some of the adsorbed hydrogen reduces a small amount of the hypophosphite at the catalytic surface to water, hydroxyl ion and phosphorus. Most of the hypophosphite present is catalytic, which oxidise to orthophosphite and gaseous hydrogen, Eq. (2.7), causing low efficiency of electroless nickel solutions for alloy coating while the deposition of nickel and phosphorus continues. Usually, 5 kg of sodium hypophosphite is required to reduce 1 kg of nickel, for an average efficiency of 37% (Gaurilow, 1979; Mallory, 1974). The coefficient of utilisation of hypophosphite vary a little with the nature of buffer additive; the highest degree of utilisation of the hypophosphite was observed in the solution containing sodium acetate, the lowest is that with sodium citrate. The main characteristic of the process is the change in the composition of the solution. The concentration of nickel salt and hypophosphite is decreased and the concentration of acid is increased during the progress of deposition. This causes the lowering of deposition rate (Mallory, 1974). Tables 2.2 and 2.3 provide the different compositions of the bath used respectively for nickel coating in acidic and alkaline baths (Agarwala, 1987; Brenner and Riddell, 1947).

Table 2.2 Compositions of the Acid Nickel Solutions (pH: 4-6, Temperature: 90-92°C).

Components of the Bath	Concentration g/l			
	I	II	III	IV
Nickel chloride, NiCl ₂ .6H ₂ O	30	30	30	-
Nickel sulphate, NiSO ₄ .7H ₂ O	-	-	-	30
Sodium hypophosphite, NaH ₂ PO ₂ .H ₂ O	10	10	10	10
Sodium glycolate, CH ₂ OHCOONa	50	10	-	-
Sodium acetate CH ₃ COONa.3H ₂ O	-	-	-	10
Sodium citrate, Na ₃ C ₆ H ₅ O ₇ . 5 ¹ / ₂ H ₂ O	-	-	10	-
General appearance of the coating	Semi-bright	Semi-bright	Semi-bright	Coarse uneven

Table 2.3 Compositions of Alkaline Ammonical Nickel Solutions (pH: 8-9, Temperature: 90-92°C).

Components of the Bath	Concentration g/l		
	I	II	III
Nickel chloride, NiCl ₂ ·6H ₂ O	30	30	30
Sodium hypophosphite, NaH ₂ PO ₂ ·H ₂ O	10	10	10
Ammonium chloride, NH ₄ Cl	50	100	--
Sodium citrate, Na ₃ C ₆ H ₅ O ₇ ·5½H ₂ O	100	--	100
Appearance of the coating	Medium Dark	Bright	Bright

(ii) Amineborane baths

Use of amineboranes in electroless Ni plating solutions are limited to two compounds: N-dimethylamine borane (DMAB) – (CH₃)₂NHBH₃, and H-diethylamine borane (DEAB) – (C₂H₅)₂NHBH₃ (Gaurilow, 1979; Mallory, 1979). DMAB is readily soluble in aqueous solutions while DEAB should be mixed with a short chain aliphatic alcohol such as ethanol, before mixing into plating bath. The amineboranes are effective reducing agents over a wide range of pH but due to evolution of hydrogen, there exists a lower limit of pH up to which the plating process can be carried out (Mallory, 1979). Nickel, in the deposit increases as pH of the bath increases. Usually, the amineborane baths have been used in the pH range of 6.0-9.0. Operating temperatures for these baths range from 50-80°C, however, they can also be used at temperature as low as 30°C. Accordingly, amineborane baths are very useful for plating non-catalytic surfaces such as plastics, nonmetals, which are their primary applications. The rate of deposition varies with pH and temperature, and it is usually in the range of 7-12 μm/h.

(iii) Sodium borohydride baths

The borohydride ion is the most powerful reducing agent available for electroless nickel plating. Any water soluble borohydride can be used, however, for optimum results sodium borohydride is preferred (Mallory, 1974). In acid or neutral solutions, hydrolysis of

borohydride ions is very rapid. In the presence of nickel ions, nickel boride may form spontaneously. If the pH of the solutions is maintained between 12 to 14, then the formation of nickel boride is suppressed and the reaction product consists of principally elemental nickel. One mol of sodium borohydride can reduce approximately one mol of nickel, therefore, it can be deduced that the reduction of 1 kg of nickel requires 0.6 kg of sodium borohydride while 5 kg of hypophosphite is required for the same nickel. Deposits from borohydride reduced electroless nickel contains 3 to 8 wt.% boron. To prevent precipitation of nickel hydroxide, complexing agents such as ethylenediamine, that are effective between 12 to 14 pH must be used. The presence of such complexing agent however reduces the reaction rate, thereby, lowering the rate of deposition. The rate of deposition at 90°C operating temperature of the baths, lies somewhere 25 to 30 $\mu\text{m}/\text{h}$.

During the course of reduction, the solution pH invariably decreases, requiring continuous additions of an alkali hydroxide. However, the highly alkaline nature of these baths poses difficulties to use for aluminium substrates.

(iv) Hydrazine baths

Hydrazine has also been used to produce the electroless nickel deposits (Levy, 1963). These baths operate in the temperature range between 90-95°C and at a pH range of 10-11. Their rate of deposition is approximately 12 $\mu\text{m}/\text{h}$. Because of the instability of hydrazine at high temperatures, these baths tend to be very unstable and difficult to control. The deposit contains high nickel content but does not have metallic appearance. These deposits are brittle and highly stressed for practical applications.

(b) Energy

Amount of energy or temperature of the electroless nickel solutions is one of the important factors affecting the rate of deposition. The rate of deposition is low at temperatures below 65°C, and increases with the increasing temperature. This is true for almost all the electroless nickel coating systems. Generally the operating temperature is about 90°C, above which the bath tends to become unstable (Baudrand, 1994).

(c) Complexing agents

One of the difficulties of reduction reaction or chemical plating is maintaining the bath composition, as the plating proceeds continuous lowering of the rate of reduction of nickel occurs. The solution cannot be replenished due to the formation of nickel phosphite. If nickel phosphite is precipitated in the bath, the surface quality of coating deteriorates resulting in rough and dark coatings. Moreover, the nickel concentration in the solution also decreases and the bath gets on to the verge of total decomposition. Sodium citrate reduces the formation of nickel phosphite and reduces the rate of deposition (Gutzeit, 1959). The ability to form nickel complexes have been attributed to some of the proposed additives like salts of glycolic, succinic or malonic acids, however, these fail to stop the precipitation of nickel phosphite.

The best results are obtained when the sodium citrate concentration is about 30 g/l. It helps in checking the coating to become porous and dull. As the reduction in the rate of deposition, accelerators like salts of carbonic acids, soluble fluorides and inhibitors like thiourea can also be added to avoid the total decomposition of bath.

2.3.2 Composite Coating

The co-deposition of a few particulate matter with electroless nickel coatings dates back to 1960's (Odekerken, 1966). In this pursuit, for improvising corrosion resistance, for nickel chromium electrodeposits, an intermediate layer containing finely divided Al_2O_3 and PVC particles distributed within a metallic matrix is used. This intermediate layer has been deposited using electroless coating technique. Various systems have been used for obtaining composite coatings have been shown in Table 2.4.

Electroless composite coating uses the conventional reduction reaction process with the suspension of particles. Generally, co-deposition of particle concentration in deposits of electroless coatings depend on various factors, like bath chemistry, particle characterisation, operating conditions etc. Each combination between a certain type of particles and the Ni-P matrix can lead to a new set of properties (Apachitei *et al.*, 1998/2).

Table 2.4 Different Electroless Composite Coatings Developed and Primarily Referred in the Literature.

Composite Coating	Reference and Year
Ni-P-Al ₂ O ₃	Odekerken, 1966 and Apachitei <i>et al.</i> , 1998/2.
Ni-P-SiC	Apachitei <i>et al.</i> , 1998/2; Li, 1997 and Grosjean <i>et al.</i> , 1997.
Ni-P-B ₄ C	Ge <i>et al.</i> , 1998 and Bozzini <i>et al.</i> , 1999.
Ni-P-B	Apachitei <i>et al.</i> , 1998/2.
Ni-P-C	Cziraki <i>et al.</i> , 1980.
Ni-P-PTFE	Narayan and Pandey, 1997; Pena-Munoz <i>et al.</i> , 1998 and Zhang <i>et al.</i> , 1998/2.
Ni-P-MoS ₂	Moonir-Vaghefi <i>et al.</i> , 1997.

2.3.2.1 Classification of Composite Electroless Coating Systems

The composite coating system can be subdivided into two groups: (a) co-deposition of hard particles and (b) co-deposition of soft particles. In this section an attempt is made to summarise the available literature on the composite electroless coatings.

(a) Co-deposition of hard particles

Co-deposition of the hard particles, with high hardness properties, into electroless nickel coatings can be effected in order to produce surfaces with extended wear protection. Gillespie (1996), reported that particles of silicon carbide (SiC), tungsten carbide (WC) and diamond (C) can be successfully entrapped within electroless deposit matrices in order to impart wear properties required for certain specialist cutting tool applications. The compatibility of a specific particle within a metallic matrix is dependent not only on chemical nature of particles and size but also on their physical form (Feldstein *et al.*, 1983). The co-deposition of SiC particles in Ni-P matrix has also been reported by Lanzoni and Martini (2000). Apachitei *et al.* (1998/1) reported that the composite coatings are sensitive to a few parameters related to the particle characteristics including shape, density, hardness, size and particle concentration.

Bozzini *et al.* (1999) reported that the presence of B₄C in Ni-P matrix enhances the crystallisation kinetics by providing nucleation sites for the precipitation of nickel in the amorphous matrix. However, Apachitei *et al.* (1998/1) indicated that for explaining the relationship between different types of particles and deposit characteristics, other than general particle characteristics such as geometry, hydrophilic and hydrophobic nature of the particles etc., a few more factors should be investigated, which include bath chemistry, particle-surfactant interaction, agitation method, rate of agitation, substrate position and movement.

(b) Co-deposition of soft particles

Co-deposition of soft particles to get electroless composite coatings normally include the dry lubricant particles namely, polytetrafluoroethylene (PTFE), molybdenum disulfide (MoS₂) and graphite (Apachitei *et al.*, 1998/1). The inclusion of PTFE particles into conventional electroless coatings has the effect of providing low friction coefficients, this is of concern where excellent wear resistance is the primary criterion for the choice of a coating. This advantage is, unfortunately, offset by a substantial reduction in corrosion protection (Gillespie, 1996). The major problems associated with co-deposition of PTFE include its non-wetting characteristic and when it is wetted, particles tend to agglomerate unless suitable dispersants are used. However, stable dispersants should not be used, otherwise the particles will not be incorporated into the deposited matrix. Use of an aqueous dispersion of positively charged PTFE resin particles solves this problem. The Ni-P-MoS₂ electroless composite coating on steel substrate can be obtained by the use of commercial hypophosphite based electroless Ni-P bath at 90°C and pH 4 - 6, in which the MoS₂ particles are wetted with a surfactant (Moonir-Vaghefi *et al.*, 1997). The Ni/MoS₂ composite brush plating layer and its tribological behaviour in vacuum has been reported by Zang *et al.* (1992). This research revealed that, grain boundaries between the MoS₂ and Nickel phases are fully continuous without voids in it. This is an indication of the fact that, the MoS₂ and Nickel phases do not form a mechanical compound in the plating layer but they are bonded very closely in the co-deposition process. In the plating solution, the

suspended MoS₂ particles can primarily adsorb Ni²⁺ ions on their surface resulting in the fine structure of such Ni-MoS₂ coating.

2.3.3 Metallic Coatings

The plating bath contains a source of metallic ions, a reducing agent, complexing agent and a stabiliser. Copper sulphates, acetates, or nitrates are used as a source of copper ions. The reducing agent generally used is formaldehyde, but other reducing agents like DMAB, sodium hypophosphite etc. can also be used. Sodium hydroxide and potassium tartrate are generally used as complexing agents while thiourea or vanadium oxide is used as bath stabiliser. The metallic coating can also be carried out by use of the electroless baths in the range of temperature from the room temperature to 70°C. The pH should be maintained at higher level, as high as 12 to obtain bright coatings, however, the bath is more stable at pH of about 9.0 (Henry, 1985).

Electroless copper coatings are being used before electroplating on plastics, ceramics, polymers and other non-conducting materials (Henry, 1985; Pedraza and Godbole, 1990 and Ramasubramanian *et al.*, 1999). Electroless copper coating is also utilised for shielding electronic devices. The thickness of these coatings generally varies from 0.12 to 3.0 μm .

2.4 FACTORS AFFECTING COATING PROCESS

The performance of coating not only depends upon the bath constituents and its chemistry but also on a few allied factors pertaining to electroless coating process viz., pH, operating temperature, bath loading factor etc. The process performance can be appreciated by the study of different properties, which have direct/indirect effect on the above mentioned operating parameters. In this respect, the effect of nickel sulphate, sodium hypophosphite, pH, operating temperature, bath loading factor and plating time has been summarised in the following part of this section.

The variation in nickel salt concentration has no noticeable influence on the rate of reduction of nickel but the variation in the hypophosphite concentration affects the process

considerably. Very high nickel concentration in the bath may make the bath turbid due to hydrolysis of Ni^{2+} , therefore, about 30-40 g/l concentration is practically used. Although increase in the hypophosphite concentrations improves the rate of reduction of nickel, extra amounts of the reducing agents should not be used as this may cause the reduction to take place in bulk of the solution. The appropriate amount of hypophosphite can be adjusted by observing the bath condition during the course of reaction. Weak hydrogen evolution is an indication of a low concentration of hypophosphite and a vigorous hydrogen evolution indicates excess hypophosphite (Gorbunova and Nikiforova, 1963). As the alkalinity of the solutions increases, the nickel content of the deposit increases or the phosphorus content decreases. Phosphorous may be present as a phosphide or as solid solution. The concentration of nickel salts has slight influence on the rate of deposition. Large concentration of the nickel salts causes deterioration in the quality of the coatings as it results in the formation of rough deposits. Sulphate and chloride baths are used for depositing amorphous alloys. The results are found to be systematic by use of the sulphate baths while with chloride baths, the results are arbitrary (Cziraki *et al.*, 1980).

Due to the evolution of hydrogen gas during the plating process, the solution pH will decrease (Apachitei and Duszczuk, 1999). Most of the electroless nickel processes contain buffers to minimise pH swings, however, periodic additions of ammonia to maintain the pH within the operating limits is required. The pH is inversely proportional to deposit phosphorus content, that is to say, the higher the pH, lower the phosphorus content and vice-versa. The role that phosphorus content plays in deposit characteristics is well documented. Because pH has such a profound effect on phosphorus content, it is clear that monitoring and controlling of solution pH is critical in producing a consistent, high quality electroless nickel deposit. Increasing pH increases plating rate, but it decreases bath stability and also results in decreased phosphite solubility.

The rate of the process increases with increase in temperature and attains a maximum at about 92°C. Beyond this temperature, it becomes difficult to maintain the pH of the solution and, therefore, the quality of the coating deteriorates.

The bath loading is one of the most important variables affecting the performance of an electroless nickel process. This term is defined as the ratio of total exposed surface area being plated to the volume of plating solution in the tank. It has a profound influence on coating rate and as well as on phosphorus content of the resulting coating. In practice, it is seen that the coating thickness, of Ni-P deposits, tends towards an optimum value after which the coating rate starts reducing therefore, an inverse relationship between this limiting value for a given situation and the corresponding bath loading parameter does exist (Gillespie, 1996).

2.5 STRUCTURE OF ELECTROLESS COATING

2.5.1 As-Coated Electroless Nickel Coatings

During deposition of electroless nickel films, the growth of the film starts at isolated locations on the substrate and complete substrate is then covered by lateral growth (Agarwala, 1987). The alloys containing lower phosphorus concentrations are characterised by the presence of crystalline and microcrystalline nickel, which indicates that the number of phosphorus atoms are not sufficient to distort the nickel lattice to an extent where amorphous nickel can be obtained. However, some very small pockets of amorphous nickel have been observed in coatings having 10.8 at.% P (Agarwala and Ray, 1988; Hur *et al.*, 1990 and Bozzini and Cavallotti, 1997). But an increase in phosphorous content to 23.4 at.% causes an increase in amorphous nickel region, due to the increase in lattice distortion caused by phosphorus atoms situated in the interstitial position of nickel. In as-coated films a number of crystalline nonequilibrium phases like Ni_{12}P_5 , Ni_5P_2 etc., have also been observed by Agarwala (1987). Appearance of a number of phases may be due to the compositional inhomogeneities

prevailing in the film in as-coated state. The presence of inhomogeneities in electroless films may energetically as well as kinetically favour different local equilibria in different regions of the film leading to the formation of different phases depending on the actual composition.

2.5.2 Heat Treated Electroless Nickel Coatings

When electroless nickel films of different phosphorus contents are heat treated at various temperatures, the phases present in the as-coated films undergo definite structural changes (Hur *et al.*, 1990). The crystallisation behaviour of electroless Ni-P film can be tentatively divided into two broad categories: (i) alloys having microcrystalline nickel as a major constituent in the as-coated state and (ii) alloys constituted mainly of an amorphous phase which do not have microcrystalline nickel as major constituent. The alloy containing 10.8 at.% P contains microcrystalline nickel as a major constituent. When this alloy is heat treated at lower temperature range of 200 to 300°C for 4 h, Ni₁₂P₅, microcrystalline nickel, and Ni₃P are seen as common phases at all temperatures. While after annealing at higher temperatures, i.e., 400 and 600°C, the commonly observed phases are crystalline nickel and Ni₃P. From this, the following can be inferred: Crystalline nickel and Ni₃P are the phases, which are obtained after complete crystallisation of the alloy (Bakonyi *et al.*, 1986). The formation of the transition phase Ni₁₂P₅ may be taken as the common characteristic transition precipitate formed while heating electroless microcrystalline nickel in the temperature range of 200 to 300°C. However, the precipitates other than Ni₃P are metastable transition phases because on continued heating for very long time periods, the precipitates disappear or transform to equilibrium Ni₃P. This observation is made by Makhsoos *et al.* (1978) for ED Ni-P films, which however, does not show such multiplicity of transition phases.

Several transition phases have been observed to form during heating of amorphous Ni-P films in as-coated state, at low temperatures. In case of Ni 14.3 at.% P film, the

transition precipitates from the amorphous phase formed in the temperature range of 250 to 300°C are Ni_5P_4 and Ni_2P . The presence of the transition phase, Ni_{12}P_5 , at lower temperatures has been attributed to the presence of microcrystalline nickel in the as-coated Ni-P films. But in case of Ni-17.8 at.% P films, the transition precipitate Ni_5P_2 is formed during annealing in the temperature range of 200 to 300°C. Therefore, formation of precipitates from the amorphous phase depends on the overall composition of the film or more particularly, on the composition of the amorphous phase. It is further indicated that just by the presence of Ni_{12}P_5 alone during annealing of an alloy containing 19.8 at.% P at low temperatures of 200 to 300°C, it can not be presumed that these precipitates have solely come from the annealing of minor amounts of microcrystalline phases but Ni_{12}P_5 partially could have been formed from the amorphous phase at this composition of the film. Ni_7P_3 is observed in the alloy containing 22.4 at.% P during low temperature annealing but in the films containing 23.4 at.% P, only equilibrium precipitates of Ni_3P are seen even at lower temperature of 200 to 250°C annealing (Agarwala, 1987; Hur *et al.*, 1990).

Hur *et al.* (1990) indicated that the formation of a particular transition phase from the amorphous phase depends on the composition. All these transition phases start to disappear and the stable Ni_3P phase forms at about 250 to 300°C. The temperature at the start of this transformation decreases with increasing phosphorus content and for films containing 23.4 at.% P, this temperature is even below 200°C. At temperatures above 350°C, there exists only two stable phases that are crystalline nickel and Ni_3P for all the films investigated, irrespective of their composition.

Irrespective of phosphorus content of the deposit and the phases present in the as-coated films, during the course of heat treatment all the phases undergo through an intermediate metastable phase before becoming Ni_3P . So at the end of the heat treatment, i.e., when the equilibrium state has attained, only two phases namely crystalline nickel and Ni_3P are observed (Hur *et al.*, 1990; Agarwala and Ray, 1992).

2.6 CRYSTALLISATION OF ELECTROLESS COATINGS

The amorphous and microcrystalline nature of as-coated electroless coatings are metastable and hence amorphous to crystalline transformation occurs at moderate temperature between 240-400°C (Mahoney and Dynes, 1985). Such crystallisation frequently involves transient formation of metastable crystalline phases prior to the formation of equilibrium phases (Masumoto and Maddin, 1975).

2.6.1 Sequence of Crystallisation of Ni-P Coatings

The crystallisation is identified as the peak positions on the DSC plots. The extent of crystallinity affects resultant properties and is a complex function of number of factors including: (i) temperature and time, (ii) heating rate, (iii) previous heat treatment history and (iv) phosphorus content. An understanding of thermal response as a function of phosphorus content is helpful in explaining differences which are reported for the properties of electroless nickel (Mahoney and Dynes, 1985).

The DSC curves for different electroless nickel coatings containing 6.3, 10.1, 11.5, 12.5 and 13.6 wt.% P are shown in Figs. 2.1 (a) to (e) respectively. The temperature of exothermic peaks in the DSC curves, as shown in above figures for the electroless nickel deposits, are shown as a function of phosphorus content in Fig. 2.2 which reveals the DSC data obtained by Hur *et al.* (1990). The DSC results obtained for electrodeposited and electroless Ni-P alloys have similar trend, as seen from Fig. 2.2.

The crystalline sequence has been studied by DSC data obtained from peak(s) observed for a specific electroless nickel coating. The crystallisation may be completed at a temperature corresponding to the main peak. Before occurrence of the peak, the matrix is amorphous and crystallisation commences in small pockets, which gives rise to a broad peak prior to the appearance of main peak as seen in Figs. 2.1 (b) and (c). Whereas such broad peak appears after the main peak at higher phosphorus content (Fig. 2.1 e). The second broader peak is attributed to the recrystallisation or grain growth process

(Agarwala, 1987). However, when a single broad peak is observed in DSC curve, as seen in Figs. 2.1 (a) and (d), the complete crystallisation occurs at the peak temperature.

2.6.2 Kinetics of Crystallisation

Since the crystallisation of metallic glass is a highly exothermic process, DSC is a very suitable means of studying the kinetics of crystallisation. The uses of this technique for crystallisation studies of electroless Ni-P coatings have been widely adopted (Allen *et al.*, 1982; Mahoney and Dynes, 1985; Criado and Ortega, 1987; Agarwala and Ray, 1988; Hur *et al.*, 1990 and Bozzini and Cavallotti, 1997).

The amorphous samples show two transformation peaks, both of which are simple and well defined, but the appearance of more than two transformation peaks may be considered to be a phenomenon caused by a large difference in phosphorus concentration along the thickness of the layer or by some other structural inhomogeneity. The work of Hur *et al.* (1990) revealed that when phosphorus content is less, i.e., for 10 wt.% in Ni-P deposits, a small peak at about 400°C occur and for its content more than 10 wt.%, a very well defined DSC peak at 340°C precedes by a broad peak ranging from 200-300°C. The first of the above mentioned peaks in phosphorus content less than 10 wt.% corresponds to crystallization of the supersaturated microcrystalline to Ni₃P phase while in the later case, the peaks represent the *fcc* nickel crystallites precipitated in amorphous matrix followed by other peak for decomposition of the remaining phosphorus-rich amorphous matrix into Ni₃P and nickel crystallites. The temperatures of exothermic peaks in DSC curves for electroless Ni-P deposits as a function of its phosphorus content is shown in Fig. 2.2, which encompasses the comprehensive data from literature.

On the basis of the results of DSC analysis, X-ray diffraction and hot stage TEM analysis have been used to evolve a schematic drawing of hypothetical free energy diagram for the phases involved in the electroless Ni-P alloys which is shown in Fig. 2.3 (Hur *et al.*, 1990). The observed reactions have been indicated by arrows. The majority of the reactions involved can be studied with respect to phosphorus content.

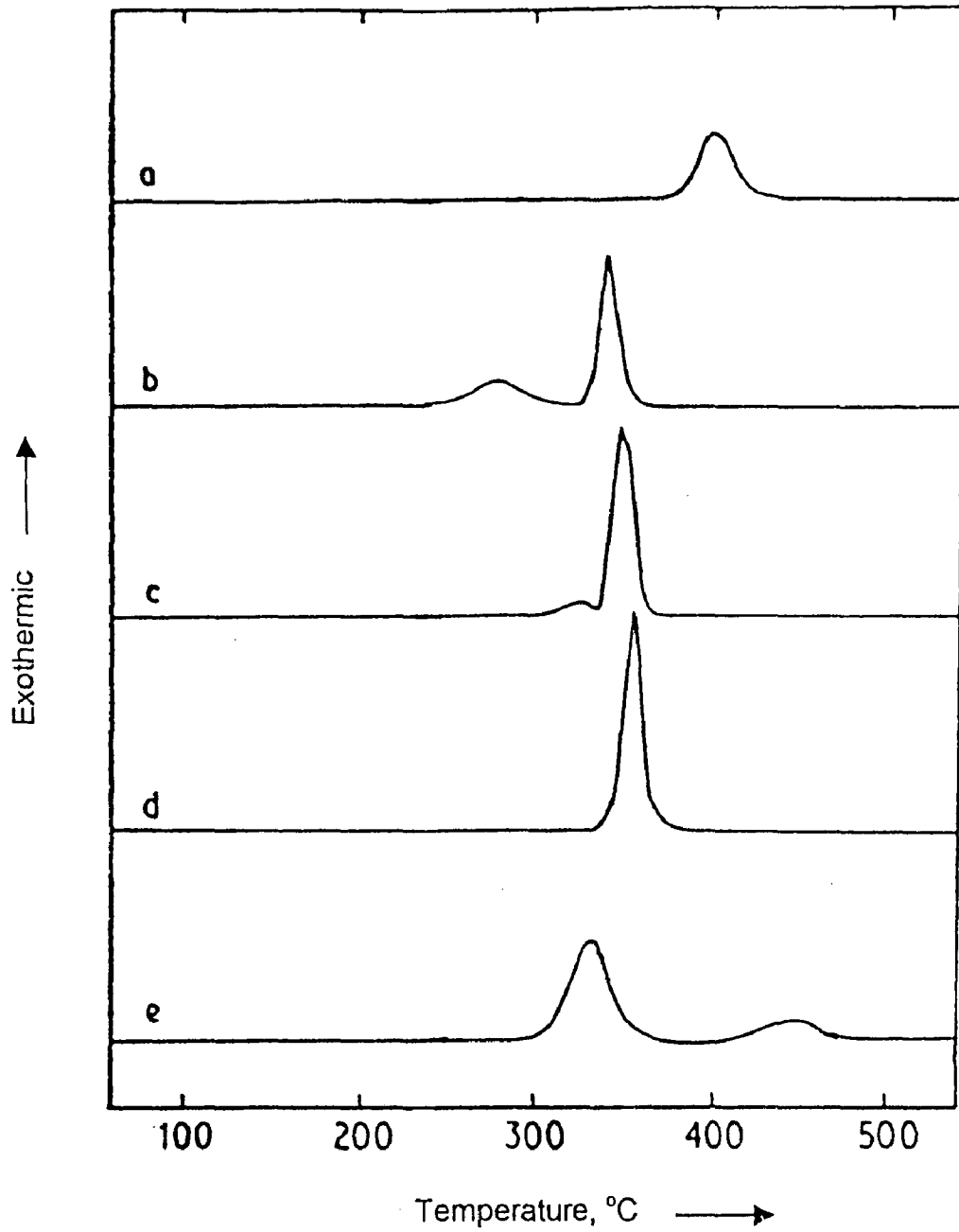


Fig. 2.1

Differential scanning calorimetry curves of the crystallisation processes for the electroless nickel deposits obtained from various solutions in terms of phosphorus, P content (a) 6.3 wt. % P, (b) 10.1 wt. % P, (c) 11.5 wt. % P, (d) 12.5 wt. % P and (e) 13.6 wt. % P (Hur *et al.*, 1990).

2.6.2.1 Application of Non-Isothermal Method to Determine Kinetics of Crystallisation

The non-isothermal technique which involves DSC, employing Kissinger's analysis (Criado and Ortega, 1987), is one of the most commonly used techniques for determining the activation energy of the crystallisation process of metallic glasses while undergoing solid state phase transformation. The kinetic equation derived by Criado and Ortega (1987) allows determining activation energy, E , and Avrami exponent, n , of the JMA kinetic equation from a set of non-isothermal experiments using DSC.

$$\alpha = 1 - e^{-(KT)^n} \quad (2.9)$$

where, α is the volume fraction transformed in time T at a particular temperature. K is a thermally activated rate constant and n is the Avrami exponent, which depends on the mechanism of nucleation and the number of dimensions of growth. Rearranging the terms in the Eq. (2.9) and differentiating with respect to T , one gets,

$$\frac{d\alpha}{dT} = Kn(1-\alpha)[- \ln(1-\alpha)]^{n-\frac{1}{n}} \quad (2.10)$$

when the value of K is written in terms of Arrhenius equation as,

$$K = K_0 e^{-E/RT} \quad (2.11)$$

where, $K_0 = C_0$, is a constant, E is the activation energy, T is the temperature (K) of the transformation and R is the universal gas constant.

Substituting Eq. (2.11) in Eq. (2.10)

$$\frac{d\alpha}{dT} = C_0 n(1-\alpha)[- \ln(1-\alpha)]^{n-\frac{1}{n}} e^{-E/RT} \quad (2.12)$$

When it is assumed that the reaction is carried out at constant heating rate, (β), Eq. (2.12) can be integrated and one gets:

$$[- \ln(1-\alpha)]^{\frac{1}{n}} = \frac{C_0 E}{\beta R} p(x) \quad (2.13)$$

where the function, $p(x)$, is the temperature integral defined as,

$$p(x) = \int_x^{\infty} \frac{e^{-x}}{x^2} dx \cong \frac{e^{-x}}{x} h(x) \quad (2.14)$$

where,

$$h(x) = \frac{x^3 + 18x^2 + 88x + 96}{x^4 + 20x^3 + 120x^2 + 240x + 120} \quad (2.15)$$

An approximation to the integral of the Arrhenius Eq. (2.14) can be written as enunciated by Doyle in 1962:

$$\ln p(x) = -5.33 - 1.05 E / RT \quad (2.16)$$

For determination of the temperature, T_m corresponds to maximum reaction rate, therefore, by differentiating the Eq. (2.12) one gets,

$$\frac{d^2\alpha}{dT^2} = \left[\frac{E\beta}{RT^2} + \frac{n \ln(1-\alpha) + n - 1}{[-\ln(1-\alpha)]^{\frac{1}{n}}} C_o e^{-E/RT} \right] \frac{d\alpha}{dT} \quad (2.17)$$

The value of T_m is defined by equating the Eq. (2.17) to zero. Therefore,

$$\frac{E\beta}{RT_m^2} = \frac{-n \ln(1-\alpha_m) + n - 1}{[-\ln(1-\alpha_m)]^{\frac{1}{n}}} C_o e^{-E/RT_m} \quad (2.18)$$

α_m , being the reacted fraction at the maximum of the reaction rate, the above Eq. (2.18) can be written in logarithmic form as,

$$\ln \frac{\beta}{T_m^2} = \frac{-E}{RT_m} + \ln \frac{C_o R}{E} + \ln \left[\frac{-n \ln(1-\alpha_m) + n - 1}{[-\ln(1-\alpha_m)]^{\frac{1}{n}}} \right] \quad (2.19)$$

According to Horowitz and Metzger (1963), in non-isothermal analysis the influence of β on T_m does not lead to any significant change in the value of E/RT_m .

Criado and Ortega (1987), further assumed that the following relationship is accomplished in a narrow range of E/RT around any particular value of E/RT_m ,

$$\ln \left[\frac{-n \ln(1 - \alpha_m) + n - 1}{[-\ln(1 - \alpha_m)]^{\frac{1}{n}}} \right] = C_1 \frac{E}{RT_m} + \ln C_2 \quad (2.20)$$

(C_1 and C_2 being constants)

After fulfillment of this relationship, from Eqs. (2.19) and (2.20) one gets the following:

$$\ln \frac{\beta}{T_m^2} = \frac{-(1 - C_1)E}{RT_m} + \ln \frac{C_2 C_o R}{E} \quad (2.21)$$

From this Eq. (2.21), Criado and Ortega (1987) concluded that the slope of the liner plot of function, $\ln \frac{\beta}{T_m^2}$ vs. $\frac{1}{T_m}$ yields an apparent activation energy, E_a , given by,

$$E_a = E(1 - C_1) \quad (2.22)$$

where, E is the actual activation energy.

To calculate the value of constants C_1 , the knowledge of order of reaction, n , is required. The Eq. (2.21) can be used which is written in following alternative form.

$$\frac{1}{n} \ln \ln \left[\frac{1}{1 - \alpha} \right] = \ln \frac{C_o E}{\beta R} + \ln p(x) \quad (2.23)$$

Substituting Eq. (2.16) in the above Eq. (2.23), it can be written as:

$$\ln \ln \left[\frac{1}{1 - \alpha} \right] = n \ln \frac{C_o E}{\beta R} - 5.33 n - \frac{1.05 n E}{RT} \quad (2.24)$$

In accordance with the above expression, straight line plot of function $\ln \ln \frac{1}{1 - \alpha}$ verses the reciprocal of the temperature, $\frac{1}{T}$, gives the value of nE , which in turn can be used to calculate the value of n by substituting the determined value of E . Prior

to use of the Eq. (2.20), the value of constant, i. e., C_1 , and C_2 , for different values of n and E/RT ranges along with percent error in the activation energy, ϵ , are as given in Table 2.5. Firstly, the value of E_a/RT is calculated. Here, E_a is the apparent activation energy, T_m is the maximum temperature in K and R is universal gas constant. Once the value of E_a/RT and n are known, the value of C_1 is worked out from Table 2.5, and the actual activation energy, E is calculated.

Table 2.5 Value of C_1 , C_2 and the Percentage of Error in the Activation Energy, ϵ , Calculated by the Least Square Method According to Eq. (2.21).

Kinetics	E/RT					
	$C_1/C_2/\epsilon$	2	5	10	30	60
n = 0.5	C_1	-0.307	-0.239	-0.053	-0.007	0.0020
	C_2	28.160	10.311	2.976	1.472	1.313
	ϵ	30.7	23.9	5.3	0.7	0.2
n = 1.5	C_1	0.132	0.028	0.008	0.001	0.0001
	C_2	0.542	0.723	0.838	0.935	0.966
	ϵ	13.2	2.8	0.8	0.1	0.03
n = 2.0	C_1	0.178	0.041	0.012	0.002	0.0004
	C_2	0.423	0.634	0.769	0.905	0.948
	ϵ	17.8	4.1	1.2	0.2	0.04
n = 2.5	C_1	0.169	0.037	0.011	0.001	0.0004
	C_2	0.449	0.662	0.787	0.915	0.953
	ϵ	16.9	3.7	1.1	0.1	0.04
n = 3.0	C_1	0.187	0.043	0.013	0.002	0.0005
	C_2	0.406	0.617	0.754	0.898	0.944
	ϵ	18.7	4.3	1.3	0.2	0.05
n = 4.0	C_1	0.196	0.047	0.018	0.003	0.0005
	C_2	0.379	0.604	0.743	0.893	0.940
	ϵ	19.6	4.7	1.8	0.3	0.05

2.7 ALUMINA-ZIRCONIA POWDER SYNTHESIS BY CHEMICAL METHODS

The commercially available powders of alumina and zirconia are of micron size range. However, synthesis of such powders by chemical reaction has led to submicron and nano size powders. The development of this kind of methods for fabrication of toughened ceramics such as $\text{Al}_2\text{O}_3\text{-ZrO}_2$, *spinel*- ZrO_2 , mullite- ZrO_2 , $\text{Si}_3\text{N}_4\text{-ZrO}_2$ and others, has gained significant research interest in recent years. Amongst these, zirconia-toughened alumina ceramics have been studied most widely (Debsikdar, 1987). $\text{Al}_2\text{O}_3\text{-ZrO}_2$ composites are of importance to fabricate wear resistant parts, and, in general, are used as cutting materials (Hong *et al.*, 1998).

The process parameters for production of ceramic powder ($\text{Al}_2\text{O}_3\text{-ZrO}_2$), should be such that both the size and the distribution of particles should be small and these particles should be homogeneously distributed in the matrix material. Several methods of preparing $\text{Al}_2\text{O}_3\text{-ZrO}_2$ powders are reported in the literature. The conventional methods involve either dry milling or wet milling a mixture of commercially available Al_2O_3 and ZrO_2 powders. The main disadvantage with the conventional approach relates to inhomogeneous mixing as regards to particle spacing and inhomogeneity of the ceramic microstructure (Debsikdar, 1987).

2.7.1 Methods of Fabrication of Alumina-Zirconia Powder

A review of literature indicates that different methods of fabrication of $\text{Al}_2\text{O}_3\text{-ZrO}_2$ powder in use are: (a) chemical polymerisation, (b) destabilisation of mixed sols and (c) co-precipitation.

(a) Chemical polymerisation

This process involves the controlled hydrolysis. In this method, aluminium secondary butoxide, $\text{Al}(\text{OC}_4\text{H}_9)_3$, is dissolved in 1-butanol containing 75 ml acetyl-acetone. The clear solution thus formed is partially hydrolysed and stirred for 1 h in the ambient

environment. Subsequently, zirconium n-propoxide, $Zr(OC_3H_7)_4$, is added and stirred for 2 h, which results in a clear (brownish) solution of < 7.0 pH. Such brownish gel prepared is then milled to produce the powder (Debsikdar, 1987).

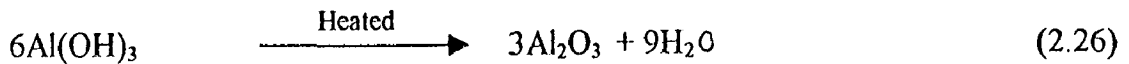
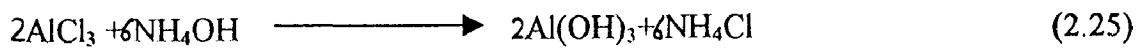
(b) Destabilisation of mixed sols

This synthesis route involves different steps such as preparation of stable Al_2O_3 and ZrO_2 (hydrous) sols, mixing these sols and finally destabilising the mixed sols. An alumina sol can be prepared by precipitating aluminium isopropoxide, $Al(OC_3H_7)_3$, in hot ($70^\circ C$) distilled water followed by peptizing the precipitate with concentrated nitric acid, HNO_3 , for approximately 5 h at the same temperature. The volume of the clear solution is reduced by evaporation. Simultaneously, an aqueous sol of zirconia can be prepared at pH 4.0, using zirconium dinitrate oxide, $ZrO(NO_3)_2$. Subsequently, the sols are mixed and treated with NH_4OH /water (in 1:10 proportion) mixture. The gel so prepared is then milled in a plastic bottle using aluminium balls for about 3 h (Debsikdar, 1987).

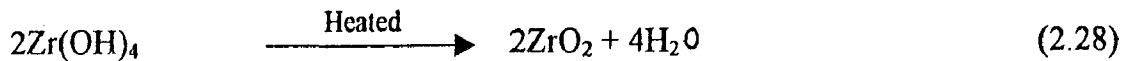
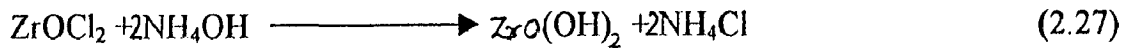
(c) Co-precipitation

The co-precipitation involves separating the insoluble molecular aggregate of hydrous oxides of aluminium and zirconium (Debsikdar, 1987). In this investigation, the $Al_2O_3/20$ mol% ZrO_2 powder has been synthesised using aluminium chloride, ($AlCl_3 \cdot 6H_2O$), and zirconium oxychloride, ($ZrOCl_2 \cdot 8H_2O$) by mixing and dissolving in distilled water. The mixed solutions are thoroughly stirred at room temperature and then ammonia solution, (NH_4OH), is quickly added while continuously stirring until complete precipitation occurs (Hong *et al.*, 1998). The average size of such powder ranges between 20 to 50 nm and the as-prepared powder is amorphous in nature (Debsikdar, 1987). After dehydration, pure Al_2O_3 gel crystallises into $\gamma-Al_2O_3$ at $400^\circ C$ and in case of ZrO_2 gel, the same takes place at $450^\circ C$ with formation of m- ZrO_2 . Most of the hydroxide groups come off in the form of water around $350^\circ C$ but some of them still remain, which can be finally removed above $1000^\circ C$. This indicates that some hydroxide groups exist in the $\gamma-Al_2O_3$ (SS) lattice structure (Hong *et al.*, 1998).

The general reaction of co-precipitation includes:



and



2.8 PROPERTIES OF ELECTROLESS COATINGS

Earlier research reported on electroless coatings is largely on the process and practice and no attention has been paid to the mechanical properties. Even now considerable attention is being paid to the electroless process; however, some work has also been directed towards the studies on physicochemical and mechanical properties of electroless coatings. Studies have observed an increase in hardness of electroless nickel after heat treatment. Initially the data of the effect of time and temperature on hardness gave rise to the belief that the enhanced hardness is due to a process similar to precipitation hardening. Later it was pointed out that certain electroless nickel coatings are amorphous to start with and for precipitation hardening a crystal lattice is required. Therefore, the structure and its correlation with mechanical properties after heat treatment should be dependent on phosphorus content in order to study the mechanical properties of electroless coatings. Electroless coatings have largely been characterised in the later half of the past decade.

Several mechanical properties of these deposits, along with a few other properties, are listed in Table 2.6. Amongst them, hardness and fatigue properties have been studied extensively. There is a general agreement that for electroless nickel based coatings, maximum hardness is obtained after heat treating at 400°C for 1 to 4 h for any content of phosphorus. This has been attributed to the formation of an equilibrium mixture of crystals consisting of solid solution of phosphorus in nickel (with a low phosphorus content) or nickel and crystals of the intermetallic compound Ni₃P.

Table 2.6 Properties of Electroless Nickel based Coatings (source- website : www.sirius-tech.com and www.enla.com).

Property	Coating System			
	Ni-3P	Ni-8P	Ni-11P	Ni-0.5B
Composition range: balance nickel	3-4 %P	6-9 %P	11-12 %P	0.5-1.0 %B
Structure*	m-c	m-c-a	a	c
Internal stress, MPa	-10	+40	-20	+500
Final melting point, °C	1275	1000	880	1440
Density, gm/cm ³	8.6	8.1	7.8	8.6
Coefficient of thermal expansion, mm/m °C	12.4	13.0	12.0	ND
Electrical resistivity, mW/cm	30	75	100	10
Thermal conductivity, W/cm/K	0.6	0.05	0.08	ND
Specific heat, J/kgK	1000	ND	460	ND
Magnetic coercivity, A/m	10000	110	0	ND
Tensile strength, MPa	300	900	800	ND
Ductility, %	0.7	0.7	1.5	ND
Modulus of elasticity, GPa	130	100-120	170	ND
Hardness As-coated, HV ₁₀₀	700	600	530	580
Hardness Heat treated, HV ₁₀₀	960	1000	1050	500

* a: Amorphous; m-c: Microcrystalline; m-c-a: Mixed crystalline and amorphous; c: Crystalline; ND: not determined.

2.8.1 Hardness of Electroless Nickel Deposits

Hardness is an important property of electroless nickel and is often one of the main reasons why it is applied. The hardness of the high melting particles co-deposited remains the same, i.e., before and after the heat treatment. Hence, the incorporation of hard particles in the Ni-P matrix increases the hardness of as-coated and heat treated layers of composite coatings (Apachitei *et al.*, 1998/2).

For some applications, high-temperature treatments cannot be tolerated because parts may warp, or the hardness of the substrate may be reduced. For these applications, longer times and lower temperatures are sometimes used to obtain the desired hardness.

This is illustrated in Fig. 2.4 (Apachitei *et al.*, 1998/1), which indicates the effect of different treatment cycles (temperature and time) on the hardness of different electroless coating systems.

2.8.2 Corrosion Characteristics

In order to achieve best corrosion protection with a thin coating, as electroless nickel, which has no complete tight cover of fluorocarbon coating, it is important that the substrate has a smooth, clean and pore-free surface. Non-metallic inclusions in the surface of the substrate material, carbides sulphides etc., emanating from alloying elements or impurities, as well as a porous or rough surface can breed pores in the coating resulting in less corrosion protection. In general, the corrosion rate of these coating is very low in most environment (www.nedox.com), the presence of oxygen and phosphorus atoms in respect of nickel atoms, invariably gives the corrosion product in the form of $\text{Ni}(\text{OH})_2 + \text{Ni}_3(\text{PO}_4)_2$ at the outer layer and $\text{NiO} + \text{Ni}_3(\text{PO}_4)_2$ as the inner layer in electroless Ni-P coatings (Lanzoni *et al.*, 1997).

2.9 WEAR AND FRICTION

The American Society for Testing and Materials (ASTM) has defined the *wear* as “damage to solid surface, generally involving the progressive loss of material, due to relative motion between that surface and a contacting substance or substances.” Wear studies are generally conducted for one or more of the following reasons (Blau, 1997):

- (i) To understand behaviour of a particular family of material under wear,
- (ii) To optimise or select materials for a particular application by simulation and screening,
- (iii) To understand the effects of certain variables on a particular type of wear and
- (iv) To support the development of predictive or descriptive models for wear in the specific tribosystem.

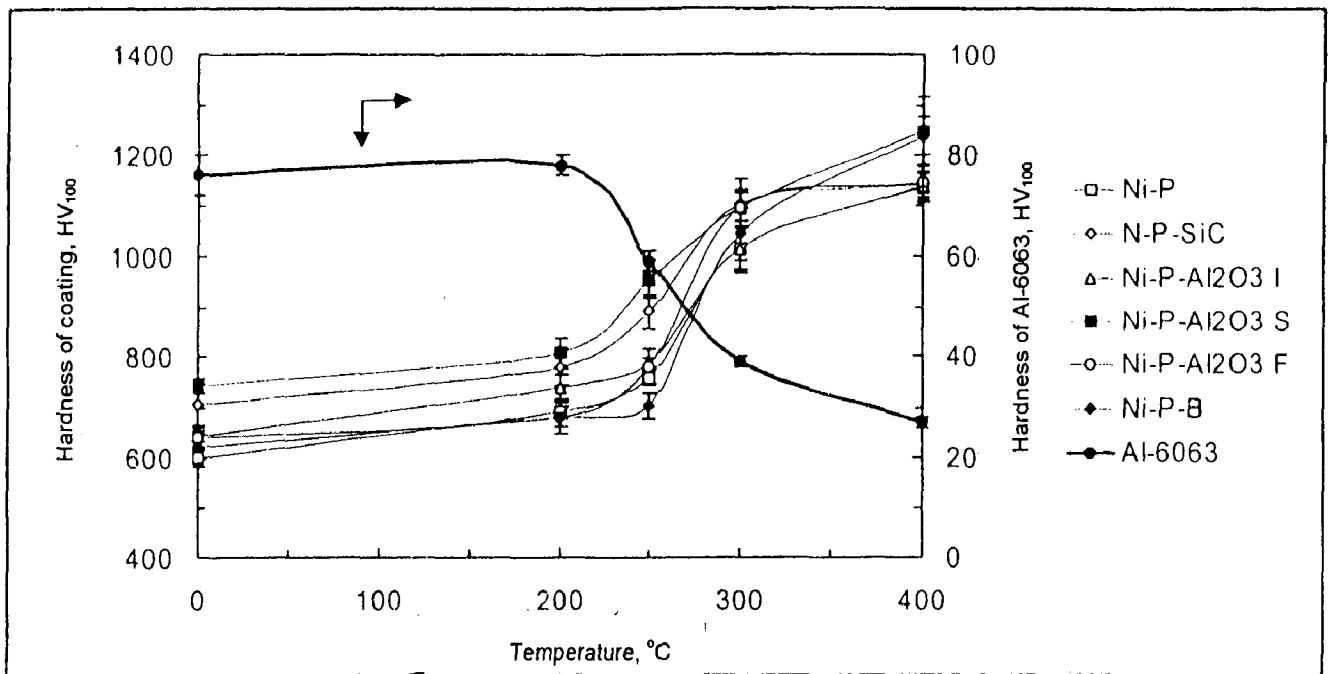


Fig. 2.4 Microhardness of the different electroless coatings and the aluminium substrate for various heat treatments at 200, 250, 300 and 400 °C for 1 h (Apachitei *et al.*, 1998/1).

a) **Types of Wear**

A variety of experimental arrangements are being used to study the sliding wear behaviour. Invariably, all the laboratory investigations of wear are carried out either to examine the mechanisms of wear involved or to simulate practical useful design data on wear rates and coefficient of friction. Figure 2.6 shows the various geometrical arrangements employed in common types of wear testing apparatus (Huchings, 1992). By far, the most common wear test employed in the assessing bulk and coatings is the pin-on-disc test, which is just one particular example of the sliding wear test. Despite the fact that pin-on-disc is only a valid representation of small fraction of possible sliding wear contact conditions but it has proved very useful for materials assessment and coating development (Bull, 1997). None of the above test apparatuses, as shown in Fig. 2.6, can be expected to provide conditions of purely one wear mechanism alone but will include other mechanisms, which acts in combination with the predominant mechanism (Gawne and Ma, 1987).

Amongst the various ways of classifying wear mechanisms, removal of material is recognised as one of the widely used ways. This classification has led to many types of wear viz., Adhesive, Abrasive, Oxidative, Fatigue, Corrosive, Delamination, Fretting etc., (Rigney *et al.*, 1984) and are summarised as under.

Adhesive wear is associated with low sliding velocity, small loads for smooth surfaces. As this type of wear occur in every type of machine, it can not be eliminated completely but can only be reduced. When asperities come in close contact, they may weld together, forming a bond at the junction. This bond has the higher rupture strength than yield strength of one of the contacting solids and in such a case, fracture may take place in one of the asperities resulting in transfer of material within sliding bodies. *Abrasive wear* occurs when two surfaces having dissimilar hardness are in sliding contact. This wear is the removal of displacement of material from one surface by harder asperities of another surface or by harder, loose particles. At times the hard loose particles may be generated due to oxidation of sliding surfaces, then it can be said that oxidative wear is followed by

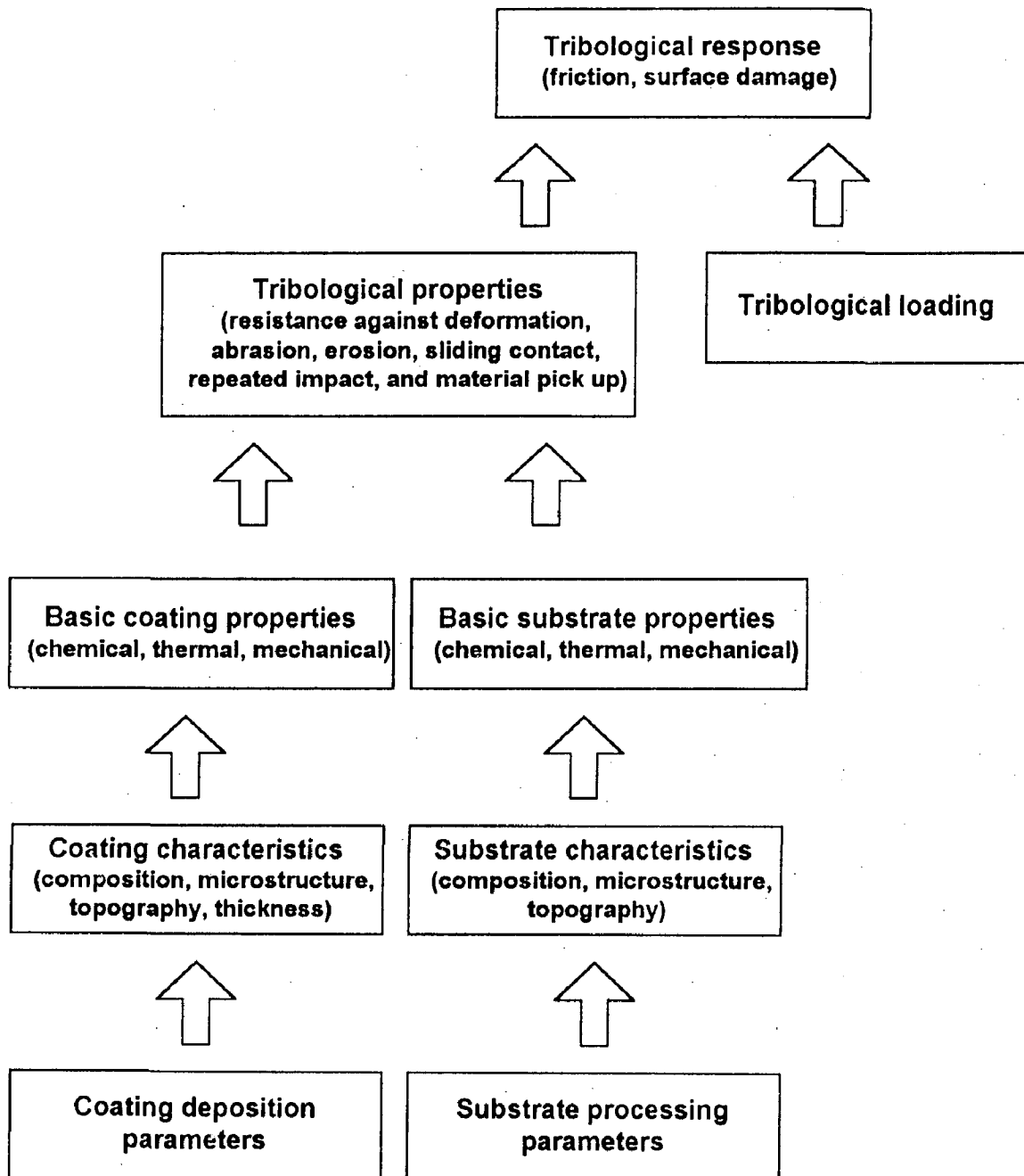


Fig. 2.5 Illustration to show the parameters of the coating deposition influences the tribological response of the coating composites through the coating characteristics which in turn determines the basic and tribological coating properties (Hogmark *et al.*, 1997).

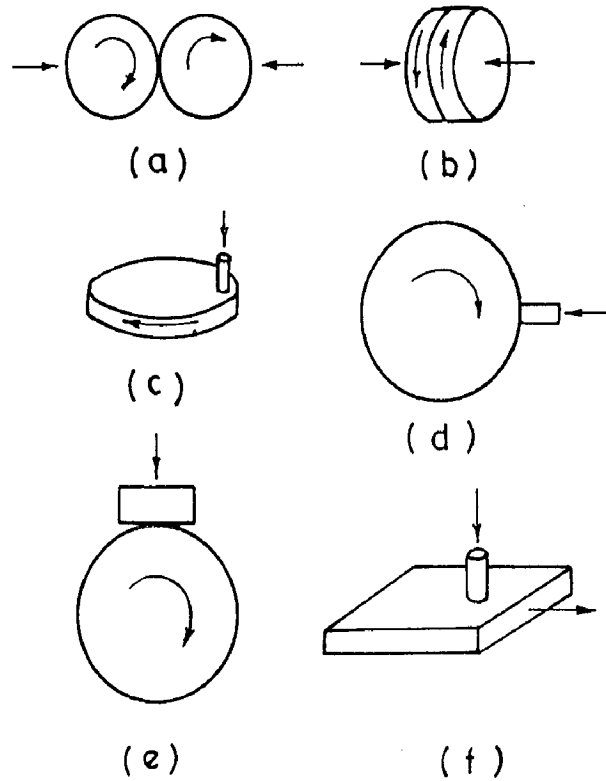


Fig. 2.6 Schematic drawing of the geometries employed in sliding wear tests: (a) ring-on-ring with line contact, (b) ring-on-ring with face to face contact, (c) pin-on-disc, (d) pin-on-rim, (e) block-on-ring and (f) pin-on-flat (Huchings, 1992).

abrasive one. In *oxidative wear*, a film of oxide on sliding surface is formed and after reaching critical thickness of oxide film it becomes mechanically unstable, and it flakes off leaving the fresh surface in oxidative environment and the cycle repeats. *Fatigue wear* refers to the cyclic loading causing imposition of stress state on the surface of a component, inducing a small degree of mechanical damage in the surface and subsurface regions with each stress pulse. Ultimately, the damage accumulation leads to failure by deformation and/or fracture at the surface. *Corrosive wear* is the synergistic effect of chemical reaction at a surface with any of the mechanical wear mechanism. The corrosive environment during sliding causes the corrosive wear by forming the reaction layer. In some cases, this reaction layer may protect the surface or even act as a lubricant. *Delamination wear* is defined as the loss of material in the form of flakes, caused by the nucleation of subsurface fatigue crack and its propagation parallel to the sliding surface. Crack nucleation below the surface layers may occur due to accumulation of plastic strain and such cracks propagate and join each other, before getting detached from the surface in form of flakes or thin sheets. *Fretting wear* also results in fatigue cracks and represents the interaction of adhesive, oxidative and abrasive wear mechanisms.

b) Friction Behaviour of Materials

The history of sliding wear research in metals can not be divorced from classical studies of friction as both involve the mechanics of solid contact (Blau, 1997). The friction behaviour of any material has tribological importance not only because of the frictional force between sliding surfaces is of interest, but also because, it generally affects the wear behaviour. The frictional force is generated as a consequence of three different mechanisms viz., asperity deformation, ploughing by wear particles, and adhesion. Therefore, the coefficient of friction is not a given material property, as it also depends on the mechanical properties of surface, counterface and the environment. (Suh, 1986). The adhesion theory of friction emphasises the importance of adhesion between asperities, in accordance with the surface energy and mutual solubility of the contacting materials (Rabinowicz, 1965).

According to this theory, it is reasonable to assume that materials with greater solubility forms strong junction more readily and thus have higher coefficient of friction.

The frictional behaviour is affected by a few factors including applied load, sliding velocity, surface roughness, sliding distance, and mechanical properties of the two mating surfaces. Bowden and Tabor (1964) have reported the basic laws of friction enunciated by Amonton (1699) which are as follows:

- (i) The friction force is proportional to normal load.
- (ii) The friction force is independent of the apparent area of contact.
- (iii) The friction is independent of sliding velocity.

Bowden and Tabor (1964) have reported that coefficient of friction decreases with increasing normal load in carbon steels and similarly, Tyagi *et al.* (2001) have shown the decrease in coefficient of friction with increasing normal load in dual phase steels. Third law suggested by Amonton (1699) has exceptions and is not obeyed in general. Rabinowicz (1965) has indicated drop in coefficient of friction with increasing sliding velocity. As sliding velocity increases, thermal softening of the interface occurs and results in lower shear strength of the outermost layer. Rabinowicz (1965) has suggested that for very smooth surfaces, the friction tends to reach higher value because of larger area of contact, whereas with very rough surfaces higher friction is attributed to higher asperities of the mating surfaces.

2.9.2 Coating Tribology and Contact Mechanisms

The tribology of contacts involving surfaces in relative motion can be understood as a process with certain energy input and output data. The energy input parameters include velocity, temperature, normal load and tangential force while energy output parameters include friction, wear, velocity, temperature and dynamics (Holmberg *et al.*, 1998). Recent advances in coating technologies now permit the deposition of films such that, coating/substrate designed as a system performs in an optimal manner. This objective is

further aided by improvement in fundamental understanding of contact mechanisms between surfaces (Blau, 1997). The complete tribological contact process in relative motion is comparatively complex due to simultaneous involvement of friction, wear and deformation mechanism of different scale levels and of different types. Holmberg *et al.* (1998) has analysed that the tribological changes take place in terms of different mechanisms, a few of them, i.e., material transfer, micromechanical effects, chemical effects, and macromechanical effects have been summarised as follows.

The material transfer is basically due to the transfer of wear fragments resulting in the formation of wear debris which may attach to the surface to form transfer layer. Such transfer layer changes the tribological behaviour of the pair significantly as if the tribo pair has changed (Holmberg *et al.*, 1998). The friction and wear phenomenon that one observes on the macro level has its origin at micro level. The micromechanical tribological mechanism describes the stress and strain formation at an asperity-to-asperity level, the crack generation and propagation, material liberation and particle formation. Typically, these phenomena are at a size level of about $1\mu\text{m}$ or less down to nanometric range (Holmberg *et al.*, 1998). Prior to the formation of wear scar and wear particle, shearing and fracture are two basic mechanisms for the nucleation of a crack and its propagation, until the material liberation results. During sliding the chemical reaction takes place at the surfaces due to repeated contacts resulting in a change of composition of outermost surface layer and its mechanical properties, which is termed as tribochemical mechanism. Such a change has a considerable influence on both friction and wear as they are determined to a great extent by the properties of the surface, where the phenomena viz., shear, cracking and asperity ploughing take place (Gee and Jennett, 1995; Holmberg *et al.*, 1998). The chemical reactions are principally influenced by the high local pressures and the flash temperatures of the spots formed by asperities collision. In normal environment, i.e., air, where oxygen is present, a thin oxide layer is formed very quickly on most metal surfaces.

The macromechanical tribological mechanisms describe the friction and wear phenomena by considering stress and strain distribution in the whole contact. Four principal

parameters have been defined which control the tribological contact behaviour between two surfaces of which at least one surface is coated. These parameters are coating and substrate hardness relationship, thickness of the coating, surface roughness, and size and hardness of any debris in contact (Holmberg *et al.*, 1998). The debris may originate from external sources or be produced by surface wear interactions themselves. The relationship between these four parameters gives rise to a number of different contact conditions, which are represented schematically with a help of Figs. 2.7 (a) - (l). The figure shows 12 such typical tribological contacts, with different mechanisms influencing friction.

The effect of hardness on sliding behaviour is much more varied and complex. Material transfer and mechanical mixing are the phenomena which occur in initial stages of sliding, modifying the relative hardness values of sliding surface at the contact junction. Hardness of such mixed material can be higher or lesser than that of the underlying substrate and this factor directly determines whether it presses in or remains as plateaus on the surface (Rigney, 1997). The hard and soft coatings are separately considered by virtue of the hardness of coating as an important parameter and its relationship to substrate hardness (Suh, 1986). Particle embedding, entrapment, hiding and crushing represent typical contact conditions, as seen from Figs. 2.7 (a) to (l). Owing to the work of Bowden and Tabor (1950), the advantage of using soft coating to reduce friction is well known but a hard coating on softer surface can decrease wear by preventing ploughing both on micro and macro scale. These coatings typically exhibit residual compressive stresses, which can prevent the likely hood of occurrence of tensile forces. Further decrease in friction and wear can be achieved by providing better load support, i. e., by use of relatively harder substrate, which in turn inhibit deflections and ploughing resulting from counterpart load. Low friction with hard coatings can be obtained if microfilm having a low shear strength is formed on the coating, so that shear takes place within the microfilm and the load is well supported by the hard coating (Holmberg *et al.*, 1998). A thick and hard coating assists a relatively softer substrate to carry the applied load and thus decrease the contact area and the friction. But thin hard coatings on soft substrates are susceptible to coating fracture due to stresses caused by substrate deformation (Holmberg *et al.*, 1998).

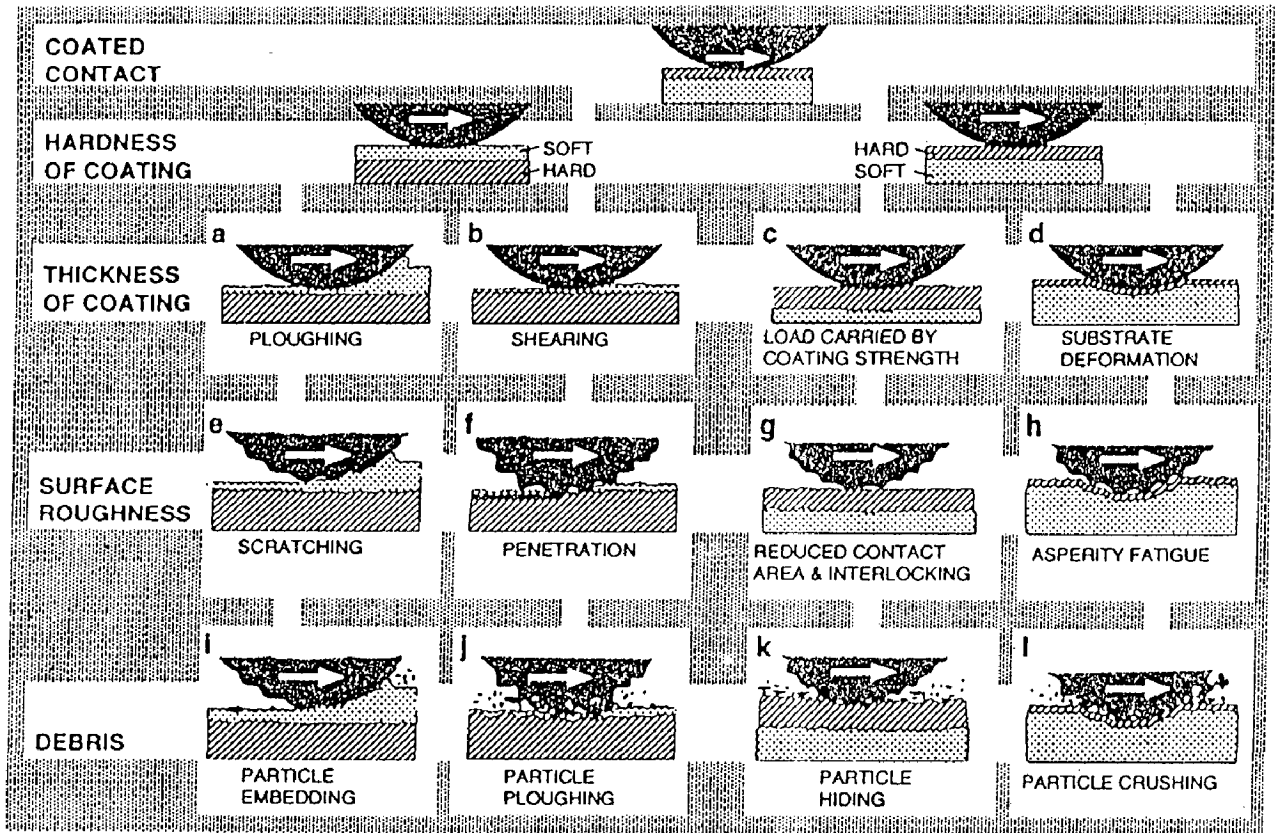


Fig. 2.7 The macromechanical contact conditions for different mechanisms that influence friction when a hard spherical slider moves on a coated flat surface (Holmberg *et al.*, 1998).

2.9.3 Wear Debris

The sliding wear is a phenomena of material removal by different mechanisms of wear like: adhesion, oxidation, delamination, abrasion, fatigue etc., which have been discussed earlier in section 2.9.1. The debris, which could either originate from the surrounding environment or be generated by different wear mechanisms, at times occupy the places at the interface of sliding surfaces. Their influence on friction and wear is of considerable importance in some contact conditions, depending upon the relationship amongst particle size, coating thickness and surface roughness. Also, the hardness relationship between the debris particle, coating and substrate does influence friction and wear behaviour (Holmberg *et al.*, 1998).

Suh (1973 and 1977) recognised plate shape or flat debris due to delamination. The direction of the force applied affects the shape of plates so at times, the debris observed could be of shapes such as plate, flake, wedge etc. Plate-like debris particles are often found in sliding wear, with ratio of thickness to width or length usually in the range from 0.1 to 0.5 (Hutchings, 1992). In case of severe wear such debris particle may also contain large proportion of substrate material.

The fine powder like debris particles are generated due to detachment of oxides (in most of the cases) from sliding surface (Hutchings, 1992). Tyagi *et al.* (2001) have indicated that such debris particle appear with dry sliding wear of dual phase steel, in which the oxidative wear of steel has been reported. Those debris were further studied to identify the different phase contents present in it so as to explore the operating mechanism of wear, which was found to be oxidative in case of dual phase steels. In most of such cases, this type of debris corresponds to mild wear regime (Razavizadeh and Eyre, 1982, 1983). However, there are increasing evidences that the delaminating material is not same, either structurally or chemically as the wear surface material. Instead, transfer of material produces the layer of such material also. Perhaps, during the sliding process, the lamellae are sheared in sliding direction and transfer material smears, flattens and fractures which contributes to debris (Rigney *et al.*, 1984).

Debris particles of other types have also been reported, which include ribbons, cylinders, spheres, cutting chips, irregular chunks and loose clusters (Rigney et al., 1984). Loose clusters are commonly observed in many systems involving steel, because small debris particles tend to attract each other by ferromagnetism. (Rabinowicz, 1977 and Rigney *et al.*, 1984). Similarly, in the systems involving steel, it is observed that fine oxide debris particles form the agglomerates or clusters (Tyagi *et al.*, 2001). Ribbon-shaped debris, resulted from electroless Ni-P particle free coating has been presented by Apachitei and Duszczyk (2000), the ribbons appear to be like long and thin twisted fragments. It is also stated that, higher hardness of surface form thin wear debris, which could be twisted easily. Such debris can be considered to be having fair possibility of abrasive or scratching action during the wear, just like the formation of chips in abrasive and polishing machining processes.

2.9.4 Wear and Friction of Electroless Coatings

The tribological properties of electroless nickel have been assessed using pin-on-disc, ball-on-disc, sphere-on-disc, ring-on-block, Tabor abraser and falax machines. Despite the substantial amount of experimental work carried out by now, the wear behaviour of electroless nickel is poorly understood. This may be partly due to the complexity of the structure of electroless nickel, the wide variety of wear apparatuses, loading conditions, environment, substrate and counterface materials used. Another reason is that many of the research workers have not related the wear of a specific coating to its microstructure, surface topography and material removal mechanism.

It is important to note that the hardness of deposit does not always correlate directly to wear resistance in a particular application. The coating lubricity, smoothness of mating surface and wear mechanism all play a crucial role in the service performance. The composition of the coatings also affects the wear performance of the components. Baudrand (1994) has reported that the phosphorus content of electroless nickel coatings up to about 10 wt.% influences their structure and tribological behaviour. The heat treatment process also eliminates severe adhesive wear during unlubricated sliding against plain

carbon steel, due to low interfacial and high free energies of the two surfaces, resulting in a high compatibility.

2.9.4.1 Electroless Ni-P Alloy Coatings

Many researchers (Gawne, 1984; Gawne and Ma, 1987; Moonir-Vaghefi *et al.*, 1997; Bozzini *et al.*, 1999; Balaraju and Seshadri, 1999; Staia *et al.*, 1996 and 1997; Yugang and Tondon 1996; Okado *et al.*, 1999 and Bin-Sudin *et al.*, 1996) have reported the wear and friction studies of electroless Ni-P coatings. However, the consolidation of wear data has become difficult due to variety of wear apparatus, different loading conditions and counterface materials used. The data generated revealed that the resistance to wear for electroless Ni-P coatings improves substantially by using heat treatment conditions which results in improvement in the hardness.

Gawne, and Ma (1987) explained the wear mechanism in electroless nickel coating in which deposits were prepared using two different hypophosphite based solutions, which gave 8.5 wt.% and 12 wt.% P coatings. Heat treatments of the coated samples were carried out in a tube furnace with soak period of 1 h in air at a temperature up to 400°C and that above this temperature in argon atmosphere. Approximately 40 μm thick coating was applied on the wear samples. In this work, the wear behaviour has been evaluated by using different wear apparatus viz., Tabor abraser, reciprocating diamond scratch test, Falex and pin-on-flat machines. The tests were carried out at 60% relative humidity and 20°C temperature, under unlubricated condition.

In pin-on-flat tests, a cylindrical pin (30 mm \times 6.35 mm) was made to slide under 10 kgf load against a flat coated specimen (75 \times 35 \times 10 mm). The pin used was of hardened steel with 1.7 GN/m² hardness and the flat with hardness of 5.5 GN/m². The reciprocating action of the pin was fixed at 150 cycles/min over the wear track of length of 30 mm. The extent of wear was determined by measuring mean depth of the wear track with a profilometer.

In reciprocating scratch tests, the coefficient of friction was observed to be least for the electroless nickel coated samples, which were heat treated at 600°C for 1 h. While, in case of as-coated (8.5 wt.% P) and heat treated at 300°C for 1 h samples, the wear depth was reported to be the least. However with 12 wt.% P, both the wear depth and the coefficient of friction have been found to be the least when these samples were heat treated at 300°C for 1 h. Almost similar results have been reported in this study when samples are subjected to Tabor abraser. As-coated 8.5 wt.% P and heat treated 8.5 wt.% P at 600°C are having same hardness but substantially different wear rates. Similar behaviour was observed in pin-on-flat test in which minimum wear depth was observed for Ni-8.5 wt.% P electroless coating when it is heat treated at 400°C for 1 h (Gawne and Ma, 1987).

The reason for adhesive wear is attributed to some material removal by ploughing of the cracked areas and ultimately large scale failure of coating. The adhesive wear of as-plated electroless Ni-P coating is due to the formation of micro welds. The tendency to form strong welds is greater if there is a high mutual solubility between the two components of the wear couple. Nickel of electroless Ni-P coating has high mutual solubility with carburised steel ring because they have low interfacial and high surface energies (Moonir-Vaghefi *et al.*, 1997).

Bozzini *et al.* (1999) carried out the study of wear performance of electroless Ni-P coating heat treated in air at 300°C in a muffle furnace and having thickness in the range of 46-55 μm . Dry sliding wear tests have been conducted at a normal load of 5 N and sliding speed of 0.6 m/s in air (relative humidity 50 to 70%) at room temperature for sliding distance of 1000 m.

Balaraju and Seshadri (1999) have prepared Ni-P electroless coating in the acidic hypophosphite bath and obtained 10-12 wt.% P in the electroless Ni-P coating. The wear resistances of the as-coated and heat treated at 400°C for 1 h conditions were assessed using a disc-on-disc method by sliding the specimens against a counterface of high-carbon, high-chromium steel having hardness of 60 HRC under unlubricated conditions for 30 min.

The tests were conducted at different normal loads of 20, 40 and 60 *N* at an angular velocity of 1000 *rpm*. The wear rate for electroless Ni-P coated and heat treated samples was observed to be substantially lower than that of as-coated samples and it has been attributed to low mutual solubility of nickel phosphide and iron. The wear rate was found to increase with increase in load for both the as-coated and heat treated specimens. When heat treated Ni-P coating (400°C) was run against carburised ring using 0.5 *kg* load (Moonir-Vaghefi, *et al.*, 1997), it showed polished appearance of the worn surface and also fine scratches were observed on the block surface, but at the loads exceeding 2.0 *kg*, the moderate adhesive transfer was found to occur. When the load was increased to about 8 *kg*, a high wear rate on heat treated Ni-P coating occurred.

Staia *et al.* (1997) has reported electroless Ni-P coating on plain carbon steel by using an acid bath based on NiCl₂. The electroless coated samples were heat treated at 260°C for 25 *h* and 400°C for 1 *h*. The modified ball cratering method was used to determine abrasive resistance of these coatings. The abrasive media employed was a mixture of 10 *ml* ethylene glycol and 1 *g* of 3 μm diamond paste. A ball bearing was used as tribological pair. The individual wear constants were determined by the use of recorded plots of crater depth vs. sliding distance. The heat treated samples at 400°C for 1 *h* have been reported to be better, in terms of wear resistance (Staia *et al.*, 1996).

Effect of temperature on wear of as-coated electroless Ni-P coating under lubricated reciprocating sliding conditions has been investigated using the ball-on-block test method by Yugang and Tandon (1996). They have reported that the temperature influences the lubricated wear of the coatings, especially at higher loads and a change in wear mechanism takes place as the temperature is raised to 100°C.

2.9.4.2 Electroless Ni-P Based Composite Coatings

(a) Composite coatings with hard particles

Bozzini *et al.* (1999) investigated the tribological behaviour of electroless Ni-P composite coating under dry sliding with a slider-on-cylinder tribometer in air at room

temperature against a PVD TiN coated HSS cylinder. Friction and wear characteristics discussed on the basis of mechanical properties include microhardness, plasticity parameter and fracture toughness of coatings, which are derived by indentation measurements at low loads. It was reported that wear depth increases with increase in annealing time, for both pure matrix and B₄C-rich composite layer. The wear volume, Q , is correlated to mechanical properties using Archard-type equations as,

$$Q = k \frac{Pl}{HV} \quad (2.29)$$

where, k is the wear coefficient, P is applied load and HV is referred to as Vickers microhardness and l is the sliding distance. The wear scar depth of the Ni-P coatings is found to be one order of magnitude higher than those of corresponding composite coatings reinforced by B₄C particles. In both the cases the tendency for the wear scar depth to increase with increase in heat treatment time is reported. SEM and optical microscope observations showed no evidence of delamination phenomena or any sign of detachment of the reinforcing particles along the wear scars produced in the testing conditions.

The morphology of wear scar suggested that, the removal of material by plastic deformation is the main cause of wear in both Ni-P coatings and Ni-P-B₄C, hence it is reasonable to use an Archard-type wear equation to correlate the wear volume and the indentation hardness of the coating. During sliding, the hard particles can move into the matrix, behaving like cutting edges, thus enhancing the wear of the coating. The wear volume was found to increase linearly with increase in applied load. At the load of 25 N, a few isolated cracks are found to nucleate on the wear surfaces of the composite coatings (Bozzini *et al.*, 1999).

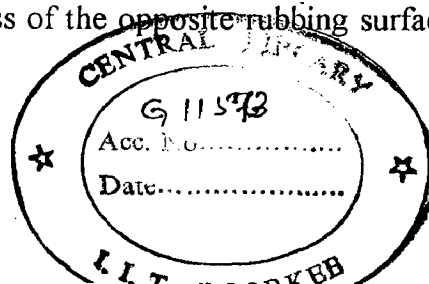
Co-deposition of tungsten in electroless Ni-P matrix reduces the phosphorus content in coating and such addition of tungsten does not affect the crystalline structure of low phosphorus Ni-P deposits (Li *et al.*, 1996). It was confirmed by abrasion test that co-deposition of tungsten improves the wear resistance of Ni-P coated samples. Electroless

Ni-P-SiC composite coatings containing 25-30 vol.% SiC have been reported to possess greater hardness, higher porosity, as well as lower adhesion and corrosion resistance (Li, 1997).

Reddy *et al.* (1998) studied the specific wear rate of electroless Ni-P/diamond coating by disc-on-disc type wear tests with a counter disc of high strength tool steel (hardness 800 *VHN*). The wear tests were carried out at 250 *rpm* and 5 *N* load without lubrication. The wear rate is correlated with the coating composition, diamond particle size and annealing temperature. The above study revealed that Ni-P diamond electroless coating containing 9-10%P and 3-6 μm size diamond particles gives the least wear rate in as-coated and heat treated condition, i. e., after heat treating at 350°C for 2 *h* followed by air cooling. The heat treatment results in improved wear resistance as compared to the corresponding as-coated specimens due to complete crystallisation of the coating.

(b) Composite coatings with soft particles

Pena-Munoz *et al.* (1998), Zhang *et al.* (1998/2) and Narayan and Pandey (1997) have reported the study of wear resistance properties of electroless Ni-P-PTFE coatings. The wear resistance of these coatings in scuffing wear conditions with mildly abrasive conditions were carried out by Tabor wear test for low duration (20000 cycles) by Narayan and Pandey (1997). It was found that addition of 18% or more PTFE gives better wear resistance. However, under abrasive wear conditions in reciprocating wear test, addition of both 18 and 28% PTFE was found to reduce the wear resistance of electroless nickel. Under abrasive wear conditions, heat treatment was found to increase wear resistance of composite coatings, but under adhesive wear conditions, heat treatment had practically no effect. However in dry sliding wear, heat treatment of the coated samples was reported to increase coefficient of friction. About 10 μm thickness coatings showed optimum performance in terms of low and almost constant coefficient of friction. The work revealed that the wear rate increases on increasing the hardness of the opposite rubbing surface for Ni-PTFE coatings.

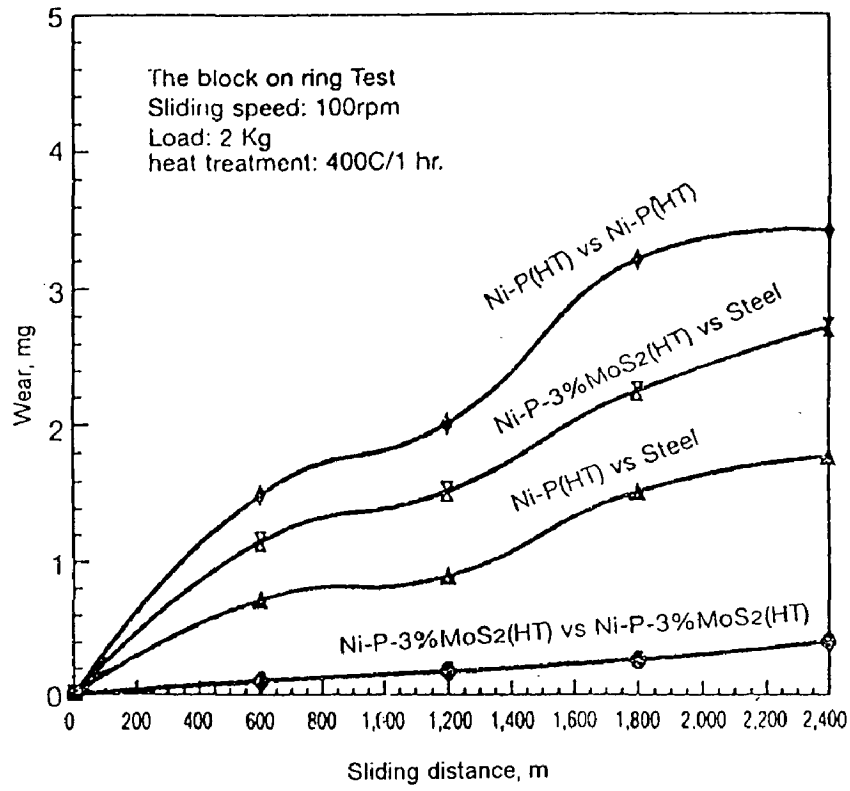


611573

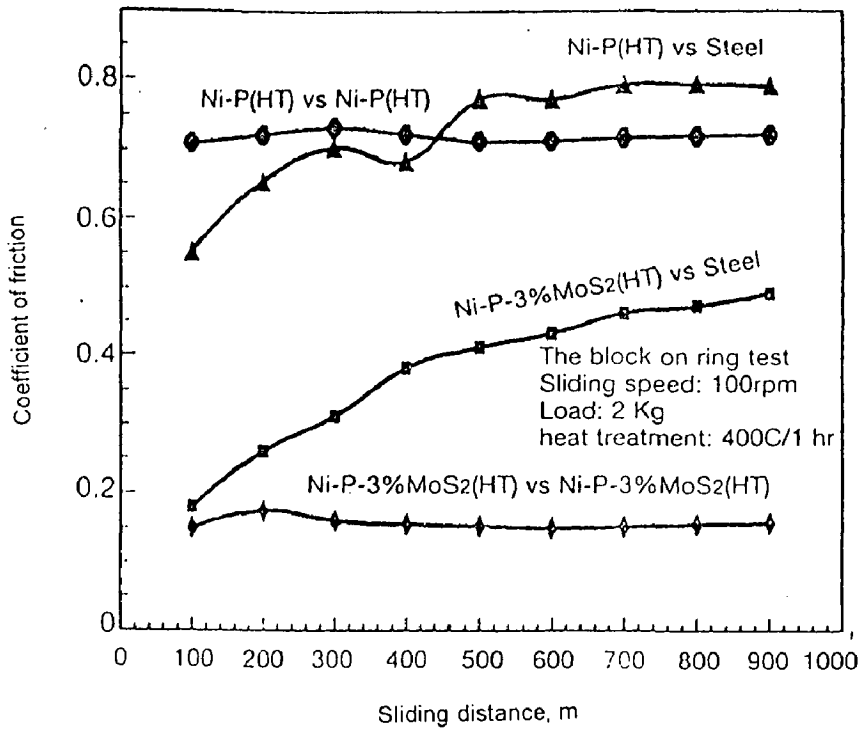
Moonir-Vaghefi *et al.* (1997) have explained the results of block-on-ring test to evaluate friction and wear characteristics of electroless Ni-10wt.%P-MoS₂ composite coatings at loads 2 and 8 kg. The worn surface exhibited severe adhesive transfer at higher loads in case of Ni-10wt.%P coatings under dry conditions. Incorporation of molybdenum disulfide (MoS₂) particles into the Ni-P matrix has been observed to improve the wear and friction properties of the coating. The Ni-P-3wt.%MoS₂ against itself has been found to have lower wear rate and coefficient of friction. The electroless Ni-P-MoS₂ heat treated coatings have also been observed to behave in the same manner as the Ni-P coatings, except that, the presence of MoS₂ reduces the friction and wear by minimising the metal to metal contact. However, it does not show the improvement in wear characteristics at higher load, i.e., 8 kg. When heat treated electroless Ni-P-3 wt.%MoS₂ coating runs against itself, the wear rate and coefficient of friction have been reported to be the lowest. The presence of MoS₂ in the film prevents spreading of the oxide layer on the carburised steel ring. Zang *et al.* (1992) have described the tribological behaviour of Ni/MoS₂ composite brush plating, the fine structure of such Ni-MoS₂ coating, sustains the MoS₂ grains quite strongly in the nickel matrix and the composite layer containing MoS₂ exhibits good wear resistance and lower coefficient of friction as shown in Fig. 2.8 (a) and (b). Bhushan and Gupta (1991) have reported improved lubricity as a result of oxidation of the top layer in the MoS₂ coatings.

2.10 COATINGS ON GRAPHITE AND CARBON FIBERS

Carbon fiber or fabrics are century old engineering materials, which were first produced by Edison for their use in electric lamps and also as electrical conductor (Gill, 1972). Its increasing use in metal matrix composites (MMCs) has made this material more popular as an engineering material for space applications. The interfacial chemical reaction between the carbon fiber and the matrix affects the performance of MMCs irrespective of the synthesising routes adopted. The better wettability of fibers/fabric with the matrix has



(a)



(b)

Fig. 2.8

Tribological performance of electroless Ni-P and electroless Ni-P-3% MoS₂ coated blocks running against various coated rings: (a) variation of wear with sliding distance and (b) variation of coefficient of friction with sliding distance (Moonir-Vaghefi *et al.*, 1997).

been considered of utmost importance (Abraham *et al.*, 1992). Although the graphite fiber reinforced aluminium matrix composite is a promising material owing to its high specific strength and stiffness, excellent high temperature properties and dimensional stability, the poor wettability and chemical reactions between graphite fibers and molten aluminium are the main hurdle in synthesising the graphite reinforced aluminium composites (Shi *et al.*, 1999). Poor wettability also results in inadequate bonding between the metal and the graphite (Ip *et al.*, 1998). Non-wetting of dispersoid with the matrix results in discontinuity at the interface and adversely affects the performance of the composite. One of the ways to get rid of these difficulties is applying the coatings on the fibers/fabric with metal or carbide which, not only improves the wettability, but also impedes interfacial reaction between graphite fibers and molten aluminium alloy (Shi *et al.*, 1999). It has been said that apart from improvement in the wettability characteristic of fabric, the metallic coatings improve metallurgical characteristics like wear resistance, corrosion resistance and mechanical strength. Abraham *et al.* (1992) reported that coatings on carbon fibers provide alluring properties to MMCs by giving suitable heat treatment after coating or by the addition of alloying elements in the matrix of the alloy.

2.10.1 Electroless Coating on Carbon Fibers

The nature of nickel base electroless coatings is well understood and easy to process (Abraham *et al.*, 1990; Shi *et al.*, 1999). The performance of MMCs largely depends upon the morphology of the less common phases present in the coatings, thickness and nature of the coatings (Agarwala, 1987). The effectiveness of the coating also depends on the coating material having low diffusivity for carbon, being stable in the matrix and not deleteriously affecting the strength of the fiber (Shi *et al.*, 1999). They also stated that electroless technique is a successful process to produce a uniform and adhesive layer of nickel on carbon fibers without any degradation of the fiber strength. They used a bath with composition: 10 g NiSO₄, 10 g NaOH, 10 ml 36% HCHO, 50 g potassium sodium tetrahydrate and balanced with water in one *l* capacity to coat the commercially available polyacrylonitrile based carbon fibers.

Caturla *et al.* (1995) have reported metal coating of copper, nickel and copper-nickel produced by electroless deposition on the graphite. Graphite was pre-activated by immersion of graphite for 30 *min* in an aqueous solution of 0.1 M SnCl₂/0.1 M HCl, followed by immersion for 30 *min* in aqueous solution of 0.0014 M of PdCl₂/0.25 M HCl. In order to facilitate the access of the reactants to the porosity, the soaking time in both of the solutions observed was relatively larger than that for other materials. For electroless copper coating, formaldehyde-based baths were used while nickel coatings were carried out using hypophosphite-based bath. Copper coating has been carried out at 12 pH whereas nickel coating at 8.75 pH, and for both the baths, 25°C temperature was maintained, but in case of copper-nickel duplex coating, the bath temperature was raised to 50°C due to non-catalytic nature of copper to nickel deposition at room temperature. The coated pieces were washed with distilled water and dried at 110°C (Caturla *et al.*, 1995). This study reveals that a few pores remain after coating of copper or nickel. However, when electroless copper coating is followed by nickel, the growth starts at the edges and corners of the copper crystals and continues to cover all copper deposit. Further growth of the nickel deposit completely isolates graphite from the exterior. The hemispherical grains of Ni-P deposits are also reported by Caturla *et al.* (1995). The isotropic growth seems to indicate that the growth front is homogeneous and the grains merge to form a continuous film. The porosity in nickel deposits decreases with increasing thickness down to a very low value of 8 μm .

Abraham (1997), reported the coating of the heat cleaned carbon fibers by electroless copper deposition. The coating was carried at 10 to 11 pH and 25°C by use of formaldehyde as the reducing agent. Abraham *et al.* (1992) reported that electroless nickel coated carbon fibers for coating thickness range of 0.1 to 0.7 μm do not decrease the strength of fiber but those coated with copper decrease the strength.

2.10.2 Wettability and Carbon Fiber/Metal Matrix Interface

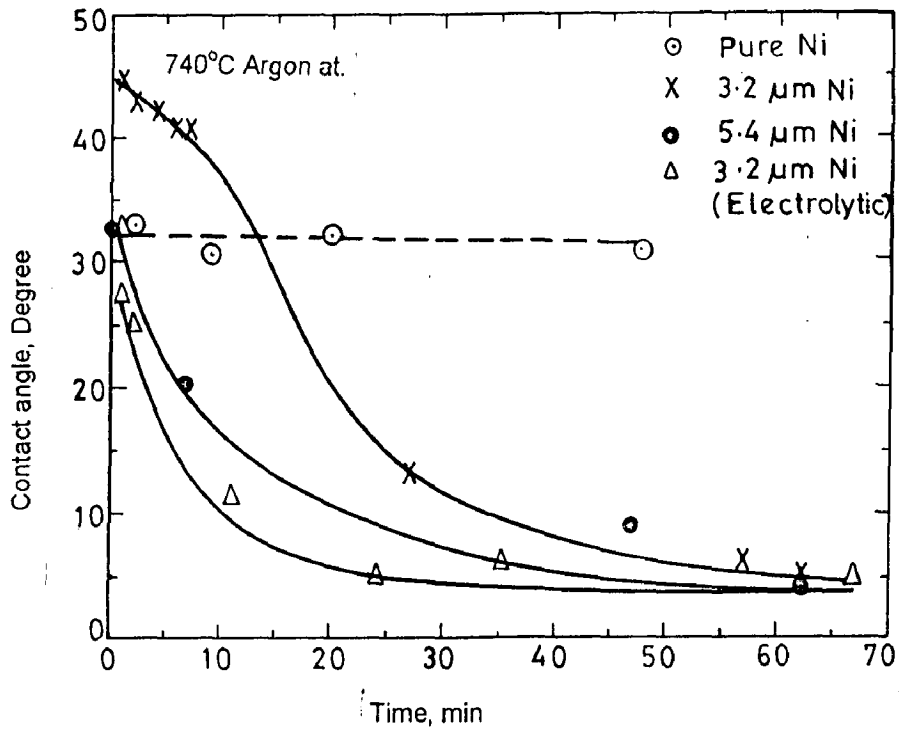
The coating on a solid generates new interface between dissimilar materials and involves consideration of wettability, spreading, interface evolution and adhesion.

Wettability of a solid by a liquid is characterised in terms of the angle of contact that the liquid makes on the solid. The contact angle, θ_c , is obtained from a balance of interfacial tensions at the boundaries between liquid, solid and vapour. The limiting values of contact angle, $\theta_c = 0$ and $\theta_c = 180^\circ$, respectively defines completely wetting and non-wetting characteristics. The condition, $\theta_c < 90^\circ$ indicates that the solid is wetted by the liquid, and $\theta_c > 90^\circ$ indicates its non-wetting characteristics (Asthana and Sobczak, 2000).

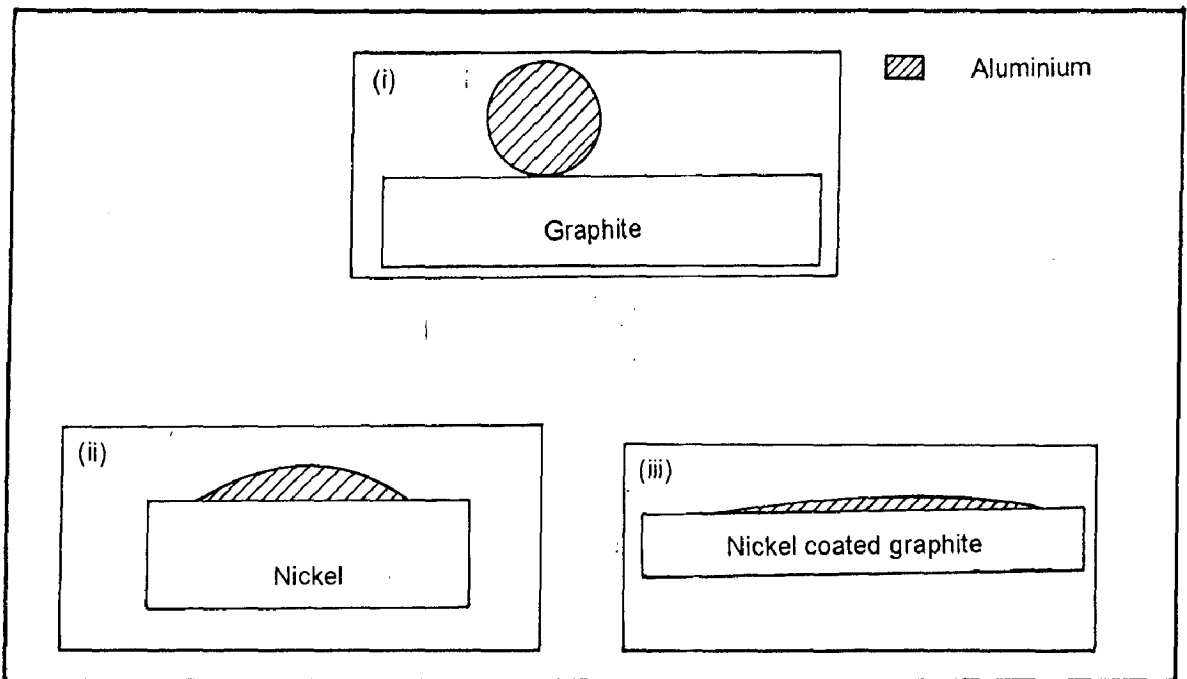
The wetting of the carbon fibers has been reported to be associated with the spontaneous formation of carbide layer of a significant thickness when liquid metal transfer agent is used at different temperatures of the melt. The coating of graphite with tungsten carbide (Himbeault *et al.*, 1988); chromium carbide (Himbeault *et al.*, 1989/1) and titanium carbide (Himbeault *et al.*, 1989/2) has been reported. In all of the above three cases the strength of fiber was observed to reduce by increase in carbide layer thickness.

Ip *et al.* (1998) studied the wettability of aluminium with graphite, electrolytic nickel and electrodeposited nickel on graphite by Sessile drop technique. The results obtained by them are shown in Figs. 2.9 (a) and (b). The above work revealed that aluminium does not wet graphite but nickel coated graphite surface provides better wetting results with less than 10° contact angle within 10 *min* at 740°C with aluminium. The formation of the reaction zone between liquid aluminium and solid nickel occurs at 740°C (Ip *et al.*, 1998). The reaction sequence in this work is reported as: (i) nickel dissolution into aluminium, (ii) precipitation of Al_3Ni at interface and (iii) reaction between Al_3Ni and nickel to form Al_3Ni_2 layer.

The structure and the properties of the interface between the reinforcement and matrix can be adjusted efficiently by modifications of the reinforcements. Modification of fiber surface, such as by coating fibers with stable compounds has been used widely to improve wettability and lower residual stress at the interface (Wang and Zhau, 1996). They reported that coating of carbon fiber by SiC improves its wettability with molten aluminium and also controls the reaction at interface. It changes the bonding state of the interface of



(a)



(b)

Fig. 2.9 Wetting behaviour of aluminium: (a) contact angle on nickel and nickel coated graphite as a function of contact time and (b) on various substrates: (i) graphite, (ii) electrolytic nickel and (iii) nickel coated graphite (Ip *et al.*, 1998).

the composite from chemical bonding type to a mixed type, so as to produce higher strength fiber reinforced aluminium composite.

Abraham *et al.* (1990) reported that the electroless nickel coatings did not show fiber matrix interaction as it had been prevented by the formation of intermetallics at the interface. According to Shi *et al.* (1999) the electroless nickel coating on carbon fibers act as a barrier between aluminium melt and carbon fiber by separating the melt and carbon fiber from contacting each other, and thus prohibits the formation of Al_4C_3 compound, whose presence is detrimental.

2.11 FORMULATION OF PROBLEM

From the critical review of the available literature, it has been observed that most of the studies carried out in the area of electroless composite coatings revolve around the coating technology and only a few concern to process development. Nevertheless, considerable scientific attention has been paid towards synthesis and characterisation of electroless Ni-P alloy coatings but relatively less attention has been focused in the direction of composite coatings. Almost all the Ni-P based composite coatings have been synthesised by co-deposition of particulate solids of the composite in to the Ni-P matrix. But the in-situ co-precipitation of solid particles within the electroless bath followed by their co-deposition has not yet been exploited by the investigators. The properties of the electroless composite coatings are sensitive to coating composite, heat treatment after coating, substrate-coating material compatibility, particle size and their distribution etc. The potential usage of electroless Ni-P based coatings for wear resistant applications has led to a limited analysis of the tribological characterisation of the coatings. Most of these studies have been directed to understand the structure-property correlation and kinetics of crystallisation of Ni-P alloy coatings as a function of phosphorus content. The efforts made to study the effect of different heat treatment conditions on hardness of the coating have also been reported commonly for the steel substrate and aluminium in a few cases. Electroless coatings on the graphite / carbon fibers have attracted a limited scientific attention.

machine at different loads and a constant sliding speed. This will help in revealing the effect of coating composition, hardness and normal load on the friction and wear behaviour of these substrate materials and coatings on them. The worn surfaces of different types of the wear pins, (i.e., as-coated and heat treated) and the wear debris collected during the sliding of those specimens could be examined to unravel the nature of the operative wear mechanism.

The electroless coating on carbon fabric can be studied in terms of its uniformity and presence of different elements of deposition in the coating. The tensile behaviour of the as-coated and heat treated specimens after coating the carbon fabric could be studied to find out the effect of coating on tensile properties of carbon fabric. Also the reinforcement of coated carbon fabric in aluminium can be carried out by use of conventional casting method. This study is expected to provide an assessment of reinforcement ability of electroless coated carbon fabric by observing the fabric-aluminium interface.

To summarise, the present investigation is an effort being made for the first time to use the in-situ co-precipitation of Al_2O_3 and ZrO_2 and co-deposition of the same along with Al_3Zr , resulting in the Ni-P-X ($X = \text{ZrO}_2\text{-Al}_2\text{O}_3\text{-Al}_3\text{Zr}$) deposition. Coating conditions and bath composition for this new type of coating have to be determined to attain the optimal level. Uniformity and reproducibility of this coating for the optimum coating conditions on different substrate materials has to be determined. The qualitative and quantitative analyses of Ni-P-X coating can be carried out using different analytical tools such as metallographic studies, X-ray diffraction, SEM, EDAX, DSC etc. The effect of heat treatment in terms of non-isothermal kinetics and hardness of the coating also could be studied. The investigation has also been aimed at unraveling the friction and wear behaviour of the composite coatings on steel and aluminium pins in both the as-coated and the heat treated conditions, by carrying out dry sliding wear tests at different loads and at a constant sliding speed. Variation in the wear pin type is expected to behave dissimilarly under different normal loads during the dry sliding wear tests. Application of Ni-P-X coating on carbon fabric and its tensile behaviour in both the as-coated and the heat treated conditions could be studied. The reinforcement feasibility for the coated carbon fabric in to aluminium matrix can also be assessed experimentally by use of conventional casting method.

This chapter deals with the experimental techniques adopted for Electroless coatings carried out in the present investigation. The details of the electroless coating setup, plating bath and co-precipitation reaction used are presented. The selection of coating parameters has been done based on maximum coating weight achieved. Synthesis of electroless Ni-P and Ni-P-X ($X = \text{ZrO}_2\text{-Al}_2\text{O}_3\text{-Al}_3\text{Zr}$) on three different substrate materials namely: aluminium, normalised steel and carbon fabric has been explained in respect of the pretreatment and the surface preparation for coating. The experimental details used for the heat treatment carried out and hardness tests performed have been enumerated. The metallographic studies conducted by using different analytical tools are explained for the qualitative and quantitative analyses of the coating. Dry sliding wear tests carried out for different loads on electroless coated substrate and the substrate as such have been explained. The different analytical tools used in the present investigation viz., Optical microscope, SEM, TEM, X-ray diffraction, EPMA (both qualitative and quantitative), SEM-EDAX, DSC etc., have also been summarised.

3.1 SUBSTRATE MATERIALS

Three different materials were used as the substrate materials for electroless coatings. Commercially pure aluminium (99.3 % pure) was supplied by Hindustan Aluminium Company (HINDALCO) whereas low carbon steel rod of 6.25 mm diameter was procured from local market. The composition analysis of the steel and aluminium was carried out by employing the spectrographic analysis. An optical emission spectrometer, T5A 181181 model supplied by Thermo Jarrell Ash Corporation, USA was used. The carbon fabric was supplied by Regional Research Laboratory, (CSIR) Thiruvananthapuram, India.

3.2 SYNTHESIS OF ELECTROLESS COATINGS

3.2.1 Substrate Preparation and Pretreatment

The normalisation of low carbon steel used was carried out at 860°C for 1 h. All samples from these substrates were meticulously prepared for the electroless coatings so as to remove the oxide layer and any other adhering material in order to ensure the good adhesion between the substrate and coating. Steel and aluminium samples were polished following the standard method using emery papers up to 4/0-grade before its preparation and pretreatment.

3.2.1.1 Steps for Surface Preparation

The steps followed for the surface preparation, based on the literature are given below:

1. Degreasing with an organic solvent (acetone),
2. Degreasing with sodium hydroxide,
3. Washing with running water,
4. Etching in dilute nitric or hydrochloric acid,
5. Washing with distilled water and
6. Drying.

3.2.1.2 Substrate Pretreatment

The steps followed in the pretreatment of the samples for initialisation and sensitization in respect of different substrate are given below:

- a) **Normalised steel substrate:**
 - i) Dipping in dilute hydrochloric acid solution for about 2 min,
 - ii) Dipping in 0.1 % stannous chloride, SnCl₂, solution for 2 min and
 - iii) Dipping in 0.01 % palladium chloride, PdCl₂, solution for 1 min.
- b) **Aluminium substrate:**
 - i) Dipping in 3 % sodium hydroxide, NaOH, solution for about 2 min,

- ii) Dipping in 0.1 % stannous chloride, SnCl_2 , solution for 1 *min* and
- iii) Dipping in 0.01 % palladium chloride, PdCl_2 , solution for 30 *sec*.

c) **Carbon fabric substrate:**

- i) Dipping in acetone for about 2 *min*,
- ii) Dipping in methanol for about 2 *min*,
- iii) Dipping in 0.1 % stannous chloride, SnCl_2 , solution for 5 *min* and
- iv) Dipping in 0.01 % palladium chloride, PdCl_2 , solution for 5 *min*.

All types of samples were subjected to thorough rinsing with distilled water and dried after each step mentioned above before proceeding for the next step.

3.2.2 Bath Composition

In the light of discussions in chapter 2, Sodium hypophosphite was used as the reducing agent in the alkaline electroless nickel bath as explained by Agarwala (1987) and Brenner and Riddell (1946). A modification by the addition of an extra buffer, (ammonium chloride) was achieved to combat the variations in the pH during the coating process in the present investigation. The composite coatings were obtained using a bath in which co-precipitation of ZrO_2 and Al_2O_3 took place followed by their co-deposition (Satyanaranayana *et al.*, 2001), whereas for Ni-P coatings, conventional electroless nickel baths were used. The effect of relative concentration of components of co-precipitation reaction on the weight of the coating was also experimentally studied, which resulted in balanced *in-situ* co-precipitation without the reduction in the bulk of the solution. Table 3.1 provides the details of the bath constituents and coating conditions. The bath was periodically stirred so as to keep the co-precipitated Al_2O_3 - ZrO_3 , floating and to prevent local overheating of the bath. Also ammonia solution was added as and when required to neutralise the acids formed during the reaction and to compensate the loss of the same due to evaporation.

Table 3.1 Bath Components and Operating Conditions for Electroless Coating.

Particulars	Description
Temperature	90 ± 2 °C
pH	9.0 ± 0.25
Bath loading	about 6000 mm ² /l
Metal salt	Nickel sulphate, 33 g/l
Reducing agent	Sodium hypophosphite, 19-21 g/l
Complexing agent	tri-sodium citrate, 84 g/l
Stabilizer	Ammonium sulphate and chloride 25 g/l each
pH controlling reagent	Ammonia solutions (a few drops for maintaining the pH at 9.0)
Co-precipitation elements (for in-situ composite coatings)	Aluminium chloride, 19.2 g/l and Zirconium oxychloride, 5.8 g/l

3.2.3 Selection of Operating Parameters

Several pilot experiments were carried out to optimise coating parameters such as pH and temperature, in respect of coating rate and general adherence of the coating with the substrate. However, this study was carried out only for the aluminium substrate and extended to other substrate materials so as to get similar coatings on the all substrates under consideration. An orthogonal array L_4 was selected to conduct these experiments and further the effect of process parameters including pH, temperature and time was studied by analysis of variance (ANOVA) technique. The ranges of the above mentioned three parameters have been chosen at two levels on the basis of available literature. Further, the study to optimise the bath loading factor and coating time was carried out at suitably determined concentration of the co-precipitation reactants, with pH value of 9.0 and temperature 90°C,

which were experimentally found to provide maximum productivity in terms of coating weight. Therefore, the optimum parameters were chosen on the basis of maximum coating rate. The coating rate for electroless Ni-P-X and Ni-P coating for the specified bath conditions were experimentally studied at maximum productivity level. The optimum bath condition so found is given in Table 3.1. All the chemicals used were of analytical grade.

Further the experimental and empirical model studies for optimising coating parameters in terms of bath loading factor and time for this coating process are discussed, in which coating uniformity and consistency in weight deposited have been considered.

3.2.4 Optimum Coating Time and Bath Loading Factor

The bath loading factor is defined as the ratio of the total area of substrate to the volume of the bath. Once the value of pH and temperature were finalized for the newly developed composite coating bath, its effectiveness with regards to the bath loading factor and coating time was studied. The electroless Ni-P-X composite coatings were prepared for different substrate areas of 6.5, 8.0, 10.0, 12.5, 15.0 and 22.5 cm^2 in the electroless bath of 200 ml volume. All of these substrates possess different bath loading factors were used to coat the aluminium samples for 15, 30, 45, 60 and 75 min of coating time. The above experimental study led to an empirical model, developed by regression analysis. This model was used to determine the theoretical coating weight of electroless Ni-P-X at 9.0 pH and 90°C bath temperature. The maximum coating weight and uniformity of the coating were considered as the process response parameters in the study.

3.2.5 Process Details

Indigenously fabricated setup, as shown in Fig. 3.1, was used for synthesis of the electroless coatings in the present study. The electroless bath prepared was placed in the copper beaker and heated electrically in the oil bath. All the samples were coated at temperature of $90 \pm 2^\circ C$ and the pH value of 9.0 ± 0.25 to obtain consistently similar

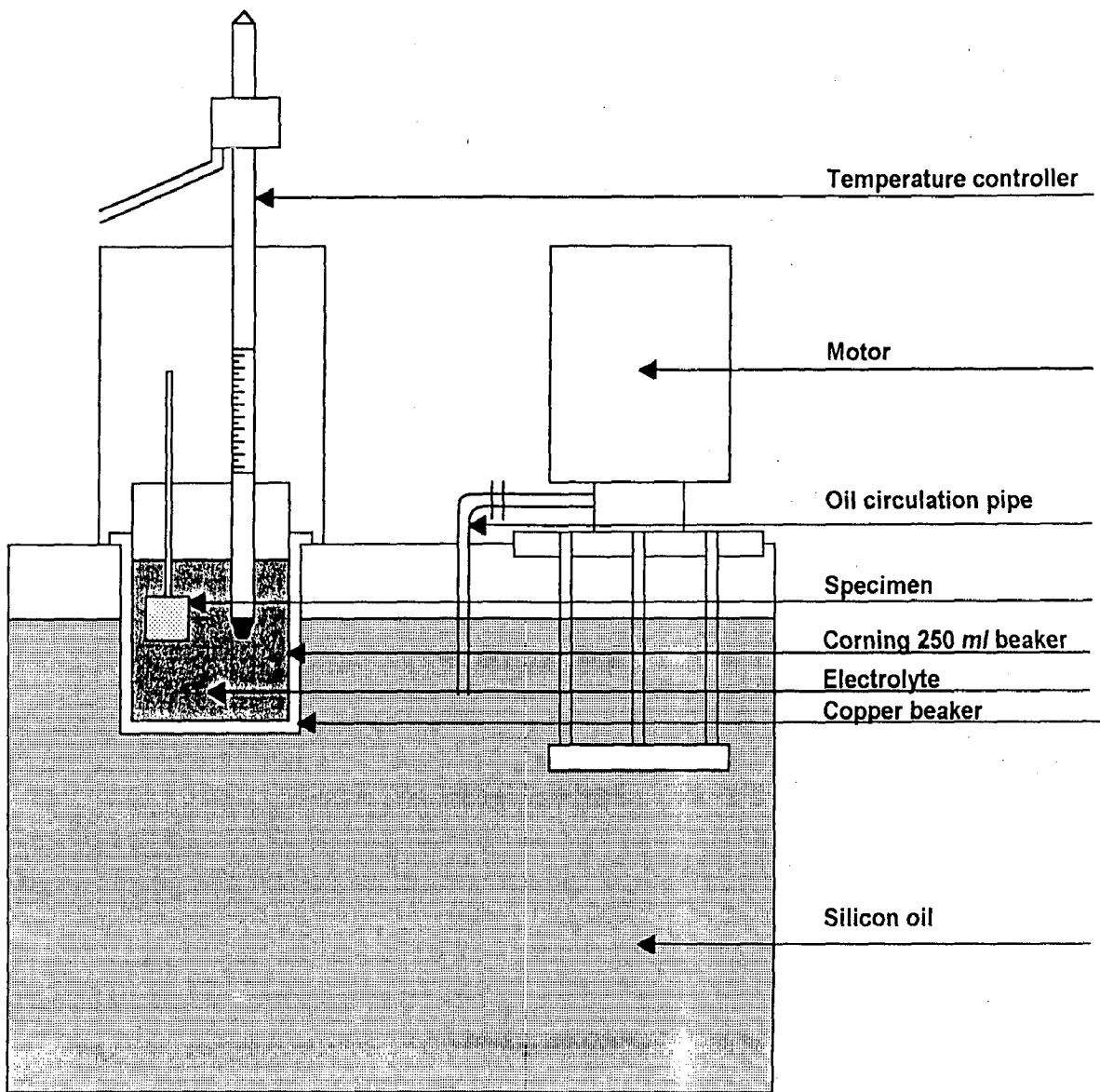


Fig. 3.1 Schematic diagram of the experimental set-up used for electroless coating

coatings in terms of composition. Due care was taken in maintaining the temperature and pH of the bath solution by using temperature controller and pH meter respectively. The bath constituted of nickel salt, hypophosphite and organic compounds which helped in preventing an increase in the concentration of hydrogen ions formed during the course of reaction. In view of avoiding the reaction in the bulk of the solution, a bath stabilizer was also added. The electroless Ni-P-X and Ni-P coatings were carried out by immersing the pretreated substrate in the bath. Before immersing the substrate into the bath, it was assured that the bath temperature had stabilized to the desired value and pH properly adjusted. In view of getting the better adherence of composite coatings, the samples were initially coated with only Ni-P for 1 *min* followed by the composite coating. The nature of reactions occurring during the coating process have already been described in chapter 2.

The pH of the bath was continuously monitored and intermittently stirred during the coating process. The stirring was used to avoid the local variations in pH and temperature of the bath; further, it also helped to keep the particles in suspension, which were available for co-deposition. After the successful coatings, the samples were dried in an oven at 70°C for 15 *min* and preserved in a desiccator for further necessary characterisation. In some cases, the coating foil was chemically stripped off from the substrate by immersing the coated sample(s) in etching solution and then those were subjected to further analysis. The samples in the form of a film of about 30-40 μm thickness were assumed to be of uniform composition, as the bath conditions were uniformly maintained throughout the process.

3.3 EXAMINATION OF CO-PRECIPIATED POWDER

The in-situ co-precipitation of ZrO_2 and Al_2O_3 has been carried out along with the electroless coating process. The co-precipitated powder was collected after the termination of Ni-P-X composite coating reaction by filtering the electroless bath solution through 42 number Wattman make filter paper. The collected powder was washed thoroughly, dried and examined under Scanning Electron Microscope, SEM (LEO 435 VP model). X-ray diffraction studies were carried out on the co-precipitated powder. The co-precipitated

powder particles were spread over the glue tape followed by gold coating before examinations under SEM and the salient features were photographed which are shown in chapter 4.

3.4 HEAT TREATMENT OF COATED SAMPLES

The heat treatment was performed in a tube furnace for three different sets of the coated samples. The schematic view of the tube furnace along with the argon gas flow arrangement is shown in Fig. 3.2. Argon gas with 99.993 % purity and 1.5 kg/cm^2 pressure was used for heat treatments of coated samples. The maximum impurity levels of different elements/compounds present in argon gas used are given in the Table 3.2.

Table 3.2 Composition of Purified Argon Gas Used for Heat Treatment.

Particulars of Impurity	O ₂	Moisture	Hydrocarbon	CO	CO ₂
Maximum Level in ppm	2.0	2.0	2.0	Nil	Nil

Three different sets of coated samples: (i) Ni-P and Ni-P-X coated steel (ii) Ni-P-X coated aluminium and (iii) Ni-P and Ni-P-X coated carbon fabric samples were heat treated. In the first set, the coated normalised steel samples were heat treated at $400 \pm 5^\circ\text{C}$ in purified argon atmosphere for 1 and 2 h followed by water quenching. In the second set, Ni-P coated aluminium substrates were heat treated at $400 \pm 5^\circ\text{C}$ for 1 h and $250 \pm 5^\circ\text{C}$ for 12 h. Third set of coated carbon fabric samples was heat treated for 400°C for 1 h. The carbon fabric samples were coated for 5 min duration and those on aluminium and steel were coated for 45 min of duration.

3.5 X-RAY DIFFRACTION ANALYSIS

The X-ray diffraction analysis was conducted to find out different phases present in the specimen, which were under study. A Philips, PW 1140/90 model of X-ray diffraction unit equipped with scintillation counter and filtered Cu K α radiation was used for diffraction studies. The X-ray diffraction studies were carried out using a copper target and nickel

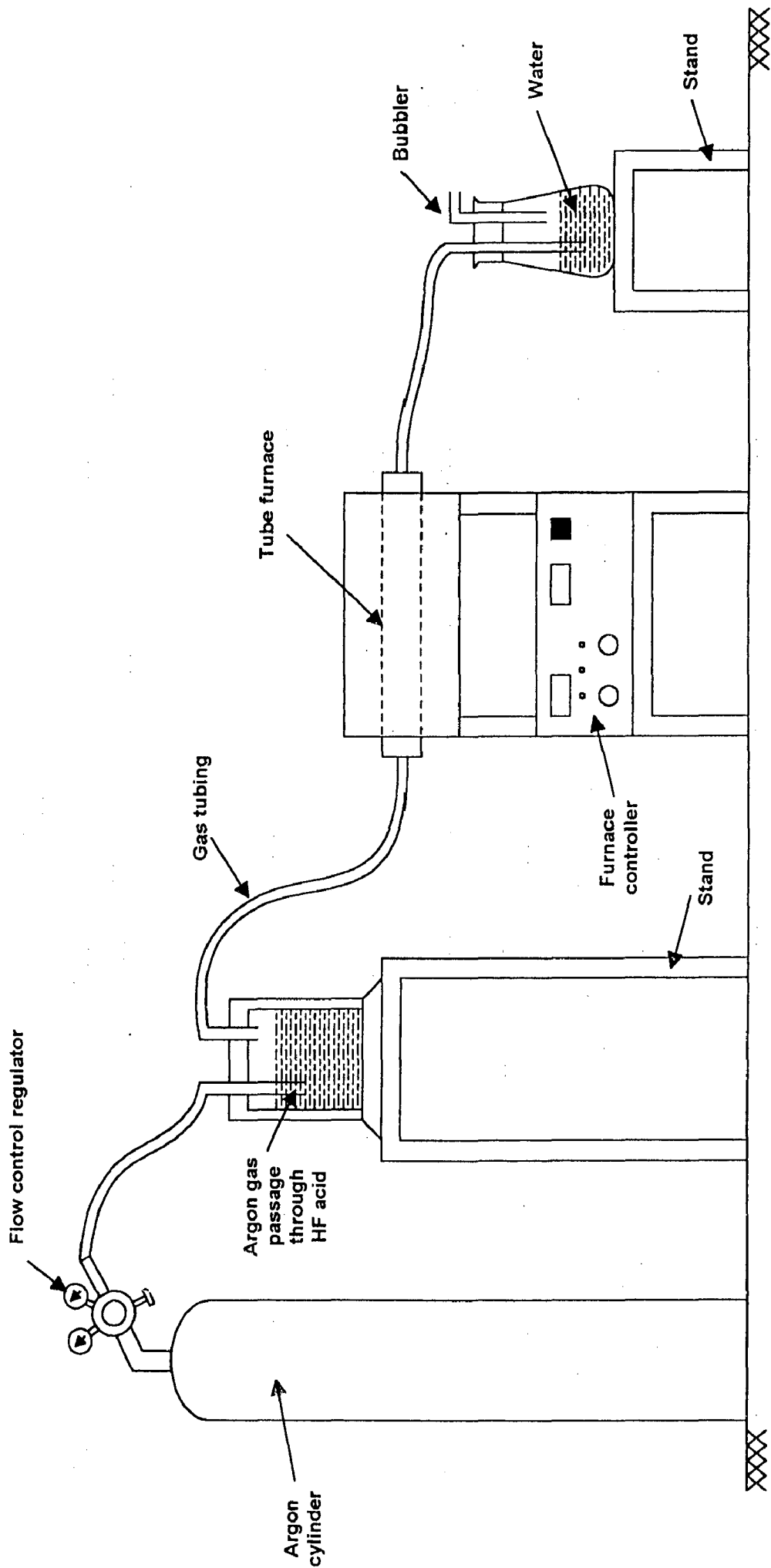


Fig. 3.2 Schematic diagram of the tube furnace alongwith argon gas flow arrangement.

filter at a current of 20 mA and voltage of 35 kV. The X-ray diffraction pattern for the co-precipitated powder was obtained for the 2θ angles between 5 to 110° and the intensity of the diffracted beam against 2θ was recorded at the chart speed of 1 cm/min, keeping the Goniometer speed of $1^\circ/\text{min}$ for all the samples. All the d values corresponding to peaks are calculated by using Bragg's law, as given below:

$$m \lambda = 2d \sin\theta \quad (3.1)$$

where, $m = 1$ and λ is the wavelength (i.e., 1.54 for Cu K_α) and θ is Bragg's angle at the peak observed corresponding to a set of hkl planes. The phases present at the corresponding d values were identified with the help of JCPDS ASTM data cards.

These analyses were conducted for: (a) co-precipitated powder, (b) Ni-P-X and Ni-P coatings in as-coated and heat treated conditions, (c) carbon fabric and coatings on it and (d) wear debris collected from testing of different types of pin wear samples.

(a) Co-precipitated powder

The powder obtained by in-situ co-precipitation reaction in the electroless composite coating bath was collected after the coatings are carried out. This powder was washed thoroughly and dried before subjecting to X-ray diffraction studies. The phases identified and their characteristic details are explained in chapter 4.

(b) Ni-P-X and Ni-P coatings in as-coated and heat treated conditions

The coating foils were chemically stripped off by immersing the coated aluminium foil in 3% NaOH solution followed by subjecting them to X-ray diffraction studies after washing and drying. The d values were calculated and the phases present in the corresponding samples were identified accordingly with the help of JCPDS ASTM data cards as explained in chapter 4.

(c) Carbon fabric and coatings on it

The carbon fabric in uncoated, as-coated and heat treated conditions were studied under X-ray diffraction. The uncoated carbon fabric was crushed gently in a ceramic

crucible so as get it in the powder form before subjecting it to X-ray diffraction study. The as-coated and heat treated specimens were placed in the fabric form in the sample holder of the X-ray diffraction unit. The X-ray diffraction patterns obtained for the carbon fabric specimens are shown in chapter 7.

(d) Wear debris

The X-ray diffraction studies of the wear debris for normalised steel, as-coated steel, heat treated steel sample after the coating, as-coated aluminium and heat treated coated aluminium samples were carried out. The debris collected from two different sets of heat treated specimens was very less to subject it to X-ray diffraction analysis, therefore, the debris of the two sets were pooled together. All the major peaks obtained in the X-ray diffraction pattern were indexed and the phases were identified accordingly. The details of the X-ray diffraction analysis of the wear debris for steel and aluminium based pin specimens are presented in chapter 5 and 6 respectively.

3.6 TRANSMISSION ELECTRON MICROSCOPY (TEM) STUDY

Firstly, the coated samples were specially prepared for 5 *min* coating duration, which were then chemically stripped, washed and dried. These samples were electrolytically thinned by using platinum electrode and examined under a Transmission Electron Microscope (TEM) of Philips EM 400T/ST make. The bright field and dark field images and as well as selected area diffraction (SAD) patterns were typically featured, and are shown in chapter 4.

The SAD patterns observed from TEM were used to confirm the phases of the electroless coating. The radius of the each ring is characteristic of the spacing of the reflecting planes in the crystal and setting of microscope lenses. This was calibrated by using gold sample. Figure 3.3 represents a schematic diagram showing the diffracted ring in a SAD pattern.

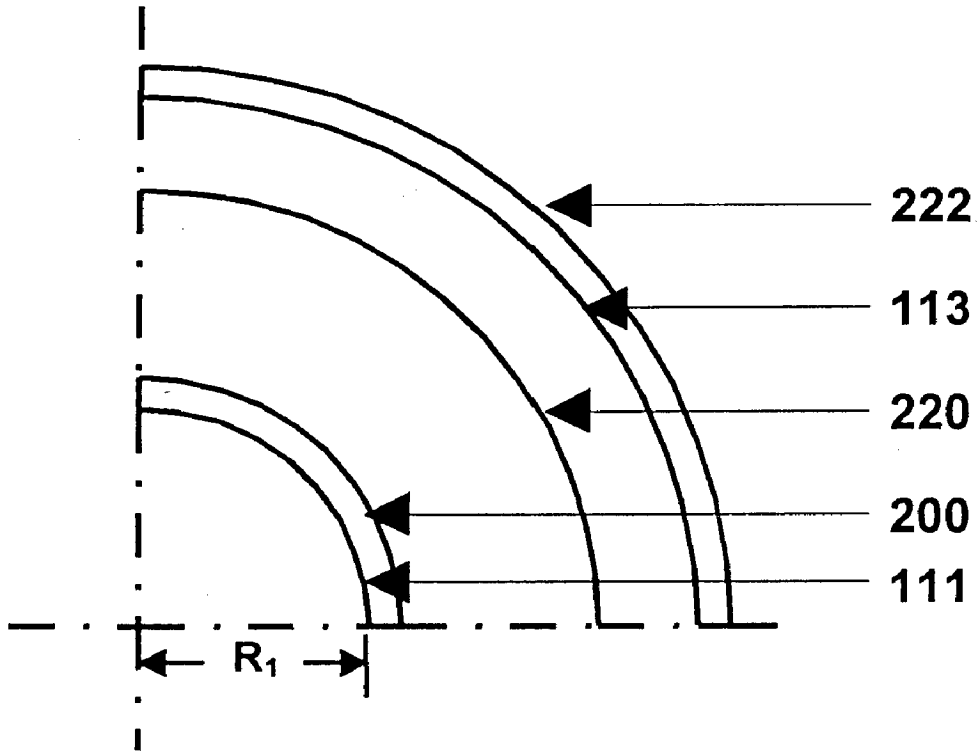


Fig. 3.3 Schematic of indexed SAD ring pattern obtained by TEM for nickel.

The radii of the rings $R_1, R_2, R_3 \dots$ etc., were measured and those obtained from the SAD pattern were converted into interplanar spacing using the camera constant as $d_i = L\lambda/R_i$, where $i = 1, 2, 3, \dots$ etc. The phases present in the deposits were identified by use of the ASTM index cards.

3.7 HARDNESS MEASUREMENTS

The microhardness measurements were carried out in the specimens of as-coated and heat treated using a Leitz Wetzlar make tester with Vickers square base pyramid diamond indenter having the angle of 136° at a load of 10 gm for 15 seconds of indentation time. The load and the indentation time were selected such that the indentation did not pierce through the coatings. The average of diagonals of square indentation observed under optical microscope at a magnification of 400 was used to find out the microhardness value. The reported values in the present study represent the average of at least five replicates of microhardness readings for each sample with the different phases.

The Vickers macrohardness of the substrates and coating-substrate systems in both the as-coated and the heat treated conditions was measured using Dia Tester 2RC hardness tester supplied by Blue Star Co (India). For aluminium samples and coatings on these samples 5 kg load was used whereas for steel and coatings on steel, the load used was 15 kg. The load was applied for 30 seconds on a sample and then the diameter of indentation was measured on the screen of the tester. At least five indentations on each of the samples were made and the average indentation diagonals were used to determine the hardness value on the Vickers scale.

3.8 METALLOGRAPHIC STUDIES OF ELECTROLESS COATINGS

The standard analytical tools, which include optical microscope, scanning electron microscope (SEM), electron probe micro analyser (EPMA), X-ray fluorescence (XRF) and SEM-EDAX were used in the present study. The metallographic studies were conducted to support the qualitative and quantitative analysis in terms of morphology of the coatings and

different elements/phases present in the coatings. These analyses gave the evidences for the presence of Ni, P, Al₃Zr, Al₂O₃ and ZrO₂ in the composite coatings under this study that is explained in the chapter 4.

The samples were first prepared by hot mounting in plastic granules by using a CISCO mounting unit. The substrate samples were made flat by motor driven emery paper belt followed by standard manual polishing treatment up to 4/0-grade emery paper. Those samples were cloth polished on a sylvet cloth using suspension of 0.1 μm alumina powder on wheel of the polishing machine. The coated steel/aluminium and coated fabric samples were examined by cleaning them with acetone. Finally all samples except aluminium substrate were etched with 2% nital (2% HNO₃ + 98% methanol), washed and dried before metallographic examinations. The aluminum samples were etched with 3% NaOH.

3.8.1 Optical and Scanning Electron Microscopic Studies

The coated samples in as-coated and heat treated conditions were examined under Reichert-Jung make Optical microscope and SEM. The aspects like: microstructure, coating globule size, coating layers along the cross section and coating thickness etc., were typically featured and the corresponding micrographs are shown in chapter 4. In case of carbon fabric coatings, continuity and the phase uniformity of coating on carbon fabric was assessed with the help of metallographic study. The surface features of carbon fabric samples in uncoated, as-coated and heat treated conditions were featured and the micrographs are shown in chapter 7.

3.8.2 X-Ray Fluorescence Studies

The as-coated Ni-P-X flat sample of 25 mm × 25 mm was subjected to XRF study so as to obtain the relative concentrations of the different elements present in the coating. Siemens SRS 3000 XRF unit was employed in the present work. The X-ray tube in the unit used was provided with voltage of 55 kV and 40 mA current for detection of nickel and

zircon whereas for phosphorus these values were respectively 40 *kV* and 70 *mA*. However, for detection of aluminium, a voltage of 30 *kV* and a current of 60 *mA* was used.

3.8.3 Area Analysis by SEM-EDAX

Four different areas in a typical Ni-P-X as-coated specimen were subjected to SEM-EDAX analysis. The X-ray scanning used for this analysis gave the intensity peaks for Ni, P, Al, Zr and oxygen leading to qualitative analysis of these elements. The output obtained from the system is shown in chapter 4.

Similarly, three different areas of the Ni-P-X coated samples were subjected to EDAX for quantitative area analysis. A few Ni rich islands (5 Nos.) and Zr rich islands (3 Nos.) were also subjected to EDAX for quantitative elemental analysis.

3.8.4 Spectrographic Analysis by SEM-EDX

A typical Ni-P-X as-coated aluminium sample was studied along a line of 10.84 μm to obtain the spectrograph showing the presence of different elements. This spectrograph also gave the profile of coating along the selected line on the coated surface of the substrate as shown in chapter 4. The carbon fabric coated with electroless Ni-P-X sample was studied by the spectrographic analysis to ascertain the presence of different elements on the surface of the fabric and the output obtained by the SEM-EDAX is shown in chapter 7.

3.8.5 Qualitative and Quantitative Analysis by Electron Probe

Micro Analyser

The qualitative and quantitative analyses of different elements present in the Ni-P-X and Ni-P coating were carried out with the help of EPMA (JOEL make, JXA-8600M

model). The flat specimen of as-coated Ni-P-X was subjected to EPMA studies so as to obtain the qualitative analysis by X-ray mapping and quantitative analysis by point analysis.

The X-ray mapping of as-coated Ni-P-X specimen was carried out and typical features were photographed, which show the distribution of different elements present in the coating, i.e., Ni, P, Al and Zr and the results are shown in chapter 4. Similarly, the samples of both the uncoated and the coated carbon fabric zone into aluminium matrix were subjected to X-ray mapping to obtain qualitative analysis for presence of aluminium, nickel and phosphorous. The samples prepared for the SEM studies were employed to EPMA and the salient features photographed as shown in chapter 7.

The quantitative analysis by EPMA was carried out by five point averaging method. For the quantitative analysis, Ni and P were separately analysed and then, Al₂O₃ and ZrO₂ were assessed by providing the oxide correction during the analysis under EPMA. The beam diameter of 300 μm was used for the present work.

3.9 DETERMINATION OF COATING GLOBULE SIZE AND ITS DISTRIBUTION

The coating globule size and its distribution give the morphological information. The globule size measurements for the as-coated Ni-P, Ni-P-Al₂O₃, Ni-P-ZrO₂ and Ni-P-X specimens were conducted by using the Heyn's intercept method (Dehoff and Rhines, 1968). In this method the number of lines, 10 in this work, of equal length were randomly drawn on the micrograph and the number of intercepts, where the line crossed the grain/particle boundary, were noted. The number of intercepts obtained in different cases were then divided by the length of the line drawn on the micrograph. The size so obtained was then scaled appropriately to get the average sizes of the coating globules along the line on the corresponding micrograph. These sizes obtained for the 10 different lines were averaged to get the final sizes that are reported in chapter 4.

3.10 KINETICS STUDY BY DIFFERENTIAL SCANNING CALORIMETER

The crystallisation of metallic glasses is highly exothermic process, therefore, their kinetics were suitably studied by use of differential scanning calorimeter (DSC). Non-isothermal kinetics of electroless Ni-P and Ni-P-X coatings, prepared by the process as described earlier, was investigated by DSC studies. The calorimeter used was a Stanton Redcroft, DSC- 1500, designed to give the output in milli watts. The coated samples were chemically etched for stripping off the film from the substrate and later these films (10 mg) were cleaned thoroughly followed by placing them into the platinum crucible of DSC for annealing in nitrogen environment. The specimens were subjected to DSC study for four different heating rates (β), i.e., $\beta = 10, 15, 20$ and $25 \text{ }^\circ\text{C}/\text{min}$ and differential energy versus temperature curves were simultaneously recorded by the X-Y recorder provided with the DSC unit. The heating was carried out up to $600 \text{ }^\circ\text{C}$ so as to attain the peak indicating the maximum transformation rate.

A suitable base line by drawing two tangents and a straight line from the peak was constructed which gave a stepped base line. The method used to construct the base line is shown in Fig. 3.4. The planimeter was used for area measurement under the curve. The activation energy E and the reaction exponent n were calculated by using Eq. (2.22) and (2.24) respectively, presented in section 2.6.2.

3.11 TENSILE TESTING OF CARBON FABRIC SAMPLES

Carbon fabric samples of $25 \text{ mm} \times 80 \text{ mm}$ were cut and then coated for 5 min as described earlier in section 3.2. Different samples of carbon fabric in uncoated, Ni-P-X/ Ni-P coated and heat treated after coatings were subjected to tensile tests at the ambient temperature (22°C) by using the Hounsfield Tensometer (H25 KS model) having maximum capacity of 25 kN . The constant test speed of $400 \text{ mm}/\text{min}$ was maintained for all the samples under consideration. The auto response load vs. extension curves for the samples

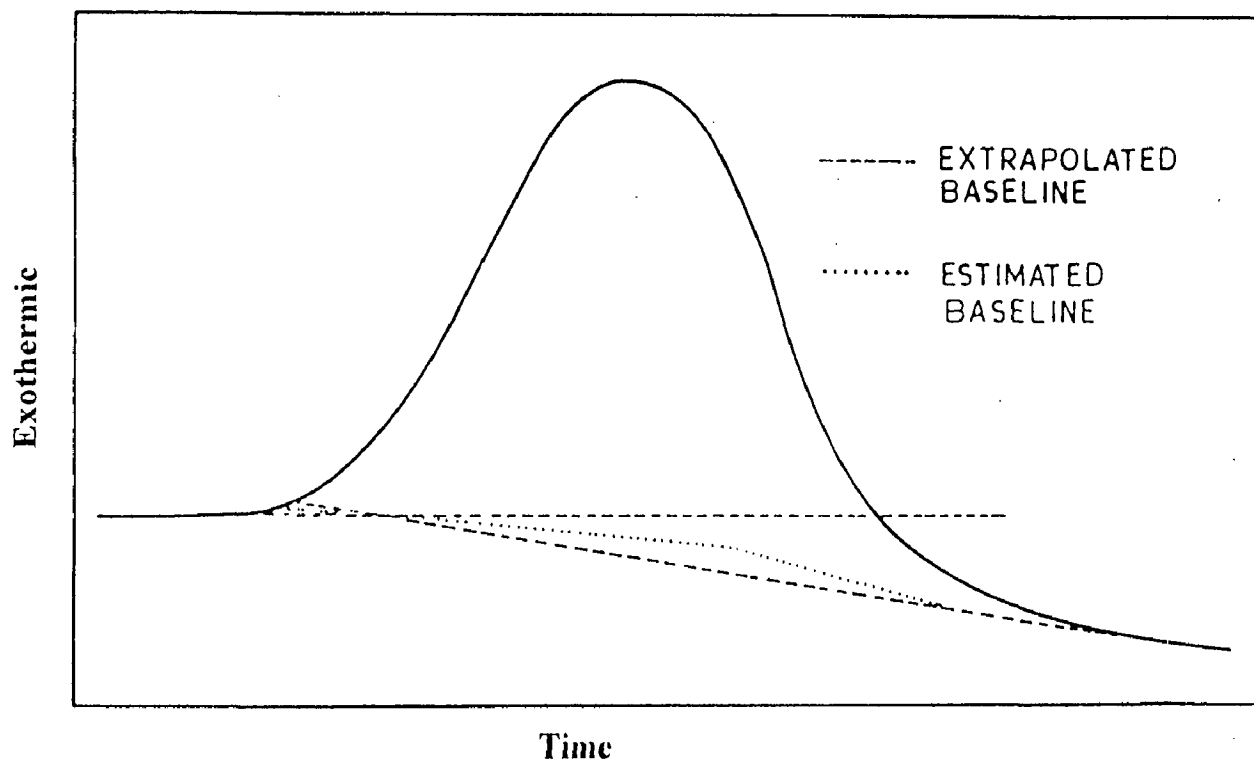


Fig. 3.4 Base line construction method used to measure area under DSC peak (Scott, M. G., 1978).

were obtained by computer interfacing provided with the tensometer. The gauge length and thickness of the samples were measured and the ultimate tensile strength (UTS) of the specimens in N/mm^2 was estimated by dividing the maximum load by the initial cross sectional area of the fabric specimen. The tensile strengths of as-coated and heat treated samples for both Ni-P-X and Ni-P electroless coatings were compared with uncoated samples and are given in chapter 7.

3.12 FRACTOGRAPHIC STUDIES

The provision of operating mode of fracture is based on fractographic studies, therefore, the fractured surfaces of the different carbon fabric specimens were subjected to this study after the tensile testing. Firstly, the broken specimens were cut into small pieces and vertically kept between two glass plates such that some portion of broken fabric remained at higher elevation than the supporting glass plates. Then these specimens were examined under SEM unit and the salient features were photographed.

3.13 EXAMINATION OF FABRIC ZONE INTO ALUMINIUM MATRIX

The uncoated and as-coated carbon fabric samples were reinforced in aluminium matrix by conventional permanent mould casting method. The temperature of the pure aluminium melt was maintained at $750 \pm 5^\circ\text{C}$ during the casting. During pouring the mould was kept in the preheated condition at a temperature of about $70\text{-}80^\circ\text{C}$. After pouring aluminium into mould, the carbon fabric fitted in the aluminium strip frame was immersed in the melt and the castings were allowed to cool in air. Castings were cooled and followed by cutting by use of a diamond cutter (Isomet-1000 model) such that the fabric zone into the matrix was visible. The samples indicating such fabric zones were cut into small pieces and hot mounted in plastic granules as explained earlier in the section 3.5, which were finally polished and then further characterised under SEM and EPMA X-ray mapping. The typical features were photographed and are shown in chapter 7.

3.14 DRY SLIDING FRICTION AND WEAR TESTING

The different types of cylindrical samples having 30 mm length and 6.25 mm ϕ were used as wear pins, as shown in Fig. 3.5. The pin samples of substrate were polished up to 4/0-grade emery paper and then coated with the electroless Ni-P-X and Ni-P coatings as explained in section 3.2. These pins were subjected to the dry sliding wear and friction tests by using pin-on-disc type wear monitor, TR 20E model supplied by Ducom, Bangalore (India). The complete photograph of the wear monitor used and its schematic view are respectively shown in Figs. 3.6 and 3.7. The pin samples, which had flat surfaces in contact region and rounded corners were held stationary against the 100 mm diameter rotating disc made of En-32 steel having hardness of 60-62 HRC. The composition of the case hardened steel disc is given in the Table 3.3. The dry sliding wear tests for all the samples were carried out in normal laboratory atmosphere at an average relative humidity of 75-80 %. During wear tests for different normal loads in this investigation, a constant sliding speed of 0.5 m/s was maintained.

Table 3.3 Chemical Composition of Case Hardened EN-32 Steel Disc (wt. %).

Element	C	Si	Mn	S	P
wt. %	0.42 (max)	0.05-0.35	0.40-0.70	0.05 (max)	0.05 (max)

The wear tests for normalised steel and coatings on it were conducted at normal loads of 29.4, 34.4 and 39.2 N, whereas specimens of aluminium and coatings on it were tested under the loads of 4.9, 7.4, 9.8 and 12.3 N. Different wear tests conducted, with pin of normalised steel, aluminum, and coatings on them are enumerated in the Table 3.4, which also represents the designations given to different types of pin samples as used in the text at the appropriate places. The higher loads were used with steel and coatings on it due to their very low wear observed in these cases as compared to that with aluminium substrate and coatings on aluminium.

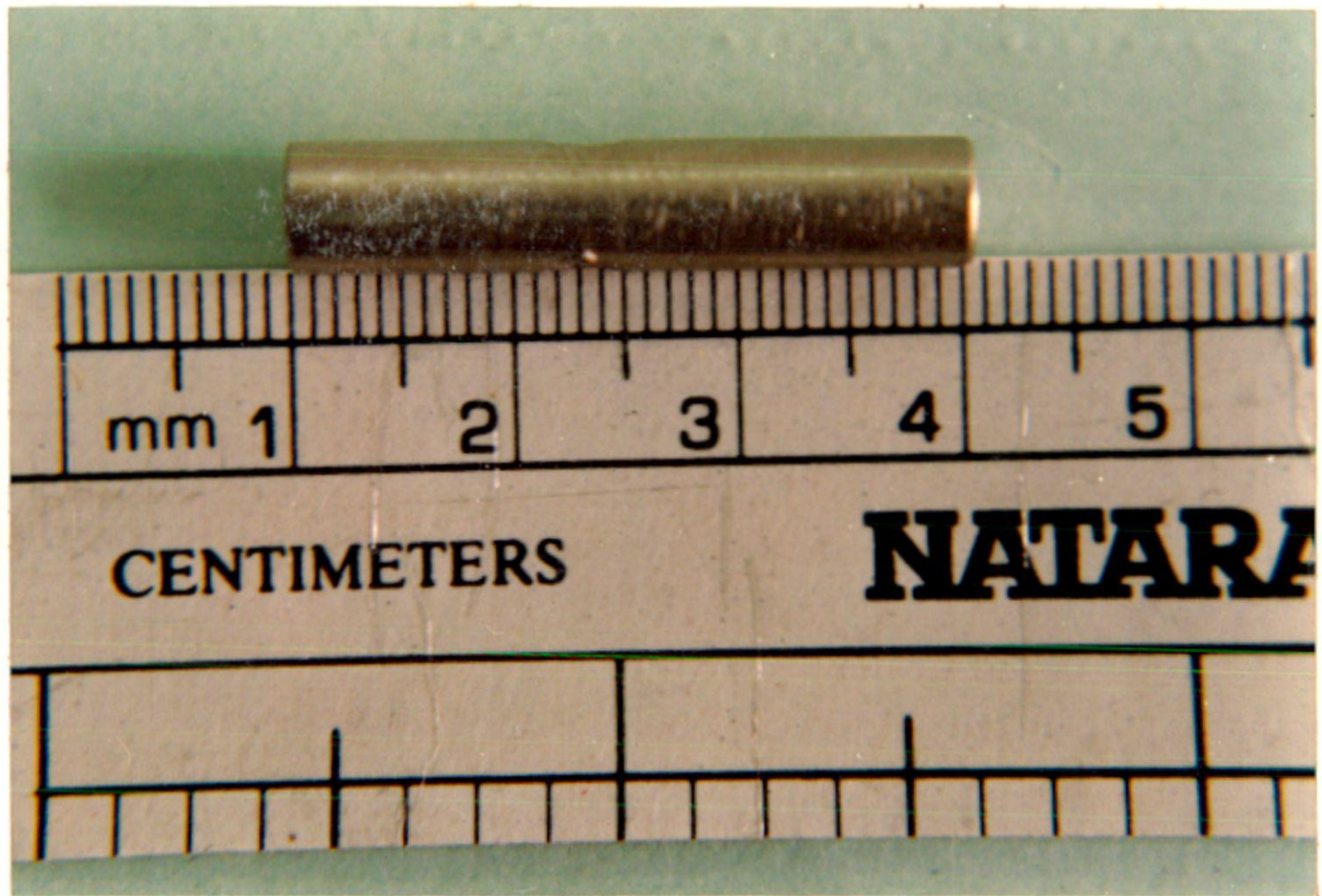


Fig. 3.5 Photograph of the wear pin sample.

Fig. 3.6 Photograph of the pin-on-disc wear testing machine.

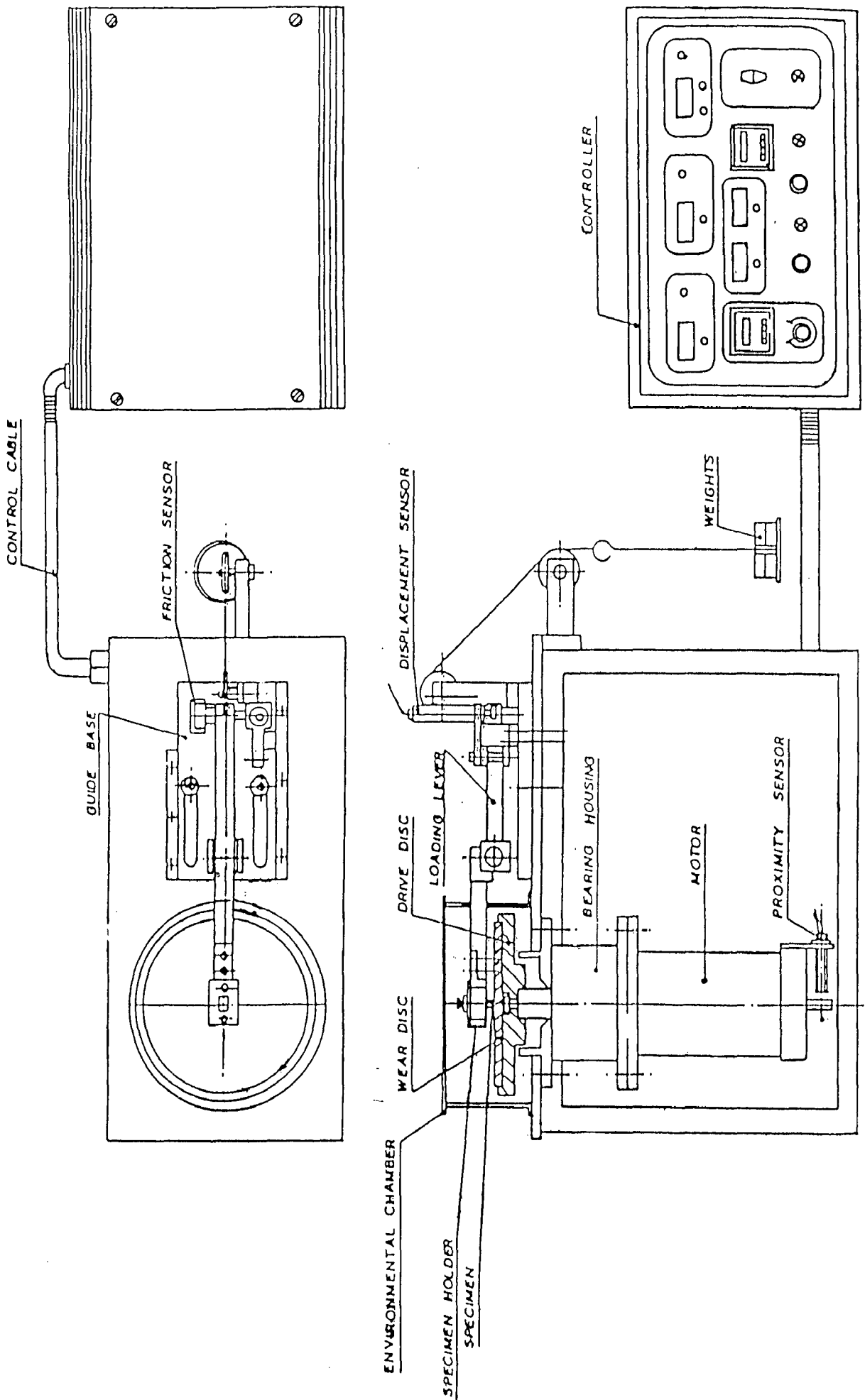


Fig. 3.7 Schematic view of the pin-on-disc wear testing machine.

A dead weight loading system was used against the pin for the wear testing. The wear track radius and the rpm of rotating disc were so adjusted that constant sliding speed of 0.5 *m/s* was consistently maintained. The new wear track was used for each type of the wear pin sample. A variation of ± 5 *rpm* was observed during the rotation of the disc. The pilot experiments on as-coated Ni-P-X steel pins were carried out by varying the coating time and the results were used to select the sliding distance for a particular load so that the wear is confined within the coating primarily throughout the test. The tangential force and the pin weight losses were recorded in the time interval of 2 or 1 *min* depending upon total sliding distance covered during the test. After each interruption of the test, the pin was removed from the holder, cleaned gently by camel hair brush to remove the loose debris if any, weighed and repositioned into the holder without changing the orientation of sliding surface. The weight was taken in a semi-micro balance having an accuracy of 1×10^{-4} *g*. The time interval of measuring the weight loss of the pin was so adjusted that at least four data points were obtained over the total distance slid in a particular run. The data obtained for the weight loss was converted to volume loss by using the density of steel, Ni-P coating and aluminium as 7800 *kg/m³* (Glaeser, 1992), 8200 *kg/m³*, (Gawne, 1984) and 2700 *kg/m³* (Tottle, 1984) respectively. As the amounts Al₂O₃, ZrO₂ and Al₃Zr content were very less and the insignificant difference in phosphorus content, the density of the Ni-P-X coating has been taken to be the same as that of Ni-P coatings. Each test at a given load and sliding velocity was repeated three times and the average data from these tests after each interval of time has been used for the analysis.

The frictional force as indicated on the wear monitor has been represented by the torque on the sample that was calibrated using a fixed distance lever arm of the machine used. The coefficient of friction was determined by dividing the frictional force by the applied normal loads.

Table 3.4 Different Wear Pin Samples Subjected to Wear and Friction Testing and their Corresponding Designations.

Sl. No.	Particulars of Pin Sample	Designation	Normal Load Applied, <i>N</i>
1.	Normalised steel substrate	NS	29.4, 34.4 and 39.2
2.	As-coated Ni-P-X steel	AC ₁	
3.	Ni-P-X coated steel and heat treated at 400°C for 1 h	HT ₁ -A	
4.	Ni-P-X coated steel and heat treated at 400°C for 2 h	HT ₂ -A	
5.	As-coated Ni-P steel	AC ₂	
6.	Ni-P coated steel and heat treated at 400°C for 1 h	HT ₁ -B	
7.	Ni-P coated steel and heat treated at 400°C for 2 h	HT ₂ -B	
8.	Aluminium substrate	Al	4.9, 7.4, 9.8 and 12.3
9.	As-coated Ni-P-X aluminium	AC ₃	
10.	Ni-P-X coated aluminium and heat treated at 400°C for 1 h	HT ₁ -C	
11.	Ni-P-X coated aluminium and heat treated at 400°C for 1 h	HT ₂ -C	

3.15 MICROSCOPIC EXAMINATIONS

3.15.1 Worn Surfaces

The sliding surfaces of substrate steel, as-coated steel and heat treated after coating the steel samples with Ni-P-X and Ni-P for different conditions mentioned in Table 3.4 were examined under SEM. Similarly the worn surfaces of aluminium substrate and the Ni-P-X coatings on aluminium in as-coated and heat treated conditions were also examined under SEM. The salient features showing the wear track, transfer layer etc., in each of above cases were photographed and are presented in chapter 5 and 6.

The samples of steel substrate, aluminium substrate, and Ni-P-X coatings on them in different conditions have been mounted in taper of 1:10 after sliding wear of given normal load. All of these specimens were polished by adopting standard metallographic practice and then subjected to SEM study for representing the distinguished features observed at the subsurface zone of the worn samples.

3.15.2 Examination of Wear Debris

The composition of the transfer layer in the tribological pair used in wear test can be assessed by examination of wear debris. The debris generated during the dry sliding wear of different types of pins, i.e., normalised steel, aluminium substrates and coatings on them in both the as-coated and the heat treated conditions was carefully collected. To collect the debris a paper is wrapped along the circumference of the disc such that it was projected about 1 *mm* above the disc surface so the debris could not fall out of the disc due to centrifugal force. The collected debris particles were examined under both the Zeiss make (MC 63 OM) stereo-microscope and the SEM. The salient features of the wear debris photographed are shown in chapter 5 and 6.

**SYNTHESIS AND CHARACTERISATION OF ELECTROLESS
Ni-P-X AND Ni-P COATINGS ON ALUMINIUM AND STEEL**

This chapter describes the results obtained for the different electroless coatings, which have been explained in terms of synthesis, qualitative analysis, quantitative analysis, DSC studies and hardness. In the synthesis part, the coating of Ni-P-X, ($X = \text{ZrO}_2\text{-Al}_2\text{O}_3\text{-Al}_3\text{Zr}$) has been explained with respect to the selection and optimisation of coating condition leading to an empirical model for the coating weight obtained. The reproducibility of the coating has also been confirmed by replicate experiments under the determined optimum coating conditions. The metallographic studies of the as-coated Ni-P-X coatings have been presented and discussed, which include the microstructure of the coatings, globule size and its distribution. The qualitative and quantitative analyses of the coating by different metallurgical tools viz., XRF, SEM-EDAX, XRD, TEM, and EPMA have been presented. The phase analysis has been carried out for Ni-P-X deposition in as-coated and heat treated conditions by X-ray diffraction studies in terms of phase constituents present and confirmed by TEM studies. The non-isothermal kinetics of transformations in electroless Ni-P-X and Ni-P coatings have been observed and parameters, like activation energy and Avrami exponent are determined for different heating rates. The micro and macrohardness measurement in as-coated and at different heat treated conditions in Ni-P-X and Ni-P coated specimens have been carried out.

4.1 RESULTS**4.1.1 Composition of Substrate Materials**

The chemical compositions of steel and aluminium substrate materials used as analysed through spectrographic method are given in the Tables 4.1 and 4.2 respectively.

Table 4.1 Composition of the Commercially Pure Aluminium (wt. %).

Element	Si	Fe	Cu	Mn	Mg	Cr	Zn	Ti
wt. %	0.15	0.08	0.13	0.01	0.004	0.011	0.33	0.01

Table 4.2 Composition of Low Carbon Normalised Steel (wt. %).

Element	C	Mn	Si	S	P
wt. %	0.14	0.056	0.04	0.014	0.034

4.1.2 Optimum Bath Conditions and Coating Parameters

The electroless coating bath used by Agarwala, (1987) has been selected for the study. The composite coating needed certain modification in the bath so as to maintain the pH for required coating time. Therefore, the amount of ammonium sulphate was decreased to 25 g/l and additional buffer, ammonium chloride (25 g/l) was added. This bath composition was found to be compatible for both electroless coatings the Ni-P-X and the Ni-P. The details of the baths used have already been given in Table 3.1. The different coating parameters viz., temperature, pH, time, bath loading factor and relative concentration of co-precipitation reaction components have been optimised in terms of maximum productivity, i.e., coating weight and is explained in the subsequent part of this section.

(a) Temperature, pH and time

In view of the correct choice for pH, temperature for optimum coating time, the pilot experimental study has been carried out with the help of experimental design technique, for which an orthogonal array L_4 is used. A 22.5 cm^2 substrate area was used in this segment of the study and the details of same along with the results of the corresponding experiments are given in Table 4.3. The experimental results for synthesis of the Ni-P-X composite coatings on aluminium substrate in terms of coating weight of

uniformly adherent coating (without any peeling) have been considered as the responses for the analyses.

Table 4.3 An Experimental Layout using 'L₄' Array and Results of the Responses.

Level 2	9.5	90	45		
Level 1	9.0	85	30		
Experiment Type	Variable			Responses	
	pH	Temp. (°C)	Time (min)	Y ₁ Coating Weight, <i>W</i> (mg)	Y ₂ Uniformity of Coating
	A	B	C		
1	1	1	1	100	Extremely uniform
2	1	2	2	150	Extremely uniform
3	2	1	2	100	Fairly uniform
4	2	2	1	60	Extremely uniform
	Total			410	

From the above results, it is observed that experiment type '2' gives the maximum coating weight of 150 mg in 45 min when the bath is maintained at 90°C and pH 9.0. This experimental condition has also been observed to result in extremely uniform deposition, which is assessed by visual examination. The analysis of variance (ANOVA) results provide information about relative dominance of variables on the process. The ANOVA results for the pH, temperature and time as the parameters are shown in Table 4.4. These results were analysed by considering the maximum weight of the coating as principal factor. The ANOVA has been carried out by two types, viz., without pooling any of the parameters, i.e., Type-I and with pooling the temperature, Type-II, as a parameter having minimum percentage contribution on the process performance. It is observed from the results for the Type-I that the pH and coating time are expected to have the maximum, i.e., 49.69 percent contribution on process performance. The temperature in the range of 85-90°C, as selected in the present work has not shown significant contribution on the

process performance. Therefore, temperature has been considered as pooling factor (Type-II) analysis and percent contribution on the process performance for both the pH and the time are perceived to be 49.07 as seen from Table 4.4.

Table 4.4 ANOVA Table for Experiments Conducted as per the Array 'L₄' as Shown in Table 4.3.

Factors	Degrees of Freedom, <i>F</i>	Sum of Squares, <i>s</i>	Mean Square Variance <i>V</i>	Variance Ratio <i>F₁</i>	Percent Contributions <i>P_c</i>
Type - I: Without pooling any factor					
pH	1	2025	2025	-	49.69
Temperature	1	25	25	-	0.613
Time	1	2025	2025	-	49.69
Error	0	0	0	-	-
Total					99.9999
Type - II: by pooling a factor, temperature					
pH	1	2025	2025	2025	49.07
Temperature	← POOLED →				
Time	1	2025	2025	2025	49.07
Error	1	25	25	-	1.84
Total					99.9818

(b) Relative concentration of co-precipitation reaction components

The co-precipitation of alumina-zirconia can take place in an aqueous solution in presence of ammonia, therefore, this route has been used for the in-situ co-precipitation in the present study. The balancing of this co-precipitation reaction can give the relative amounts of aluminium chloride (AlCl₃) and zirconium oxychloride (ZrOCl₂.8H₂O) as 19.2 and 5.8 g/l respectively. Figure 4.1 shows the coating weight observed for different concentrations of the co-precipitation reactants, in terms of the concentration of AlCl₃, i.e., $r_1 \times$ concentration of ZrOCl₂.8H₂O, where

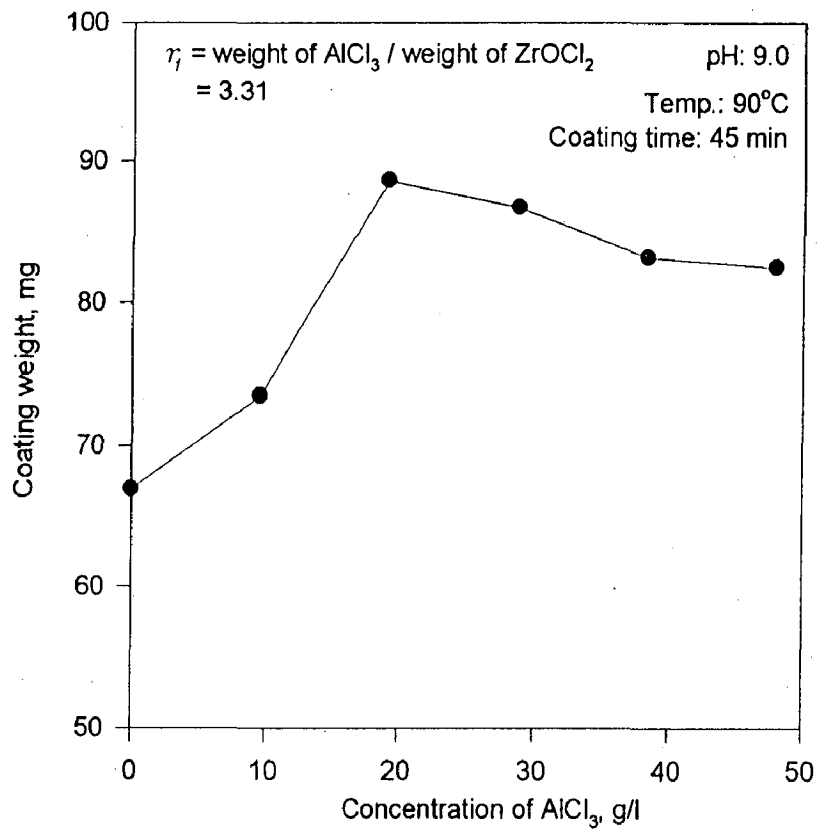


Fig.4.1 Variation in coating weight for different concentrations of co-precipitation reactants within electroless nickel bath.

r_1 is the ratio of weight of AlCl_3 to that of $\text{ZrOCl}_2 \cdot 8\text{H}_2\text{O}$ and is found to be 3.31. It is observed that the in-situ co-precipitation results in higher coating weight as compared to that in Ni-P alloy coating in the present study. The maximum coating weight has been found to be about 88.6 mg for the optimum concentrations of co-precipitating elements. The coating weight for all the other concentrations is found to be relatively lower than 88.6 mg. The weight of Ni-P-X coating has been found to reach 82.5 mg with the increase in concentration of AlCl_3 to 48 g/l whereas without co-precipitation reaction (i.e., deposition of only Ni-P), the coating weight is observed to be 66.9 mg.

4.1.3 Empirical Model

As mentioned earlier operating parameters including the temperature, pH and coating time are selected for the determination of the optimum performance. In this study, an attempt has been made to explain the effect of the bath loading factor in terms of surface area coated and the coating time for maximum productivity. The bath loading factor has been defined in chapter 3 as the ratio of the area of substrate immersed in coating bath to the initial volume of bath used. In this study, a series of experiments to deposit Ni-P-X on six distinct areas of 32.5, 40, 50, 62.5, 75 and 112.5 cm^2/l bath loading factors for different coating times viz., 15, 30, 45, 60 and 75 min have been carried out by using 200 ml bath at 90 °C and 9.0 pH. Thus, the experimental data has been used for the empirical model developed.

(a) Assumptions made for developing the empirical model

Despite the uniform and reproducible results of electroless coatings, the consumption of nickel ions and local changes in the bath composition lead to variation of coating weight deposited with time for specific bath loading area. To cover up the discrepancies due to these, following assumptions have been made:

- (i) The local bath chemistry does not affect the coating weight during the process.

- (ii) The surface area of similar type of samples for replicate experiments is same and is free from the surface irregularities.
- (iii) The temperature and pH of the bath are constant irrespective of location from heat source.
- (iv) The variation of coating weight with both the time and the surface area follows a second order polynomial.

(b) Model development

The variation of coating weight in electroless Ni-P-X coating with time is shown in Fig. 4.2 (a) while the plot after taking the natural logarithm of coating weight and time is demonstrated in Fig. 4.2 (b). It has been observed that the coating weight increases at a higher rate initially but later on saturates for different bath loading factors viz., 32.5, 40.0, 50.0, 62.5, 75.0, and 112.5 cm^2/l as seen from Fig. 4.2 (a). The empirical relation obtained from Figs. 4.2 (a) and (b) for the variation of coating weight, W in mg , with time, t , for Ni-P-X deposition can be given as:

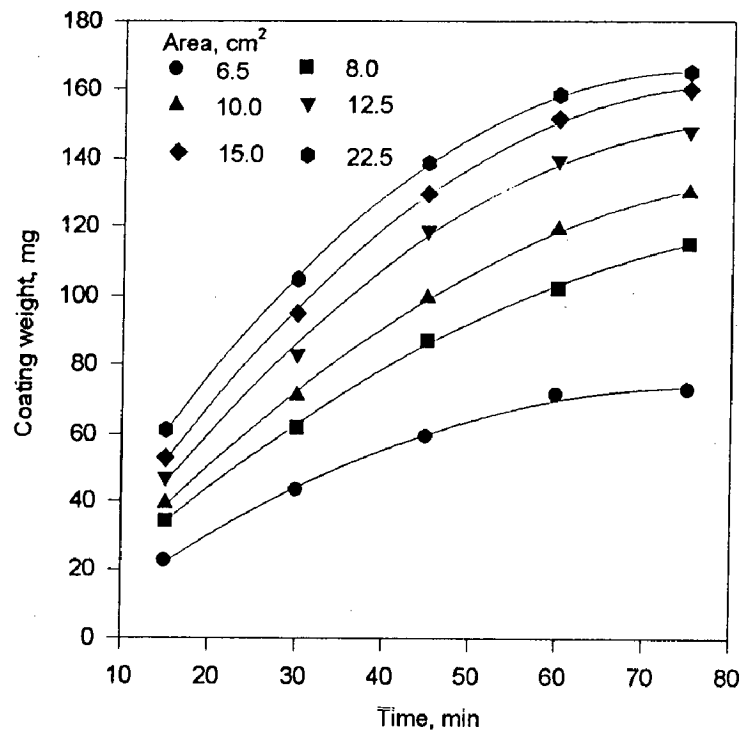
$$W = k_1 t^{n_1} \tag{4.1}$$

where, k_1 is the coefficient and n_1 is an exponent. The coefficient, k_1 significantly changes with bath loading area immersed for coating but the change in the value of n_1 has been found to be insignificant, therefore, it is not a function of bath loading area. An average value of n_1 has been found to be 0.73. The k_1 and n_1 values for different bath loading factors are reported in Table A.1, given in appendix. The coefficients of correlation between $\ln(W)$ and $\ln(t)$ as reported in Table A.2, given in appendix, reveal the linear relationship between them.

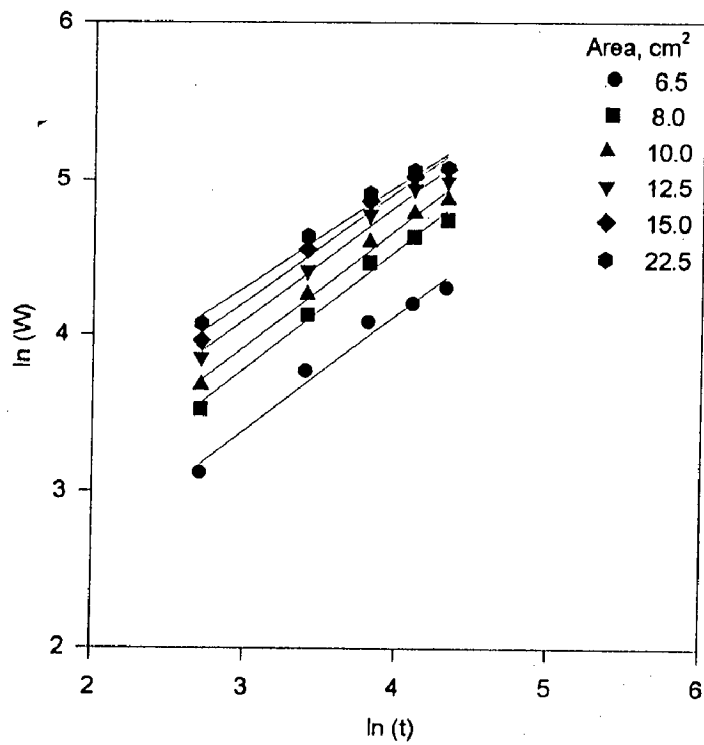
The linear increase in $\ln(k_1)$ with increasing $\ln(A_s)$ as shown in Fig. 4.3 (a) indicates that k_1 is a function of bath loading area and is given by:

$$k_1 = 0.59 A_s^{0.96} \tag{4.2}$$

where, A_s is the area of the substrate in cm^2 .



(a)



(b)

Fig. 4.2 Variation of (a) coating weight in electroless Ni-P-X composite coating with time for different bath loading areas and (b) logarithmic plot for the coating weight vs. time for different bath loading areas.

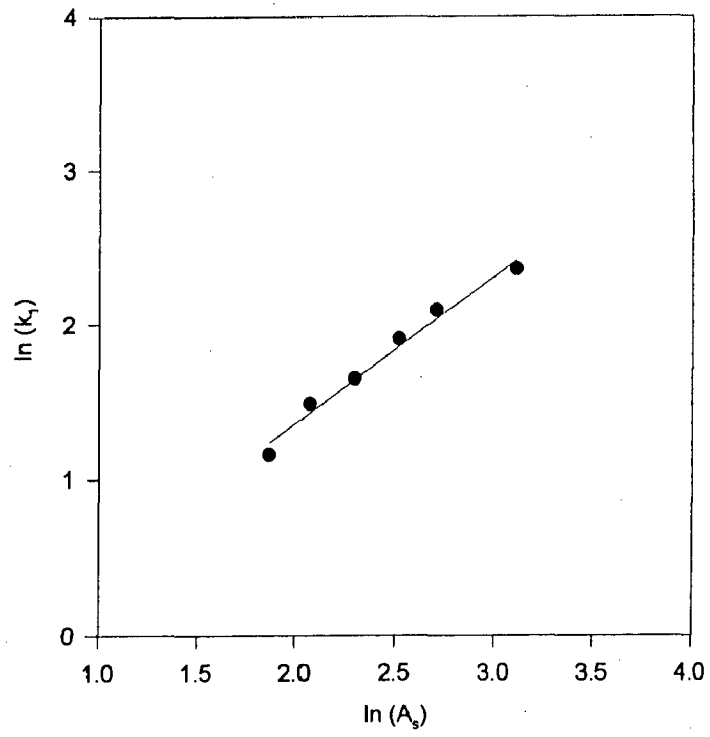
Figure 4.3 (b) shows the variation of difference between calculated and experimental k_1 , i.e., $k_{\text{calculated}} - k_{\text{experimental}}$ (Δk_1) with area. The Δk_1 has been observed to be almost consistent and found to fluctuate around zero for different bath loading factors of up to $75 \text{ cm}^2/\text{l}$, but when this factor is increased further to $112.5 \text{ cm}^2/\text{l}$, the value of Δk_1 is found to be significantly higher. Figures 4.4 (a) to (e) show the effect of substrate area on variation in calculated and experimental coating weight with time. The variation in difference between calculated and experimental coating weight, ΔW (i.e., $W_{\text{calculated}} - W_{\text{experimental}}$) with substrate area for different coating time is shown in Fig. 4.5. It is observed that calculated and experimental values for coating weight are almost in agreement with each other till the value of bath loading factor attains a value of $75 \text{ cm}^2/\text{l}$ and it is not influenced by coating time as seen from Figs. 4.4 (a) to (e) and Fig. 4.5.

4.1.4 In-situ Co-precipitation

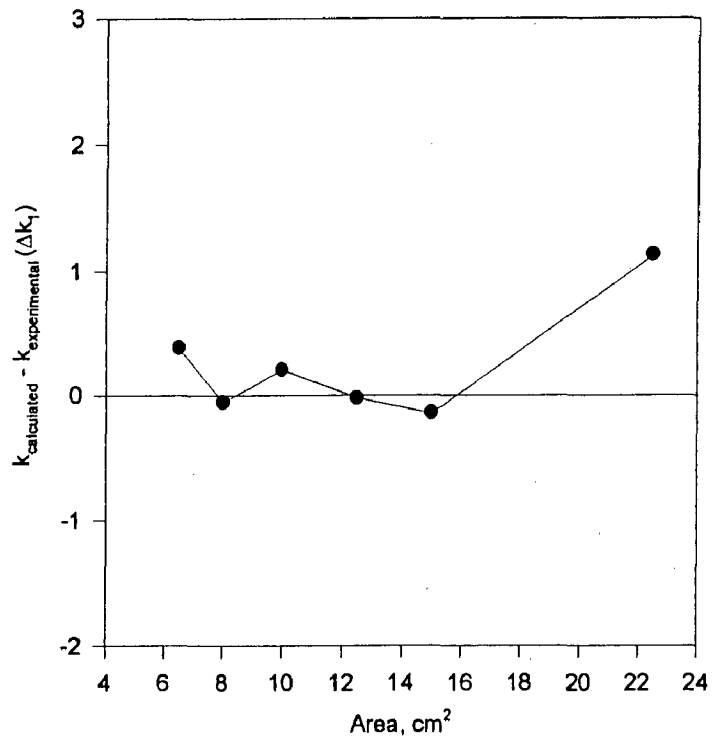
Once the relative concentration of aluminium chloride (AlCl_3) and zirconium oxychloride ($\text{ZrOCl}_2 \cdot 8\text{H}_2\text{O}$) have been determined as discussed in the section 4.1.2, the co-precipitation reaction has been studied by the examination of co-precipitation reaction product. The SEM and X-ray diffraction studies of the co-precipitated substance, which remained within the bath are presented in the subsequent part of this section.

(a) Reaction Involved in Co-Precipitation

During the co-precipitation reaction, Cl atoms from 2AlCl_3 are replaced by OH^- ions out of $6\text{NH}_4\text{OH}^-$, to result in the formation of $2\text{Al}(\text{OH})_3$, NH_4^+ combines with Cl^- to give $6\text{NH}_4\text{Cl}$, which provides the reaction product, Al_2O_3 . Similarly, from ZrOCl_2 , Cl ions are replaced by OH^- ions giving rise to $\text{ZrO}(\text{OH})_2$ and $2\text{NH}_4\text{Cl}$, which provides ZrO_2 as a reaction product. The reaction can be schematically explained as under:

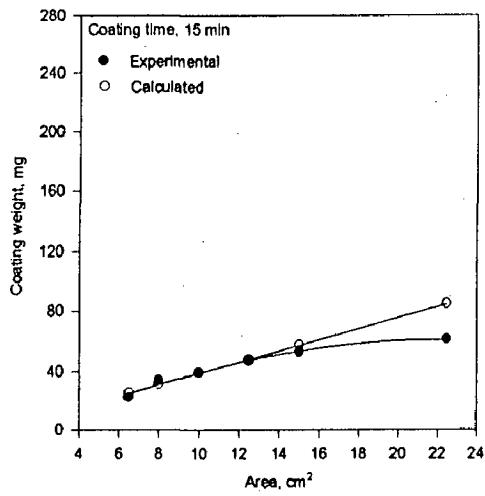


(a)

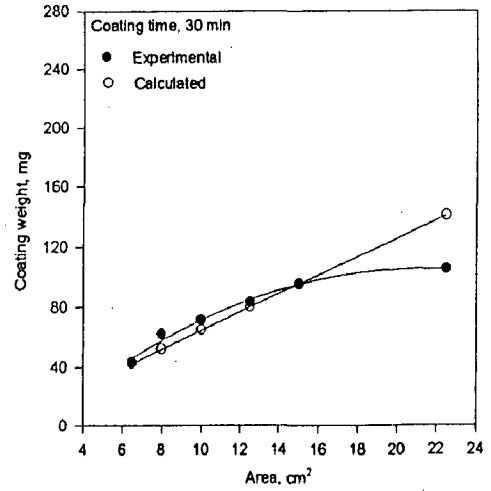


(b)

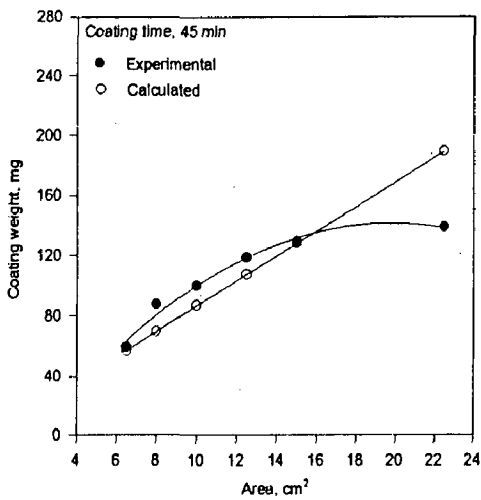
Fig. 4.3 Variation in (a) logarithmic plot for the coefficient, k_1 vs. bath loading area, A_s in accordance of the Eq. (4.1) and (b) difference between the calculated and experimental coefficients, $k_{\text{calculated}} - k_{\text{experimental}}$, Δk_1 , with bath loading area.



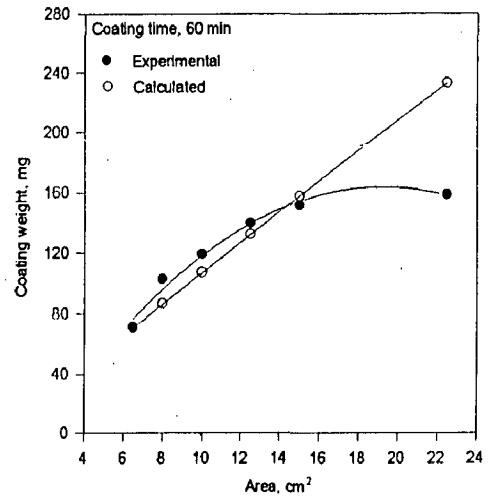
(a)



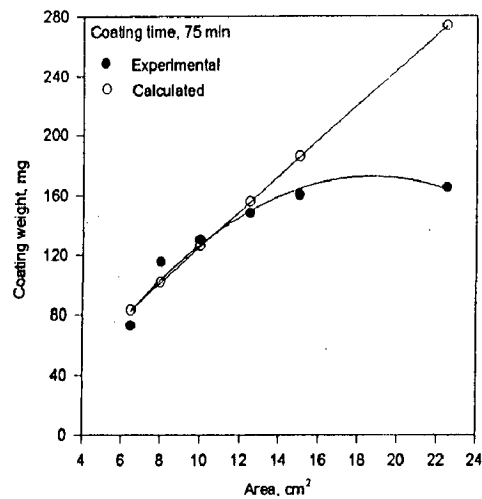
(b)



(c)



(d)



(e)

Fig. 4.4 Calculated and experimental values of the coating weight in Ni-P-X deposition for different time of coating: (a) 15 min, (b) 30 min, (c) 45 min, (d) 60 min and (e) 75 min.

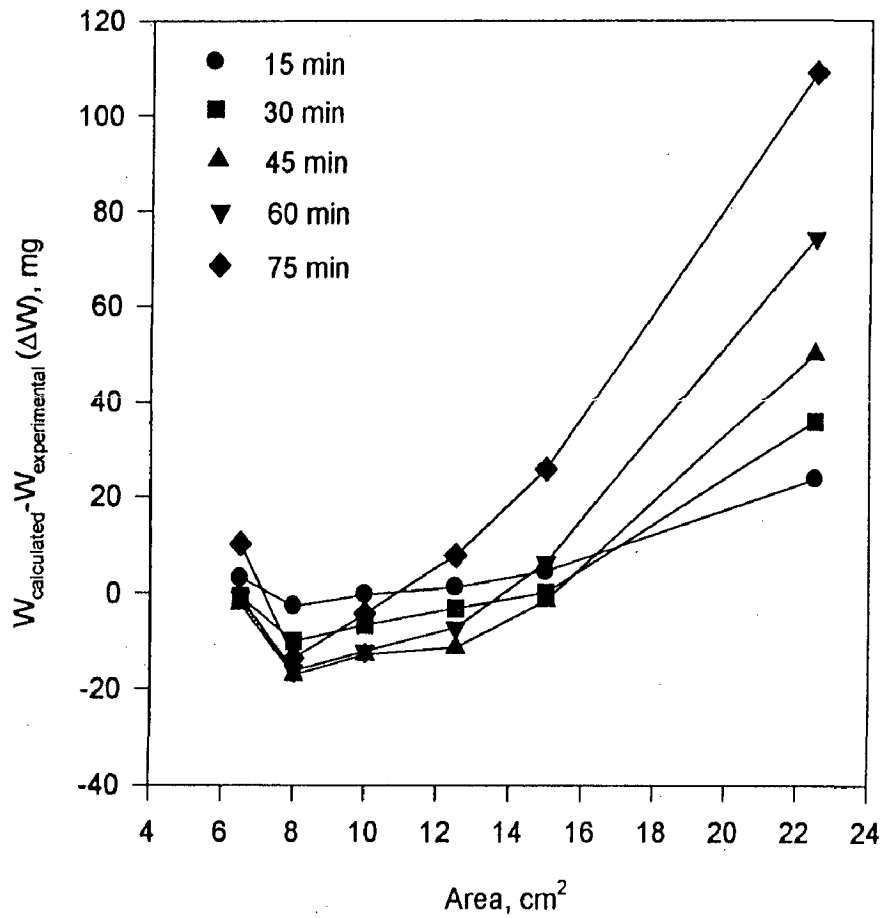
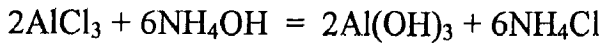
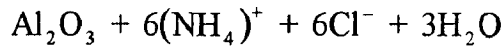
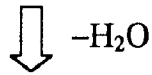
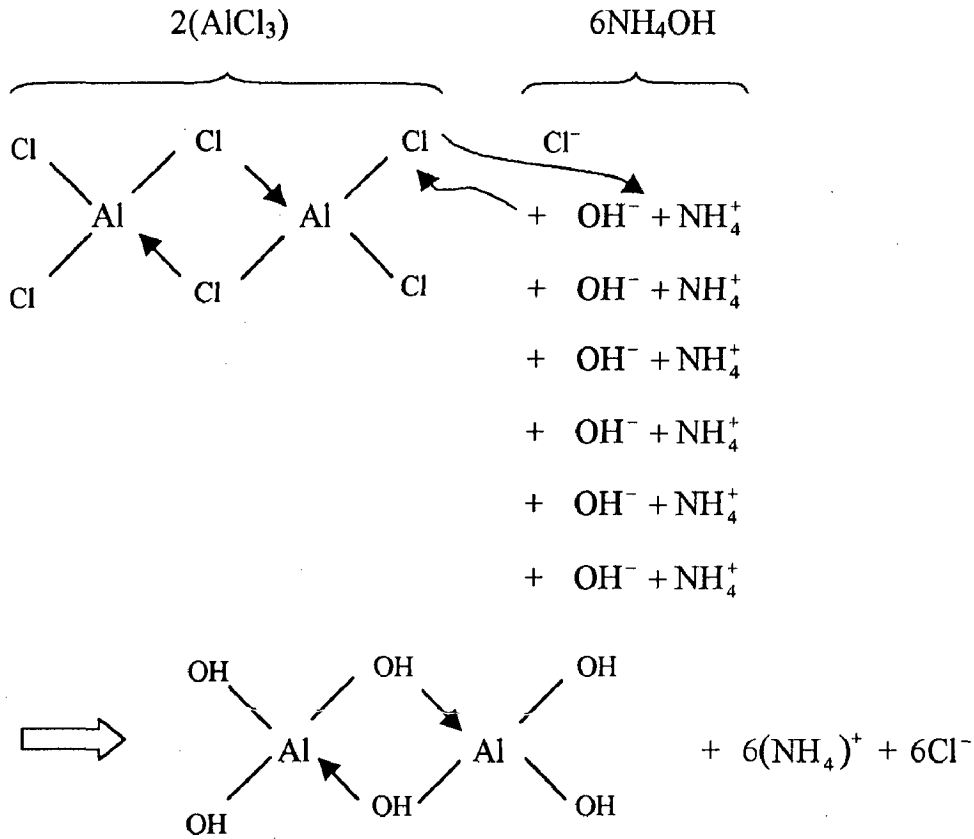
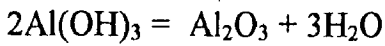


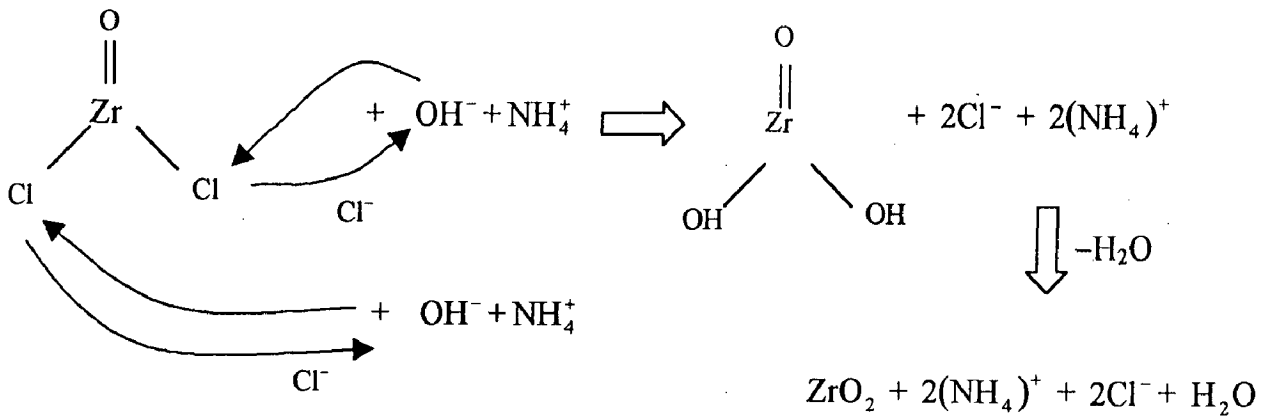
Fig. 4.5 Variation in difference between coating weight calculated and experimental, $W_{\text{calculated}} - W_{\text{experimental}}$ with bath loading area in the Ni-P-X deposition for different time.



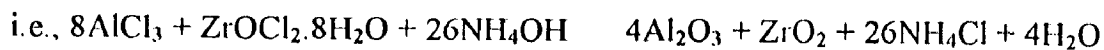
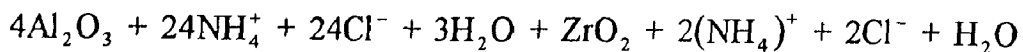
on dehydration



similarly,



\therefore For 80% mol Al_2O_3 and 20% mol ZrO_2



(b) Characterisation of co-precipitation reaction product

The reaction product collected after synthesis of the electroless composite coating by using in-situ co-precipitation of ZrO_2 and Al_2O_3 , has been examined under SEM. In order to know the phase constituents of co-precipitation reaction product, remaining in the beaker after has been filtered from bath solution, cleaned, dried and then subjected to X-ray diffraction studies.

(i) Examination of co-precipitated powder

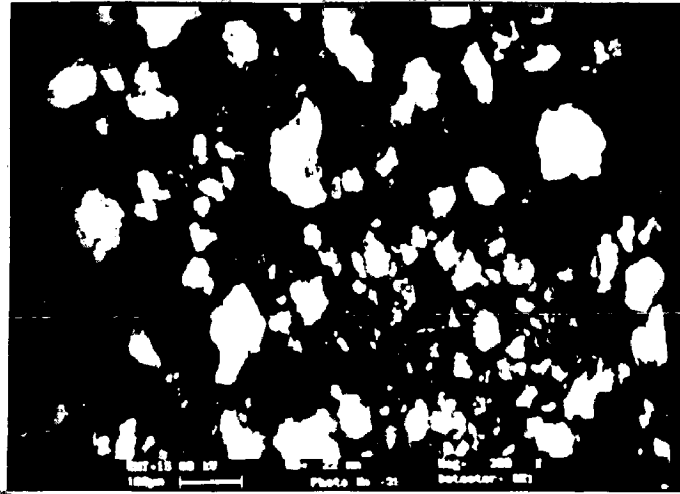
Figures 4.6 (a) and (b) show micrographs of the product of co-precipitation under SEM at two different magnifications. The powder obtained is found to be the mixture of fine particles and a few agglomerates. The obtained powder possesses fine particles and clusters of irregular shapes, having about $100 \mu m$ size. The larger sized particles may be formed due to clustering of smaller particles as demonstrated in Fig. 4.6 (b).

(ii) X-ray diffraction analysis of co-precipitated powder

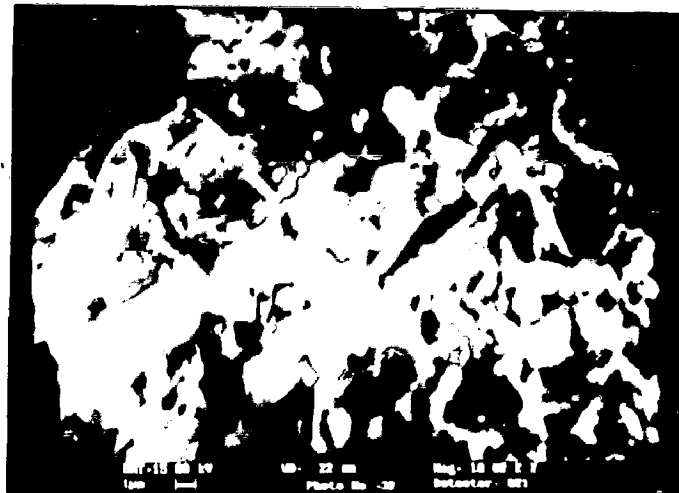
X-ray diffraction pattern obtained for the co-precipitated product is shown in Fig. 4.7, while the various phase constituents identified, by referring to ASTM data cards, are enumerated in the Table A.3, given in appendix. The X-ray diffraction pattern revealed that different phase constituents including Al_2O_3 , $(ZrO_{3.5}) 2.7 H$, Zr_3O_{1-x} , Zr_5P_3 , Na_3AlH_6 , NiP_2 and $NiZrH_3$ are commonly observed in co-precipitated powder. The characteristics of these phases are given in Table A.3.

4.1.5 Coating Thickness

To obtain similar coating thickness, in terms of uniform coating weight, as required for wear study purposes, $12.5 cm^2$ substrate area (i.e., $62.5 cm^2/l$ bath loading factor) and 45 *min* coating time are chosen in the present investigation. Figures 4.8 (a) and (b) represent the typical micrographs showing cross section of electroless Ni-P-X and Ni-P coating respectively. The coating thickness of electroless Ni-P-X deposits has been observed to be about $40 \mu m$ when coated for 45 *min* whereas for Ni-P coatings it is



(a)

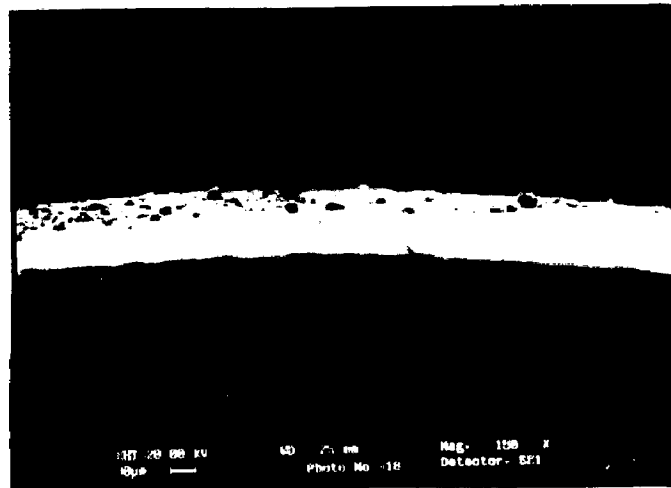


(b)

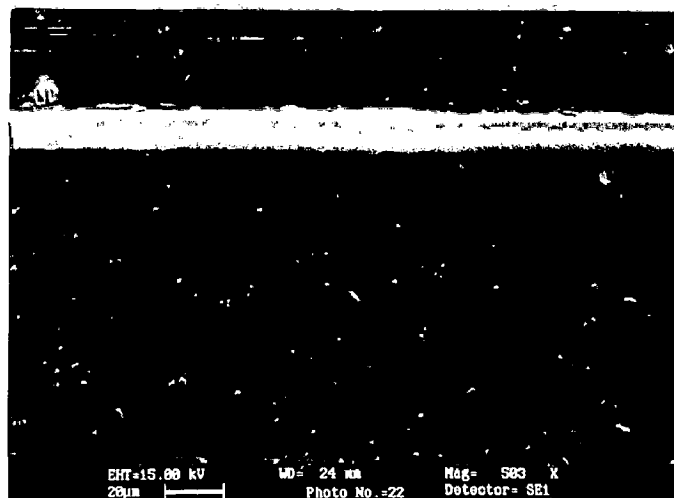
Fig. 4.6 SEM micrographs of the co-precipitated powder: (a) fine particles and coarser agglomerates at $\times 300$ and (b) Cluster of many particles at $\times 10,000$.



Fig. 4.7 X-ray diffraction pattern of the powder obtained by co-precipitation reaction within the electroless bath.



(a)



(b)

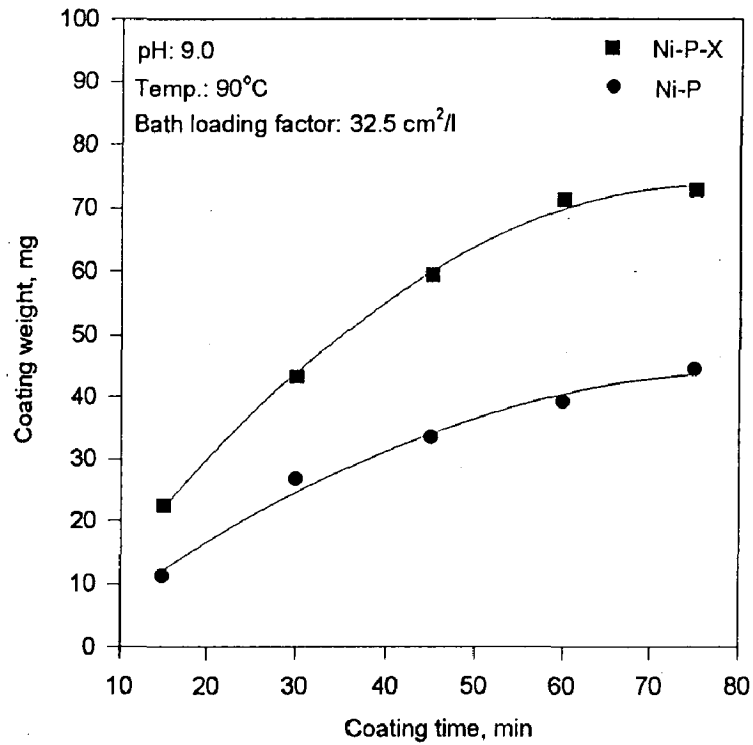
Fig. 4.8 Cross section of the electroless coating under SEM showing uniform thickness in (a) Ni-P-X deposition and (b) Ni-P deposition.

observed to be about 30 μm for the same coating conditions. Fairly uniform thick layer of the coating has been observed, which takes the exact shape of the substrate surface profile irrespective of surface undulations.

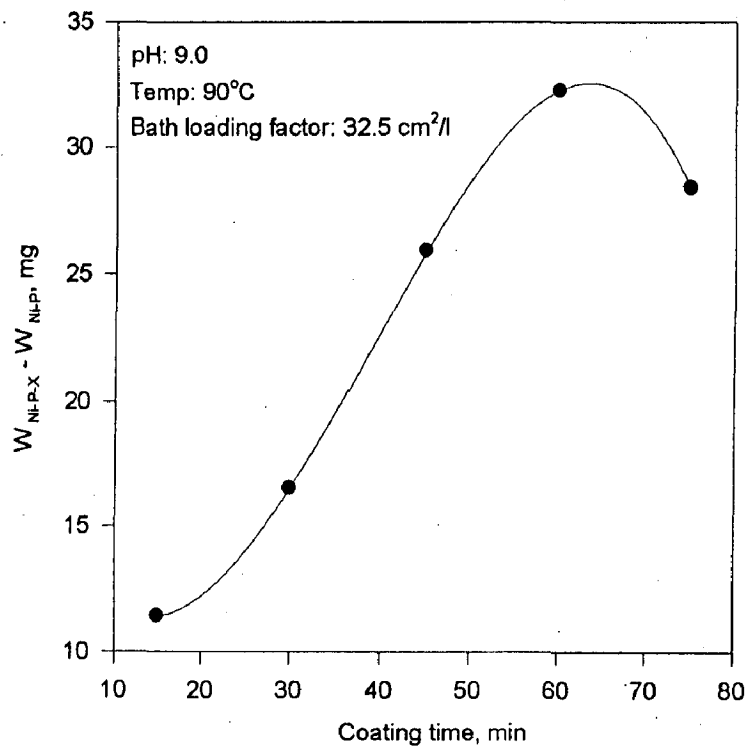
4.1.6 Coating Rate

Figure 4.9 (a) shows the variations of coating weight with time in both the Ni-P-X and the Ni-P coatings for the optimum bath condition. It is observed that the deposition weight in Ni-P-X and Ni-P coatings increases with increasing coating time in the range of 15 to 75 *min* but the rate is found to reduce after 45 *min* of coating time. For the 45 *min* coating, the coating weight in Ni-P-X has been found to be 59.3 *mg* whereas that for Ni-P deposition is 33.4 *mg*. After coating for 15 *min*, the Ni-P-X and the Ni-P coating weights have been respectively observed to be 11.1 and 22.5 *mg*, whereas for 75 *min* of coating, the corresponding coating weights are found to be 72.8 and 44.4 *mg*. The variation in difference between the coating weight for Ni-P-X and Ni-P coatings ($W_{\text{Ni-P-X}} - W_{\text{Ni-P}}$) with coating time is shown in Fig. 4.9 (b). It is observed that difference in coating weights of these two types of coatings increases up to a time of 60 *min* and decreases thereafter. The weight difference in coating is found to be 11.4 *mg* for 15 *min* coating time and it has been observed to reach the maximum value of 32.2 *mg* in 60 *min*, however, after 75 *min* of coating, the difference decreases to 28.4 *mg*.

Ni-P- Al_2O_3 and Ni-P- ZrO_2 coatings have been carried out by using the same bath conditions as mentioned in chapter 3 except the use of co-precipitation reaction, i.e., composite coatings containing Al_2O_3 or ZrO_2 have been obtained only by co-deposition technique by external addition of the particles. The coating rates of both the types of electroless deposition are compared with that for Ni-P-X and Ni-P coatings as shown in Fig. 4.10. It is observed from this figure that the Ni-P-X deposition has the highest coating rate whereas the rate is lowest for Ni-P deposition. The composite coatings, in general, have higher coating rate than Ni-P alloy coatings, irrespective of the route adopted for synthesis. The coating rate observed for different



(a)



(b)

Fig. 4.9 Variation of (a) coating weight in electroless Ni-P-X and Ni-P coating on aluminium substrate for the specific coating conditions and (b) difference between the coating weight of Ni-P-X and Ni-P deposits, $W_{Ni-P-X} - W_{Ni-P}$ with time.

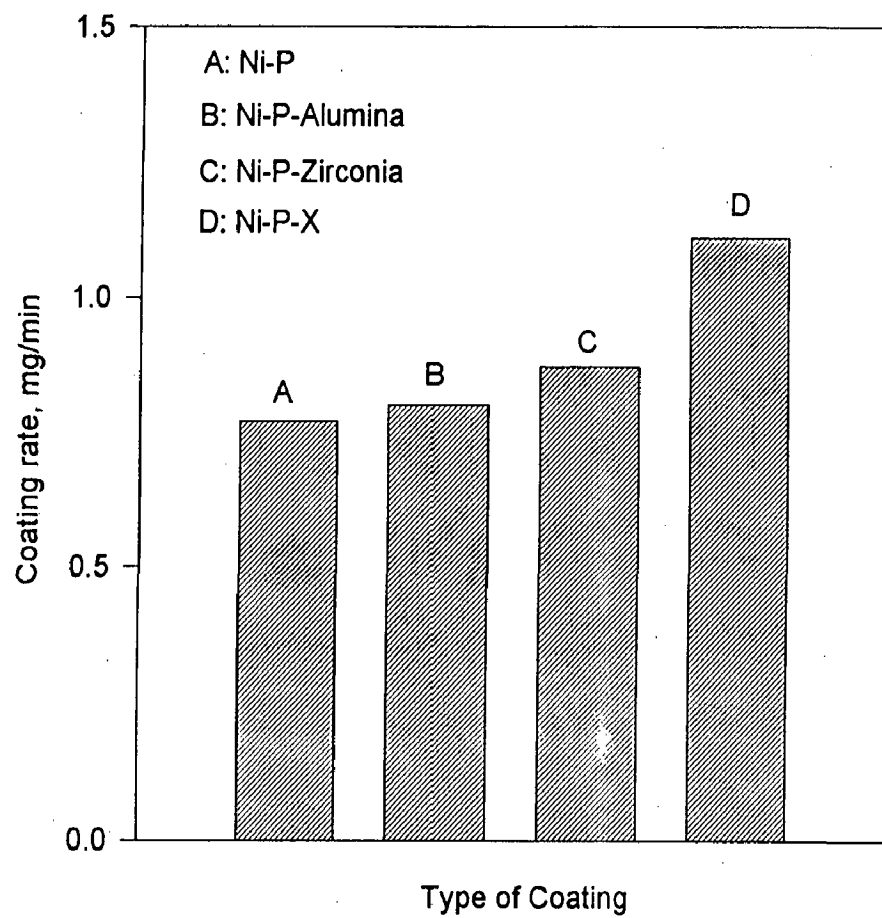


Fig. 4.10 Coating rates observed in different types of electroless coatings with bath temperature 90°C and 9.0 pH (X = $ZrO_2-Al_2O_3-Al_3Zr$).

types of electroless coating systems, i.e., Ni-P, Ni-P-Al₂O₃, Ni-P-ZrO₂ and Ni-P-X are 0.77, 0.80, 0.87 1.11 *mg/min* respectively as shown in Fig. 4.10.

4.1.7 Reproducibility of Electroless Coatings

The weight of coatings observed after conducting the replicate experiments for Ni-P-X deposition on normalised steel (20 samples) and aluminium (16 samples) are shown in Figs. 4.11 and 4.12 respectively, while that for electroless Ni-P deposition on steel pins (16 samples), are shown in Fig. 4.13. The observed scatter in Ni-P-X coatings on steel and aluminium is found to be in the ranges of 52.5-68.0 *mg* and 50.8-61.1 *mg* respectively whereas that for the Ni-P coatings on steel is observed to be in the range of 32.1-41.5 *mg*. The mean coating weight has been found to be 59.3 *mg*, 54.4 *mg* and 35.8 *mg* for Ni-P-X deposit on steel, Ni-P-X deposit on aluminium and Ni-P deposit on steel samples respectively.

4.1.8 Morphological Studies of Electroless Coatings

In this section, an attempt has been made to present the results of metallographic studies of the electroless Ni-P-X and Ni-P coatings in terms of coating mechanism, globule size and its distribution. SEM has been used as the tool for this study.

(a) Examination of surface of coatings

Figures 4.14 (a) and (b) show the SEM micrographs of electroless Ni-P-X deposit in as-coated condition while those for Ni-P deposit are shown in Figs. 4.15 (a) and (b). The hemispherical shaped globules like structure of coatings have commonly been observed in above figures. A very small sites of submicron size and a few coagulated islands of particles are also observed those cover the part of globular features as seen in Fig. 4.14 (a). The boundaries of the coating globules can be seen from the back scattered SEM micrograph of Ni-P-X in as-coated condition and the presence of a coagulated island of particles can be noticed at arrow mark in Fig. 4.14 (b). Many submicron sized grains within the coating globule are also observed. The coating globules contain cluster

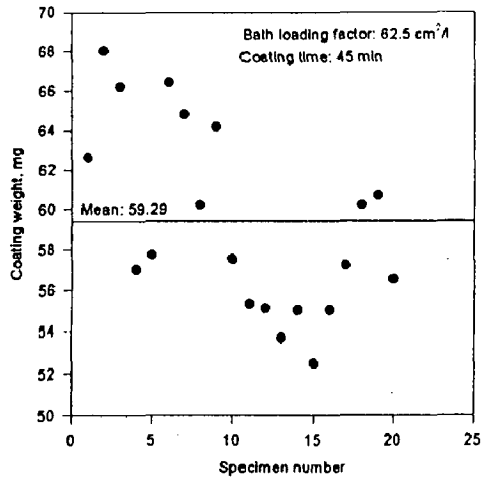


Fig. 4.11 Scatter observed in weight of electroless Ni-P-X composite coating on aluminium substrates at 9.0 pH and 90°C.

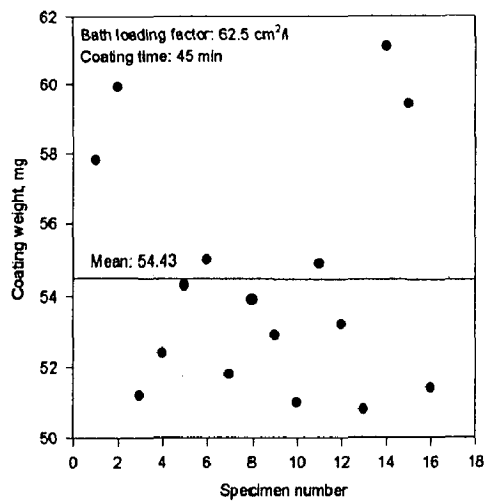


Fig. 4.12 Scatter observed in weight of electroless Ni-P-X composite coating on steel substrates at 9.0 pH and 90°C.

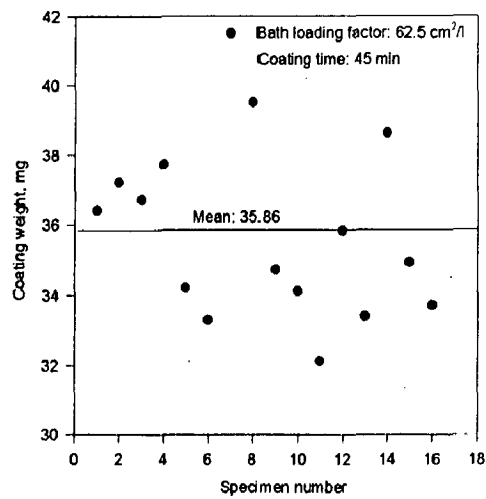
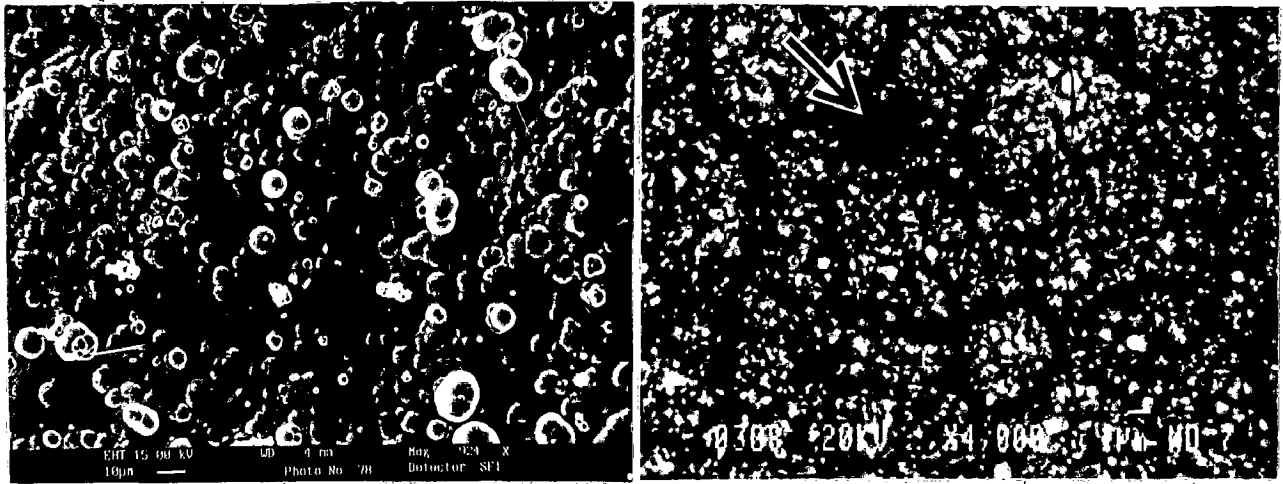


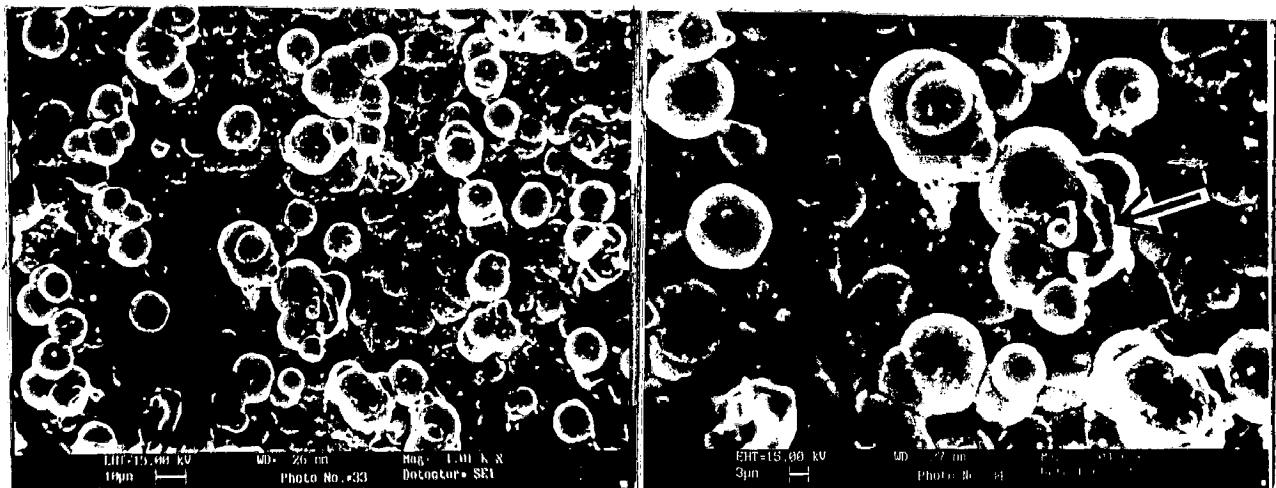
Fig. 4.13 Scatter observed in weight of electroless Ni-P alloy coating on aluminium substrates at 9.0 pH and 90°C.



(a)

(b)

Fig. 4.14 SEM micrograph of electroless Ni-P-X composite coating in as-coated condition (a) $\times 924$ and (b) back scatter image at $\times 4000$.



(a)

(b)

Fig. 4.15 SEM micrograph of electroless Ni-P alloy coating in as-coated condition (a) $\times 1001$ and (b) coating globule fracture at $\times 2004$.

of many grains and such nanosized grains have been identified in Ni-P-X coatings, which is reported in the subsequent sections. The coating systems, i.e., the Ni-P-X and the Ni-P are found to be fairly uniform in terms of globules seen in the micrographs. However, in a localised region in the Ni-P coated sample, the growth of globule has been found to be abnormal in terms of size and shape and it has appeared like globular fracture, as observed in Fig. 4.15 (b). The SEM micrographs of electroless Ni-P-Al₂O₃ and Ni-P-ZrO₂ deposits in as-coated condition are shown in Figs. 4.16 and 4.17 respectively and the globular structure of these electroless coatings has been observed in these figures. A few irregularly shaped and smaller sites in these figures are observed. The clustering of the particles around the grain boundaries is seen in Fig. 4.17, as marked by an arrow.

Figures 4.18 (a), (b) and (c) show the SEM micrographs of the coating after heat treatment at 400°C for 1 h, 400°C for 2 h and 250°C for 12 h, respectively. From these figures, it is commonly observed that the heat treatment causes coarsening of globules, which in turn results in the flattening of coating globules, thus making the globules relatively coarser. The precipitation of phases also appears to take place at some locations, which is identified in the subsequent sections in this chapter. Figure 4.19 (a) represents the typical area in the Ni-P-X coating after heat treating at 400°C for 1 h, in which the bright areas in the vicinity of coating globule have been observed. However, at higher magnification, i.e., in Fig. 4.19 (b) the dark area near the boundary of coating globules has been predominantly noticed along with uniformly distributed irregular shaped white submicron sized particles. The coating globules consisting of many submicron sized grains within the globule can be predominantly observed in the back scatter image of the coating as seen in Fig 4.19 (c).

(b) Examination of cross section of coatings

In order to study the mechanism of the coating development, cross-section of Ni-P-X coating has been examined under SEM and the micrographs at the magnification of 250, 2001 and 2004 are respectively shown in Figs. 4.20 (a), (b) and (c). These figures reveal uniform coating layer thickness of about 40 μm , appearing

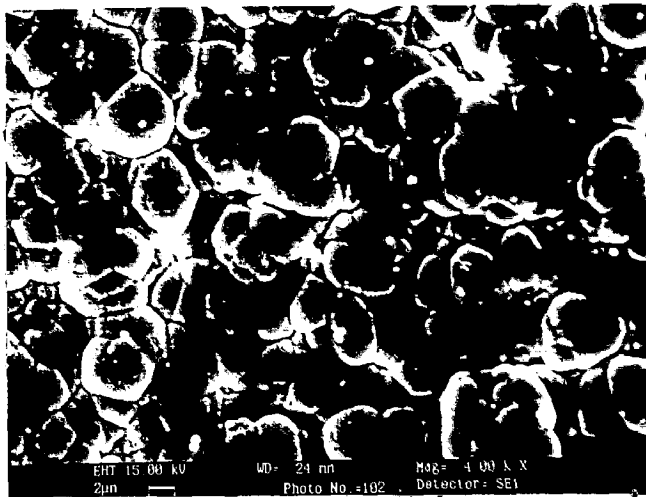


Fig. 4.16 SEM micrograph of electroless Ni-P-Al₂O₃ deposition in as-coated condition.

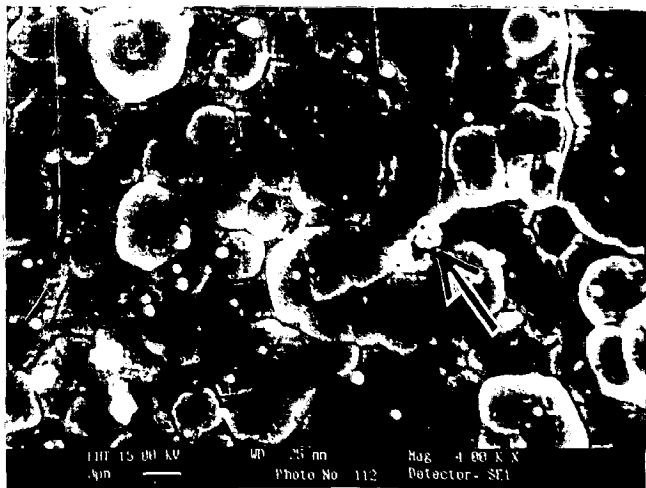
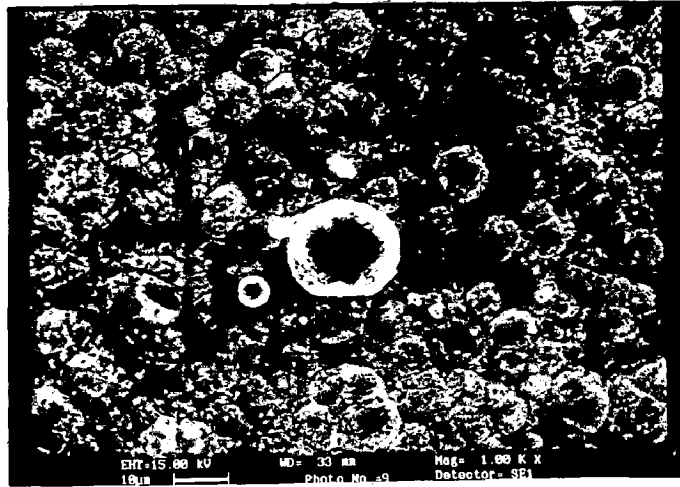
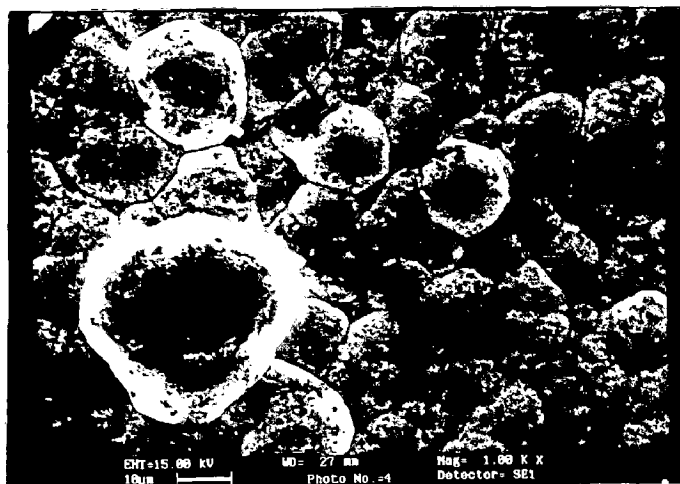


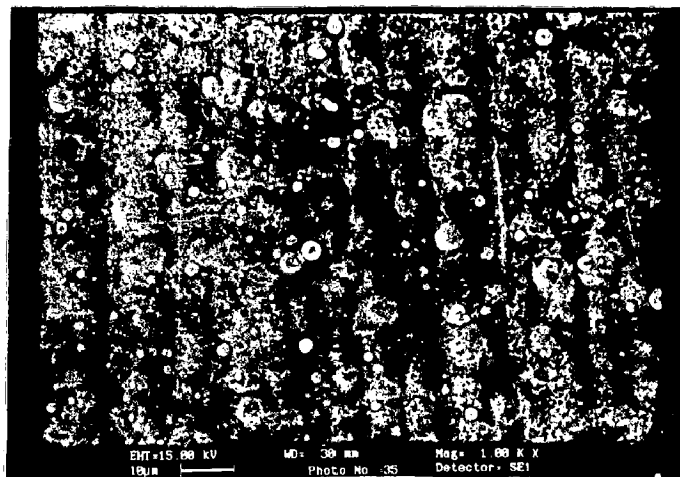
Fig. 4.17 SEM micrograph of electroless Ni-P-ZrO₂ deposition in as-coated condition.



(a)

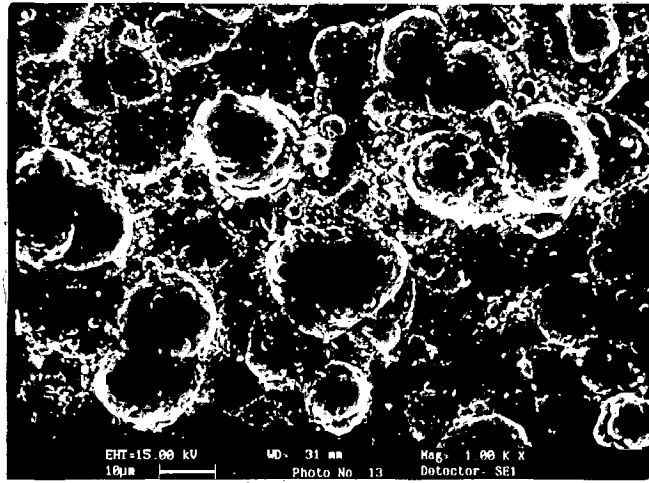


(b)

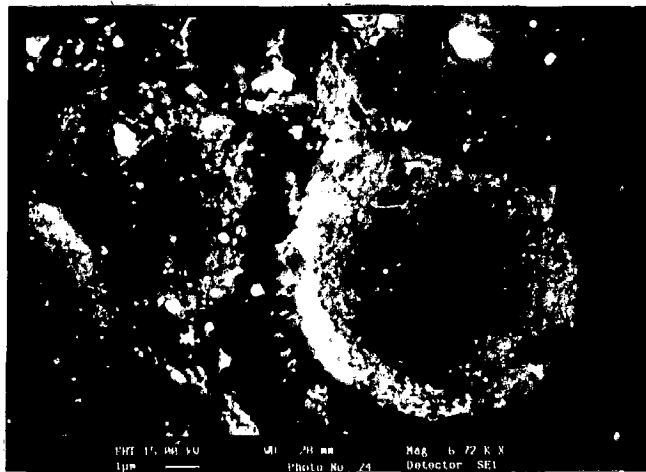


(c)

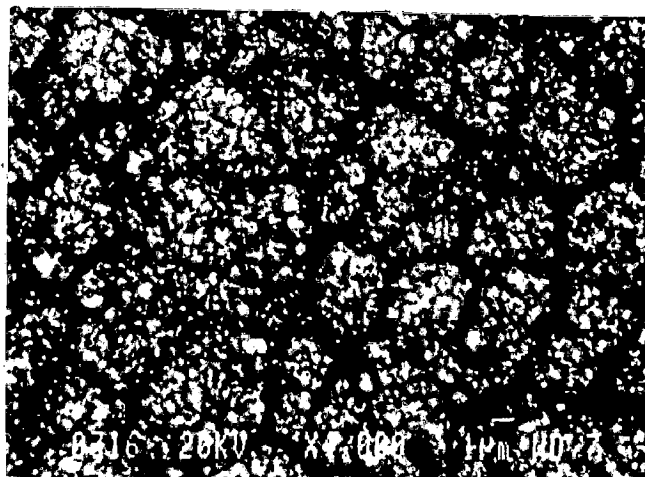
Fig. 4.18 SEM micrograph of electroless Ni-P-X composite coating on aluminium substrate after heat treatment at: (a) 400°C for 1 h, (b) 400°C for 2 h and (c) 250°C for 12 h.



(a)

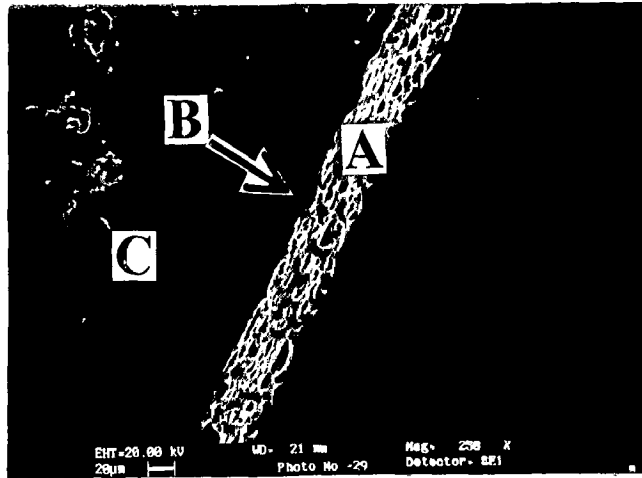


(b)

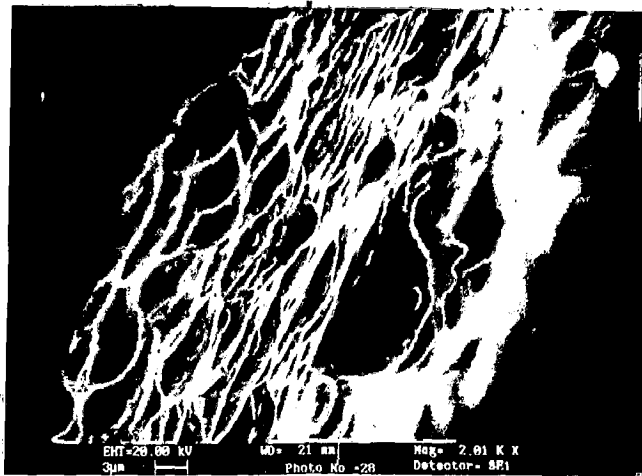


(c)

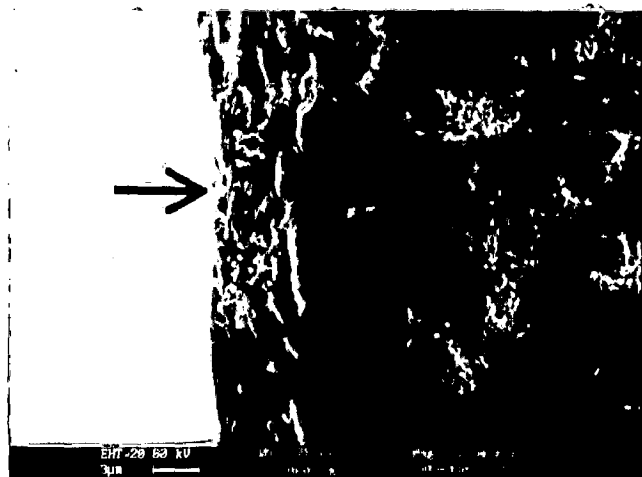
Fig. 4.19 SEM micrographs of electroless Ni-P-X composite coating on aluminium substrate after heat treatment at 400°C for 1 h (a) showing the precipitation of Ni₃P and (b) cracking near grain boundary and (c) back scatter image at × 4000.



(a)



(b)



(c)

Fig. 4.20 Cross section of the electroless Ni-P-X coating after developing the deposition layer: (a) $\times 250$, (b) $\times 2000$ and (c) substrate-coating interface, $\times 2004$.

at the section as marked *A* in Fig. 4.20 (a), similarly another layer of about 10 μm thickness is marked as *B* at the interface between coating and substrate, marked as *C*, is observed in the same figure. The layered structure of Ni-P-X coating is clearly evident from Fig. 4.20 (b) and an arrow as seen in Fig 4.20 (c) indicates the strong interface between the coating and the substrate.

(c) Coating globule size and its distribution

Coating globule size and its distribution for different electroless coatings, i.e., Ni-P, Ni-P-Al₂O₃, Ni-P-ZrO₂ and Ni-P-X have been determined by using Heyn's intercept method as described in chapter 3. The SEM micrographs for as-coated Ni-P, Ni-P-Al₂O₃, Ni-P-ZrO₂ and Ni-P-X are shown earlier in Figs. 4.14 (a), 4.15 (a), 4.16 and 4.17 respectively and those have been used for determination of coating globule size. Figures 4.21 (a) to (d) represent the coating globule size variation and its frequency distribution in electroless Ni-P, Ni-P-Al₂O₃, Ni-P-ZrO₂ and Ni-P-X coatings respectively. The frequency distribution of globule size in electroless Ni-P and Ni-P-X coatings is found to be uniform as seen in Figs. 4.21 (a) and (d) respectively. However, in case of electroless co-deposited Ni-P-Al₂O₃ and Ni-P-ZrO₂ coatings, more scatter in globule size variation with respect to frequency distribution has been correspondingly observed from Figs. 4.21 (b) and (c). The average coating globule size for the different electroless coatings is shown in Fig. 4.22, which has been determined from globule size frequency distribution presented in Figs. 4.21 (a) to (d). The average globule size of as-coated Ni-P is found to be about 6.0 μm and that for Ni-P-X coated is observed to be about 5.0 μm as evident from Fig. 4.22; while the globule sizes of electroless Ni-P-Al₂O₃ and Ni-P-ZrO₂ coatings are found to be 4.8 μm and 6.1 μm respectively as seen from Fig. 4.22.

4.1.9 Composition of Electroless Ni-P-X Coatings

The electroless Ni-P-X coatings synthesised as described earlier have been analysed by qualitative and quantitative techniques such as: XRF, EPMA, SEM-EDAX. In order to know the presence of different elements in the Ni-P-X coating, the area analysis, line analysis and point analysis have been conducted and the results of all these analyses are reported in the subsequent subsections.

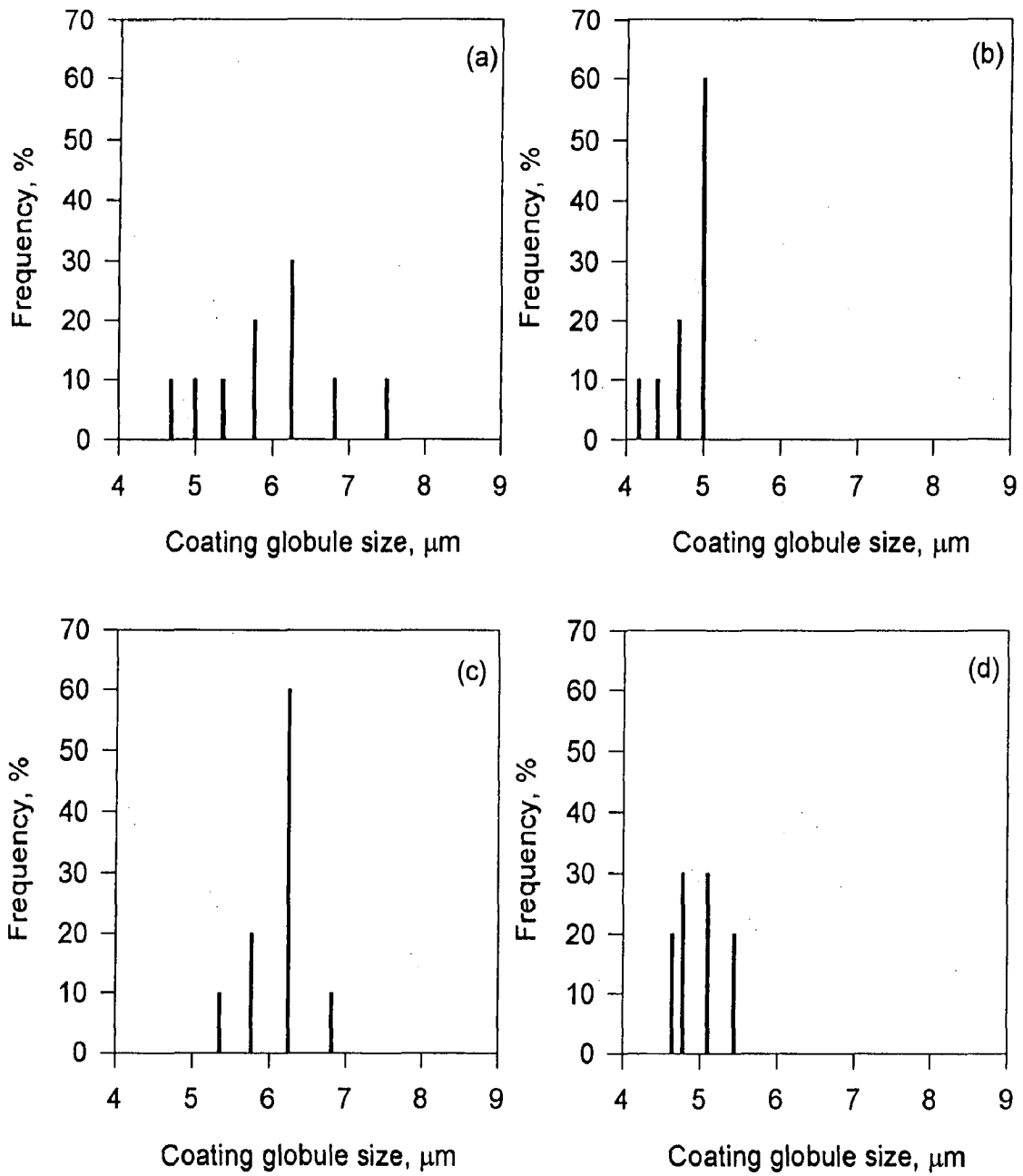


Fig. 4.21 Coating globule size distribution in different electroless coating systems: (a) Ni-P, (b) Ni-P-Al₂O₃, (c) Ni-P-ZrO₂, and (d) Ni-P-ZrO₂-Al₂O₃-Al₃Zr.

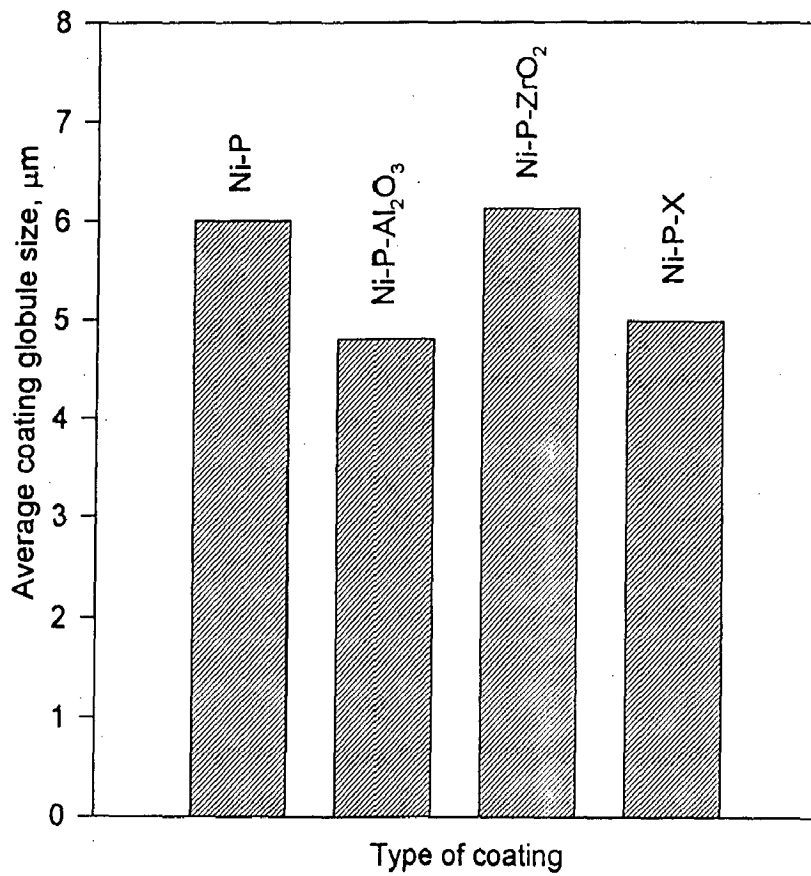


Fig. 4.22 Average coating globule size in different electroless coating systems (X = $\text{ZrO}_2\text{-Al}_2\text{O}_3\text{-Al}_3\text{Zr}$).

4.1.9.1 Qualitative Analysis

(a) X-ray fluorescence

The qualitative results of XRF indicating the presence of different elements, i.e., Ni, P, Zr and Al are shown in Figs.4.23 (a), (b), (c) and (d) respectively. The peaks in Figs. 4.23 (a) and (b) corresponding to the presence of Ni and P are found to be predominant as they have shown the intensity of 413.98 and 3.055 *KCps* respectively. Apart from above major constituents, the presence of minor constituents like Zr and Al is also indicated by the corresponding peaks in Figs. 4.23 (c) and (d), respectively of 1.80 and 0.96 *KCps*. The XRF results showing the intensity and position (2θ) for different elements are given in Table A.4 as given appendix.

(b) Area analysis

Four different areas of about $28 \mu m \times 22 \mu m$ from the electroless Ni-P-X deposited film are selected randomly and SEM-EDAX have been carried out to confirm the presence of Ni, P, Al, Zr and O (oxygen) in the coating. Figure 4.24 (a) shows a typical micrograph of area selected from film of Ni-P-X coating. The uniform coating globules and submicron sized grains can be observed under SEM at a magnification of 4000 as seen in this figure. The SEM-EDAX results for such four different areas, viz., I, II, III and IV are shown in Fig. 4.24 (b). The presence of Al, Zr and O, apart from principal elements Ni and P are also noticed from Fig. 4.24 (b). In all the areas, most significant peak has been found to be for Ni while relatively weaker peaks for Al and oxygen are commonly observed in all the four areas under consideration. In part (I) of Fig. 4.24 (b), no significant peaks corresponding to Al and Zr could be seen, but after area analysis of another regions, i.e., (II), (III) and (IV) of Fig. 4.24 (b), the peaks corresponding to those elements seem to be relatively more significant along with the indication of the presence of Ni, P and O.

4.1.9.1 Qualitative Analysis

(a) X-ray fluorescence

The qualitative results of XRF indicating the presence of different elements, i.e., Ni, P, Zr and Al are shown in Figs.4.23 (a), (b), (c) and (d) respectively. The peaks in Figs. 4.23 (a) and (b) corresponding to the presence of Ni and P are found to be predominant as they have shown the intensity of 413.98 and 3.055 *KCps* respectively. Apart from above major constituents, the presence of minor constituents like Zr and Al is also indicated by the corresponding peaks in Figs. 4.23 (c) and (d), respectively of 1.80 and 0.96 *KCps*. The XRF results showing the intensity and position (2θ) for different elements are given in Table A.4 as given appendix.

(b) Area analysis

Four different areas of about $28 \mu\text{m} \times 22 \mu\text{m}$ from the electroless Ni-P-X deposited film are selected randomly and SEM-EDAX have been carried out to confirm the presence of Ni, P, Al, Zr and O (oxygen) in the coating. Figure 4.24 (a) shows a typical micrograph of area selected from film of Ni-P-X coating. The uniform coating globules and submicron sized grains can be observed under SEM at a magnification of 4000 as seen in this figure. The SEM-EDAX results for such four different areas, viz., I, II, III and IV are shown in Fig. 4.24 (b). The presence of Al, Zr and O, apart from principal elements Ni and P are also noticed from Fig. 4.24 (b). In all the areas, most significant peak has been found to be for Ni while relatively weaker peaks for Al and oxygen are commonly observed in all the four areas under consideration. In part (I) of Fig. 4.24 (b), no significant peaks corresponding to Al and Zr could be seen, but after area analysis of another regions, i.e., (II), (III) and (IV) of Fig. 4.24 (b), the peaks corresponding to those elements seem to be relatively more significant along with the indication of the presence of Ni, P and O.

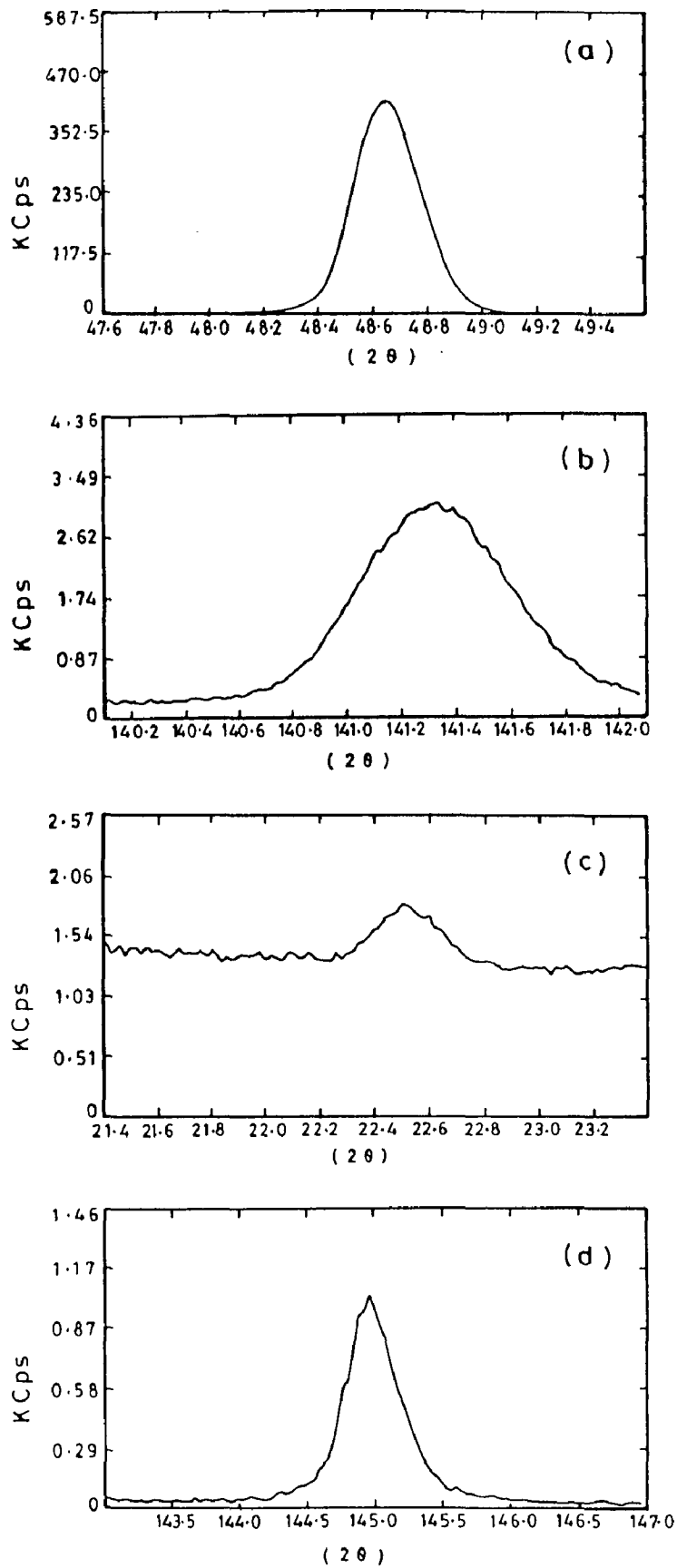
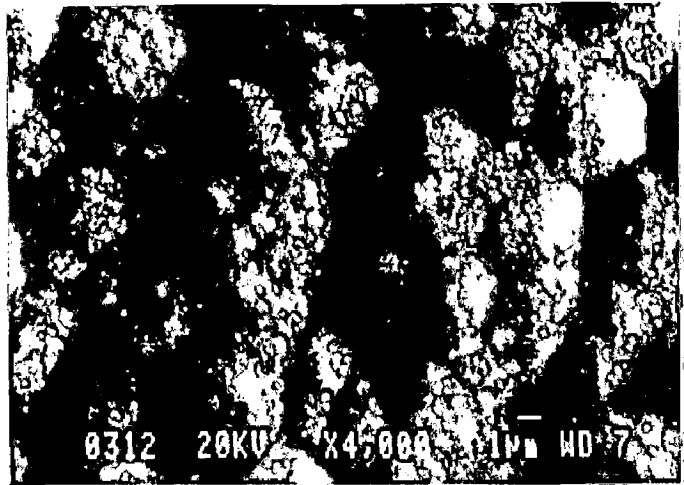
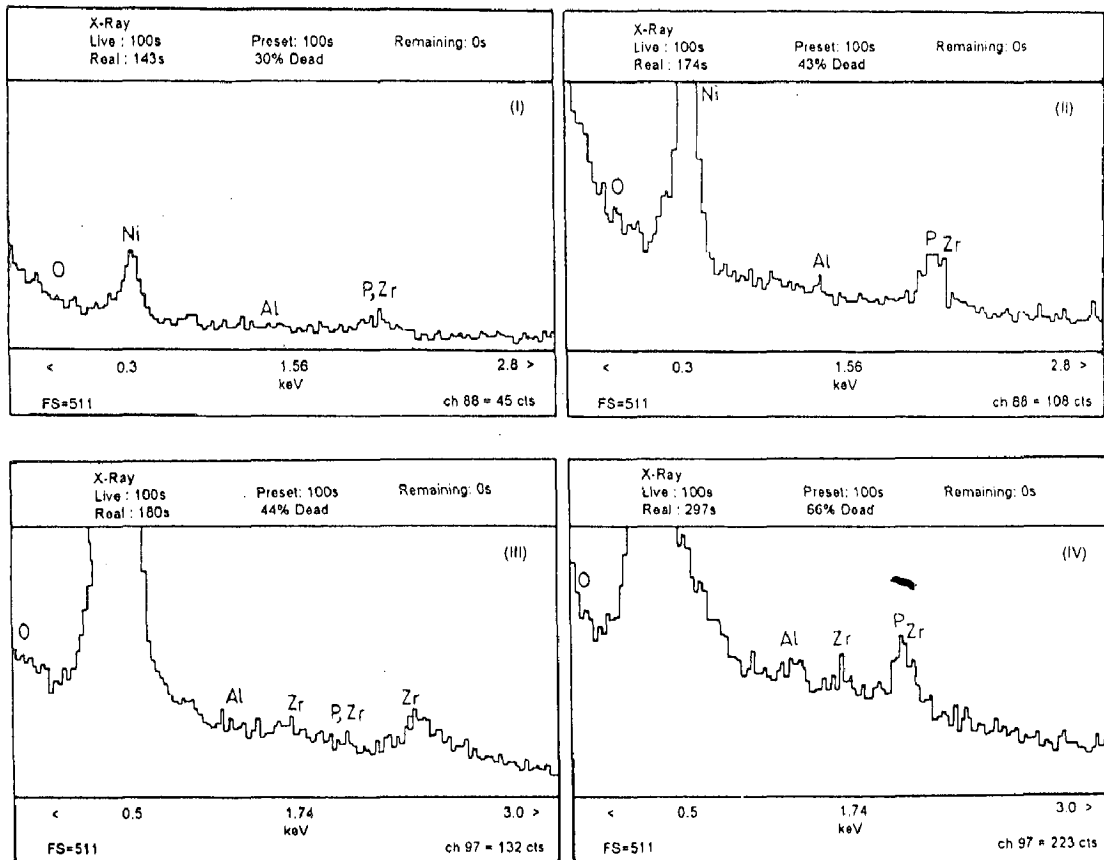


Fig. 4.23 Qualitative analysis of the different elements present in the electroless Ni-P-X composite coating: (a) Ni, (b) P, (c) Zr and (d) Al.



(a)



(b)

Fig. 4.24 Qualitative analysis of different elements present in the electroless Ni-P-X coating by SEM-EDAX area analysis (a) micrograph of the typical area and (b) peaks showing the presence of different elements viz., Ni, P, Zr and Al.

(c) Line analysis

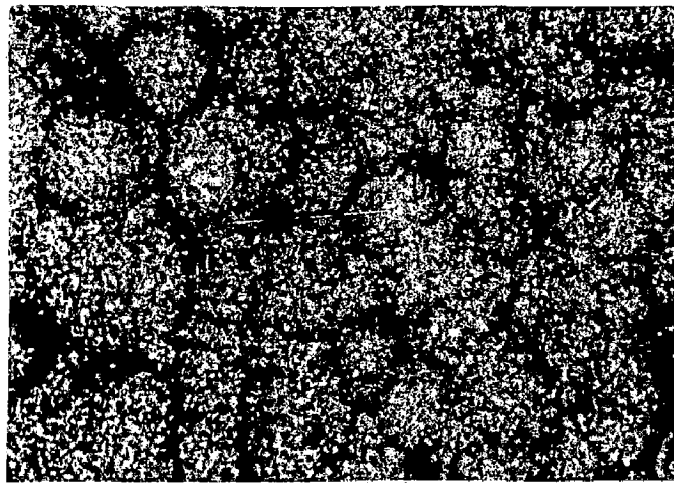
In order to get the composition of different elements by spectrographic technique, the Ni-P-X coated film as shown in Fig. 4.25 (a) has been subjected to line analysis under SEM. The line of $10.84 \mu\text{m}$ length, which has been selected for the analysis can be seen in Fig. 4.25 (a) and the SEM spectrograph obtained along this line is shown by seven different sectors in Fig. 4.25 (b). The length of each sector is equal to length of the line, i.e., $10.84 \mu\text{m}$ and height of the sector from the base of it represents the relative concentration of the element labeled at the sector. The sector marked as (I) shows the profile of the coating surface along the line shown in Fig. 4.25 (a) while other sectors marked as (II), (III), (IV), (V), (VI) and (VII) indicate the qualitative presence of O K_{α} (oxygen), Al K_{α} , P K_{α} , Zr L_{α} , Ni K_{α} and Zr K_{α} respectively. Fairly flat surface profile along the line can be observed from Fig. 4.25 (b-I). The highest relative concentration of Ni is evident from sector (VI) in Fig. 4.25 (b). Similarly from other sectors, it is observed that P K_{α} has substantially higher concentration when compared to that of Zr K_{α} , Zr L_{α} , Al K_{α} and O K_{α} .

(d) Point analysis

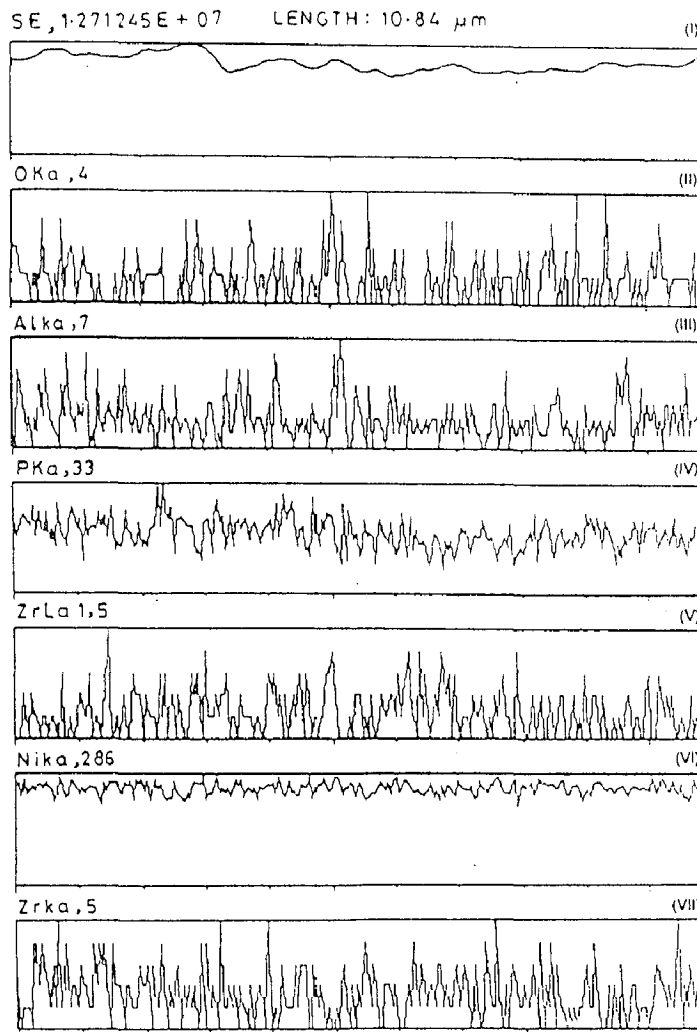
Qualitative analysis by EPMA has been carried for a typical point of size $2 \mu\text{m}$, diameter from the Ni-P-X coated sample and the results obtained for the same are shown in Figs. 4.26 (a) and (b). The peaks corresponding to Ni, P and Al are evidenced from Fig. 4.26 (a) but the peak corresponding to Zr could not be observed in this figure. However, the peaks corresponding to Zr and P are observed by increasing the spectrum scale for these target elements, as shown in Fig. 4.26 (b). Intensities for Ni and P are observed to be predominantly higher but those for remaining elements, i.e., Zr and Al are seen to be substantially lower.

(e) X-ray mapping

The X-ray mapping is a capability of EPMA, which can provide the information regarding the composition of the sample. Figure 4.27 (a) represents the area of Ni-P-X coating selected for X-ray mapping while Figs. 4.27 (b) to (e) show the results of



(a)



(b)

Fig. 4.25

SEM spectrographic analysis results in terms of distribution of different elements present (a) micrograph showing the line selected for spectrographic analysis and (b) spectrograph along 10.84 μm line for I- profile of coating along the line, II- O K α , III- Al K α , IV- P K α , V- Zr L α , VI- Ni K α and VII- Zr K α .

26-DEC-01 QUALITATIVE ANALYSIS

File no. : 37
 Comment : S1: ZR & P

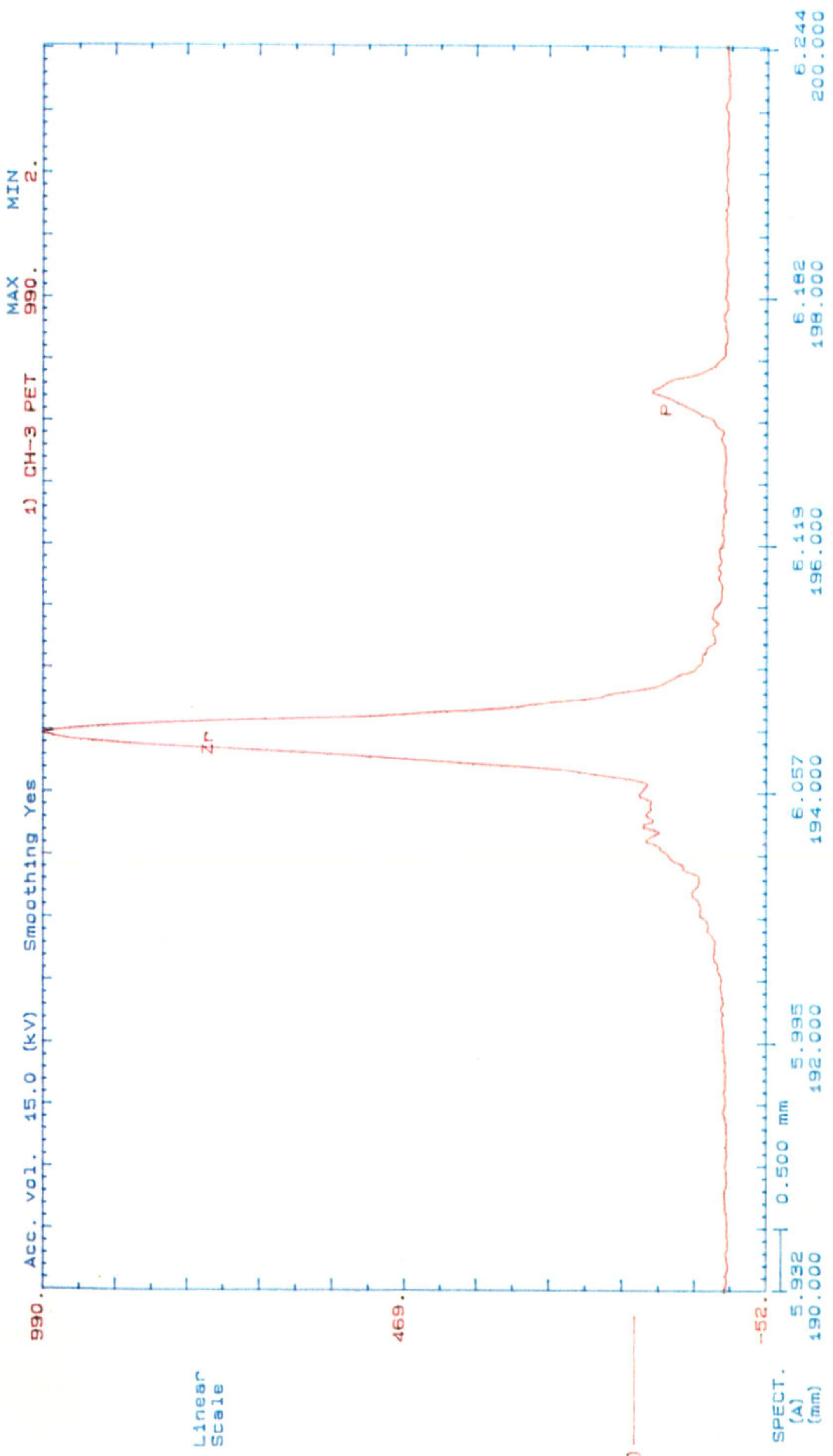
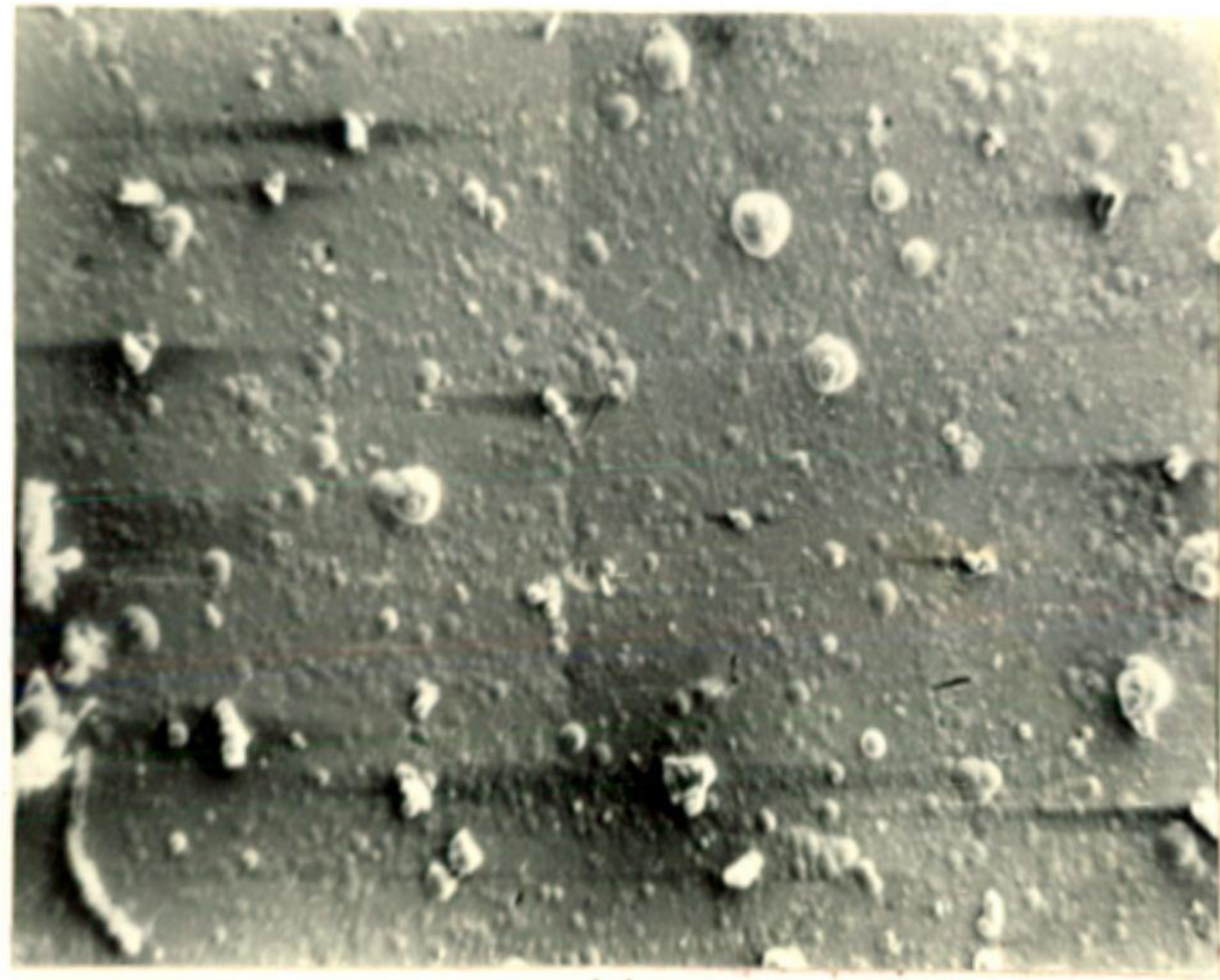
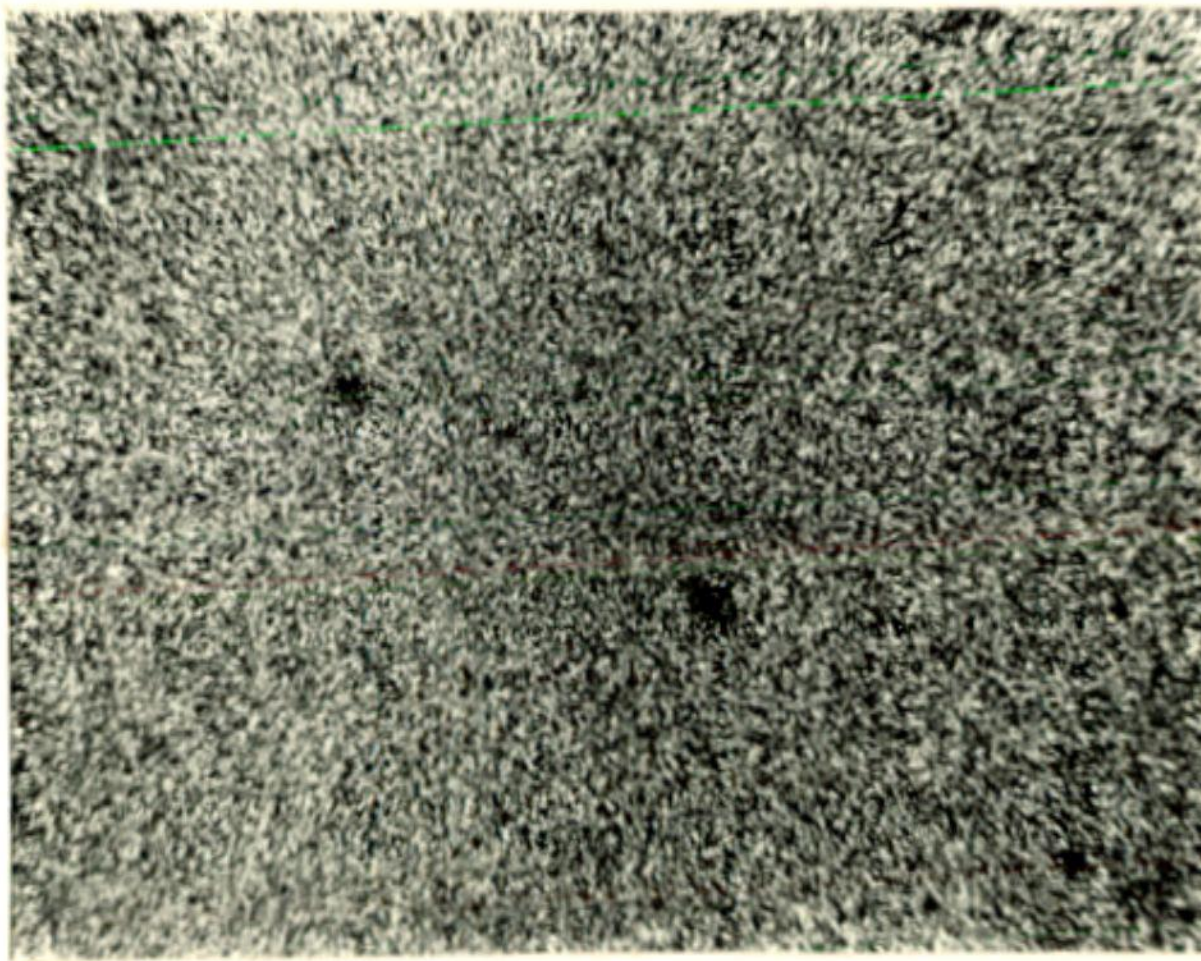


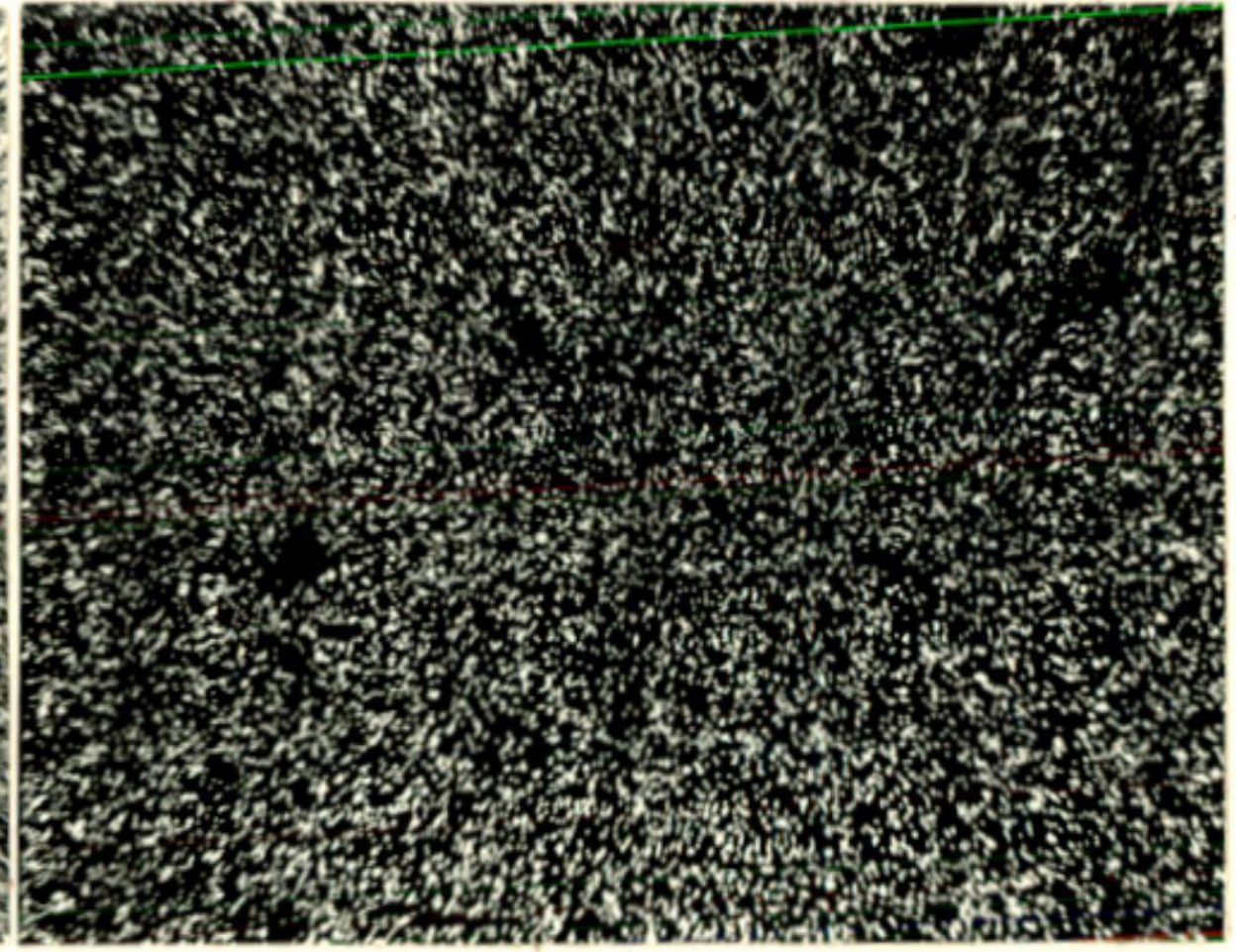
Fig. 4.26 EPMA qualitative analysis of the electroless Ni-P-X coating (a) showing the presence of Ni, P and Al and (b) showing the presence of Zr along with P.



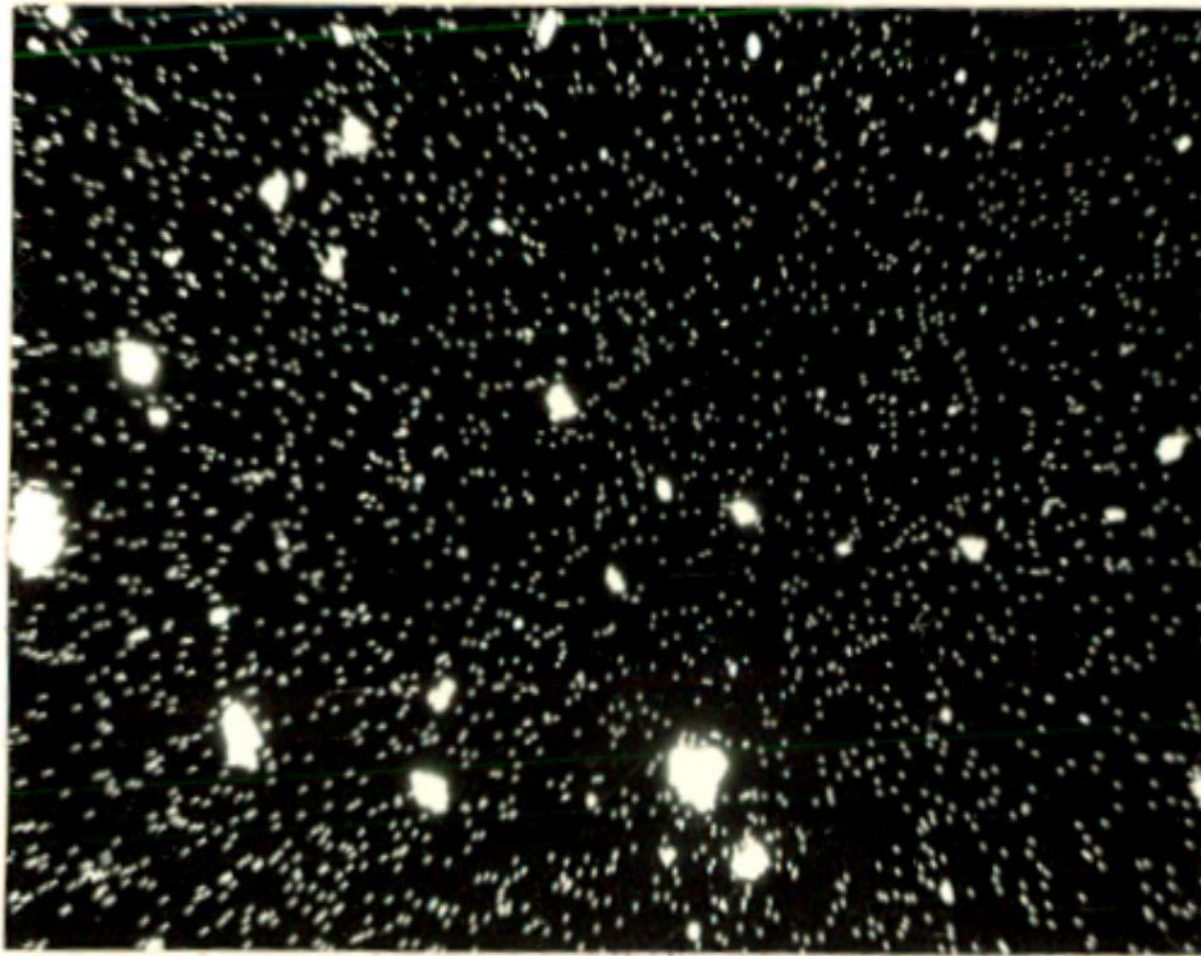
(a)



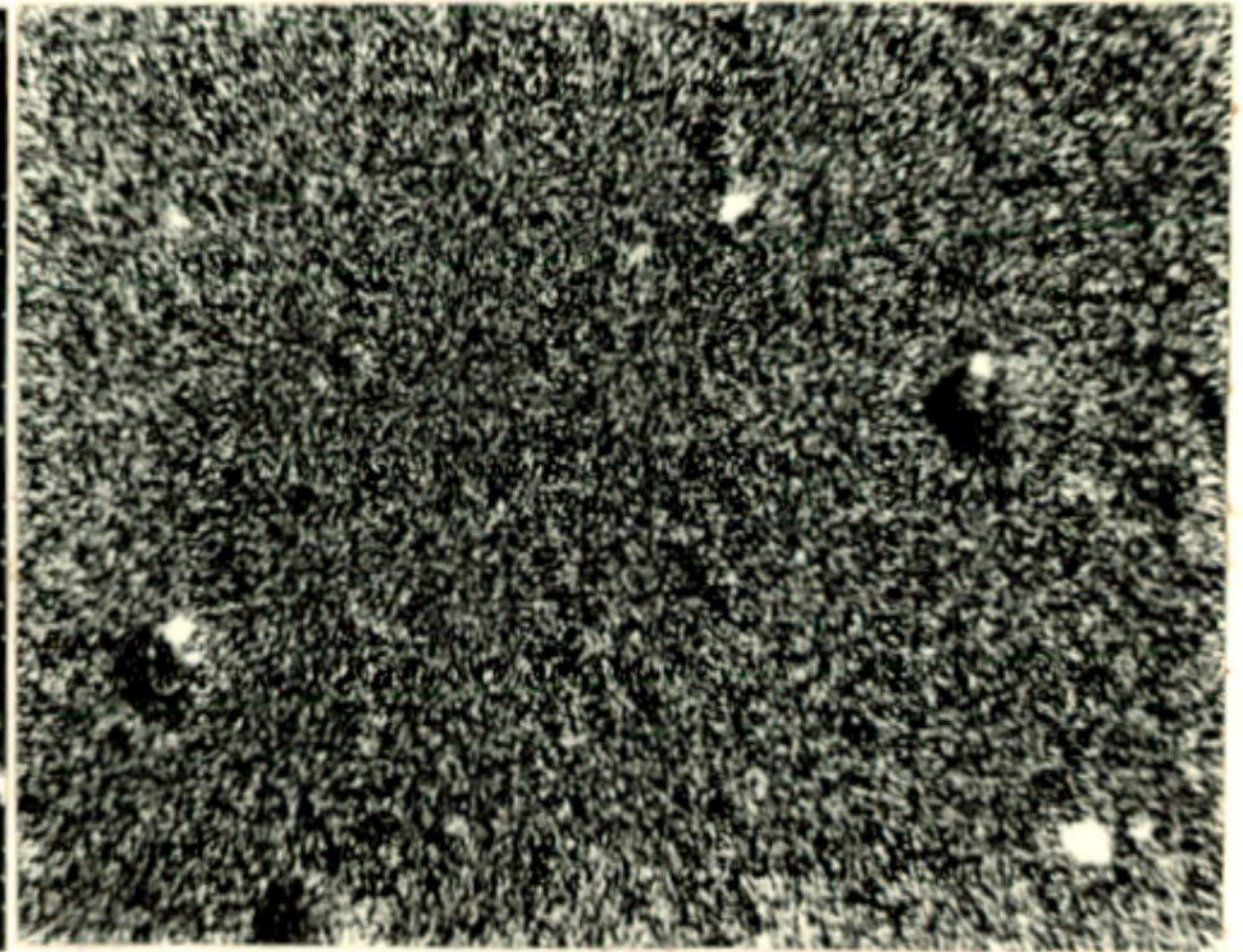
(b)



(c)



(d)



(e)

Fig. 4.27 Micrographs showing the X-ray mapping of electroless Ni-P-X coating under EPMA (a) area selected for mapping, (b) distribution of nickel, (c) distribution of phosphorus, (d) distribution of zirconium and (e) distribution of aluminium.

scanning for Ni, P, Zr and Al in a typical Ni-P-X coating. These figures reveal that the Ni and P are distributed uniformly and predominantly as seen from Figs 4.27 (b) and (c) respectively. But the distribution of Zr and Al in the same area is found to be of non-uniform size of islands over the selected area as shown in Figs. 4.27 (d) and (e). Relatively more areas for Zr can be observed compared to those for Al, as seen in Figs. 4.27 (d) and (e).

4.1.9.2 Quantitative Analysis of Ni-P-X Coating

(a) EPMA point analysis

The electroless Ni-P-X and Ni-P coatings have been carried out especially on glass substrate followed by its preparation for EPMA as explained in chapter 3. The results obtained by EPMA point analysis for a typical region indicate the coating constituents as shown in Tables 4.5 and 4.6 respectively for Ni-P-X and Ni-P coatings. The values given in these tables are obtained from the five points averaging methods. The size of each point considered in the study is of 2 μm diameter. The glowing nature during the analysis has also been visually observed.

Table 4.5 Quantitative Analysis of Electroless Ni-P-X Coating.

Element/Compound	wt. %
P	9.0
Al ₂ O ₃	0.17
ZrO ₂	0.23
Ni	90.6

Table 4.6 Quantitative Analysis of Electroless Ni-P Coating.

Element	wt. %
P	9.5
Ni	90.5

(b) SEM-EDAX

The quantitative analysis for Ni-P-X coated specimen has been conducted by SEM-EDAX by two different methods, viz., area scan and point scan. EDAX has been carried out for three different regions including two areas covering $730 \mu\text{m} \times 330 \mu\text{m}$ and one covering $485 \mu\text{m} \times 220 \mu\text{m}$, the average composition obtained has been reported in this section. Similar EDAX has also been conducted for a few nickel rich points and zirconium rich points and the composition at these points is reported in the subsequent part of this section.

(i) Area scanning

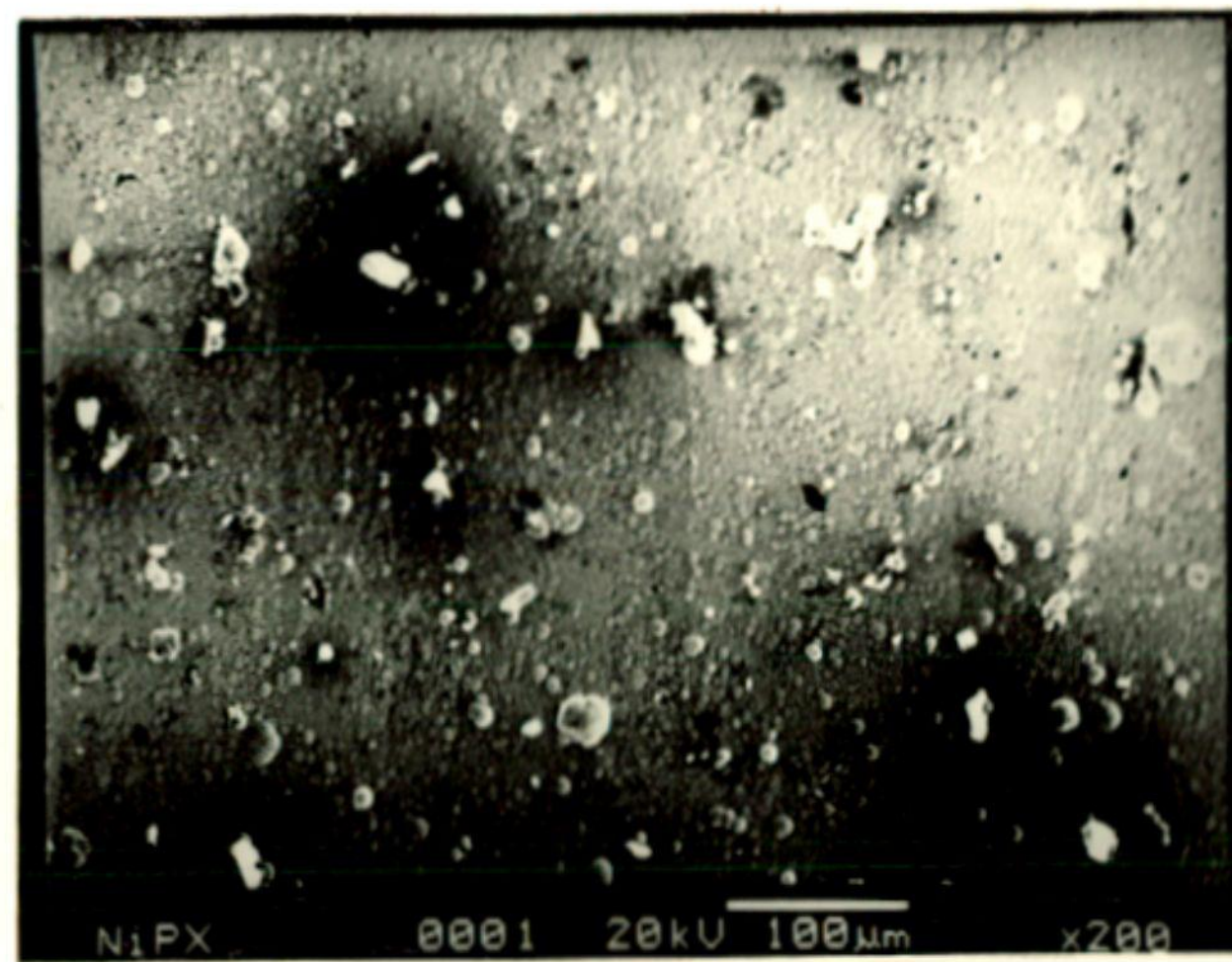
The SEM micrographs showing the three different areas of Ni-P-X coating under this study are shown in Figs. 4.28 (a) to (c). The average of elemental composition obtained for electroless Ni-P-X coating by EDAX is given in Table 4.7.

Table 4.7 Composition of Electroless Ni-P-X Coated Sample as Shown in Figs. 4.27 (a) to (c) by Area Scan under SEM-EDAX.

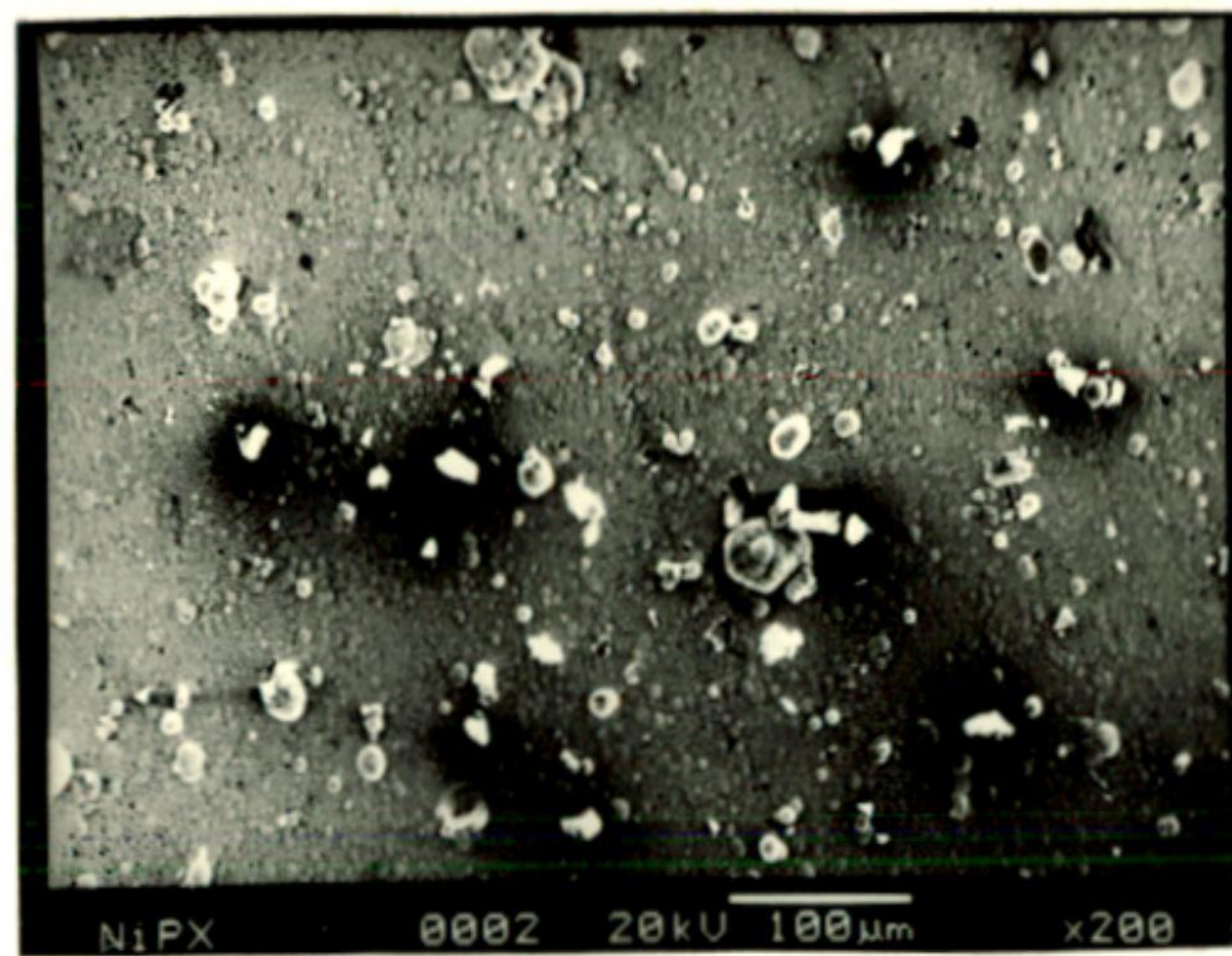
Element	Ni	P	Zr	Al
wt. %	90.7	8.9	0.21	0.16

(ii) Point scanning

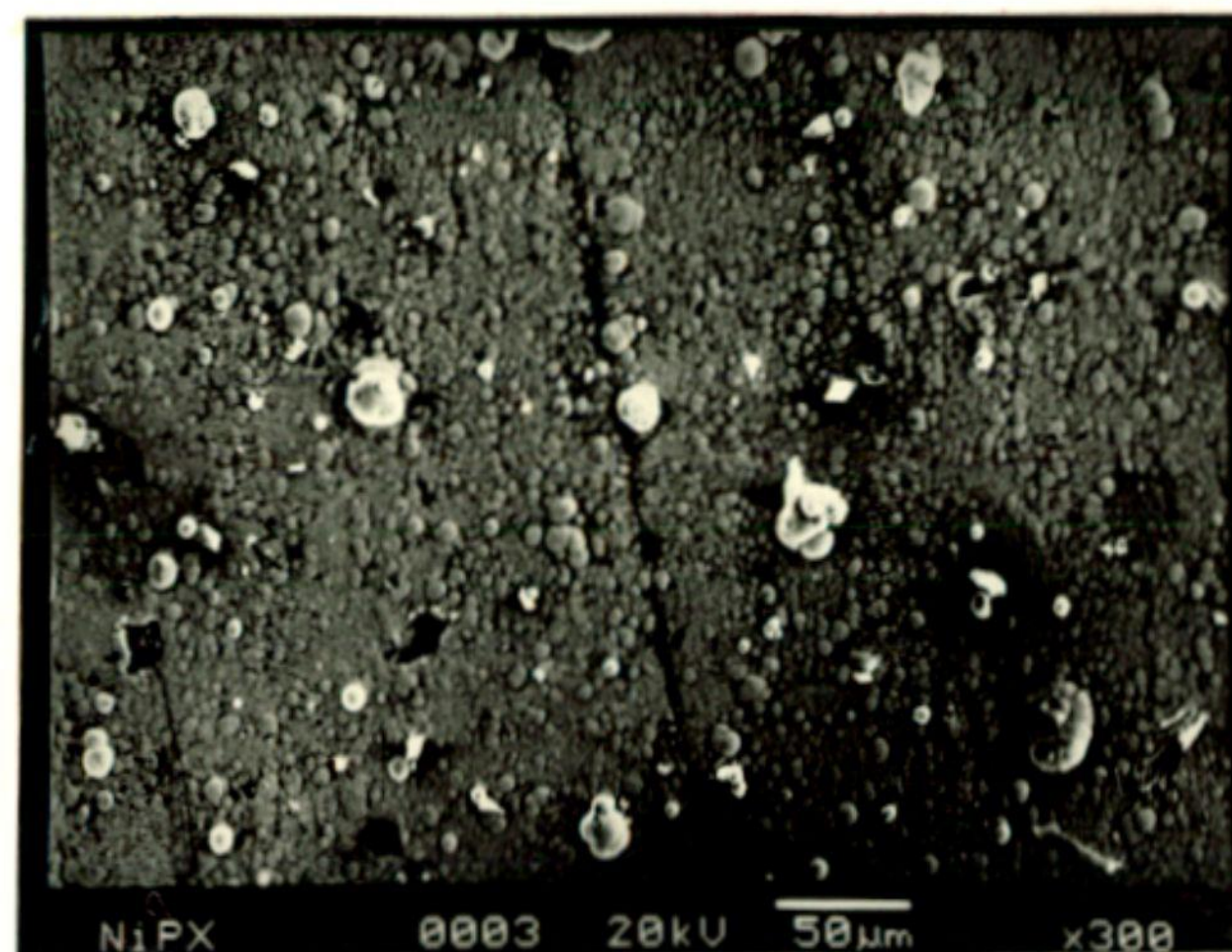
Figure 4.29 (a) represents five different nickel rich points (marked as 1 to 5 on the micrograph), for which the quantitative analysis by EDAX for Ni, P, Zr, and Al has been carried out. Figure 4.29 (b) demonstrates the variation in the presence of these elements at the five points under the study. The amount of Al is observed to be lower than that of Zr at all the five points. It is observed that when minimum Ni (86.9%) at point '1' appears, the amounts of P, Zr and Al are found to be the maximum. The Zr is found to be 4.44% at point '1' but at other points even its trace could not be noticed. However, the Al can be seen at all the five points as shown in Fig. 4.29 (b). Similarly, the micrograph showing three different Zr rich points is shown in Fig. 4.30 (a) while Fig. 4.30 (b) shows



(a)

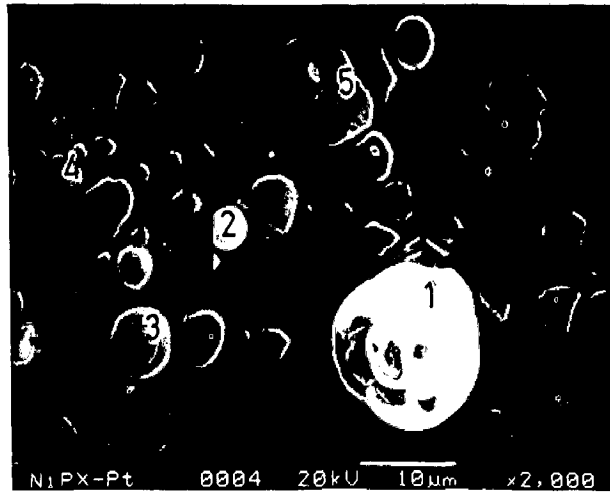


(b)

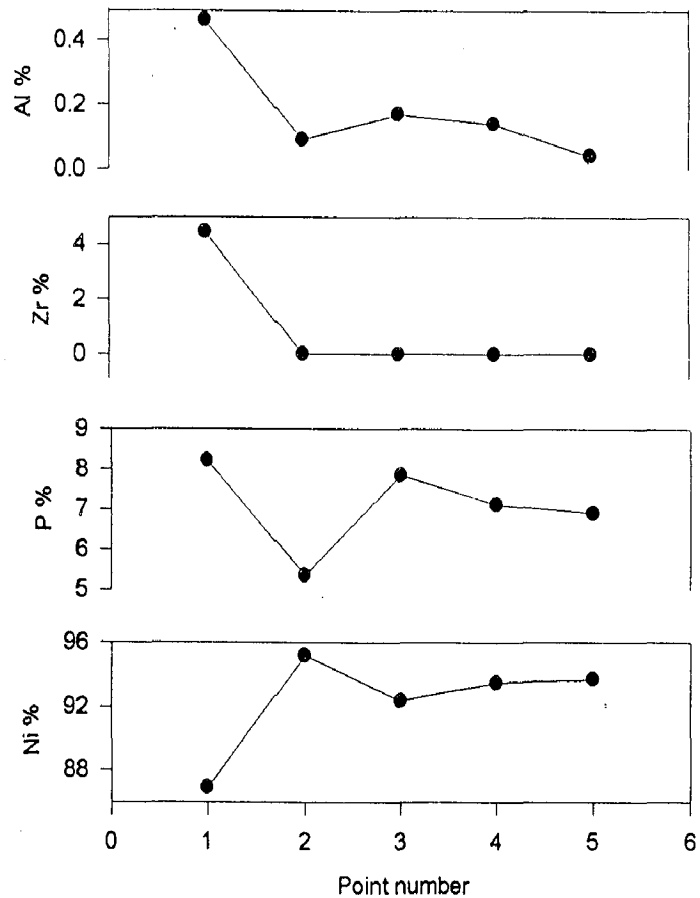


(c)

Fig. 4.28 Micrographs showing three different areas of Electroless Ni-P-X coated sample subjected to quantitative analysis by SEM-EDAX.

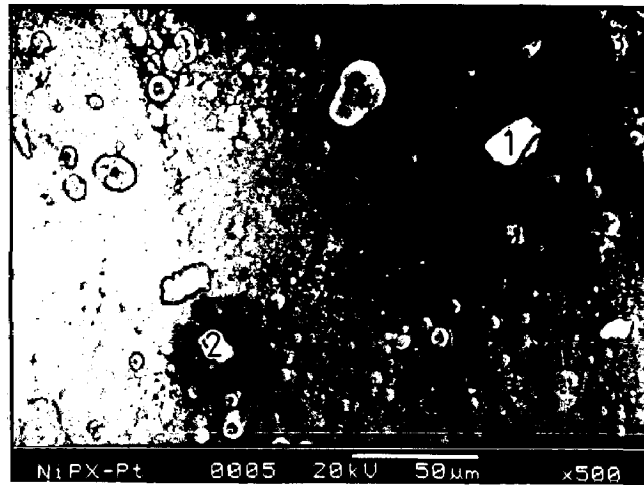


(a)

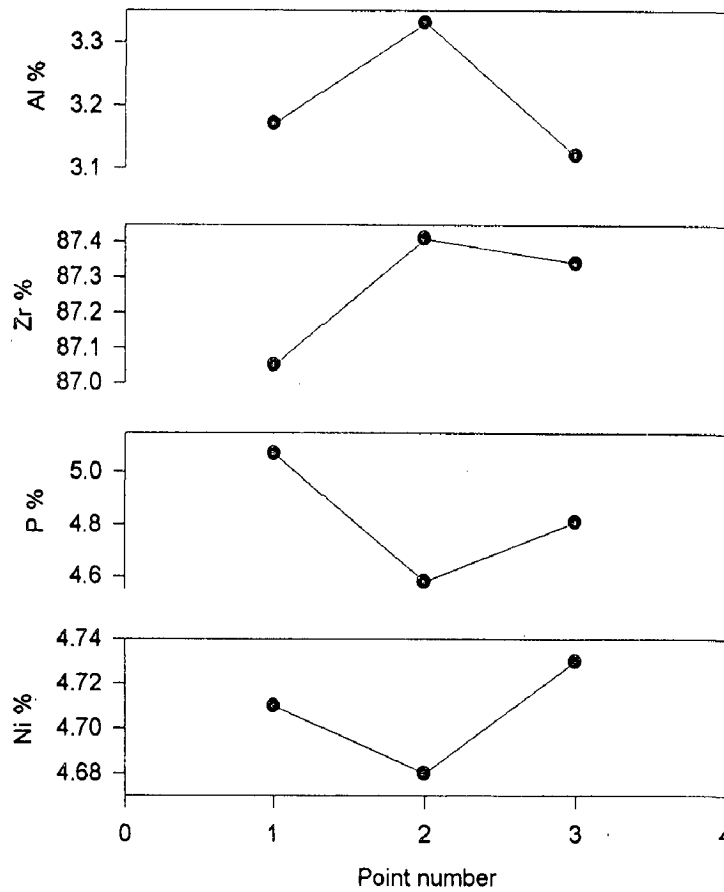


(b)

Fig. 4.29 Point analysis by SEM-EDAX on typically nickel rich points in the electroless Ni-P-X coating (a) micrograph showing different nickel rich points as marked on it and (b) distribution of different elements in wt. % for the points marked in the above micrograph.



(a)



(b)

Fig. 4.30

Point analysis by SEM-EDAX on typically zirconium rich points in the electroless Ni-P-X coating (a) micrograph showing different zirconium rich points as marked on it and (b) distribution of different elements

the amounts of different elements, i.e., Ni, P, Zr and Al at these points. The point '2' is found to have maximum amount of Zr (87.41%) and at this point, the amount of Al has been found to be the highest with the value of 3.33%. The presence of Ni and P is also evidenced in all the three points as seen in Fig. 4.30 (b). A typical point size of 0.35 μm diameter has been used for these analyses.

4.1.10 Phase Analysis

As explained in chapter 3, the X-ray diffraction studies have been carried out for the electroless Ni-P-X coatings in different conditions, i.e., as-coated, heat treated at 400°C for 1 h, heat treated at 400°C for 2 h and heat treated at 250°C for 12 h. The Ni-P coating has also been analysed in as-coated condition for comparison purpose. TEM studies on as-coated Ni-P-X and Ni-P deposit films have been carried out for confirming the phase constituents present in the as-coated conditions.

(a) As-coated films

Figure 4.31 shows a typical X-ray diffraction pattern of as-coated Ni-9wt.%P-X film, a predominant broad peak and a few small peaks are evidenced in it indicating the possibility of existence of a few phases other than microcrystalline nickel. The phase that appears frequently, i.e., matrix phase is referred to as common phase while that appearing at a few places in lesser amount is termed as less common phase. It is observed that, the Ni-P-X coating in as-coated state primarily consist of microcrystalline Ni as a common phase present. Nickel phosphites like Ni (am), Ni₅P₂, Ni₁₂P₅, Ni_{2.55}P, NiP₂ (Ni_xP_y) and Ni₃P along with Al₃Zr, Al₂O₃ and ZrO₂ have also been identified as less common phases in the as-coated Ni-P-X coatings. The characteristic peaks corresponding to different phase constituents present in the coating are reported in Table A.5 of the appendix.

The X-ray diffraction pattern obtained for as-coated Ni-9.5wt.%P film given in Fig. 4.32, shows a single broad peak indicating the amorphous/microcrystalline nature of the film. The characteristic peaks identified from this X-ray diffraction pattern are enumerated in Table A.6, given in appendix, which also indicate the presence of microcrystalline Ni as common phase and Ni (am), Ni₅P₂, Ni₁₂P₅, Ni_{2.55}P, and NiP₂ as less common phases in the as-coated Ni-P coatings.

TEM micrographs of Ni-9wt.%P-X film given in Figs. 4.33 (a) and (b) show the bright and dark field images of the coating respectively. Some nanosized islands or the particles of the order 5-8 nm can be clearly seen in these micrographs. The selected area diffraction (SAD) pattern for the same region is shown in Fig. 4.33 (c), which reveals a diffused ring pattern. The diffused rings have been indexed as the amorphous nickel (111) having the d value as 2.03 Å. The presence of other less common phases, viz., Ni₅P₂, Ni₁₂P₅, Ni₃P along with Al₃Zr, Al₂O₃ and ZrO₂ in the same region can also be seen in Fig. 4.33 (c). These phases are identified after indexing the SAD pattern as listed in Table A.7, given in appendix. A bright field image under TEM is shown in Fig. 4.34 (a), which reveals the presence of uniformly distributed nanosized particles in Ni-P-X coating. Relatively larger cluster like particle has also been featured in the same electroless Ni-P-X film (from another region) under TEM as shown in Fig. 4.34 (b). The SAD pattern of this cluster of particles is shown in Fig. 4.34 (c). The SAD pattern as seen in Fig. 4.34 (c) is an indication of microcrystalline nature of the coating. The presence of less common phases has been identified after indexing the pattern and the phases are reported in Table A.7.

Above results of TEM studies for the electroless Ni-P-X coatings are compared with that of as-coated Ni-9.5wt.%P coating, for which the bright field image, dark field image and its SAD pattern are respectively shown in Fig. 4.35 (a), (b) and (c). The finely distributed particles of the order 5-10 nm are seen in Figs. 4.35 (a) and (b). The SAD pattern for the Ni-P coating, i.e., Fig. 4.35 (c) is indexed, which revealed the presence of nickel in as-coated condition. One distinct diffused ring and two dull diffused rings could be seen under the film reader and the d values calculated from the same are found to be 2.03, 1.762 and 1.246 Å and all these d values are corresponding to the Ni phase.

Structure and stability data of different phases such as nickel phosphite, aluminium oxide and zirconium oxides have been identified from ASTM data cards. The data for Ni₃P has been referred from the work of Makhsoos *et al.* (1978) while a handbook by Pearson (1967) is used for the data of NiP₂ phase.

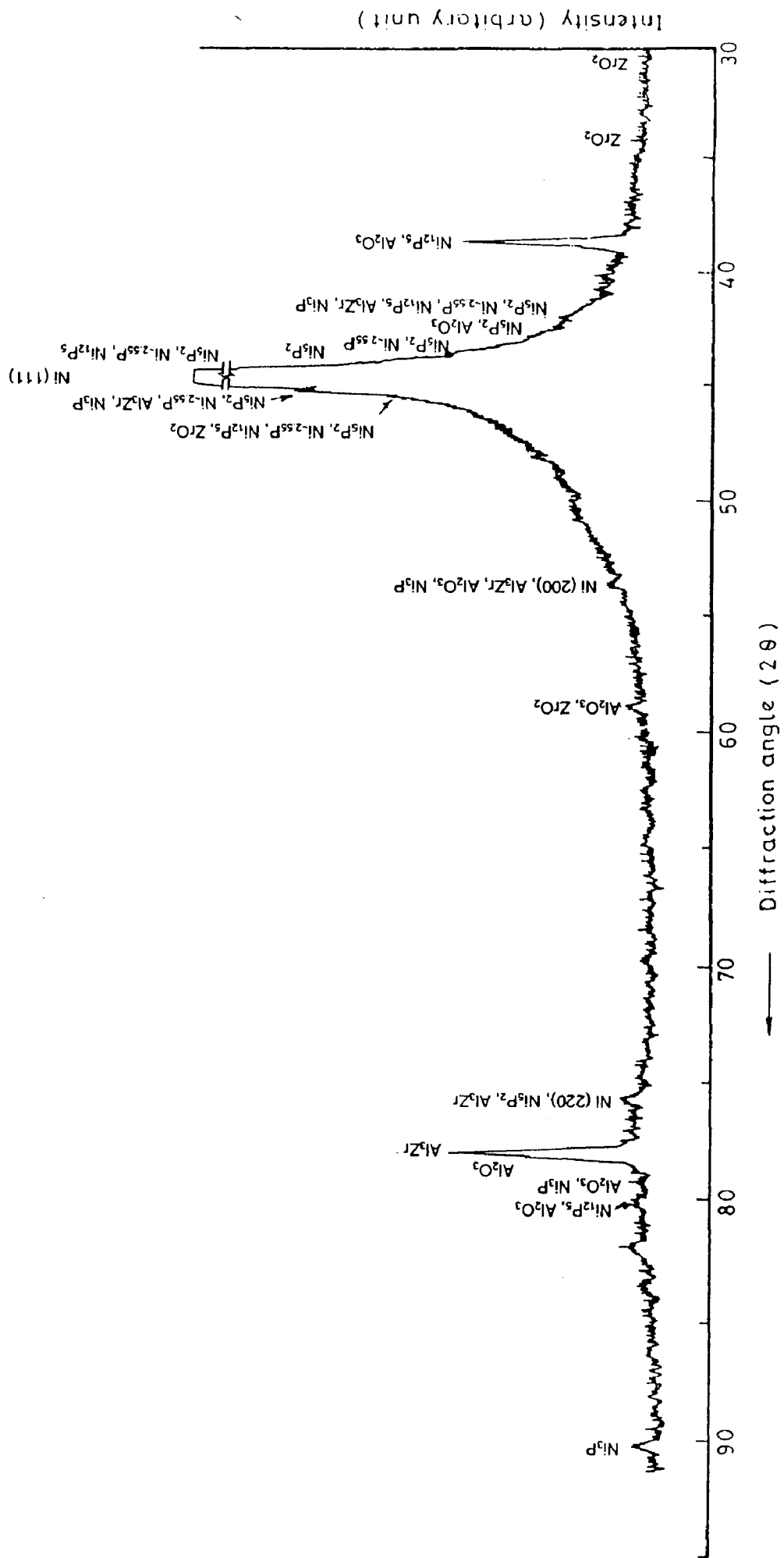


Fig. 4.31 X-ray diffraction pattern of electroless Ni-P-X coating in as-coated condition.

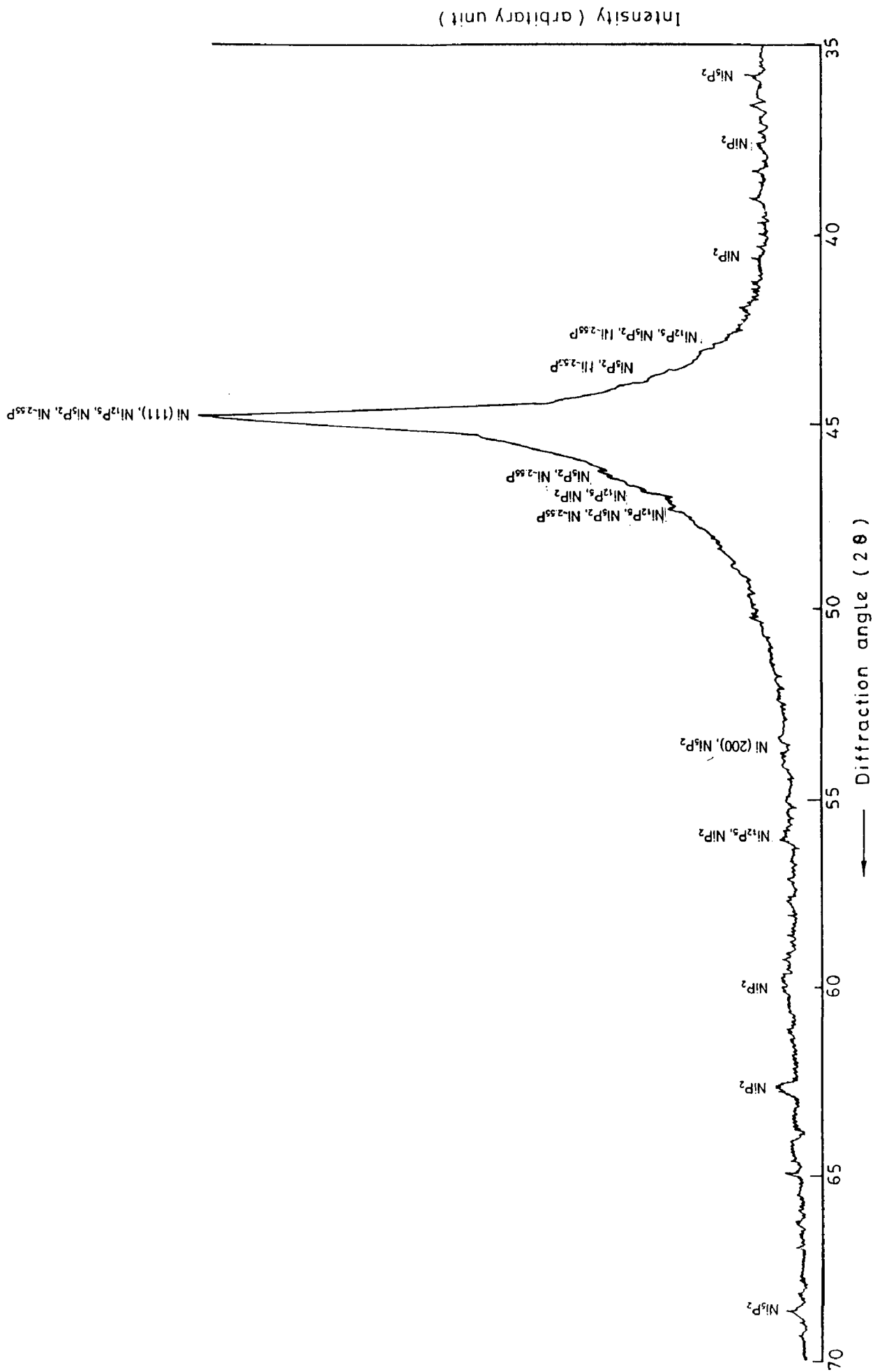


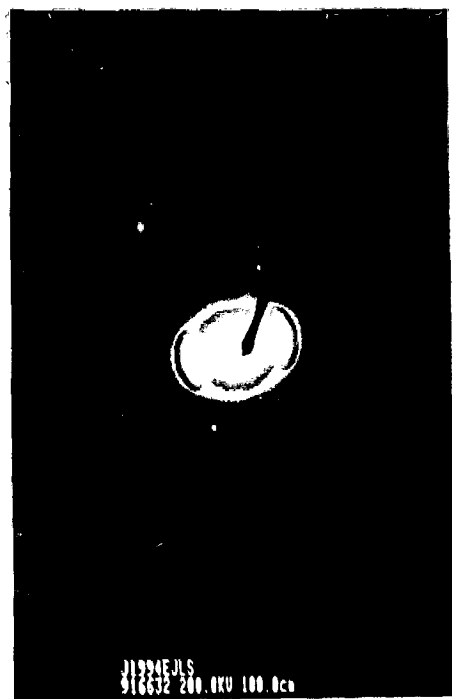
Fig. 4.32 X-ray diffraction pattern of electroless Ni-P coating in as-coated condition.



(a)



(b)



(c)

Fig. 4.33 TEM micrographs of electroless Ni-P-X coating (a) bright field image, (b) dark field image and (c) SAD pattern of (a).



(a)

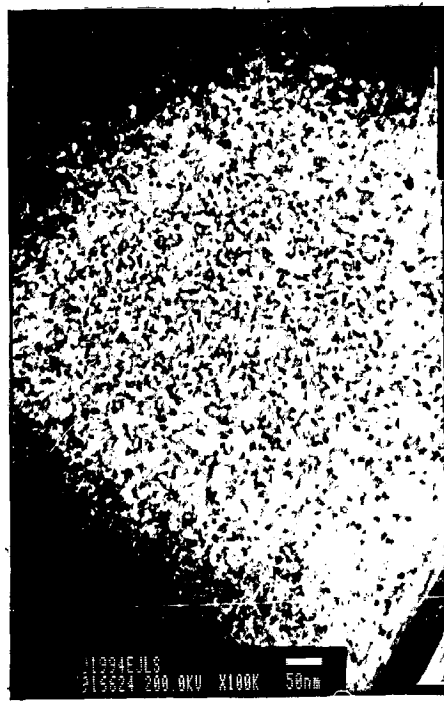


(b)

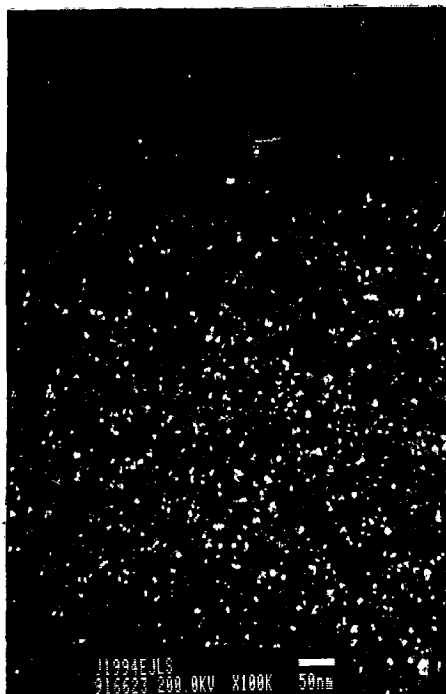


(c)

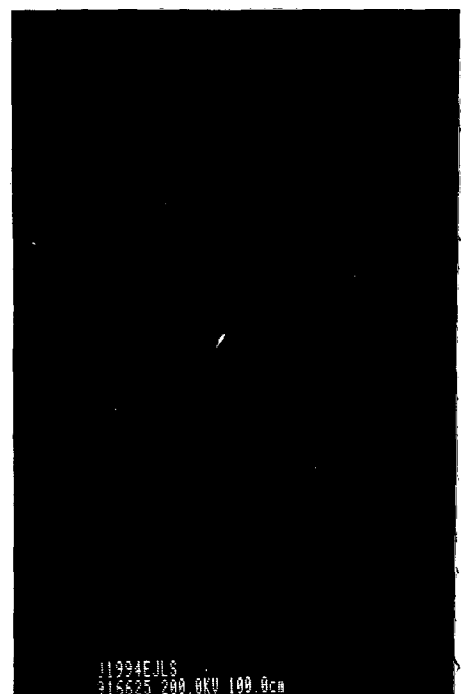
Fig. 4.34 TEM micrographs of electroless Ni-P-X coating (a) bright field image, (b) bright field image of the clustered of particles and (c) SAD pattern of (b).



(a)



(b)



(c)

Fig. 4.35 TEM micrographs of electroless Ni-P coating (a) bright field image, (b) dark field image and (c) SAD pattern of (a).

(b) Heat treated films

The X-ray diffraction patterns of heat treated electroless Ni-9wt.%P-X coatings at 400°C for 1 h, 400°C for 2 h and 250°C for 12 h have been obtained, which show similar phase constituents after heat treatment. A typical case X-ray diffraction pattern for Ni-9wt.% P-X coated and heat treated at 400°C for 1 h is shown in Fig. 4.36 and the phase constituents identified for the same are reported in Table A.8, given in appendix. Ni and Ni₃P appear to be common phases whereas Al₃Zr, Al₂O₃ and ZrO₂ are as less common phases in the heat treated films.

Common and less common phases identified from different X-ray diffraction patterns for electroless Ni-9wt.%P-X coatings in different conditions, i.e., as-coated, heat treated at 400°C for 1 h, heat treated at 400°C for 2 h and heat treated at 250°C for 12 h and that for electroless Ni-9.5wt.%P in as-coated condition have been reported in Table A.9, given in appendix. The Table A.9 reveals that heat treatment results in the transformation of Ni_xP_y phases into Ni + Ni₃P as common phases present.

4.1.11 Non-Isothermal Kinetics of Transformation

In this section, results on study of non-isothermal kinetics for electroless Ni-P-X and Ni-P coatings, using Differential Scanning Calorimetry (DSC), have been presented. The parameter viz., activation energy (E) and reaction exponent or Avrami exponent (n) for transformation are experimentally determined using Kissinger analysis. The determination of kinetics parameters, may^{be} helpful in explaining the transformation taking place in the material under study.

Figures 4.37 (a) to (d) and 4.38 (a) to (d) represent DSC response curves obtained with electroless Ni-P-X and Ni-P coatings respectively, for four different heating rates (β), i.e., 10, 15, 20 and 25 °C/min. A single DSC peak in both types of the coatings at all the four heating rates is observed from above figures. The magnitude of the peak is found to increase with increasing heating rate. The smallest peak is evidenced with 10 °C/min heating rate and the largest one at a heating rate of 25 °C/min as shown in Figs. 4.37 (a)

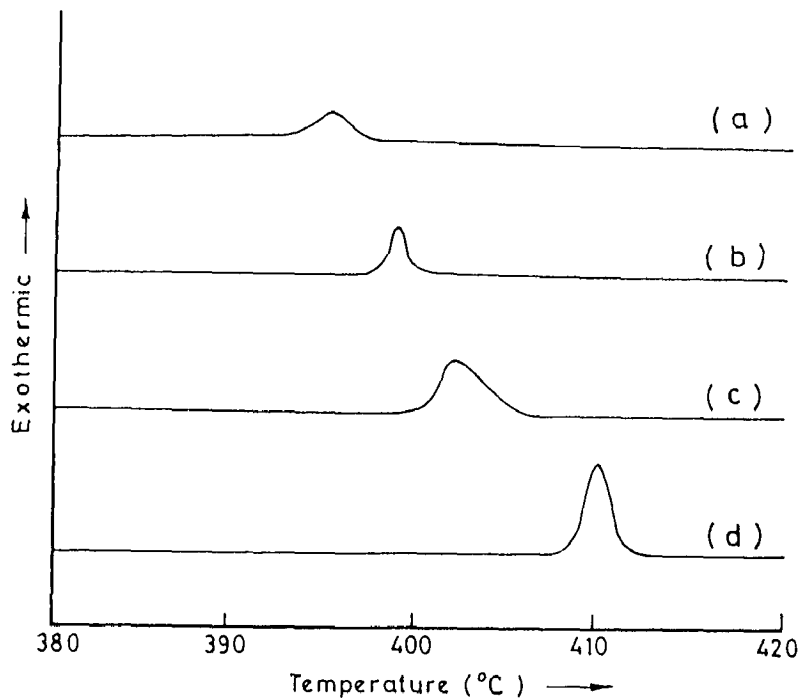


Fig. 4.37 Differential Scanning Calorimeter (DSC) response curves for electroless Ni-P-X coating obtained at different heating rates (a) $10\text{ }^{\circ}\text{C}/\text{min}$, (b) $15\text{ }^{\circ}\text{C}/\text{min}$, (c) $20\text{ }^{\circ}\text{C}/\text{min}$ and (d) $25\text{ }^{\circ}\text{C}/\text{min}$.

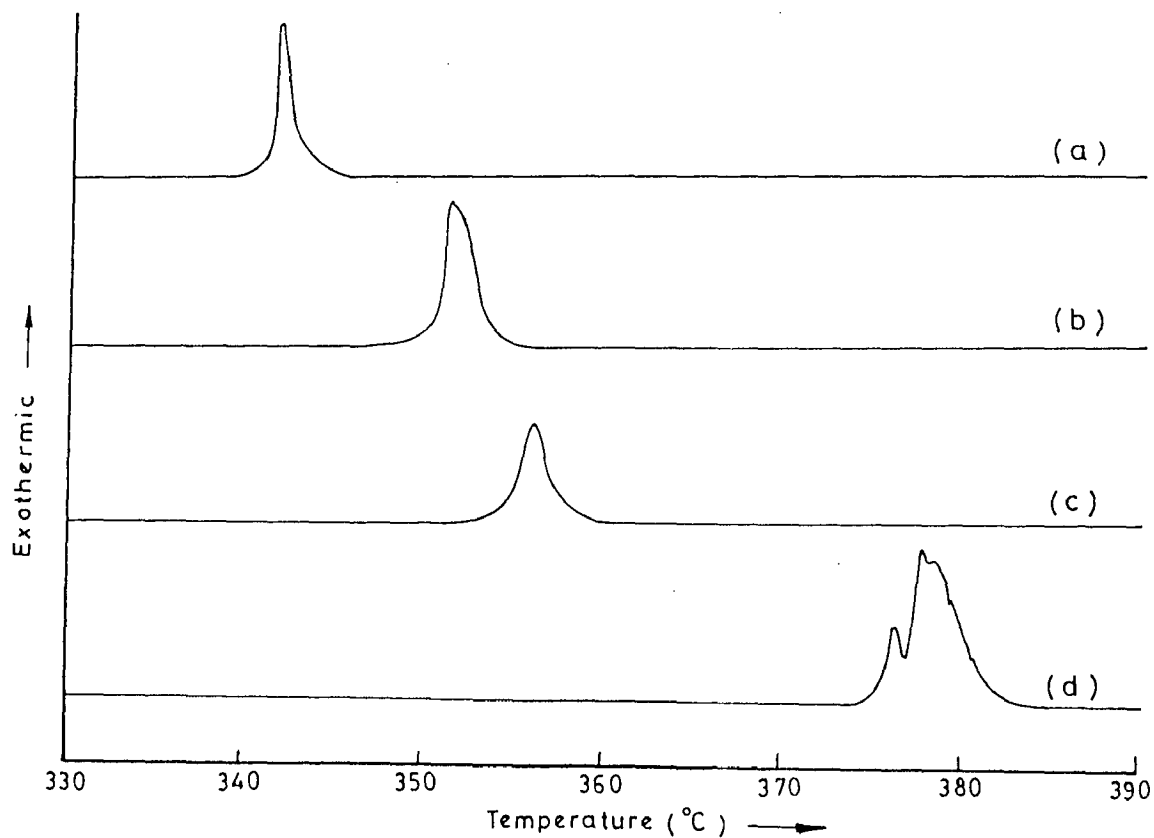


Fig. 4.38 Differential Scanning Calorimeter (DSC) response curves for electroless Ni-P coating obtained at different heating rates (a) $10\text{ }^{\circ}\text{C}/\text{min}$, (b) $15\text{ }^{\circ}\text{C}/\text{min}$, (c) $20\text{ }^{\circ}\text{C}/\text{min}$ and (d) $25\text{ }^{\circ}\text{C}/\text{min}$.

and (d) respectively. Only a marginal increase in the peak temperature, T_m , is found with the increase in heating rate. The peak temperature readings observed for different heating rates of 10, 15, 20 and 25 °C/min are reported in Table A.10 given in appendix. Similar peaks are also observed in DSC response curves for electroless Ni-P coatings and are shown in Figs. 4.38 (a) to (d). However, a relatively smaller peak is seen corresponding to the heating rate of 20 °C/min whereas that observed corresponding to 25 °C/min heating rate is a stepped peak. The values of T_m observed for peaks in electroless Ni-P coating are in the range of 668K to 683K as reported in Table A.10. Kissinger plots between parameters $\ln(\beta/T_m^2)$ and $1/T_m$ for both the electroless Ni-P-X and the Ni-P coatings are shown in Fig. 4.39. Almost linear nature of the Kissinger plots is observed, the slope of which yields the value of apparent activation energy (E_a).

The order of reaction or Avrami exponent, n , is calculated by using Eq. (2.24), for which plots of parameter $\ln \ln \left(\frac{1}{1-\alpha} \right)$ vs. $1/T$ are drawn for both the types of the coatings studied. These linear plots for electroless Ni-P-X and Ni-P coatings, for heating rates of 10, 15, 20 and 25 °C/min, are presented in Figs. 4.40 (a) to (d) respectively. The fraction transformed (α) at any temperature (T) is the ratio of the area under DSC response curve under the peak between the starting point of the peak and the vertical line at that temperature to the total area under the peak. Further, the slope of these linear plots determined by least square fit lines, yields the value of parameter nE using Eq. (2.30). The values of the parameters, nE and E , can yield the value of n . Values of activation energy and Avrami exponent, so calculated for electroless Ni-P-X and Ni-P coatings are given in Table 4.8. Figure 4.41 shows the variation of E/RT with heating rate for Ni-P-X and Ni-P coatings. It is observed that E/RT is constant and does not change significantly with increasing heating rate for both the coatings. However, E/RT is higher for Ni-P-X coating as compared to that for Ni-P coating for all the heating rates used in the present study as seen from Fig. 4.41.

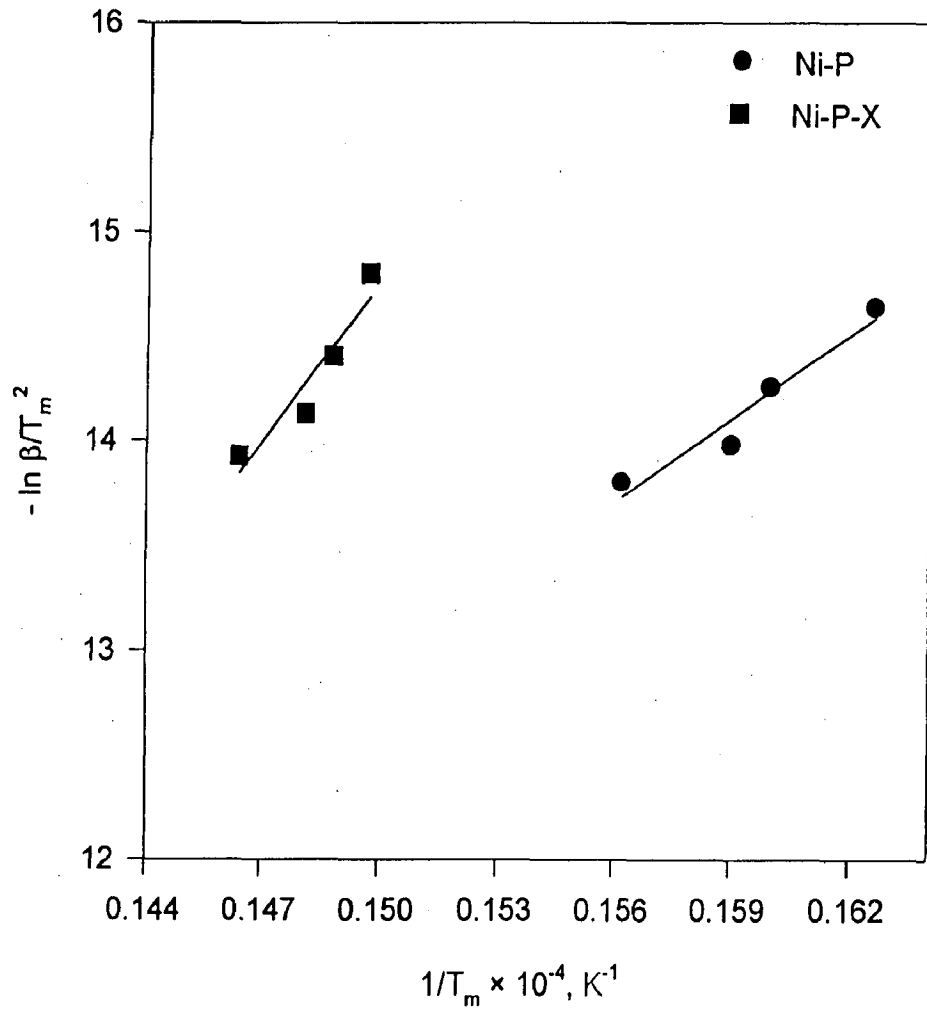
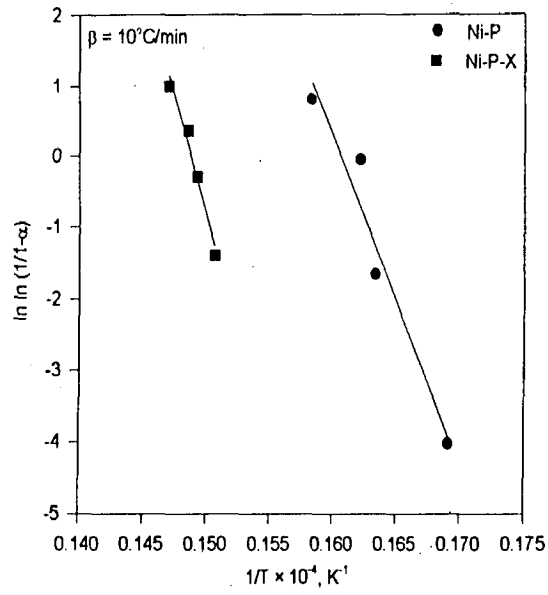
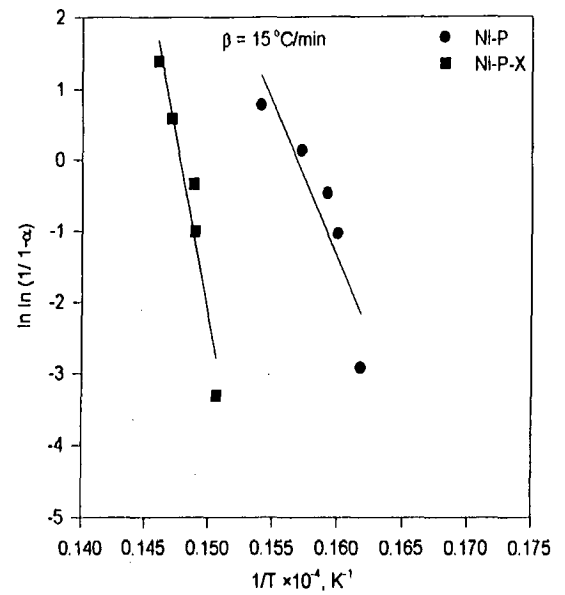


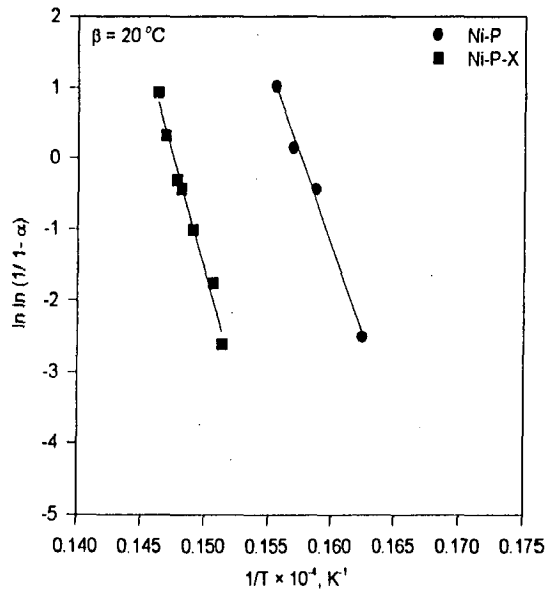
Fig. 4.39 Kissinger plot of $-\ln (\beta/T_m^2)$ vs. $(1/T_m)$ for the curves shown in Figs. 4.37 and 4.38.



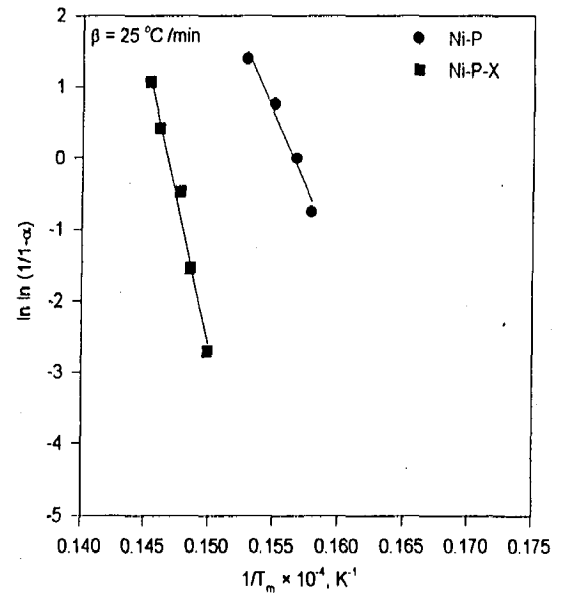
(a)



(b)



(c)



(d)

Fig. 4.40 $\ln \ln(1/(1-\alpha))$ vs. $(1/T)$ plots for electroless Ni-P-X and Ni-P coatings at different heating rates (a) $10^\circ C/min$, (b) $15^\circ C/min$, (c) $20^\circ C/min$ and (d) $25^\circ C/min$.

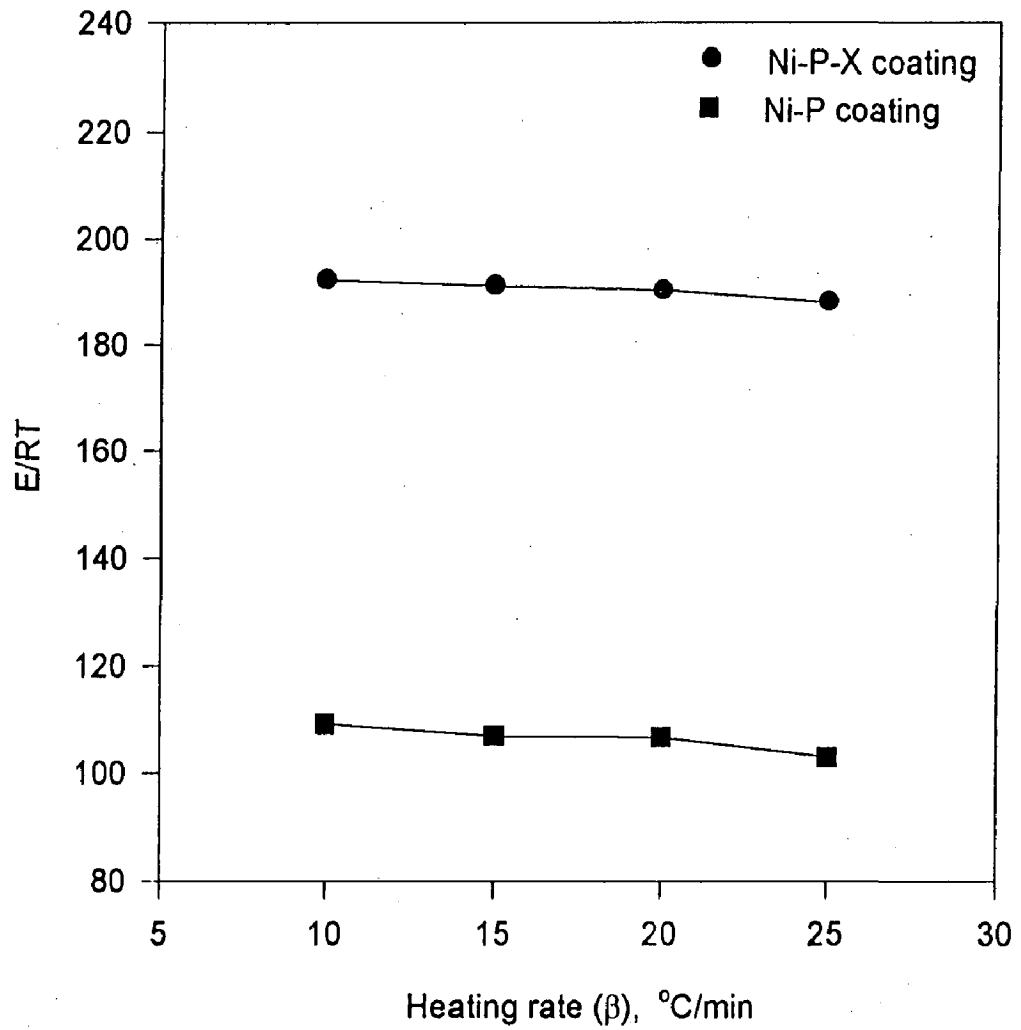


Fig. 4.41 Variation of E/RT with heating rate in electroless Ni-P-X and Ni-P coatings.

Table 4.8 Kinetics Parameters of Transformation in Electroless Ni-P-X and Ni-P Coatings.

Electroless Coating	Activation Energy, E KJ/mol				Avrami Exponent n			
	Heating rate, $^{\circ}C/min$				Heating rate, $^{\circ}C/min$			
	10	15	20	25	10	15	20	25
Ni-P-X	256.9				2.61	3.77	2.48	3.17
Ni-P	134.326				3.42	3.25	3.72	3.16

4.1.12 Hardness

The microhardness and macrohardness measurements have been carried out on different specimen viz., normalised steel (NS); normalised steel specimens as-coated with Ni-P-X (AC₁), heat treated steel samples after Ni-P-X coating at 400°C for 1 h (HT₁-A) and that at 400°C for longer time of 2 h (HT₂-A); normalised steel specimens as-coated with Ni-P (AC₂), heat treated steel samples after Ni-P coating at 400°C for 1 h (HT₁-B) and that at 400°C for longer time of 2 h (HT₂-B). Similarly, the microhardness and the macrohardness measurements have also been carried out on aluminium substrate (AL); aluminium specimens as-coated with Ni-P-X (AC₃), heat treated aluminium samples after Ni-P-X coating, at 400°C for 1 h (HT₁-C) and that at 400°C for longer time of 2 h (HT₂-C).

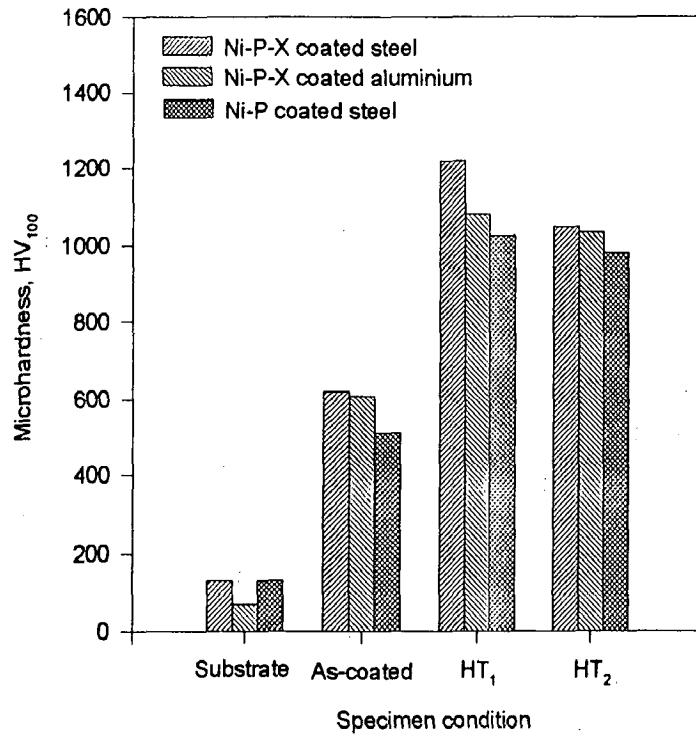
Microhardness of electroless coatings for different conditions has been measured randomly at five different points on the each type of the coating and average value is reported. Figures 4.42 (a) and (b) show respectively the microhardness and macrohardness observed in Ni-P-X and Ni-P coated samples in different conditions. The microhardness of Ni-P-X and Ni-P coatings on steel in AC₁ and AC₂ conditions respectively have been found to be 620 HV_{100} and 510 HV_{100} while that in Ni-P-X as-coated aluminium (AC₃) has been found to be 608 HV_{100} . The increase in hardness with increase in heat treatment temperature is commonly observed till 400°C. The maximum hardness of 1219 HV_{100} for HT₁-A type of sample has been observed while at this heat treatment the maximum

hardness for HT₁-C is found to be 1080 HV_{100} . When heat treatment was carried at 400°C for 2 h the hardness value has experienced a little decrease as it is found to be 1048 HV_{100} in Ni-P-X coated steel sample. After heat treatment at 250°C for 12 h, i.e., HT₂-C sample, the hardness is found to be 1034 HV_{100} . Microhardness of Ni-P-X and Ni-P coated surfaces have been measured in terms of HV_{100} and reported in Table A.11 as given in appendix.

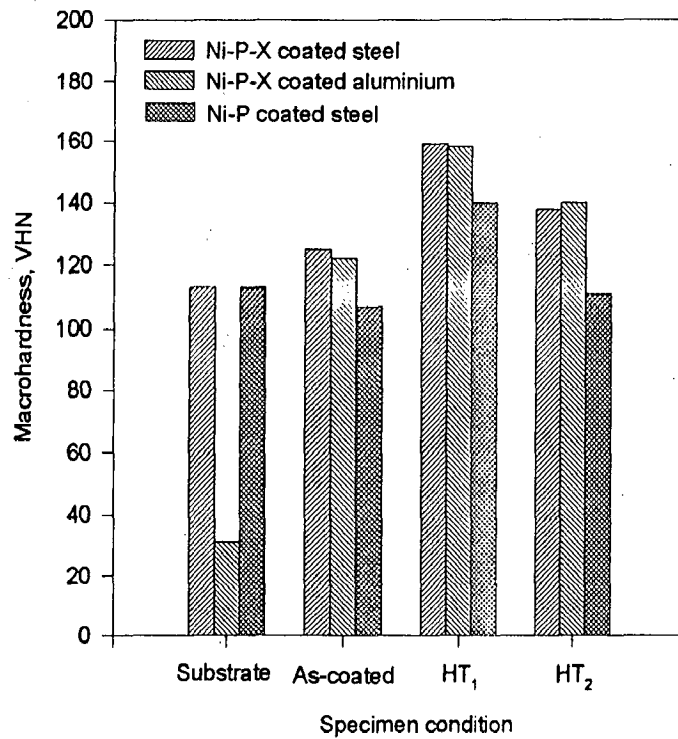
Microhardness of the matrix of the Ni-P-X coating in as-coated condition is observed to be 585 HV_{100} while that for less common phases like ZrO₂, Al₂O₃ and Al₃Zr is found to be in the range of 1446-2284 HV_{100} as reported in Table A.12 given in appendix. The heat treatment resulted in an increase in hardness due to precipitation of Ni₃P phase, which is found to be 1176 HV_{100} as given in Table A.12.

In order to use the hardness data for coated substrate for explaining tribological behaviour in the subsequent chapters 5 and 6, the macrohardness measurements have also been carried out and the values observed are reported in Table A.13 given in appendix. The maximum macrohardness of 159 VHN has been found for HT₁-A type sample and the minimum of 23 VHN in AC₃ type of sample. The hardnesses in Ni-P-X and Ni-P as-coated on steel are found to be 125 and 122 VHN respectively. The data from Table A.13 reveals that the change in hardness due to coated layer is insignificant as the indentation may pierce through the coating. Heat treatment of coated steel samples results in a little increase in hardness value.

The microhardness and macrohardness of NS type sample are observed to be 131 HV_{100} and 113 VHN respectively while those for aluminium as such (AL) sample are found to be respectively 69 HV_{100} and 23 VHN . The data given in Table A.14 reveals that the hardness of steel substrate is insensitive to the heat treatment up to 400°C. Microhardness and macrohardness of AL sample after heat treatment at 400°C are found to decrease up to 45 HV_{100} and 18 VHN respectively. However, aluminium has been found to retain its hardness after heat treatment at 250°C for 12 h.



(a)



(b)

Fig. 4.42 Hardness observed in different conditions for electroless Ni-P-X and Ni-P coatings (a) microhardness and (b) macrohardness.

4.2 DISCUSSION

(a) Synthesis

Electroless coating baths play a major role in the process of coating by controlling the reactions taking place within the bath. This coating process is sensitive to a few parameters including bath temperature, pH, bath loading factor, bath stirring type and its speed and location of specimen with respect to bath container (Gillespie, 1996; Vasudevan, 1998). Apart from the above mentioned parameters, the composite coating is also sensitive to the characteristics of particulate matter made available for coating which in turn get embedded into matrix of the coating. Different properties of the particulate matter viz., type, shape and size, and its catalytic nature are of major concern to the composite coatings (Feldstein, 1983; Apachitei, 1998/1).

In the present investigation, an alkaline hypophosphite electroless nickel bath has been used. Once the electroless process has commenced, the hydrogen evolution starts and continues as the process proceeds, which results in an increase in the acidity of the bath, therefore, the pH reduces. This reduction in pH value is very fast in case of electroless nickel baths, which hinders the consistency in getting the coatings of the same composition (Agarwala, 1987). The co-precipitation of alumina-zirconia takes place in the presence of ammonia (Hong *et al.*, 1998), therefore, the alkaline bath becomes compatible for alkaline bath as used in the present study. It has been observed that, when this reaction take place within electroless nickel bath, performance of the coating bath improves in terms of slow and small change in the pH due to higher concentration of NH_4OH in the composite bath. Therefore, compositionally uniform coatings throughout the volume of the coating are expected.

The in-situ co-precipitation reaction in electroless bath is expected to give Al_2O_3 and ZrO_2 as products of the reaction and at catalytic island, when three atoms of Al and one of atom Zr come in the vicinity of each other it is expected to form an intermetallic compound Al_3Zr . Therefore, such co-precipitation reaction along with electroless Ni-P coating is expected to result in Ni-P-X ($X = \text{ZrO}_2\text{-Al}_2\text{O}_3\text{-Al}_3\text{Zr}$) composite coating. The

work of Hong *et al.* (1998) and Debsikdar (1987) also confirms alumina and zirconia as reaction products through a co-precipitation reaction.

As the finer particles have the natural tendency to float/remain in suspension, the probability of co-deposition of finer particles from all the particles present in the bath is higher than that of the coarser particles. Thus, finer particles (submicron and nanosized) in electroless Ni-P-X deposition are observed to be embedded as can be seen from Figs. 4.14 (b), 4.19 (c), 4.33 (a) and 4.34 (a). Debsikdar (1987) has reported that alumina and zirconia prepared by co-precipitation reaction possess nanosize (about 20 nm) with stringy and amorphous in nature of the material.

Zirconium oxide in form of $(ZrO_{3.5}) \cdot 2.7H$ and Zr_3O_{1-x} , appeared in the powder and both of these oxides of zirconium possesses hexagonal lattice structure. Apart from these, other phases observed such as: nickel zirconium hydride ($NiZrH_3$), aluminium zirconate (Al_3Zr) and sodium aluminium hydride (Na_3AlH_6) as seen from Fig. 4.7 and Table A.3 given in appendix. These phases have appeared due to the reaction of nickel and sodium atoms, with zirconium oxychloride and aluminium chloride within the aqueous bath primarily. However, alumina (Al_2O_3) and nickel phosphide (NiP_2) and zirconium phosphide (Zr_3P_3) were also observed as less common phases, because of small amounts of these phases present in the co-precipitated powder. The phase constituents as identified indicate the existence of hydrates, which possess the cluster forming ability, therefore, it is expected that the coatings may consist of clustered islands along with the fine particles embedded in it. As the systematic study concerned to the processes involved during the in-situ co-precipitation reaction has not been planned in the investigation, the mechanism of formation of different phases and the sequence of reaction taking place are not fully explicable. The cluster forming ability with the coating containing ZrO_2 as seen from Fig. 4.17 may also be responsible for appearance of a few clustered particles in Ni-P-X coatings. Therefore, formation of clusters of Zr rich islands in Ni-P-X coated specimen result as observed from Figs. 4.14 (a), 4.30 (a) and 4.34 (b).

The increase in coating weight by use of in-situ co-precipitation reaction in electroless nickel bath as observed in Fig. 4.1 may be attributed to catalytic nature of the co-precipitation reaction product and embedding of the same in a growing Ni-P matrix. This can also be seen from lesser coating weight observed for Ni-P-X deposit when lower amounts of the co-precipitation reactants are used (i.e., it tends towards the Ni-P alloy coating condition), as shown in Fig. 4.1. Therefore, increase in catalytic nature of the reaction may lead to higher coating rate. As explained earlier, a few hydrate compounds including Na_3AlH_6 and NiZrH_3 also appeared along with oxides of aluminium and zirconium and these hydrates may cause the coagulation of particles, which result in coarser agglomerates of such compounds in the Ni-P-X coatings as seen from Figs. 4.14 (b)-(c), 4.27 (a), 4.28 and 4.34 (b). This may be responsible for relatively more number of zirconium rich areas in the Ni-P-X coating when compared to those for Al rich areas, which could not be noticed predominantly. Therefore, the higher coating weight in Ni-P-X can also be contributed by the embedded clusters of the particles within the Ni-P matrix. The catalytic nature of Al_2O_3 and ZrO_2 has been experimentally confirmed by coating substrate without any pretreatment, i.e., immersing in SnCl_2 and PdCl_2 solutions prior to immersion into the bath. The amount of reaction product obtained in powder form varies with the change in concentration of co-precipitation reactants. The higher coating rate of this composite coating is also because of the co-deposition of these particles. When the co-precipitated powder is present in excess, the increase in coating rate can be ascribed to the reduction reaction that occurs at several places in the bath. However, when the amount of co-precipitated powder available in the bath is higher, the reduction reaction may not necessarily occur on the substrate only, but it may take place at many stray locations within the bath. Higher coating rates in electroless Ni-P based composite coatings than that of Ni-P coatings have also been reported by Feldstein (1983).

The feasible use of in-situ co-precipitation for electroless composite coating as discussed above is expected to be further beneficial if the optimum process parameters are used. Therefore, temperature, pH and coating time for optimum performance of the

process in terms of obtained coating weight are of concern for this study and it is expected that the design of experiment may provide useful evaluation of the process. The effect of these process parameters has been studied by ANOVA technique in the present study and the experimental layout and results are given in Tables 4.3 and 4.4. The electroless composite coating bath having a temperature of 90°C and pH 9.0 is expected to perform in an optimum manner over 45 *min* of coating time as indicated in Table 4.3. In many cases the optimum condition need not be one of the trial runs as observed in present case, therefore, general optimum performance has been calculated for the data given in Tables 4.3 and 4.4 by using following equation (Roy, 1990):

$$Y_{opt} = T_g / N_r (A_1 - T_g / N_r) + (\bar{B}_2 - T_g / N_r) + (\bar{C}_2 - T_g / N_r) \quad (4.3)$$

where T_g = Grand total of all results

N_r = Total number of results

Y_{opt} = Optimum performance in terms of coating weight at optimum variable level, i.e., A_1 , B_2 and C_2 in this case.

\bar{A} , \bar{B} , \bar{C} = Average performance of corresponding variable.

By substituting the values of \bar{A} , \bar{B} and \bar{C} in Eq. (4.3)

$$Y_{opt} = 150 \pm \Delta Y \quad (4.4)$$

where, ΔY is the difference between the optimum and obtained result.

The calculated Y is the result obtained, which is in agreement with experiment type '2', therefore, the operating conditions or process parameters for the same have been considered to be optimum.

The ANOVA results presented in Table 4.4 reveal that pH and time of coating in selected range have predominant effect on the weight of composite coating by this process. This analysis without pooling any factor suggests that the temperature chosen in the two steps of 85°C and 95°C has got minimum contribution on process response,

therefore, this factor was pooled and about 49% contribution of both the pH and the time has been deduced. Once the pH, bath temperature and coating time have been determined, the other parameters selected for study, i.e., the concentration of co-precipitation reaction components and the bath loading factor are of the interest to deal with.

A second order polynomial for determination of coating weight, W , as given in Eq. (4.1) provides the empirical relation between bath loading factor, time and coating weight. In fact as the coating proceeds, the consumption of metal ions reduce the coating rate and this rate is higher for larger areas to be coated, therefore, the coating weight seems to saturate with time. The marginal scatter observed in difference between calculated and experimental coating weight up to $75 \text{ cm}^2/\text{l}$ bath loading factor as shown in Fig. 4.5 may be due to almost the similar coating weight observed in calculated and experimental values.

The uniform coating thickness for electroless Ni-P-X and Ni-P coatings is seen in Figs. 4.8 (a) and (b) respectively. This uniformity can be due to atom by atom deposition of the alloy and fine particles in the coatings, rather than by the bulk of the material deposition onto the substrate. Therefore, the coating layer was found to take the shape of the surface itself, which would not alter the roughness or flatness of the component and the post processing machining or finishing operation is also not needed, this has led to inherent additional credential to electroless coatings (Tromans *et al.*, 1984). A moderately flat surface or an optically flat surface can be obtained in this process, as shown in the SEM spectrograph, i.e., Fig. 4.25 (b-I), indicating the profile of the coated surface along the line as shown in Fig. 4.25 (a). The higher thickness of composite coating is attributed to its higher coating rate observed from Figs. 4.9 (a)-(b) and 4.10. The identical coating conditions in electroless coating are expected to perform in the similar way, therefore, it is not surprising that fairly good reproducibility is achieved as observed from Figs. 4.11, 4.12 and 4.13. The average coating weight for the Ni-P-X coated steel samples has been determined as 59.3 mg and that on aluminium as 54.4 mg . indicating that the values are almost in similar range. The average coating weight of Ni-P deposition on steel substrate

was observed to be 35.8 *mg*. The empirical model developed in this work gives 53.5 *mg* coating weight for Ni-P-X by applying the same conditions against 54.4 and 59.3 *mg* for Ni-P-X coatings on aluminium and steel respectively, which shows a fair agreement between both the calculated and the experimental values.

The higher coating rate of Ni-P-X composite coatings may increase the heterogeneous nucleation sites of the same potential as those created by immersing in SnCl₂ and PdCl₂ solutions on which Ni-P gets deposited atom by atom. Figure 4.10 reveals that the composite coatings commonly possess higher coating rate and the Ni-P-X coating possesses highest coating rate amongst all the three systems, i.e., Ni-P, Ni-P-Al₂O₃ and Ni-P-ZrO₂, investigated under present study. The coating rate in case of Ni-P-ZrO₂ co-deposition is more than that of Ni-P-Al₂O₃. The better catalytic nature of ZrO₂ in the bath may be attributed to the particles which are suspended very near to substrate-solution interface and in due course of time these particles get embedded in Ni-P matrix, as seen in Fig. 4.17. The particles co-precipitated during the reaction are of submicron size, as seen in Fig. 4.6 (a) and large number of such particles which were embedded within Ni-P coating matrix must have acted as the sites for heterogeneous nucleation resulting in high nucleation rates.

(b) Metallographic study

In the electroless coating, several globules nucleate at isolated sites and grow laterally and vertically to cover the entire surface of the substrate. The hemispherical islands grow gradually and cover the substrate area by repeated nucleation and lateral growth. Faster growth in the lateral direction than that in vertical direction results in pore free coating layer as the different molecules occupy the places within the layer. Thus, globular structure of different types of electroless coatings, i.e., Ni-P, Ni-P-Al₂O₃, Ni-P-ZrO₂ and Ni-P-X have been observed as shown in Figs. 4.14 (a)-(b), 4.15 (a), 4.16, 4.17, 4.19 (a)-(b), 4.24 (a), 4.25 (a), 4.29 (a) and 4.30 (a). This mechanism has been observed for both the Ni-P alloy and the Ni-P-X composite coating for all three substrate materials used for this investigation. In composite coatings, the particulate matter available

in the bath gets entrapped in to developing layer (Henry, 1985). This coating mechanism is also evident from the white and round newer nuclei as seen in almost all of the above mentioned figures showing the micrographs for the Ni-P-X composite coating, which can be attributed to the sustained coating reaction for repeated nucleation during development of the layer. A part of the co-precipitated particles available in the bath might have been entrapped in the coating matrix so certain particles were visible at the surface and the others buried beneath. The similar results in terms of coating mechanism of electroless deposition have also been reported by Srivastava *et al.* (1992), Bedingfield *et al.* (1991) and Moonir-Vaghefi *et al.* (1997) for electroless Ni-P, Ni-B and Ni-P-MoS₂ deposits respectively.

A uniform coating layer of about 40 μm thickness and another gray layer along the cross section of the Ni-P-X coating layer, as observed in Figs. 4.20 a-b, indicate coated layer and initial broken layer due to immersion in palladium chloride solution during the sensitisation steps.

Despite the uniform growth of coating due to sustained reaction, the abnormal growth and the cauliflower like fracture of the coating globule has been observed as shown in Fig. 4.15 (b). The local disturbance in the coating bath during addition of ammonia solution followed by mechanical stirring for maintaining the pH can be the principal reason for such globule fracture. The layer development may also be disturbed during stirring of the bath due to entrapment of hydrogen bubbles. Further sustained coating reaction may hinder the growth of newer nuclei of coating thus, resulting in the cauliflower like distorted globule at the corresponding sites.

The coating globules contain many grains, which are nanosized and a few clusters of relatively coarser size, which have been observed in a back scattered image of Ni-P-X coating, as shown in Figs. 4.14 (c) and 4.19 (c). The nanosized grains are also evidenced in Figs. 4.33, 4.34 and 4.35. The nanosized grains with electroless coatings have also been reported in the work of Graham *et al.* (1965) and Hur *et al.* (1990). The data pertaining to coating globule size and its distribution, is shown in Figs. 4.21 and 4.22. These figures

reveal that when Al_2O_3 is present as less common phase in the electroless coating, its average globule size has been observed to be less than when the coating contains ZrO_2 particulate. The growth of globules might be lower due to the presence of Al_2O_3 , but such lowering of growth has not been observed in the coatings containing ZrO_2 . The difference between average globule size in Ni-P- ZrO_2 and Ni-P-X deposition indicates that the presence of Al_2O_3 results in growth retardation more predominantly than in ZrO_2 , which can be ascribed to smaller globules observed in Ni-P- Al_2O_3 coatings especially in the particle rich region as featured in Fig. 4.16 while the globule size in the particle deficient region is relatively higher. This can be attributed to agglomeration of these particles as seen in the TEM image shown in Fig. 4.34 (b). Similarly, observation with Fig. 4.17, for Ni-P- ZrO_2 coating, did not show any significant variation of globule size within it. Scatter in the globule size distribution for the coatings obtained by co-deposition (Figs. 4.16 and 4.17) can be attributed to the preferential grain refinement in the regions where co-deposited particles are situated. As the $\text{ZrO}_2/\text{Al}_2\text{O}_3$ particles, which added from outside were of less than $45 \mu\text{m}$ size are seen in the micrograph. Similarly, when the particles are formed by in-situ co-precipitation the presence of Al_2O_3 results in smaller globule size compared to Ni-P and Ni-P- ZrO_2 coatings as evidenced in Fig. 4.22. However, the submicron size particles/clusters could not be differentiated significantly under SEM owing to their smaller size embedded into Ni-P matrix. Lanzoni and Martini (2000) reported that the dispersion of SiC particles in electroless Ni-P coatings acts as grain refiner.

It is a fact that phosphorus atoms get into the lattice of nickel and uniform concentration of P in Ni can be obtained within the electroless deposits in terms of different nickel phosphite (Ni_xP_y) phases. The co-deposition of particles into Ni-P matrix gives the composite coating (Apachitei *et al.*, 1998/1; Bozzini *et al.*, 1999; Narayan and Pandey, 1997 and Feldstein *et al.*, 1983). The various methods used are expected to provide the confirmation of different elements present in the Ni-P-X coatings as expected from the in-situ co-precipitation of alumina and zirconia within the electroless nickel bath.

Examination of Ni-P-X coating surface carried out reveals the globular structure with embedded composite matter (powder prepared by co-precipitation reaction) and it results in a few clustered islands of the particles also as explained in earlier paragraph. The different qualitative analysis methods like XRF, SEM-EDAX, SEM spectrography along a line, point analysis by EPMA and X-ray mapping by EPMA give the elemental contents in the material. All of the above mentioned tools have been used in the present investigation to identify and confirm the composition and phases present in the newly developed Ni-P-X coating system under this study. The presence of different elements, viz., Ni, P, Al and Zr has been evidenced in the results of these analyses as can be observed from Figs. 4.23 (a)-(d), 4.24 (a)-(b), 4.25 (a)-(b), 4.26 (a)-(b) and 4.27 (a)-(e). The presence of O (oxygen) has also been observed in SEM-EDAX area analysis (Fig. 4.24) and SEM spectrographic analysis (Fig. 4.25). Predominant peaks for Ni and P in Figs. 4.23 (a), 4.24 (b), 4.25 (b-VI) and 4.26 (a) are attributed to higher amounts of Ni and P in the coating, which are found to be about 90.5 wt.% and about 9.5 wt.% respectively as obtained by SEM-EDAX results by scanning through the three different areas as shown in Figs. 4.28 (a), (b) and (c) and reported in Table 4.5. The Zr rich regions have been evidenced in Fig. 4.30 (a), which can be ascribed to embedding of the clustered particles during in-situ co-precipitation reaction used. Hence it is expected that the coating under study may contain a few Zr rich points and a few Zr deficit areas but the micrographic studies as explained earlier reveal that the distribution of these elements within the respective areas are uniform. The Zr rich area can be seen through X-ray scanning by EPMA as shown in Fig. 4.27 (e). From the SEM-EDAX point analysis as reported in Figs. 4.29 (a)-(b) and 4.30 (a)-(b), one can observe higher amount of Al at the points of higher concentration of Zr, which has been evidenced in both the Ni rich points and the Zr rich points. In the area analysis as shown in Fig. 4.24 (b-I), the insignificant peaks for O (oxygen), Zr and Al can be attributed to Zr deficit region as explained above, but in the similar analysis with other areas as seen in Fig. 4.24 (b-II, III and IV), relatively clear peaks indicate the presence of these elements. The peaks occurring due to the presence of O K_{α} , Zr L_{α} , Zr K_{α} , and Al K_{α} , along the line of 10.84 μm as shown in

Fig. 4.25 (a) can also provide the evidence of these elements even if these are present in small fractions. SEM-EDAX area analysis shows 0.16 wt.% and 0.21 wt.% of Al and Zr respectively as reported in Table 4.5. The presence of O (oxygen) in the coating is expected to form the oxides of aluminium and zirconium, therefore, quantitative analysis by EPMA by using oxide correction has been conducted and it is found that Al_2O_3 and ZrO_2 are present in 0.17 wt.% and 0.23 wt.% amounts respectively. As explained earlier in Zr rich areas relatively higher amount of Al also occurs as seen from Figs. 5.29 (b) and 5.30 (b) and as mentioned earlier, when three atoms of Al and one atom of Zr come in contact on the catalytic island, stoichiometric intermetallic compound, Al_3Zr forms. Hence, this can be ascribed for the presence of Al_3Zr as one of the phases constituents identified by X-ray diffraction studies of the Ni-P-X coatings as reported in Tables A.6 to A.9.

The X-ray diffraction patterns for different materials are helpful in explaining the structure and phase constituents present in it. The electroless coatings possess the glassy structure and in electroless Ni-P based coatings, its structure in as-coated condition is directly influenced by phosphorus content. The amorphous nature of the coating has been observed with the increasing phosphorus content (Agarwala, 1987; Hur *et al.*, 1990). The X-ray diffraction patterns of as-coated Ni-9%P-X and Ni-9.5%P films are compared, the former shows a few peaks more than that for latter, which may be attributed to the basic difference in bath compositions used for the synthesis. The nature of the peak seen in the above figures may be attributed to its microcrystalline/amorphous nature and embedded particles of composites into Ni-P matrix might have caused a few extra peaks in Ni-P-X deposit that are not seen in the Ni-P film. It is also observed that the in-situ co-precipitation reaction not only evidenced the peaks for Al_2O_3 and ZrO_2 but also Al_3Zr . Small amounts of these compounds present in the coatings may be responsible for the corresponding peaks with relatively less intensity. The nature of the X-ray diffraction pattern obtained for Ni-P as-coated film and the crystalline nature of the heat treated film consisting of Ni_3P phase as resulted in this work is in agreement with the work of Park and Lee (1988),

Balaraju and Seshadri (1999), Apachitei *et al.* (1998/2), Bozzini and Cavallotti (1997), Zhang *et al.* (1998/1) and Vasudevan *et al.* (1998).

Further, in view of confirming this microcrystalline Ni phase in the matrix of the coating the TEM study could be helpful. Growth of these Ni crystals are seen to a grown size of about 10 nm islands as seen in Figs. 4.33 (a) and (b), which may be attributed to particles in Ni-P-X coating while in another area, the cluster of particles in form of an island of about 200 nm can be observed in Figs. 4.34 (a) and (b). The SAD patterns for these areas as shown in Figs. 4.33 (c) and 4.34 (c) reveal the diffused rings along with a few spots that may be due to nanosized grains of a polycrystalline material. The phase constituents identified in X-ray diffraction and SAD patterns for the Ni-P-X as-coated film are found to be in agreement with each other as given in Tables A.5 and A.7 that confirms the presence of Ni microcrystalline as a common phase and other less common phases like: Ni₁₂P₅, Ni₅P₂, Ni_{-2.55}P, Ni₃P, Al₃Zr, Al₂O₃, ZrO₂ and Ni (am). Similarly, the occurrence of a broad peak in the Ni-P as-coated deposit may be because of presence of microcrystalline Ni as a common phase and other less common phases like Ni₁₂P₅, Ni₅P₂, Ni_{-2.55}P, NiP₂, and Ni (am), which is confirmed by X-ray diffraction analysis and TEM. From Figs. 4.33 to 4.35 it is revealed that within the amorphous phase fine Ni crystals of about 10 nm are nucleated uniformly throughout the matrix. Fine Ni crystals coagulate to form bigger Ni crystals and at certain regions microcrystalline Ni is also found to be present. The above study of as coated Ni-9wt.%P-X coating by both the TEM and the X-ray diffraction revealed that the addition of second phase particles within the Ni-9.5 wt.%P matrix reduces phosphorus content of composite coating even after carrying the coating at same temperature and pH. Despite the fact that structure of electroless coating is sensitive to phosphorus content, its reduction by about 0.5 wt.% does not change the structure of the coating. The reduction of phosphorus content due to co-deposition of particulate matter in the coatings has also been reported by Li *et al.* (1996). The work of Agarwala and Ray (1989), Hur *et al.* (1990) and Bozzini and Cavallotti (1997) reveals that in the range of 9-11 wt.% P the coatings show the microcrystalline nature, which is in agreement with the results of the present study.

It has been established that heat treatment causes definite structural changes in the different phases of Ni_xP_y of as-coated film by transforming them to an intermetallic, Ni_3P , phase (Agarwala and Ray, 1988; Hur *et al.*, 1990). The amorphous to crystalline transformation in as-coated electroless coating occurs at moderate temperature between $240-400^\circ C$ (Mahoney and Dynes, 1985). Therefore, the X-ray diffraction studies on Ni-9wt.%-P-X are carried out after heat treating at $400^\circ C$ for 1 h, $400^\circ C$ for 2 h and $250^\circ C$ for 12 h with the expectations that different phases of Ni_xP_y and microcrystalline Ni transform to Ni_3P and crystalline Ni respectively. The X-ray diffraction analysis for Ni-9 wt.% P-X reveals that heat treatment at $400^\circ C$ for 1 h causes the transformation of microcrystalline Ni to crystalline Ni and other less common phase $Ni_{-2.55}P$ to Ni_3P but a few phases like $Ni_{12}P_5$ and Ni_5P_2 may remain amorphous in some pockets as reported in Fig. 4.36 and Table A.8. The transformation begins with formation of transition phases like Ni_5P_4 , Ni_2P followed by transformation to Ni_3P phase. The transition phase $Ni_{12}P_5$ may be attributed to presence of microcrystalline Ni in as-coated condition while the presence of Ni_5P_2 can be ascribed to insufficient temperature or holding time for complete crystallisation. This can be an indication of the presence a few pockets of intermediate metastable phases in the composite coating even after heat treatment at $400^\circ C$ for 1 h. After heat treatment at $400^\circ C$ for 2 h, Ni_5P_2 phase has been observed to transform in to Ni_3P as can be seen from Table A.9 given in appendix, however, $Ni_{12}P_5$ phase appears in the composite coating even after the heat treatments as mentioned above. Similarly, when the Ni-P-X composite coating is heat treated at $250^\circ C$ for 12 h the transformation of microcrystalline Ni to crystalline Ni and other less common phase $Ni_{-2.55}P$ to Ni_3P occurs but a few phases like $Ni_{12}P_5$ and Ni_5P_2 may remain amorphous in some pockets as reported in Table A.9 given in appendix. The incomplete transformation can be ascribed to the presence of intermediate transition phases like $Ni_{12}P_5$ and Ni_5P_2 . Therefore, in Ni-9 wt.% P-X electroless composite coatings, none of the above mentioned heat treatments result in complete transformation to crystalline Ni and Ni_3P . Such transient formation of metastable phases has also been reported by Masumoto and Maddin (1975). In the work of Bakonyi *et al.* (1986), Hur *et al.* (1990) and Agarwala and Ray (1992), complete

crystallisation has been referred to as transformation to Ni crystalline and Ni₃P. The presence of Ni₁₂P₅ in Ni-9.5wt.%P film has been attributed to microcrystalline Ni in as-coated condition as reported by Agarwala and Ray (1988), which is in agreement with the results of this investigation.

Suitable heat treatment to electroless coatings can tailor the properties to suit the specific applications. The effect of heat treatment in terms of transformation of different phases has already been explained. The changes may alter the microstructure also, therefore, it is planned to examine the microstructure of Ni-P-X coatings after heat treatment and the relevant SEM micrographs are shown in Figs. 4.18 (a)-(c) and 4.19 (a)-(c). The heat treatment results in flattening of coating globules as commonly observed in above mentioned figures. The extent of globule flattening due to heat treatment at 400°C for 2 h is found to be more as compared to that with other two heat treatments, which can be attributed to coarser globules as seen from Fig. 4.18 (b). The rate of this precipitation may result in the formation of a void or crack near the globule boundary as shown in Fig. 4.19 (b). This may be attributed to change in specific volumes of constituent phases during transformation of Ni_xP_y to Ni₃P and also due to the evolution of hydrogen bubbles, which may be existing over the sub-surface of coatings. The bright spots observed in Fig. 4.19 (a) may be attributed to the precipitation of Ni₃P. When Ni-P coating is heated above 220-320 °C, structural changes begin to occur and at temperatures above 320°C, the deposit begins to crystallise and loses its amorphous character; with continued heating, nickel phosphite particles conglomerate and a two-phase alloy forms (Baudrand, 1994). So far it is established that heat treatment of Ni-P coatings at 400°C for 1 h provides complete transformation to crystalline Ni and Ni₃P of the coating as reported in the literature. (Agarwala and Ray, 1992 and 1988; Hur *et al.*, 1990).

In fact the crystallisation of metallic glass is a highly exothermic process and DSC has been widely used for crystallisation studies of electroless Ni-P coatings as reported in the literature including the work of Allen *et al.* (1992), Mohoney and Dynes (1985), Criado and Ortega (1987) and Hur *et al.* (1990). The size or area under DSC exothermic

peaks is indicative of energies associated with atomic processes because area under the peak is directly proportional to the enthalpy change associated with the process involved. When a single broad peak appears in the DSC curve, complete crystallisation occurs at the peak temperature (Hur *et al.*, 1990). The maximum energy of the exothermic reaction obtained has been attributed to the crystallisation of the amorphous phase into Ni₃P and crystalline Ni (Apachitei *et al.*, 1998/1). In this investigation, the Ni-P-X and Ni-P coatings have been subjected to thermal changes for different heating rates of 10, 15, 20 and 25 °C/min in a differential scanning calorimeter and the study was planned for determination of kinetics parameters, i.e., activation energy, E and reaction exponent, n by using Kissinger analysis. As shown in Figs. 4.37 and 4.38 (a)-(d), the single broad peak observed exhibits the exothermic nature. The single broad peak may be due to irreversible reaction, as no peak was observed during cooling. Higher temperature, T_m , of peak for Ni-P-X coatings compared to that for Ni-P coatings as shown in Figs. 4.37 and 4.38 and Table A.10 may be ascribed to the presence of X into the Ni-P matrix. As the heating rate, β is increased, T_m also increases with the increase in area under peak, which can be evidenced from Figs. 4.37 and 4.38. Any reaction involving transformation of parent phase to product phase can be considered to be an atomic process and because of presence of Al₂O₃, ZrO₂ and Al₃Zr this process may be retarded and may need more energy for transformation. The slope of Kissinger plot as shown in Fig. 4.39 gives the apparent activation energy, E_a and as explained earlier, using this value of apparent activation energy, E_a , value of actual activation energy, E , can be calculated using Eq. (2.24) on substitution of value of constant C_1 , which is derived from the data presented in Table 2.5 from the work of Criado and Ortega (1987). E_a is independent of temperature, this would simply yield an exponential kinetic equation. However, E_a is not likely to be a constant, but it should increase with time as the structure becomes more relaxed (Guntherodt and Beck, 1981). The slope of plots shown in Figs. 4.40 (a)-(d) gives the parameter nE and therefore, the exponent, n , can be calculated. It is observed that the value of n for Ni-P-X is lower than that for the Ni-P coatings, which may be attributed to lower growth rate during the transformation during the atomic reaction involved. Therefore, the presence of

Al_2O_3 , ZrO_2 and Al_3Zr in the composite coating can be primarily responsible for lower values of n commonly observed at all the heating rates in-between $10\text{ }^\circ\text{C}/\text{min}$ to $25\text{ }^\circ\text{C}/\text{min}$. The values of Avrami exponent, n at $15\text{ }^\circ\text{C}/\text{min}$ and $25\text{ }^\circ\text{C}/\text{min}$ have been found to be 3.77 and 3.17, which are abnormally higher and this can be ascribed to change in fraction transformed, α , due to relatively less height of the peak at these temperatures. The presence of even a few islands of dissimilar particles at localised area where, the atomic reaction is taking place may change the reaction path. Thus, it is primarily responsible for higher energies associated with Ni-P-X coatings. Therefore, the variation in value of Avrami exponent, n in the Ni-P-X coatings may be due to localised dissimilarity in composition of coating in terms of the composite, X, content. As explained earlier such variations have also been pointed out in qualitative analysis of different elements present in the Ni-P-X coating. The activation energy is sensitive to T_m and α and it is the measure of transformation rate, e.g., for faster transformation lower activation energy has been observed.

The activation energy for Ni-P-X composite coatings has been observed to be almost double than that for Ni-P alloy coating, this may be ascribed to more predominant peaks at relatively lower temperatures ($342\text{-}378^\circ\text{C}$) in Ni-P coatings as compared to relatively less predominant peaks at higher temperatures ($395\text{-}410\text{ }^\circ\text{C}$) in the Ni-P-X coatings. The activation energy does not change significantly due to increase in heating rate and it can be attributed to almost consistent E/RT value in electroless coatings as observed in Fig. 4.41. The higher activation energy may have resulted due to higher value of E/RT in Ni-P-X coatings.

The higher hardness is a major additional source of interest with electroless Ni-P based coatings and that can be further enhanced to almost double by appropriate heat treatment. Such enhanced hardness due to heat treatment of electroless Ni-P based coatings have invariably been reported by many of the research workers including: Mallory (1980), Gawne and Ma (1987), Strafford *et al.* (1990), Mai *et al.* (1988), Baudrand (1994), Li (1997), Apachitei *et al.* (1998/1), Zhang *et al.* (1998/1) and Balaraju

and Seshadri (1999) and also have shown that heat treatment at 400°C for 1 *h* provides maximum hardness to electroless Ni-P coatings, which is irrespective of phosphorus content. Apachitei *et al.* (1998/1) have reported that the microhardness of composite coating does not strictly depend on microhardness of embedded particles. The higher microhardness obtained after heat treatment in both the Ni-P alloy and the Ni-P-X composite coatings may^{be} primarily due to precipitation of hard intermetallic compound, Ni_3P . The variation in microhardness and macrohardness values in different conditions for the different samples investigated are shown in Figs. 4.42 (a) and (b) respectively. The microhardness in Ni-P-X as-coated steel increases due to heat treatment at 400°C for 1 *h*, but when it is heat treated at 400°C for 2 *h*, the hardness has been observed to be relatively less. Similar results have been observed in Ni-P-X coated aluminium and Ni-P coated steel, which also reveal the increase of hardness, reaching to the maximum and further decrease. The maximum hardness of coated samples after heat treating at 400°C for 1 *h* can be ascribed to crystallisation of Ni_xP_y phases in to Ni_3P phase. The decrease in hardness due to continued heat treatment at 400°C till 2 *h* can be ascribed to coarsening of the globules. The maximum hardness of coating obtained after heat treatment at 400°C for 1 *h* is in agreement with the literature as mentioned earlier in the paragraph. The decrease in hardness of Ni-P coated sample at this temperature beyond 1 *h* has also been reported by (Baudrand, 1994; Mallory, 1980). Similar results with electroless Ni-B coatings have been reported by Bedingfield *et al.* (1991). The composite component, X, also contributes to increase in hardness of Ni-P-X coatings as explained earlier and the better compatibility of steel with nickel may be responsible for higher hardness with steel substrate when compared to that of aluminium. The heat treatment at 250°C for 12 *h* of Ni-P-X coated aluminium sample results in marginally less hardness (1034 HV_{100}) than that heat treated at 400°C for 2 *h* with steel substrate (1080 HV_{100}). Relatively less hardness of Ni-P coatings due to heat treating in the temperature range $200\text{-}300^{\circ}\text{C}$ has also been reported by Baudrand (1994). The different phases present possess different hardness and may be responsible for the variation in the standard deviation. Therefore, relatively the higher

value of standard deviation with Ni-P-X coated specimens are observed when compared to those in Ni-P coated samples.

The indentation depth during macrohardness measurements on the coated samples may be higher than the thickness of the coating, thus, the hardness of the substrate also plays a role as depicted from the presented results in Table A.11 given in appendix. Therefore, when the hardness of the substrate is retained during heat treatment it is expected that the similar hardnesses could be obtained even after heat treatments. Thus, it is not surprising that relatively lower hardness of coated and heat treated (400°C for 1 h) aluminium samples has been observed when compared to those in the steel substrates. This result obtained in the present study is in agreement with the work reported by Apachitei *et al.* (1998/1). Aluminium substrate is found to be sensitive to change in hardness due to heat treatment at 400°C for 1 h (Apachitei, 1998/2); and as expected steel substrate do not show any change in hardness due to heat treatment in the temperature range selected for this study.

**FRICITION AND WEAR BEHAVIOUR OF ELECTROLESS
Ni-P-X AND Ni-P COATINGS ON STEEL**

Electroless Ni-P-X ($X = \text{ZrO}_2\text{-Al}_2\text{O}_3\text{-Al}_3\text{Zr}$) and Ni-P coatings on steel substrate have been heat treated at 400°C for 1 *h* and at 400°C for 2 *h* in order to arrive at the desirable heat treatment for achieving better tribological properties under dry sliding friction and wear against the counterface of case hardened steel. The normalised steel specimens as-coated with Ni-P-X, heat treated after coating, at 400°C for 1 *h* and at 400°C for 2 *h* are designated as AC₁, HT₁-A and HT₂-A respectively. The same steel as-coated with Ni-P, heat treated after coating, at 400°C for 1 *h* and at 400°C for 2 *h* are designated respectively as AC₂, HT₁-B and HT₂-B. The normalised steel pins as such without any coating are given the designation NS. The primary objective of the study is to understand the effect of the nature of coating and its heat treatment on the dry sliding friction and wear behaviour of coated steel pins. The results have been discussed to develop a coherent understanding of the tribological behaviour of coated steel in terms of the composition of the coating, the changes taking place during heat treatment and their consequence on tribological properties in the context of changes observed in the hardness and the mechanical properties.

5.1 RESULTS

Dry sliding wear tests have been carried out against hardened steel counterface at the constant sliding speed of 0.5 *m/s* under different normal loads of 29.4, 34.3 and 39.2 *N*, by using pin-on-disc wear testing machine as described in chapter 3. The steel pin samples coated with electroless deposition of Ni-P-X and Ni-P, and those heat treated after Ni-P-X or Ni-P coatings at 400°C for 1 *h* have been tested for cumulative wear volume, wear rate, wear coefficient and coefficient of friction under the specified loads and the sliding velocity.

In addition, steel samples coated with Ni-P-X and Ni-P have been heat treated at 400°C for 2 h and tested for the same properties under the same sliding conditions. The results obtained are also compared with those observed for normalised steel (NS) pin samples that are used as the substrate material for coating in this segment of study. In order to confine the wear within the coating, sliding distances for a given load with different types of pin wear samples have been limited on the basis of preliminary studies in respect of volume loss behaviour and micrographic observations. For a load of 29.4 N, the variation in the volume loss in wear for different Ni-P-X coating thickness obtained at different coating times show sudden change in slope at specific sliding distances as shown in Fig. 5.1. Microscopic observations indicate that the change in slope is associated with the progress of volume loss from coating into the steel substrate of the pin. Figure 5.2 shows the variation of limiting sliding distance with coating time if wear is to be confined into coating primarily. The above experimental result has been extended for Ni-P coating on steel samples by considering the weight loss data observed in Ni-P-X coating on steel such that the wear is confined in the coatings. The limiting sliding distance selected on the basis of the above study for different types of wear pin samples at loads of 29.4, 34.3 and 39.2 N are given in Table 5.1.

Table 5.1 The Sliding Distances Selected for Different Types of Wear Pins (NS, AC₁, HT₁-A, HT₂-A, AC₂, HT₁-B and HT₂-B) for the Tests under Different Loads.

Sl. No.	Designation of the Wear Sample	Sliding Distance (<i>m</i>) as Selected for the Load (<i>N</i>)		
		29.4	34.3	39.2
1.	NS	480	480	480
2.	AC ₁	300	300	150
3.	HT ₁ -A	600	420	300
4.	HT ₂ -A	600	300	150
5.	AC ₂	240	240	150
6.	HT ₁ -B	540	420	300
7.	HT ₂ -B	420	420	150

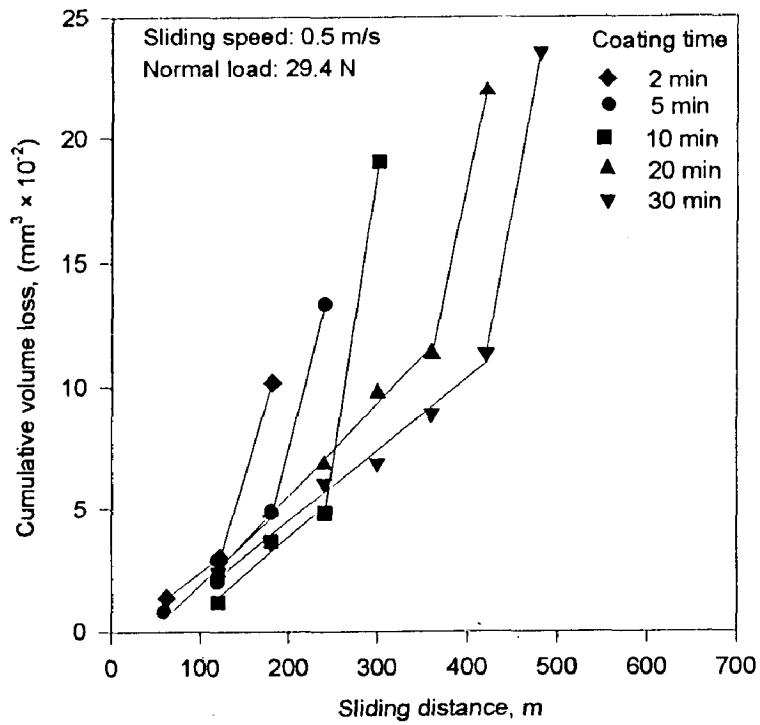


Fig. 5.1 Cumulative wear volume with sliding distance at 29.4 N load in electroless Ni-P-X coatings on steel for different coating times.

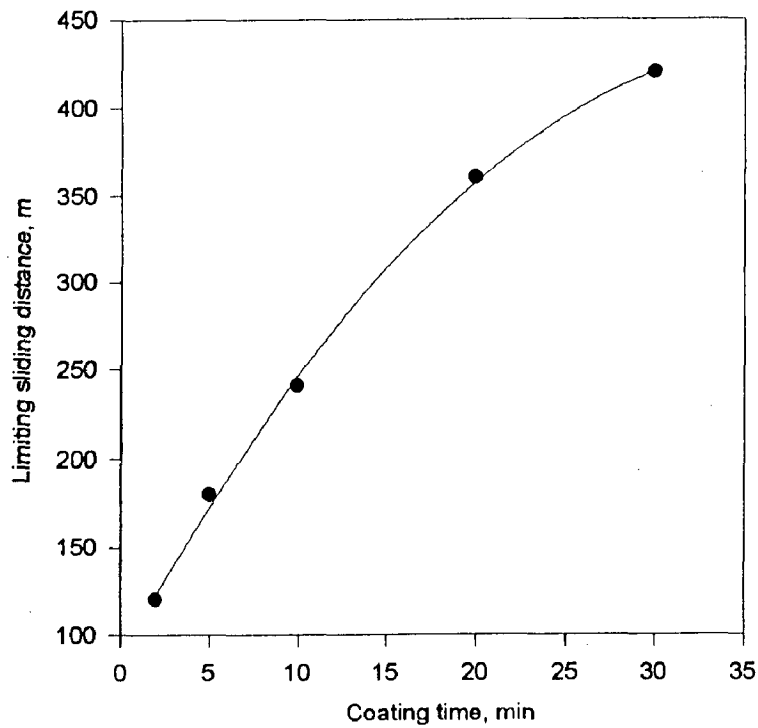


Fig. 5.2 Variation of limiting sliding distance with time at 29.4 N load in electroless Ni-P-X coatings on steel.

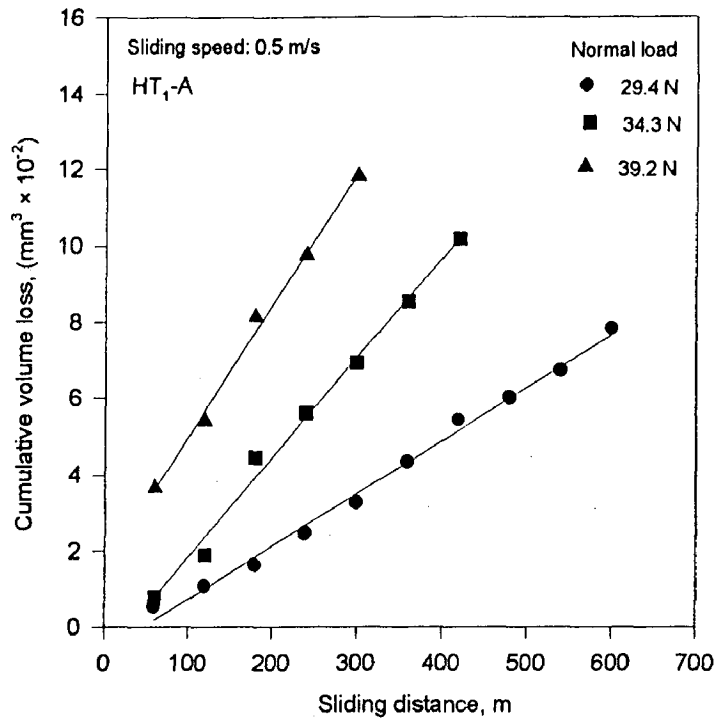


Fig.5.5 Cumulative wear volume with sliding distance at different loads in electroless Ni-P-X coated and heat treated at 400°C for 1 h specimens (HT₁-A).

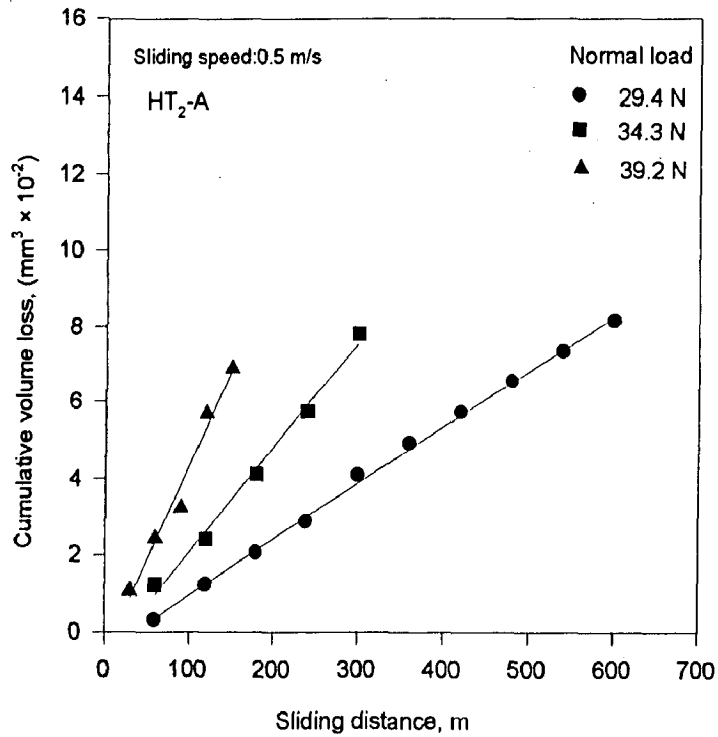


Fig. 5.6 Cumulative wear volume with sliding distance at different loads in electroless Ni-P-X coated and heat treated at 400°C for 2 h specimens (HT₂-A).

Figure 5.7 shows the variation of cumulative volume loss with sliding distance of as-coated Ni-P steel pin (AC_2) samples during dry sliding wear. Similar to Ni-P-X coated steel (AC_1), the cumulative volume loss of Ni-P coated steel (AC_2) also increases linearly with sliding distance. The increasing load also increases the cumulative volume loss. The cumulative volume loss of AC_2 increases from $3.81 \times 10^{-2} \text{ mm}^3$ to $5.7 \times 10^{-2} \text{ mm}^3$ when the load increases from 29.4 to 34.3 N for 120 m sliding. At the highest load of 39.2 N , the volume loss in wear is found to be $8.9 \times 10^{-2} \text{ mm}^3$ after sliding through the same distance. This data reveals that the Ni-P coated steel (AC_2) shows higher wear volume than Ni-P-X coated steel (AC_1) although the volume loss of AC_2 is substantially lower than that for the steel substrate (NS) as mentioned in above paragraphs.

Figure 5.8 represents the variation of cumulative volume loss with sliding distance for Ni-P coating on steel pin samples heat treated at 400°C for 1 h (HT_1-B) during dry sliding. The cumulative volume loss increases linearly with increasing sliding distance and also with increasing load. Figure 5.8 reveals that for the loads of 29.4 and 34.3 N , the cumulative volume losses after sliding through 120 m , are found to be $1.69 \times 10^{-2} \text{ mm}^3$ and $2.54 \times 10^{-2} \text{ mm}^3$ respectively. But at the load 39.2 N , the cumulative volume loss increases relatively faster and its value is found to reach as high as $7.2 \times 10^{-2} \text{ mm}^3$ after sliding through the same distance. The cumulative volume loss in Ni-P coating heat treated at 400°C for 1h is less than that observed in the substrate as such (NS) as well as with Ni-P coating on steel (AC_1) at any sliding distance under the different loads employed in this investigation.

Variation of cumulative volume loss with sliding distance for the Ni-P coated steel pin samples after heat treatment at 400°C for longer period of 2 h (HT_2-B) during dry sliding is shown in Fig. 5.9. The cumulative volume loss increases linearly with sliding distance for different loads as seen in Fig. 5.9. At the load of 39.2 N , the volume loss is found to be $7.8 \times 10^{-2} \text{ mm}^3$ after sliding through only 120 m distance, which is substantially larger than that observed at relatively lower loads of 34.3 and 29.4 N having the corresponding values of $3.0 \times 10^{-2} \text{ mm}^3$ and $2.1 \times 10^{-2} \text{ mm}^3$ respectively. This experimental data reveals that the HT_2-B type of pins show relatively higher wear volume than HT_1-B

type of samples but substantially lower than that for NS type of pins as mentioned in earlier paragraphs for all the loads employed in entire range of sliding distance covered.

Wear rate is defined as the wear volume loss per unit sliding distance. Therefore, the slope of the cumulative volume loss with increasing sliding distance plots has been used to determine the wear rate. The primary objective of this part of study is to determine the wear rate of Ni-P-X coating on steel pin samples with and without heat treatment, i.e., AC₁, HT₁-A and HT₂-A, during dry sliding wear against hardened steel counterface at constant sliding speed of 0.5 *m/s* under the applied normal loads of 29.4, 34.3 and 39.2 *N*. This study also includes the determination of the wear rate of Ni-P coated steel pin samples under similar conditions as mentioned above for Ni-P-X coating on steel pin samples in order to understand the capability of X (ZrO₂-Al₂O₃-Al₃Zr) in improving wear resistance. The experimental results obtained are compared with that of normalised steel (NS) pin samples under the similar loads of 29.4, 34.3 and 39.2 *N*. Figure 5.10 demonstrates the variation of wear rate of as-coated Ni-P-X steel pin (AC₁) samples for applied load of 29.4 *N* during dry sliding wear test for the coating of different thickness obtained after coating time of 2, 5, 10, 20 and 30 *min*. The wear rates observed are fairly reproducible with a standard deviation of ± 0.43 for AC₁ samples.

Variation of wear rate with applied normal load in different types of wear pins during dry sliding wear has been shown in Fig. 5.11. Wear rate is found to increase with load for different wear pins. The wear rates at a given load and the deviation from linearity are decreasing for NS, AC₁, HT₁-A and HT₂-A types of pins. Wear rate for the substrate steel has been observed to be the highest when compared to any of the Ni-P-X coating on steel in either as-coated or heat treated conditions. The wear rate of AC₁ type of pins has been observed to be substantially lower than that of substrate steel (NS), and it decreases further on heat treatment. Increasing heat treatment time from 1 *h* to 2 *h* does not decrease the wear rate as observed from the wear rates of HT₁-A and HT₂-A samples which are similar at the loads of 29.4 and 34.3 *N*. At higher load of 39.2 *N*, the wear rate of HT₂-A is relatively larger compared to that in HT₂-A indicating deterioration of wear resistance with longer heat treatment.

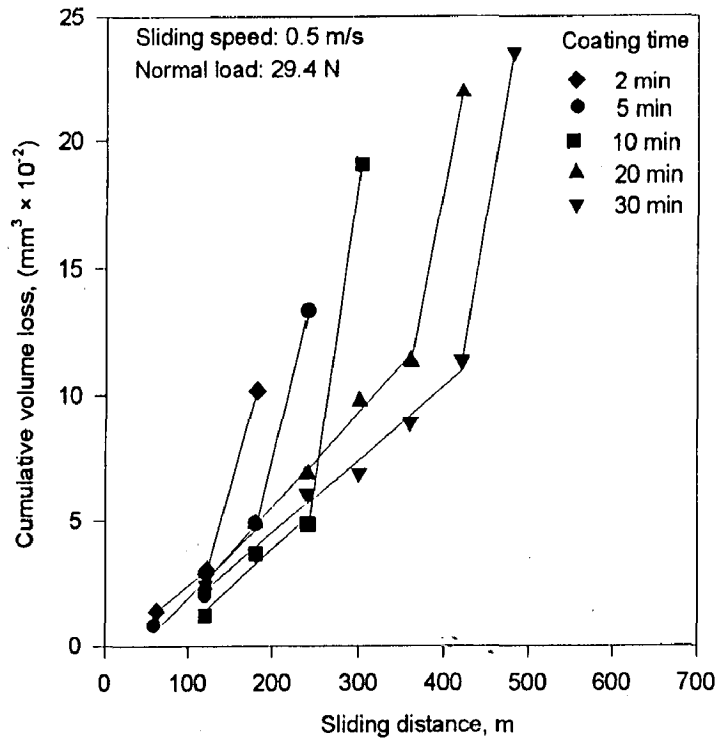


Fig. 5.1 Cumulative wear volume with sliding distance at 29.4 N load in electroless Ni-P-X coatings on steel for different coating times.

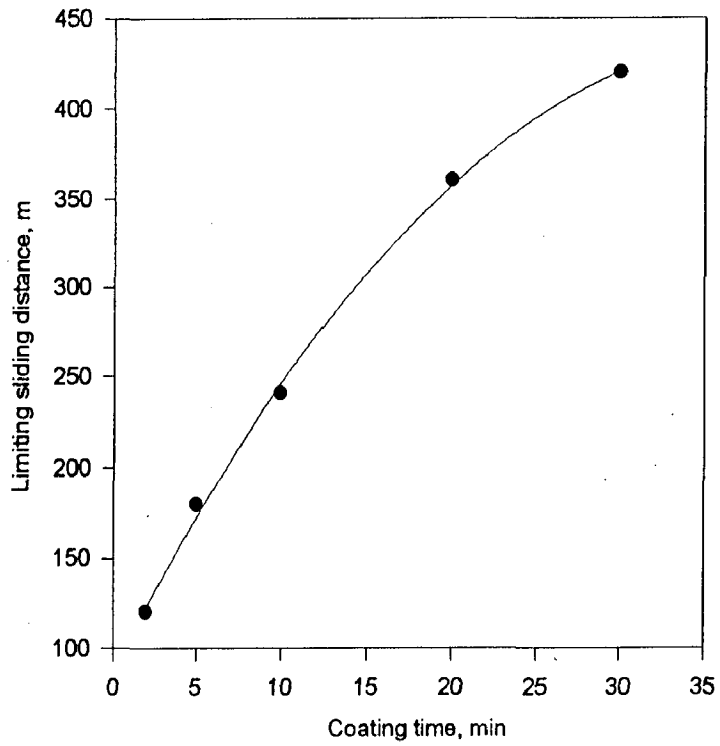


Fig. 5.2 Variation of limiting sliding distance with time at 29.4 N load in electroless Ni-P-X coatings on steel.

5.1.1 Dry Sliding Friction and Wear Behaviour

(a) Wear behaviour

The cumulative volume loss under dry sliding wear is a functional parameter in worn out engineering components. Therefore, it has been computed for each of the data points and variation of cumulative volume loss with increasing sliding distance, plotted at different normal loads. The firm lines in the plot represent the linear least square fit of the variation of cumulative volume loss with sliding distance.

Variation of cumulative volume loss with sliding distance for normalised steel (NS) pin samples during dry sliding wear against the counterface of hardened steel is shown in Fig. 5.3. The cumulative volume loss increases linearly with sliding distance. At the given load of 29.4 *N*, the cumulative volume loss increases linearly from $5.5 \times 10^{-2} \text{ mm}^3$ to $46.6 \times 10^{-2} \text{ mm}^3$ when the sliding distance increases from 60 *m* to 480 *m*. Similarly, a linear increase in cumulative volume loss has also been observed for other loads. At a given sliding distance, the cumulative volume losses increase with increasing load, as seen from Fig. 5.3.

Figure 5.4 illustrates the variation of cumulative volume loss during dry sliding in steel pin sample coated with Ni-P-X (AC₁). A linearly increasing cumulative volume loss with sliding distance has been commonly observed for all the three different loads used for the present investigation. The cumulative volume loss is also observed to increase with increasing applied normal load. The cumulative volume losses of AC₁ at 29.4 and 34.3 *N* loads have been observed to be $3.66 \times 10^{-2} \text{ mm}^3$ and $4.88 \times 10^{-2} \text{ mm}^3$ respectively after 120 *m* sliding and that at 39.2 *N* load is found to be $8.5 \times 10^{-2} \text{ mm}^3$ after sliding through the same distance. The corresponding cumulative volume losses have been observed to be substantially lower than those observed in NS type of pins, which were found to be 10.2×10^{-2} , 14.4×10^{-2} and $28.4 \times 10^{-2} \text{ mm}^3$ respectively for the loads of 29.4, 34.3 and 39.2 *N* after 120 *m* of sliding.

Variation of cumulative volume loss of Ni-P-X coated pin samples of steel and those heat treated at 400°C for 1 h (HT₁-A) during dry sliding is shown in Fig. 5.5. The cumulative volume loss of HT₁-A, while sliding dry against the hardened steel counterface at load of 29.4 N increases linearly with the sliding distance. Similar trends of linearly increasing cumulative volume loss with sliding distance are also observed for other loads of 34.3 and 39.2 N as shown in Fig. 5.5. The wear volume loss is found to be 1.1×10^{-2} , 1.9×10^{-2} and $4.5 \times 10^{-2} \text{ mm}^3$ after sliding through a distance of 120 m at normal loads of 29.4, 34.3 and 39.2 N respectively. These wear volumes are significantly less than those observed for both the NS and the AC₁ types of pin wear samples mentioned in the previous paragraph. The cumulative volume loss in Ni-P-X coating heat treated at 400°C for 1 h (HT₁-A) is less than that observed in the substrate as such (NS) as well as with Ni-P-X coating (AC₁) at any sliding distance under the different loads employed in the investigation.

Variation of cumulative volume loss with sliding distance of Ni-P-X coated pin samples of steel heat treated at 400°C for a longer time of 2 h (HT₂-A), during dry sliding is shown in Fig. 5.6. The linearly increasing cumulative volume loss in wear with sliding distance has been observed under the different loads employed in this investigation as seen from Fig. 5.6. From this figure, the effect of applied load on cumulative volume loss shows that the volume loss in wear increases with increasing applied load for the entire range of sliding distance covered. Cumulative volume loss of 1.2×10^{-2} , 2.4×10^{-2} and $5.7 \times 10^{-2} \text{ mm}^3$ have been observed for different loads of 29.4, 34.3 and 39.2 N respectively, for the sliding distance of 120 m. At lower load of 29.4 N, the wear volume in HT₁-A is found to be $1.1 \times 10^{-2} \text{ mm}^3$ after sliding through 120 m, which is not significantly different than that observed in HT₂-A pin. At higher load of 39.2 N, HT₁-A has shown $4.5 \times 10^{-2} \text{ mm}^3$ wear volume after sliding of 120 m, whereas the corresponding volume loss observed in HT₂-A pin has been found to be $5.7 \times 10^{-2} \text{ mm}^3$. HT₂-A type of pins show a relatively higher volume losses than HT₁-A type of pin samples, particularly at the higher loads and sliding distance at a sliding speed of 0.5 m/s. HT₂-A pins show significantly lower volume loss in wear when compared with AC₁ and NS types of pins.

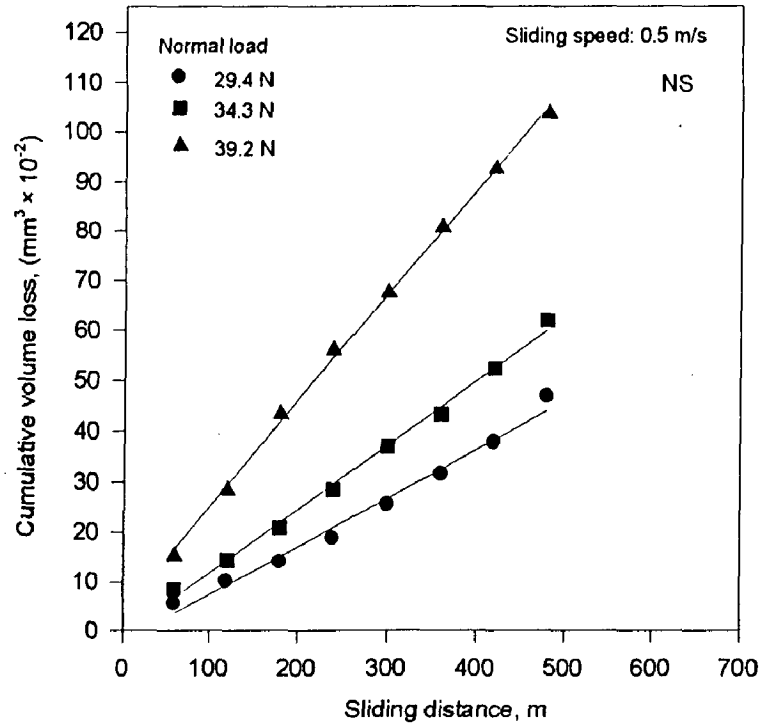


Fig. 5.3 Cumulative wear volume with sliding distance at different loads in normalised steel (NS).

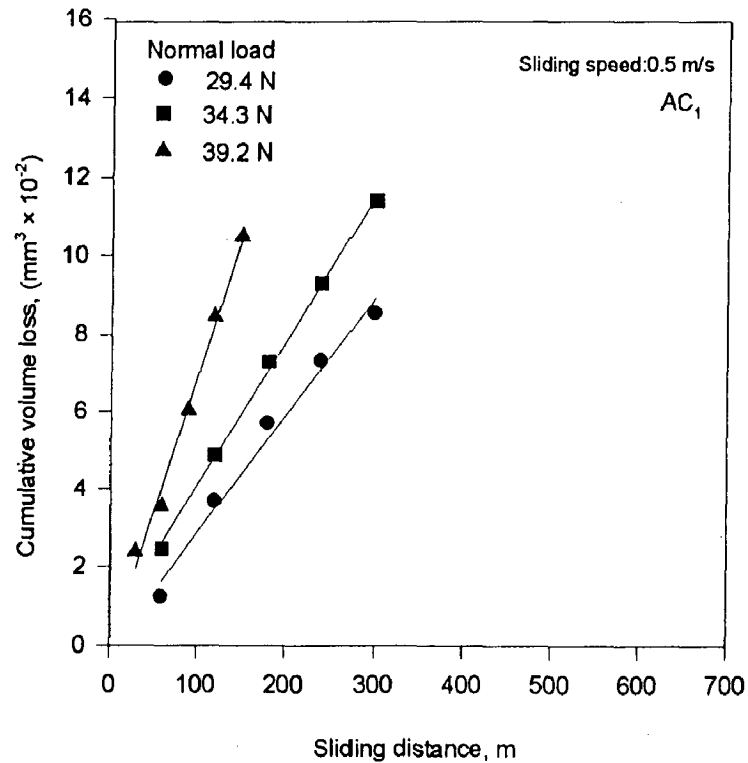


Fig. 5.4 Cumulative wear volume with sliding distance at different loads in electroless Ni-P-X as-coated steel (AC₁).

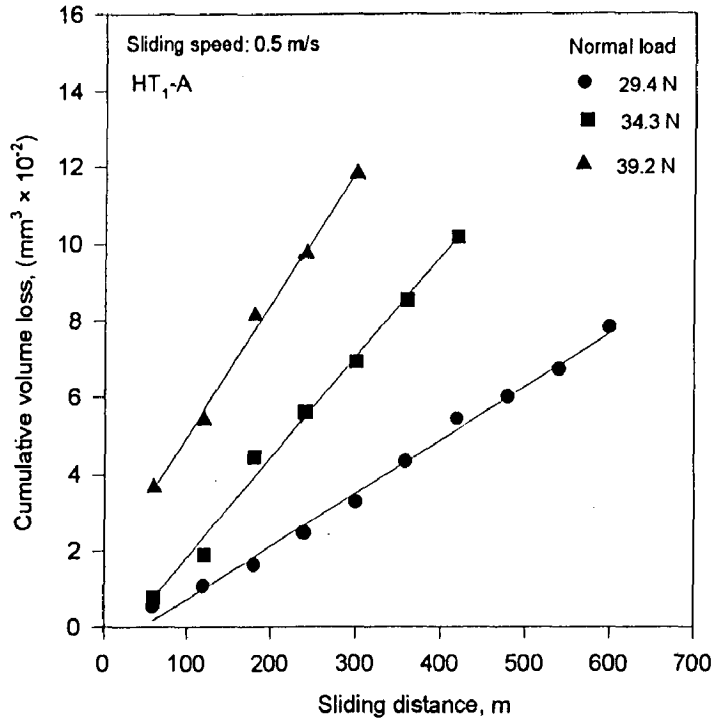


Fig.5.5 Cumulative wear volume with sliding distance at different loads in electroless Ni-P-X coated and heat treated at 400°C for 1 h specimens (HT₁-A).

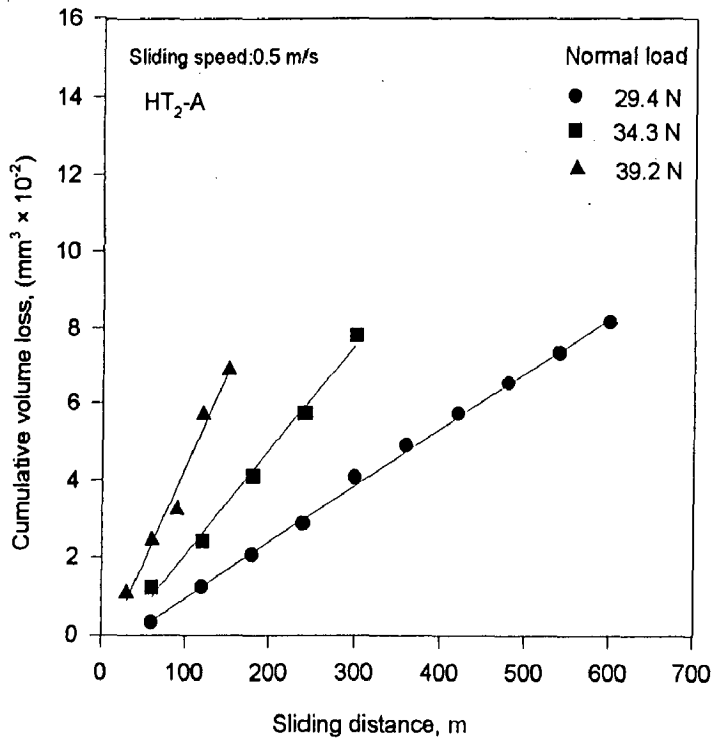


Fig. 5.6 Cumulative wear volume with sliding distance at different loads in electroless Ni-P-X coated and heat treated at 400°C for 2 h specimens (HT₂-A).

Figure 5.7 shows the variation of cumulative volume loss with sliding distance of as-coated Ni-P steel pin (AC_2) samples during dry sliding wear. Similar to Ni-P-X coated steel (AC_1), the cumulative volume loss of Ni-P coated steel (AC_2) also increases linearly with sliding distance. The increasing load also increases the cumulative volume loss. The cumulative volume loss of AC_2 increases from $3.81 \times 10^{-2} \text{ mm}^3$ to $5.7 \times 10^{-2} \text{ mm}^3$ when the load increases from 29.4 to 34.3 N for 120 m sliding. At the highest load of 39.2 N , the volume loss in wear is found to be $8.9 \times 10^{-2} \text{ mm}^3$ after sliding through the same distance. This data reveals that the Ni-P coated steel (AC_2) shows higher wear volume than Ni-P-X coated steel (AC_1) although the volume loss of AC_2 is substantially lower than that for the steel substrate (NS) as mentioned in above paragraphs.

Figure 5.8 represents the variation of cumulative volume loss with sliding distance for Ni-P coating on steel pin samples heat treated at 400°C for 1 h (HT_1-B) during dry sliding. The cumulative volume loss increases linearly with increasing sliding distance and also with increasing load. Figure 5.8 reveals that for the loads of 29.4 and 34.3 N , the cumulative volume losses after sliding through 120 m , are found to be $1.69 \times 10^{-2} \text{ mm}^3$ and $2.54 \times 10^{-2} \text{ mm}^3$ respectively. But at the load 39.2 N , the cumulative volume loss increases relatively faster and its value is found to reach as high as $7.2 \times 10^{-2} \text{ mm}^3$ after sliding through the same distance. The cumulative volume loss in Ni-P coating heat treated at 400°C for 1h is less than that observed in the substrate as such (NS) as well as with Ni-P coating on steel (AC_1) at any sliding distance under the different loads employed in this investigation.

Variation of cumulative volume loss with sliding distance for the Ni-P coated steel pin samples after heat treatment at 400°C for longer period of 2 h (HT_2-B) during dry sliding is shown in Fig. 5.9. The cumulative volume loss increases linearly with sliding distance for different loads as seen in Fig. 5.9. At the load of 39.2 N , the volume loss is found to be $7.8 \times 10^{-2} \text{ mm}^3$ after sliding through only 120 m distance, which is substantially larger than that observed at relatively lower loads of 34.3 and 29.4 N having the corresponding values of $3.0 \times 10^{-2} \text{ mm}^3$ and $2.1 \times 10^{-2} \text{ mm}^3$ respectively. This experimental data reveals that the HT_2-B type of pins show relatively higher wear volume than HT_1-B

type of samples but substantially lower than that for NS type of pins as mentioned in earlier paragraphs for all the loads employed in entire range of sliding distance covered.

Wear rate is defined as the wear volume loss per unit sliding distance. Therefore, the slope of the cumulative volume loss with increasing sliding distance plots has been used to determine the wear rate. The primary objective of this part of study is to determine the wear rate of Ni-P-X coating on steel pin samples with and without heat treatment, i.e., AC₁, HT₁-A and HT₂-A, during dry sliding wear against hardened steel counterface at constant sliding speed of 0.5 *m/s* under the applied normal loads of 29.4, 34.3 and 39.2 *N*. This study also includes the determination of the wear rate of Ni-P coated steel pin samples under similar conditions as mentioned above for Ni-P-X coating on steel pin samples in order to understand the capability of X (ZrO₂-Al₂O₃-Al₃Zr) in improving wear resistance. The experimental results obtained are compared with that of normalised steel (NS) pin samples under the similar loads of 29.4, 34.3 and 39.2 *N*. Figure 5.10 demonstrates the variation of wear rate of as-coated Ni-P-X steel pin (AC₁) samples for applied load of 29.4 *N* during dry sliding wear test for the coating of different thickness obtained after coating time of 2, 5, 10, 20 and 30 *min*. The wear rates observed are fairly reproducible with a standard deviation of ± 0.43 for AC₁ samples.

Variation of wear rate with applied normal load in different types of wear pins during dry sliding wear has been shown in Fig. 5.11. Wear rate is found to increase with load for different wear pins. The wear rates at a given load and the deviation from linearity are decreasing for NS, AC₁, HT₁-A and HT₂-A types of pins. Wear rate for the substrate steel has been observed to be the highest when compared to any of the Ni-P-X coating on steel in either as-coated or heat treated conditions. The wear rate of AC₁ type of pins has been observed to be substantially lower than that of substrate steel (NS), and it decreases further on heat treatment. Increasing heat treatment time from 1 *h* to 2 *h* does not decrease the wear rate as observed from the wear rates of HT₁-A and HT₂-A samples which are similar at the loads of 29.4 and 34.3 *N*. At higher load of 39.2 *N*, the wear rate of HT₂-A is relatively larger compared to that in HT₁-A indicating deterioration of wear resistance with longer heat treatment.

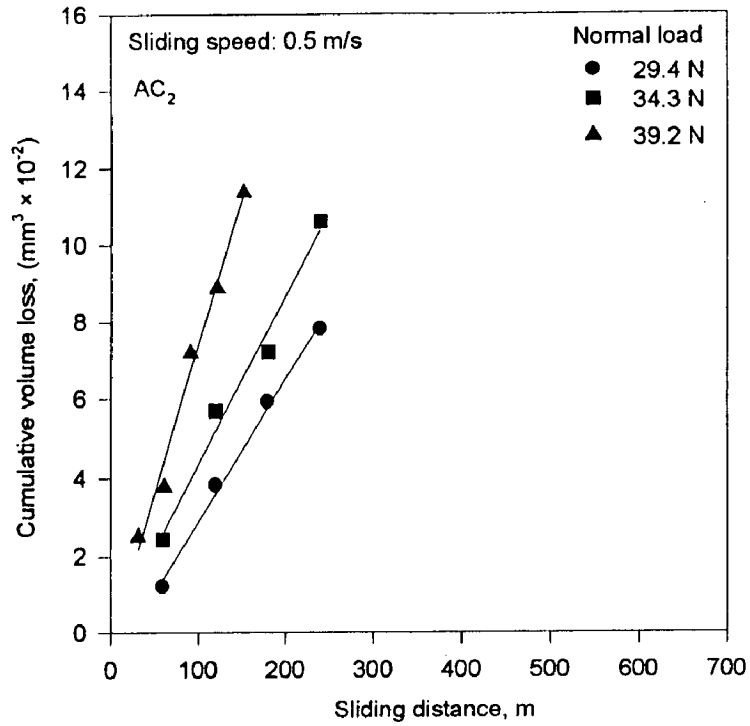


Fig. 5.7 Cumulative wear volume with sliding distance at different loads in electroless Ni-P as-coated steel (AC₂).

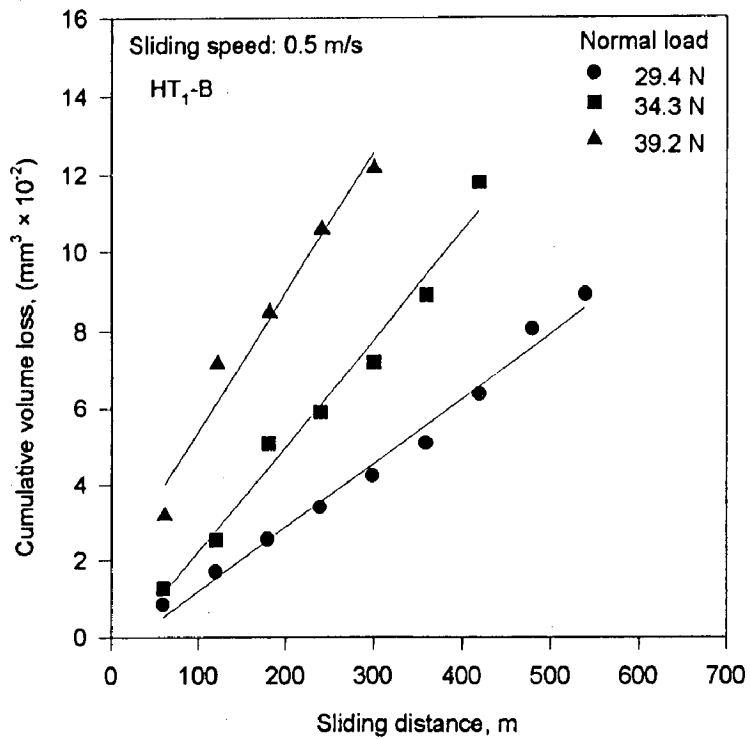


Fig. 5.8 Cumulative wear volume with sliding distance at different loads in electroless Ni-P coated and heat treated at 400°C for 1 h specimens (HT₁-B).

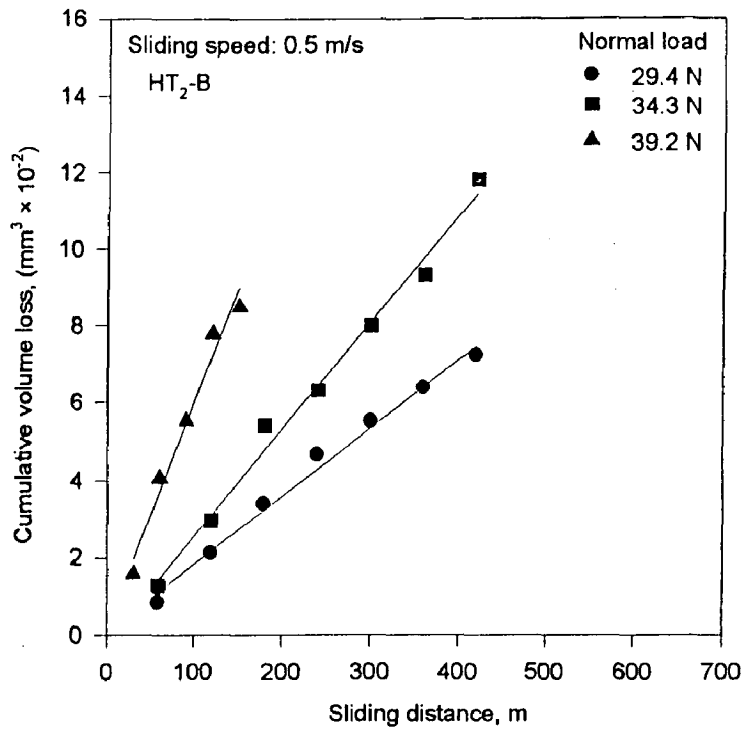


Fig. 5.9 Cumulative wear volume with sliding distance at different loads in electroless Ni-P coated and heat treated at 400°C for 2 h specimens (HT₂-B).

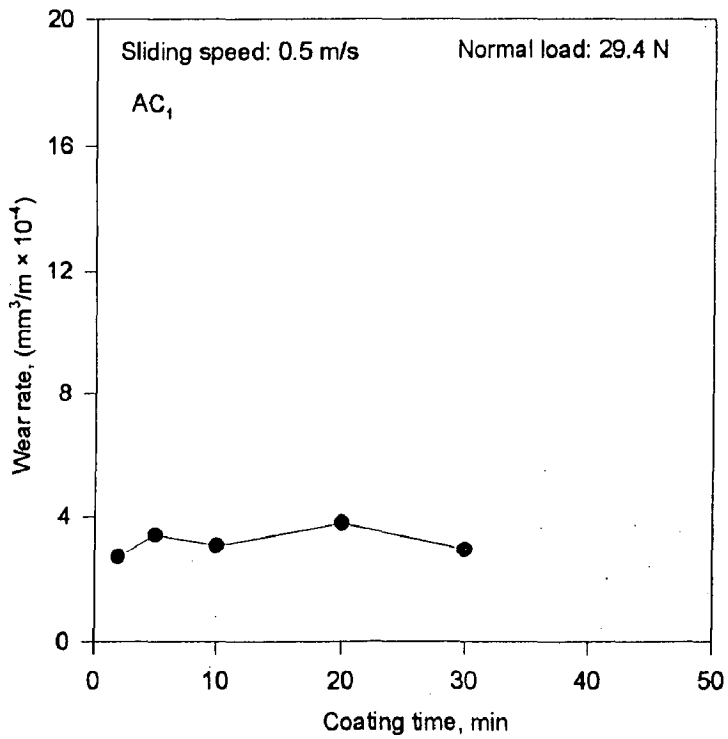


Fig. 5.10 Wear rate with coating time at 29.4 N load in electroless Ni-P-X as-coated steel (AC₁) specimens.

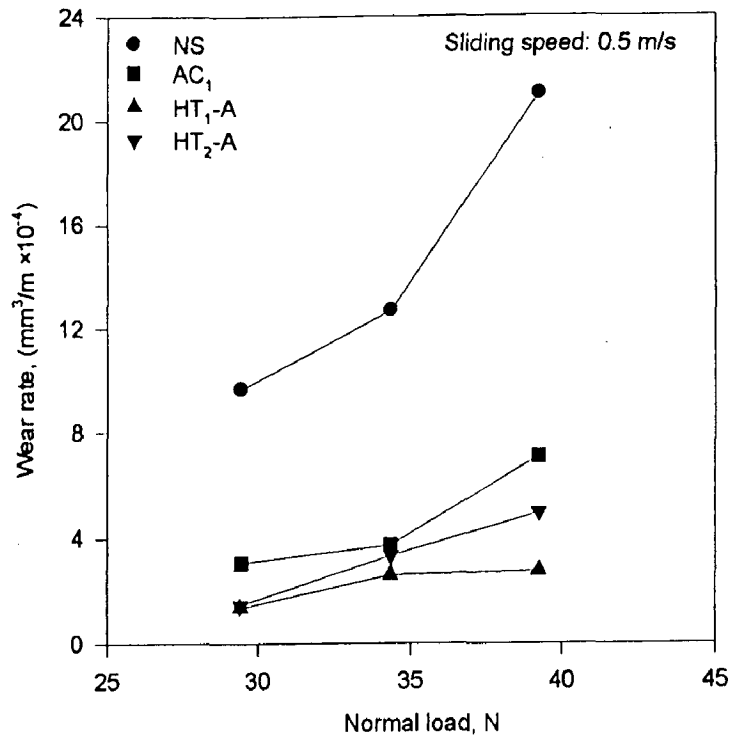


Fig. 5.11 Variation of wear rate with normal load in normalised steel (NS), electroless Ni-P-X as-coated steel (AC₁), electroless Ni-P-X coated and heat treated at 400°C for 1 h specimens (HT₁-A) and electroless Ni-P-X coated and heat treated at 400°C for 2 h specimens (HT₂-A).

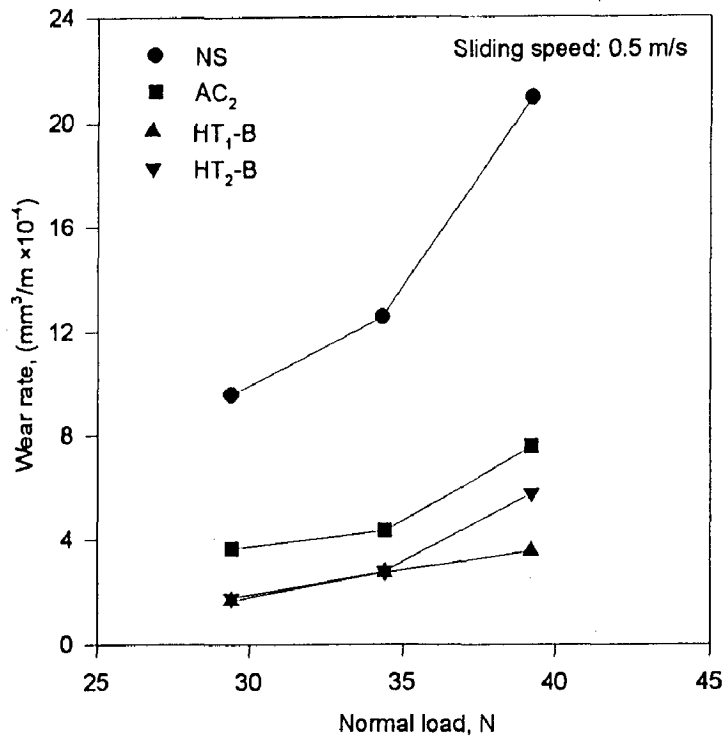


Fig. 5.12 Variation of wear rate with normal load in normalised steel (NS), electroless Ni-P as-coated steel (AC₂), electroless Ni-P coated and heat treated at 400°C for 1 h specimens (HT₁-B) and electroless Ni-P coated and heat treated at 400°C for 2 h specimens (HT₂-B).

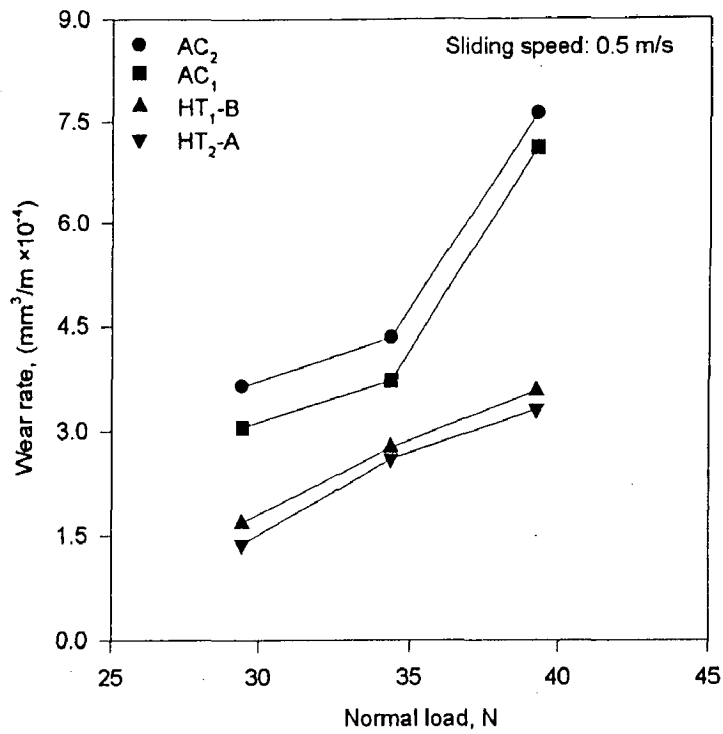


Fig. 5.13 Comparison of wear rates in Ni-P-X and Ni-P coatings for as-coated and heat treated specimens at different loads.

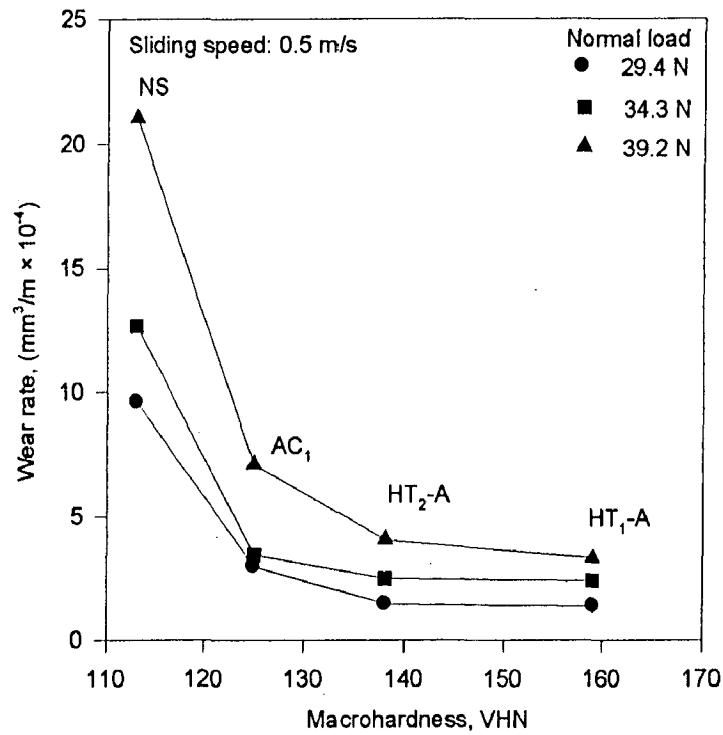


Fig. 5.14 Variation of wear rate with macrohardness of the wear pin specimen in normalised steel (NS), electroless Ni-P-X as-coated steel (AC₁), electroless Ni-P-X coated and heat treated at 400°C for 1 h specimens (HT₁-A) and electroless Ni-P-X coated and heat treated at 400°C for 2 h specimens (HT₂-A) at different normal loads.

(b) Friction behaviour

The Friction study cannot be divorced from wear, keeping in view the integrated tribological performance of a material. Therefore, measurement of frictional force has been carried at definite intervals of time without interrupting the test. When the sliding distance covered during the test is 300 *m* or more the interval is 2 *min* and it is reduced to 1 *min* when the total distance slid is 150 *m*. The coefficient of friction has been computed by dividing the frictional force by applied normal load. The variation of coefficient of friction with sliding distance provides the basic data for understanding the friction behaviour of a material.

Variation of coefficient of friction with sliding distance during dry sliding wear of steel substrate (NS) for 29.4, 34.3 and 39.2 *N* is shown in Fig. 5.16. For all the three loads, the coefficient of friction is found to fluctuate around a mean level and the ranges of fluctuation of the coefficient of friction for the applied normal loads of 29.4, 34.3 and 39.2 *N* are 0.56-0.62, 0.56-0.60 and 0.54-0.58 respectively during sliding through a distance of 480 *m* as shown in Fig. 5.16. The range of fluctuation of coefficient of friction in different types of samples investigated in the present study at the specified load and sliding distance are given in Table 5.3.

Variation of coefficient of friction with sliding distance for Ni-P-X coated steel pins (AC_1) is shown in Fig. 5.17 for different loads of 29.4, 34.3 and 39.2 *N*. The coefficient of friction for AC_1 samples has been observed to fluctuate in relatively lower range of values as compared to those for steel substrate (NS) for similar loads as shown in Fig. 5.17. Ranges of fluctuation of coefficient of friction observed under different loads are given in Table 5.3.

The variation in coefficient of friction observed during dry sliding of steel pins heat treated at 400°C for 1 *h* after coating with Ni-P-X (HT_1-A), is demonstrated in Fig. 5.18 under different normal loads of 29.4, 34.3 and 39.2 *N* employed during sliding. At the load of 29.4 *N*, the value of coefficient of friction is found to fluctuate between 0.48-0.58 over 600 *m* of sliding distance covered, which is relatively lower than that observed for both the

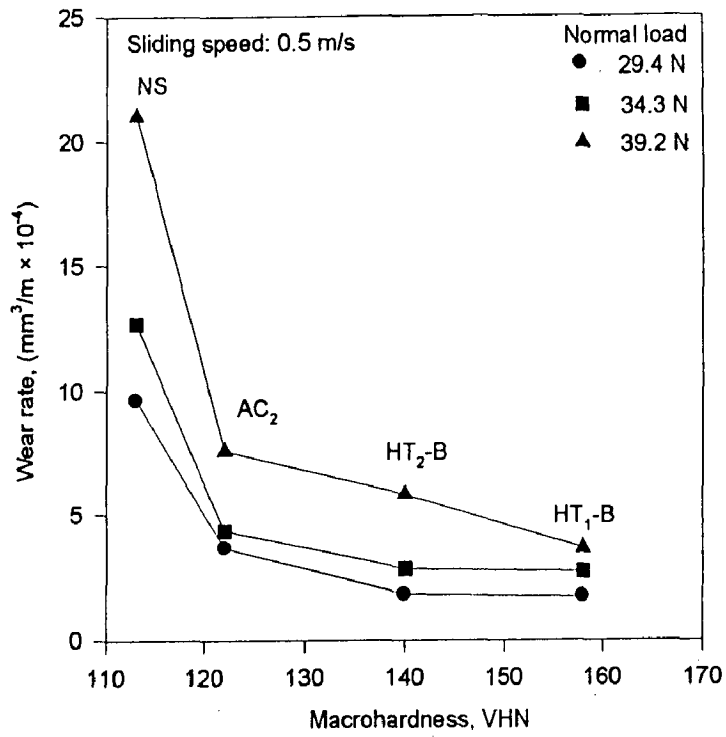


Fig. 5.15 Variation of wear rate with macrohardness of the wear pin specimen in electroless Ni-P as-coated steel (AC₂), electroless Ni-P coated and heat treated at 400°C for 1 h specimens (HT₁-B) and electroless Ni-P coated and heat treated at 400°C for 2 h specimens (HT₂-B) at different normal loads.

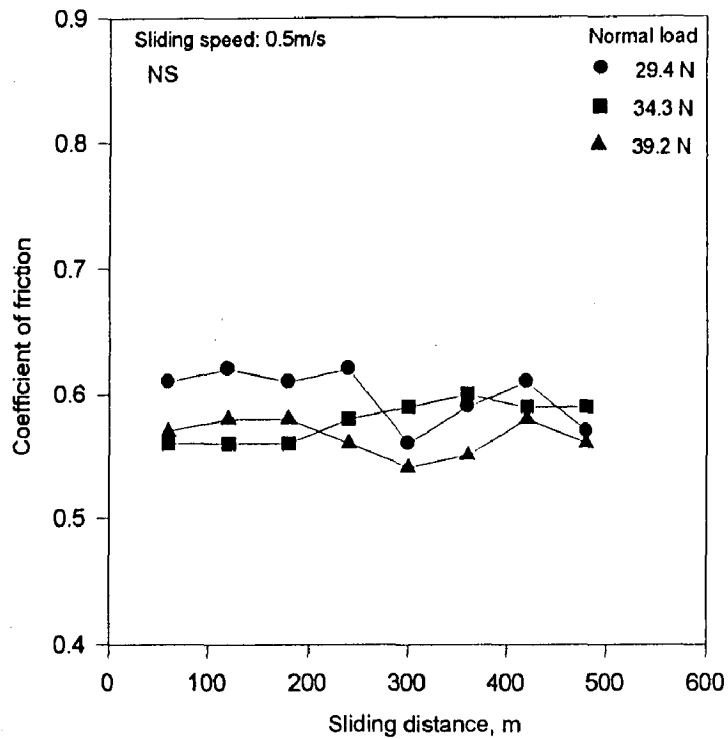


Fig. 5.16 Variation of sliding friction coefficient with distance at different loads in normalised steel (NS).

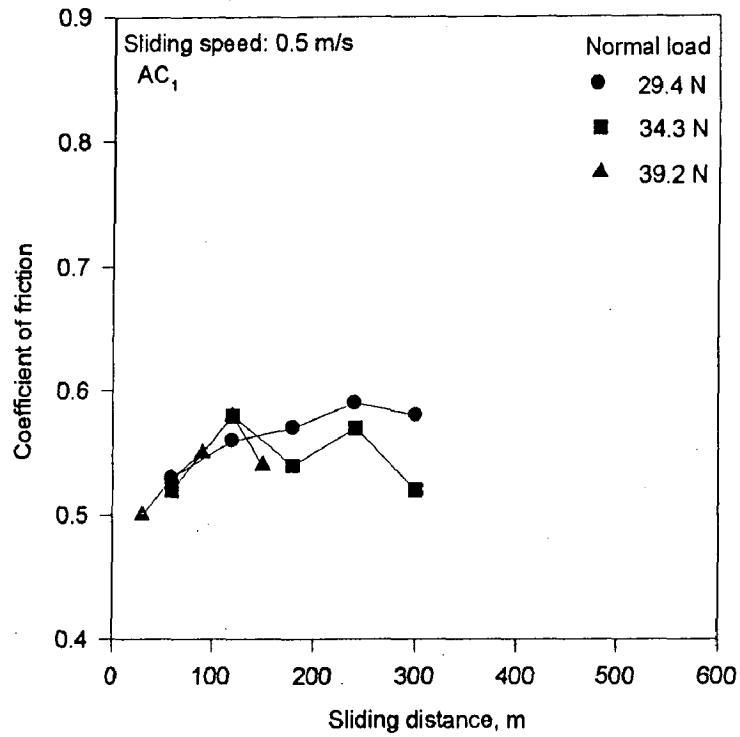


Fig. 5.17 Variation of sliding friction coefficient with distance at different loads in electroless Ni-P-X as-coated steel (AC₁).

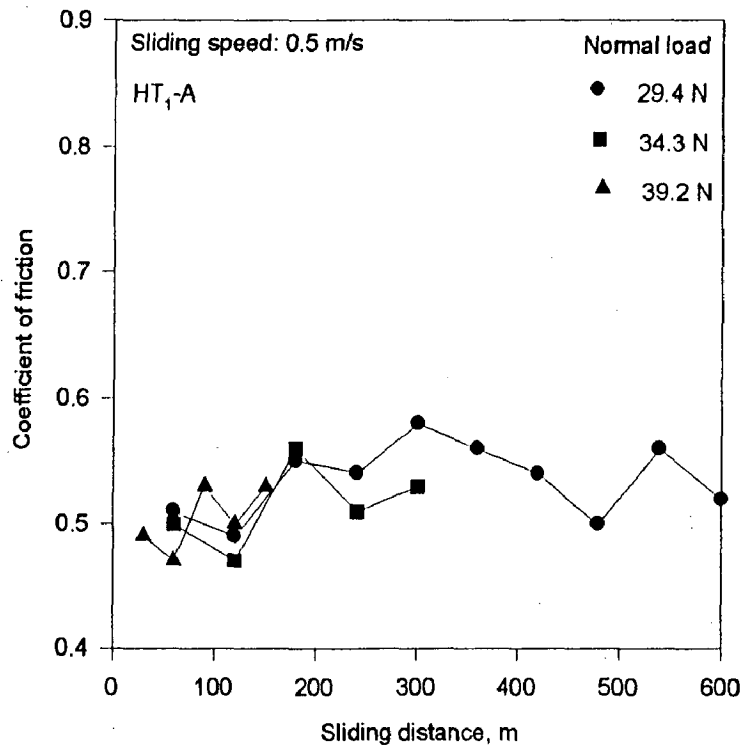


Fig. 5.18 Variation of sliding friction coefficient with distance at different loads in electroless Ni-P-X coated and heat treated at 400°C for 1 h specimens (HT_{1-A}).

Variations in coefficient of friction with sliding distance for Ni-P-X coated samples after heat treatment at 400°C for a longer period of 2 h steel (HT₂-A) is shown in Fig. 5.19 at different loads of 29.4, 34.3 and 39.2 N. For all the three loads, the coefficient of friction is found to fluctuate around a mean level and the ranges of coefficient of friction observed for the applied normal loads employed and corresponding sliding distances covered are given in Table 5.3. The values of coefficient of friction for HT₂-A pin samples have been observed to fluctuate in relatively higher range of values as compared to those for HT₁-A samples but in relatively lower range of values as compared to those for both the NS and the AC₁.

Variation in average coefficient of friction with normal load is shown in Fig. 5.20 for NS, AC₁, HT₁-A and HT₂-A types of wear pin samples. The coefficient of friction decreases linearly with increasing load for all the types of pins investigated, as shown in Fig. 5.20. The average coefficient of friction for different loads in the steel substrate (NS) is more than those observed for the specimens coated by Ni-P-X with or without heat treatment. The average coefficient of friction for Ni-P-X coated steel (AC₁) is more than those observed for coated samples heat treated at 400°C (HT₁-A and HT₂-A). The minimum values of coefficient of friction in Ni-P-X coated samples have been observed in those heat treated at 400°C for 1 h as shown in Fig. 5.20.

Figure 5.21 illustrates the variation in coefficient of friction with sliding distance for Ni-P coated steel (AC₂) pins at different loads of 29.4, 34.3 and 39.2 N. At a load of 29.4 N, during sliding through 300 m, the coefficient of friction is observed to fluctuate between the range of 0.49-0.60, which is relatively higher than that found for Ni-P-X coated steel (AC₁) samples, and this trend is also observed at higher loads of 34.3 and 39.2 N. The range of values of coefficient of friction in Ni-P coated samples (AC₂) is lower than that observed for steel substrate (NS) as revealed from Table 5.3.

Variation in coefficient of friction with sliding distance for Ni-P coated steel samples heat treated at 400° C for 1 h (HT₁-B) is shown in Fig. 5.22 at different loads of

29.4, 34.3 and 39.2 *N*. For all the three loads investigated, the coefficient of friction is found to fluctuate around a mean level and the ranges of the coefficient of friction during the specified sliding distance covered are given in Table 5.3. The values of coefficient of friction for HT₁-B samples have been observed to vacillate within a relatively lower range of values as compared to those for both the HT₁-A samples and the steel substrate as such (NS) samples. At all the loads employed, the ranges of coefficient of friction for HT₁-B samples has been observed to ^{be} lower than those for Ni-P coated (AC₂) samples.

Figure 5.23 shows the variation in coefficient of friction with sliding distance for Ni-P coated steel samples heat treated at 400° C for a longer time of 2 *h* (HT₂-B) at different loads of 29.4, 34.3 and 39.2 *N*. At a load of 29.4 *N*, during sliding through a distance of 420 *m*, coefficient of friction is observed to fluctuate between the range of 0.49-0.61, which is more or less the same as observed for Ni-P-X coated samples heat treated at 400°C for 1 *h* (HT₂-A) only. The coefficient of friction for HT₂-B type pin samples have been observed to fluctuate in relatively higher range of values as compared to those for Ni-P coated and heat treated steel (HT₁-B) but it is lower than the range of values of coefficient of friction in steel substrate (NS) for similar loads.

Variation of average coefficient of friction with normal load for NS, AC₂, HT₁-B and HT₂-B types of wear pins at different loads of 29.4, 34.3 and 39.2 *N* is shown in Fig. 5.24. Linear decrease in average coefficient of friction with increasing load has been observed for different types of wear pins as shown in Fig. 5.24. The average coefficient of friction for HT₁-B type specimens is found to be the lowest of all the Ni-P coated and heat treated samples. The coefficient of friction for steel substrate (NS) is observed to be the maximum for all the loads investigated. Although the average coefficient of friction values for Ni-P coated steel (AC₂) are relatively less than those observed for the steel substrate, as-coated samples show higher coefficient of friction compared to those of Ni-P coated samples heat treated at 400°C (HT₁-B and HT₂-B) as given in Fig. 5.24.

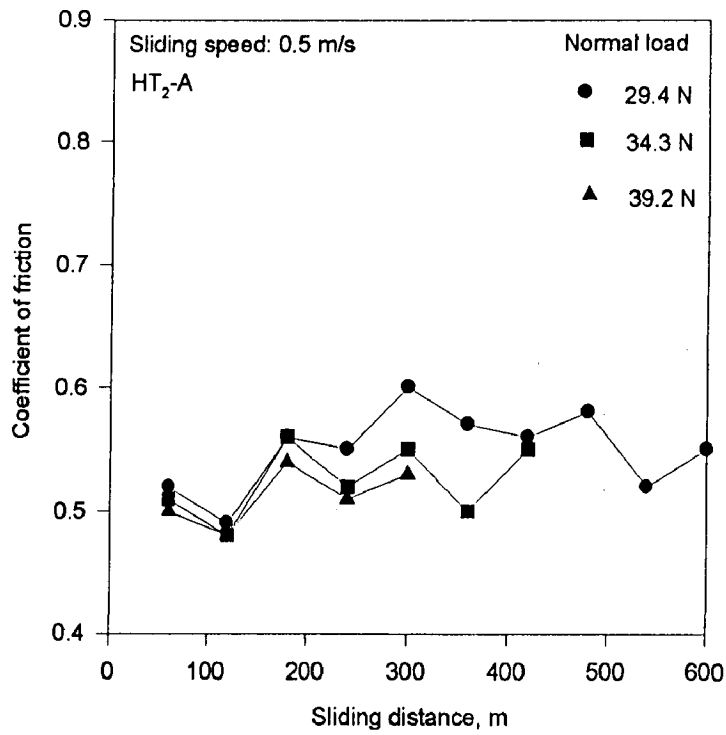


Fig. 5.19 Variation of sliding friction coefficient with distance at different loads in electroless Ni-P-X coated and heat treated at 400°C for 2 h specimens (HT₂-A).

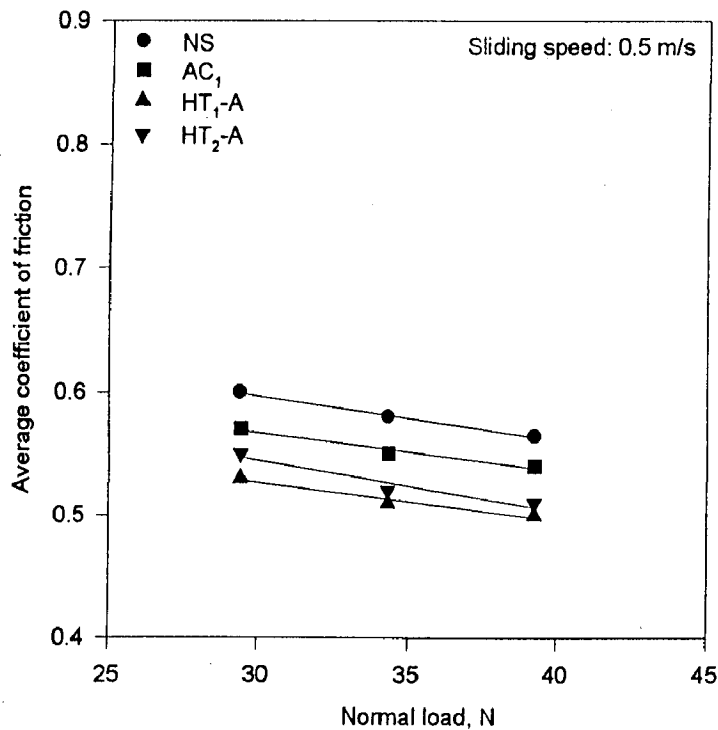


Fig. 5.20 Variation of coefficient of friction averaged over the distance of sliding during wear in normalised steel (NS), electroless Ni-P-X as-coated steel (AC₁), electroless Ni-P-X coated and heat treated at 400°C for 1 h specimens (HT₁-A) and electroless Ni-P-X coated and heat treated at 400°C for 2 h specimens (HT₂-A).

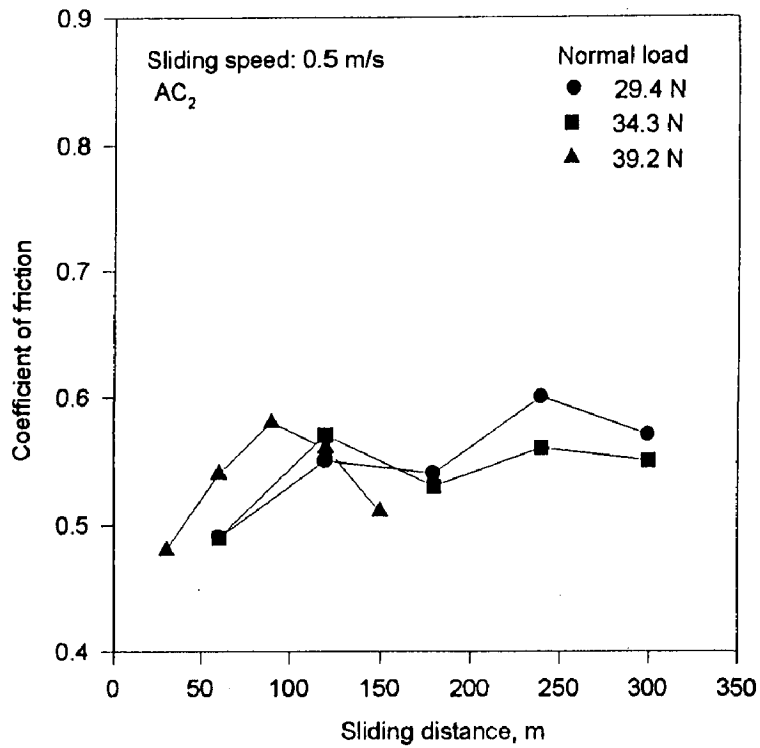


Fig. 5.21 Variation of sliding friction coefficient with distance at different loads in electroless Ni-P as-coated steel (AC₂).

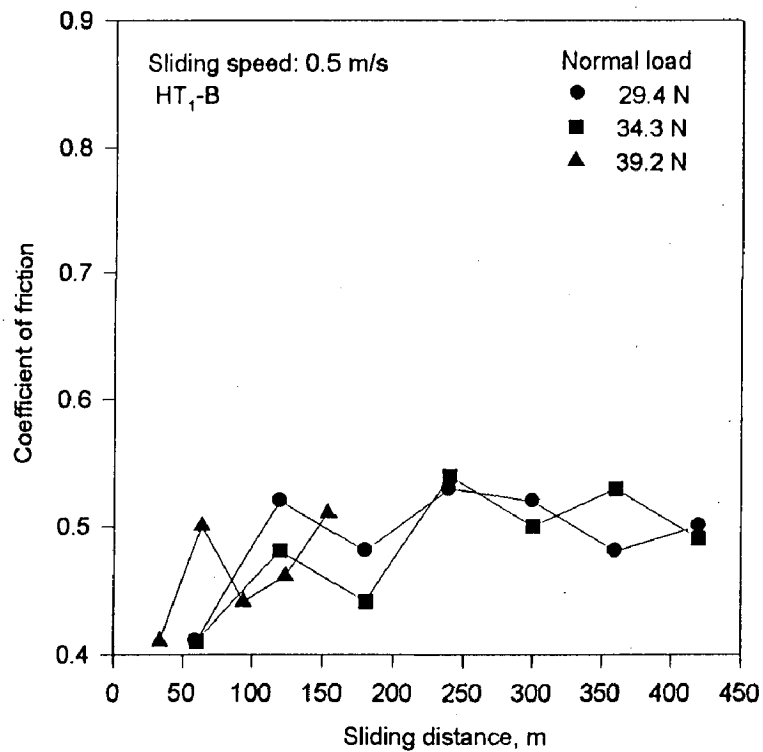


Fig. 5.22 Variation of sliding friction coefficient with distance at different loads in electroless Ni-P coated and heat treated at 400°C for 1 h specimens (HT₁-B).

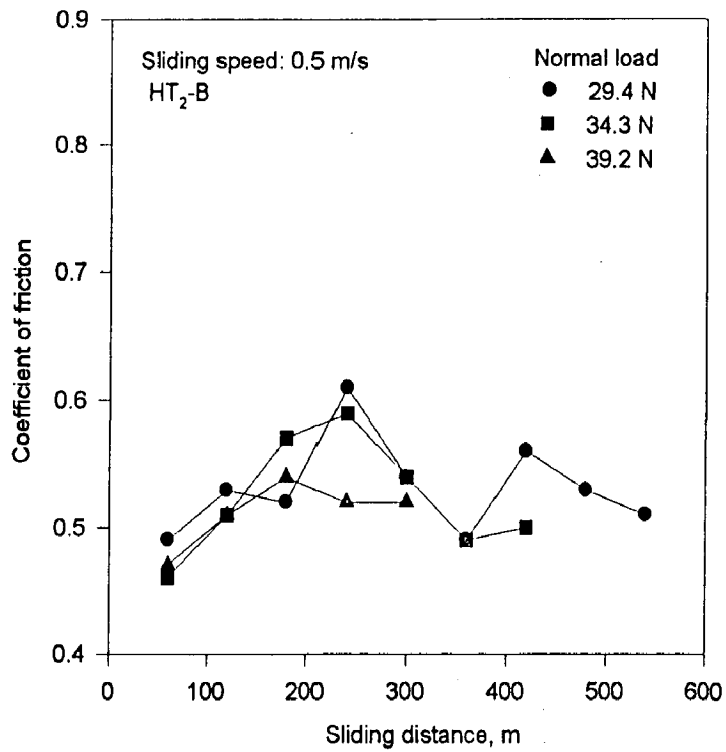


Fig. 5.23 Variation of sliding friction coefficient with distance at different loads in electroless Ni-P coated and heat treated at 400°C for 2 h specimens (HT₂-B).

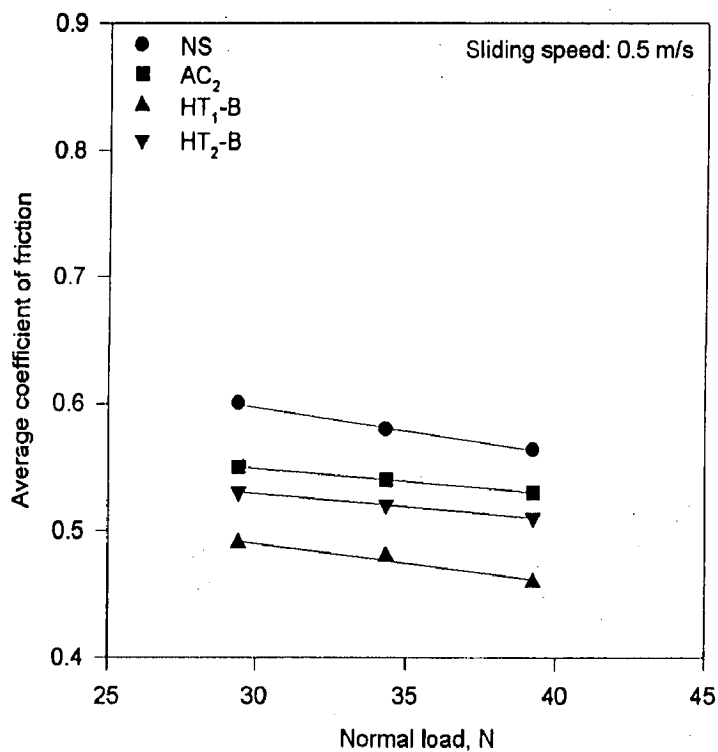


Fig. 5.24 Variation of coefficient of friction averaged over the distance of sliding during wear in normalised steel (NS), electroless Ni-P as-coated steel (AC₂), electroless Ni-P coated and heat treated at 400°C for 1 h specimens (HT₁-B) and electroless Ni-P coated and heat treated at 400°C for 2 h specimens (HT₂-B).

In order to understand the discrimination in friction behaviour due to the presence of X ($ZrO_2-Al_2O_3-Al_3Zr$), Ni-P-X and Ni-P coated steel in as-coated/heat treated conditions are compared in terms of average coefficient of friction at different loads. Figure 5.25 shows the comparison of values of average coefficient of friction observed in AC₁, AC₂, HT₁-A, HT₁-B, HT₂-A and HT₂-B samples at 29.4, 34.3 and 39.2 *N* loads. The average coefficient of friction values for different types of pins investigated decreases linearly with increase in applied load. Heat treated samples were commonly observed to have lower coefficient of friction in both the Ni-P-X and the Ni-P coated steel. The Ni-P coated steel (AC₂) samples show lower values of coefficient of friction than Ni-P-X coated steel (AC₁) samples. Similarly, the samples heat treated at 400°C after Ni-P coating (HT₁-B and HT₂-B) also show lower values of coefficient of friction when compared to samples heat treated at 400°C after Ni-P-X coating (HT₁-A and HT₂-A). Heat treatment at 400°C for longer time of 2 *h* results in relatively higher coefficient of friction compared to the specimens heat treated at 400°C for 1 *h* after both the Ni-P-X and the Ni-P coatings at all the loads investigated as shown in Fig. 5.25. The presence of X results in relatively smaller difference in the coefficient of friction values as observed by comparing the results for AC₂ and AC₁ samples. Similar relatively smaller difference in coefficient of friction is observed in HT₂-A and HT₂-B type of samples. However, when the coated samples are heat treated at 400°C for 1 *h*, the presence of X increases the average coefficient of friction significantly resulting in much larger difference as inferred from comparing the results in Fig. 5.25.

The variation of average coefficient of friction with hardness of the Ni-P-X and Ni-P coated steel at a normal load of 29.4 *N* has been compared and shown in Fig. 5.26. This figure reveals that the average coefficient of friction commonly decreases with increasing hardness attained by heat treatment of the Ni-P-X/Ni-P coatings on steel substrate. The similar decrease in coefficient of friction has been observed with increasing hardness imparted by heat treatment of the Ni-P-X/Ni-P coatings on steel substrate for other loads. It is interesting to note that the variations of coefficient of friction with hardness are linear for both the coatings but Ni-P-X coating shows a relatively faster decrease in coefficient of friction with increasing hardness.

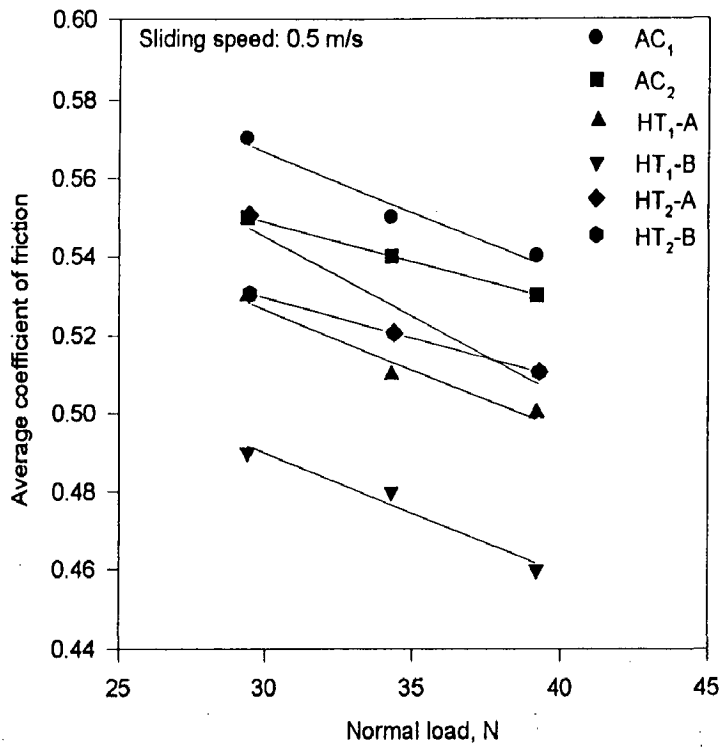


Fig. 5.25 Comparison of average coefficient of friction in Ni-P-X and Ni-P coatings for as-coated and heat treated specimens at different loads.

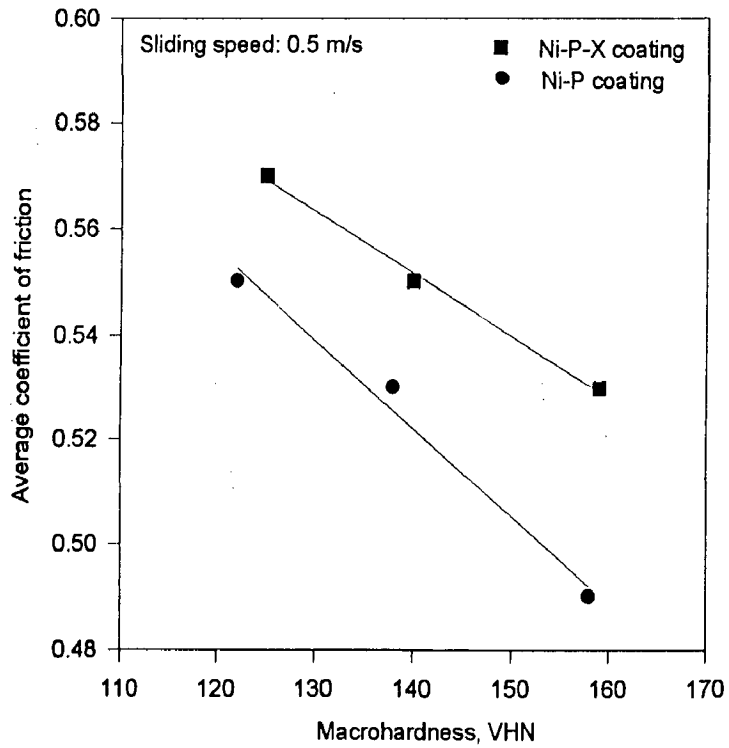


Fig. 5.26 Variation in average coefficient of friction with hardness during wear in electroless Ni-P-X and Ni-P coated steel specimens at a load of 29.4 N under dry sliding condition.

5.1.2 Examination of Wear Surfaces and Wear Debris

The wear surfaces of different types of pins i. e. NS, AC₁, HT₁-A, HT₂-A, AC₂, HT₁-B and HT₂-B have been examined under SEM while wear debris generated during dry sliding of the different types of pin are examined under both the stereo optical microscope and the SEM; and the observations made are outlined in the following paragraphs. Wear debris examination provides the information of size and shape of debris, which in turn, may be helpful in explaining the operating wear mechanism. The wear debris has been carefully collected during the wear tests for specified types of pins and are observed under optical microscope. The debris particles have been spread over the white paper and photographed under optical microscope while those are gold plated for SEM examination.

Figures 5.27 (a) to (c) show the wear surface of the normalised steel (NS) samples after dry sliding through 480 *m* respectively at normal loads of 29.4, 34.3 and 39.2 *N*. At a load of 29.4 *N*, transfer layer of oxide can be clearly identified in Fig. 5.27 (a) on the wear surface as relatively brighter patches along with the wear tracks. Similar transfer layers on the worn surfaces of NS samples at higher loads of 34.3 and 39.2 *N* are observed in Figs. 5.27 (b) and (c) respectively. The extent of the transfer layer increases with increasing applied load. The wear tracks also become relatively deep with increasing load as observed from Figs. 5.27 (a) to (c).

Figures 5.28 (a) and (b) show micrographs of wear debris collected during the wear test of normalised steel (NS) under optical microscope and SEM respectively. Some finer debris (primarily of oxide) particles and a few larger agglomerates of oxide are observed from Fig. 5.28. A few flaked off particles from the transfer layer of oxide also can be seen in the above micrographs.

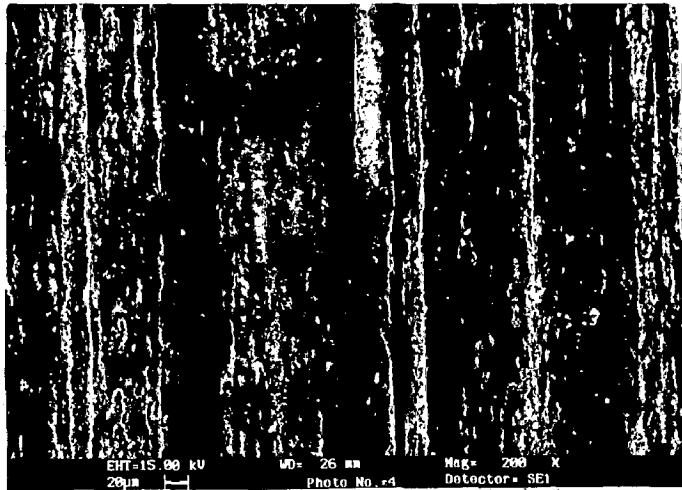
Figures 5.29 (a) through (c) illustrate the SEM micrographs of the worn surfaces of Ni-P-X coated steel (AC₁) samples at applied loads of 29.4, 34.3 and 39.2 *N* respectively after sliding through the specified sliding distances. At all the loads investigated, the

transfer layer of compacted wear debris forms very clearly as compared to that observed on NS sliding surfaces under similar loads. As the load increases from 29.4 to 34.3 *N*, increasing extent of transfer layer is clearly seen in Figs. 5.29 (a) and (b). And when the load is increased further to 39.2 *N*, the continuous wear tracks are hardly visible because of cover provided by the highly compacted transfer layer of wear debris as observed from Fig. 5.29 (c).

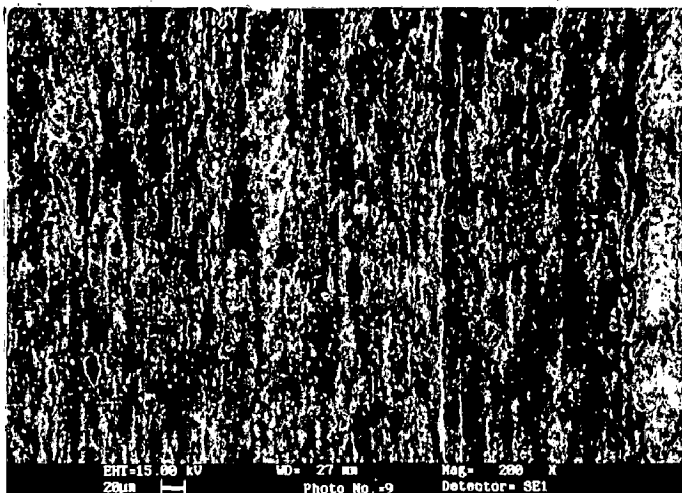
Figures 5.30 (a) and (b) show the wear debris particles collected during dry sliding of AC₁ type of pins under optical microscope and SEM respectively. Some finer oxide particles and a few larger oxide agglomerates are observed from this figure, which is an indication of oxidative type of wear of as-coated Ni-P-X coated steel samples. The fine particles of debris along with a few bright irregular particles are also observed as marked by an arrow in Fig. 5.30 (a). These particles may generate due to flaking off the coating layer indicating debonding of coating at a few localised areas from the substrate during sliding.

The wear surfaces of Ni-P-X coated samples heat treated at 400°C for 1 *h* (HT₁-A), after dry sliding through a specified distance, at the loads of 29.4, 34.3 and 39.2 *N* is shown respectively in Figs. 5.31 (a), (b) and (c). In HT₁-A type samples also the extent of transfer layer has been observed to increase with increasing load as mentioned for Ni-P-X coated steel (AC₁) in earlier paragraph. Relatively larger extent of compacted layer is seen to hide the wear tracks in Ni-P-X coated and heat treated (HT₁-A) samples at the highest load of 39.2 *N* as seen from Fig. 5.31 (c).

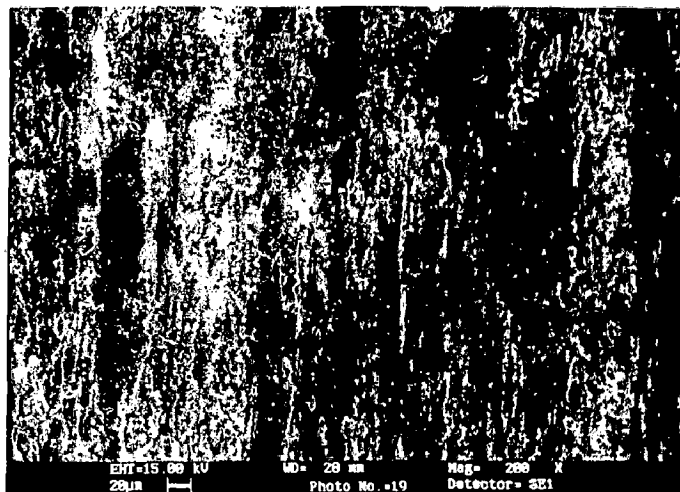
Wear debris collected during dry sliding of Ni-P-X coated steel samples heat treated at 400°C for 1 *h* (HT₁-A) are shown under optical microscope and SEM in Figs. 5.32 (a) and (b) respectively. Coarser flaky debris and agglomerates of fine oxide particles are observed in above micrographs. The flaked off wedge shape debris laminae from the transfer layer are also observed as marked by an arrow in Fig. 5.32 (b).



(a)



(b)

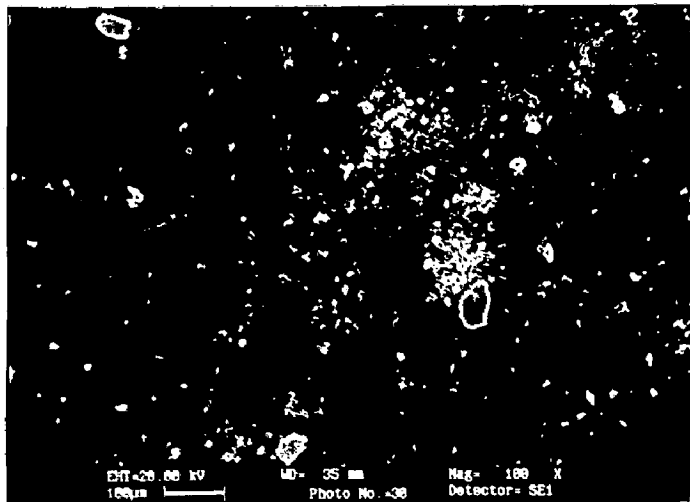


(c)

Fig. 5.27 Wear surfaces of the specimens of normalised steel (NS) after sliding through a distance of 480 m at the normal loads of (a) 29.4 N, (b) 34.3 N and (c) 39.2 N.

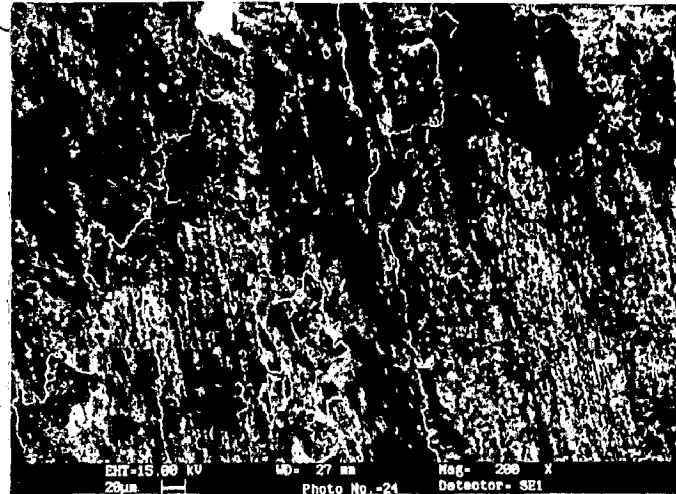


(a)

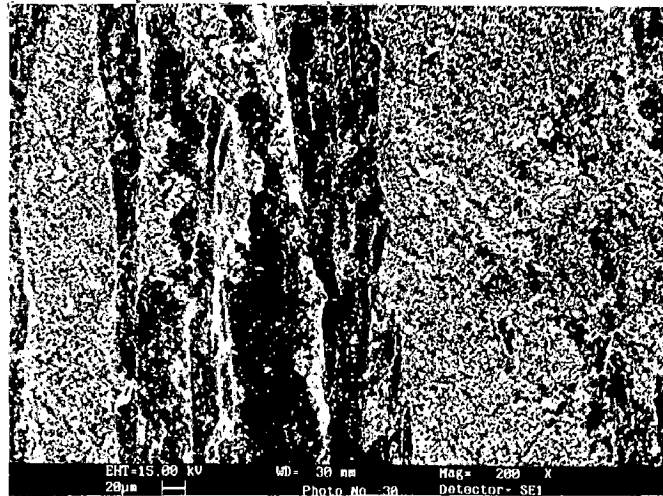


(b)

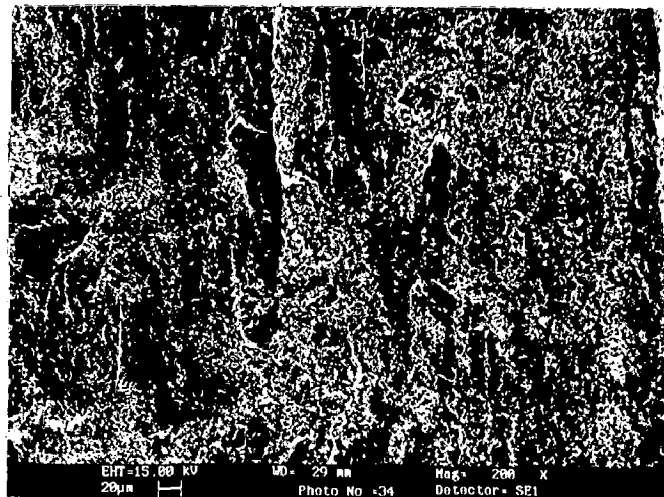
Fig. 5.28 Wear debris of normalised steel (NS) after spreading on white paper (a) optical micrograph at magnification of $\times 25$ and (b) SEM micrograph.



(a)



(b)

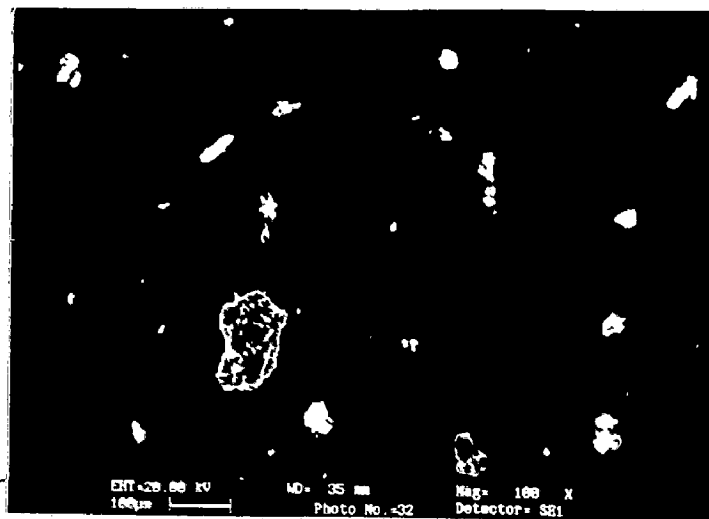


(c)

Fig. 5.29 Wear surfaces of the specimens of electroless Ni-P-X as-coated steel (AC_1) after sliding through (a) 300 *m* at 29.4 *N*, (b) 300 *m* at 34.3 *N* and (c) 150 *m* at 39.2 *N*.

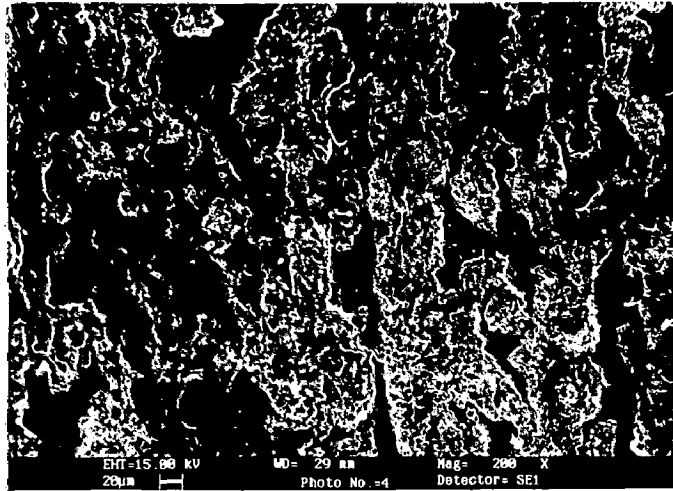


(a)

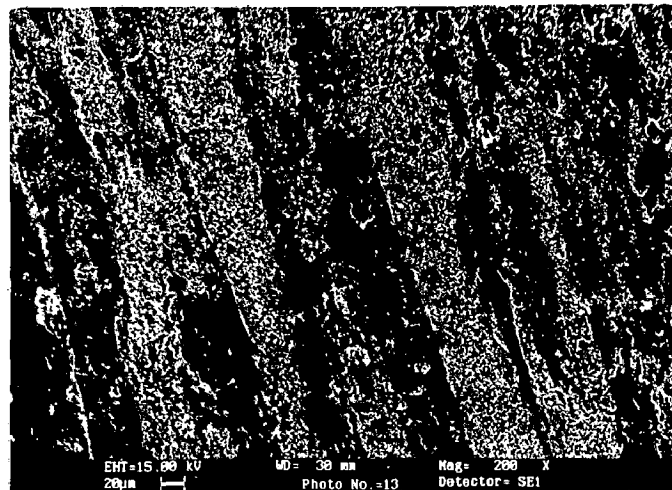


(b)

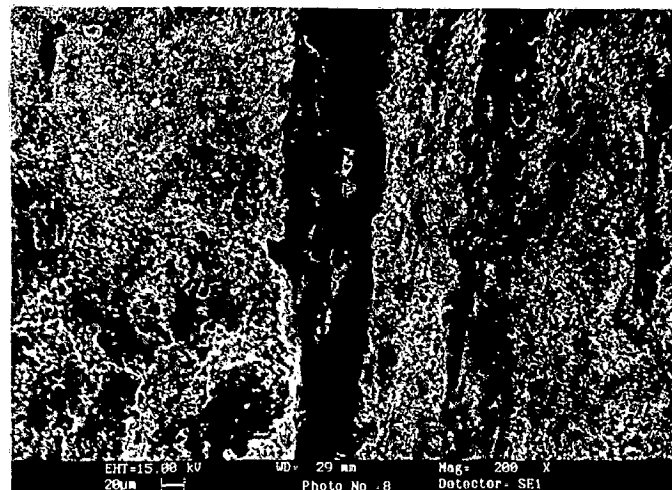
Fig. 5.30 Wear debris of electroless Ni-P-X as-coated steel (AC_1) after spreading on white paper (a) optical micrograph at magnification of $\times 25$ and (b) SEM micrograph.



(a)



(b)



(c)

Fig. 5.31 Wear surfaces of the specimens of electroless Ni-P-X coated and heat treated at 400°C for 1 h specimens (HT₁-A) after sliding through (a) 600 m at 29.4 N, (b) 420 m at 34.3 N and (c) 300 m at 39.2 N.



(a)



(b)

Fig. 5.32 Wear debris of electroless Ni-P-X coated and heat treated at 400°C for 1 h specimens (HT₁-A) after spreading on white paper (a) optical micrograph at magnification of × 25 and (b) SEM micrograph.

The SEM micrographs of the wear surface for Ni-P-X coated steel samples heat treated at 400°C for a longer time of 2 h (HT₂-A) after sliding through the specified distances at different loads of 29.4, 34.3 and 39.2 N are shown in Figs. 5.33 (a), (b) and (c) respectively reveal transfer layers and wear tracks similar to those observed in HT₁-A and AC₁ samples. Similar compacted transfer layer of wear debris, as observed on HT₁-A samples, is also seen on HT₂-A samples.

Figures 5.34 (a) and (b) respectively show the optical and SEM micrographs of wear debris collected during dry sliding of HT₂-A types of wear pin specimens. The coarser and irregular shaped debris formed with Ni-P-X coated steel samples heat treated at 400°C for a longer time period of 2 h (HT₂-A) is commonly observed apart from a few finer oxide particles in Figs 5.34 (a) and (b).

Worn surfaces of Ni-P coated steel (AC₂) samples after sliding through specified distances at different applied loads of 29.4, 34.3 and 39.2 N are shown in Figs. 5.35 (a), (b) and (c) respectively. As compared to Ni-P-X coated steel (AC₁) samples, relatively deeper grooves of wear tracks have been observed in Ni-P coated steel (AC₂) samples along with the transfer layer as seen in Figs. 5.35 (a) to (c). However, the extent of transfer layer increases with increasing load as is evident from Figs. 5.35 (a) to (c). The wear tracks are not much clearly visible even at the highest load of 39.2 N because of well adherent cover provided by the highly compacted transfer layer of wear debris as seen in Fig. 5.35 (c).

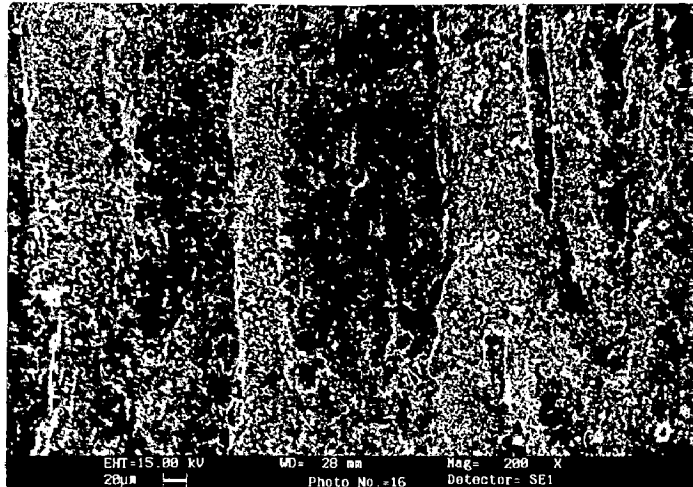
Figures 5.36 (a), (b) and (c) show respectively the SEM micrographs of the worn surface of Ni-P coated samples heat treated at 400°C for 1 h (HT₂-B) at different applied loads of 29.4, 34.3 and 39.2 N after dry sliding through the specified distances. The transfer layer of compacted wear debris is clearly observed along with the wear tracks in these micrographs. As compared to wear surfaces of Ni-P-X coated and heat treated steel (HT₁-A) samples, better compaction of transfer layer has been observed and it is found to increase with increasing load as seen from Figs. 5.36 (a) to (c). The wear tracks are hardly visible because of cover provided by the highly compacted transfer layer of wear debris similar to that on wear surface of HT₁-A.

Wear surfaces of Ni-P coated samples heat treated at 400°C for a longer period of 2 h (HT₂-B) after sliding through specified distances at different loads of 29.4, 34.3 and 39.2 N are shown in Figs. 5.37 (a), (b) and (c) respectively. The discontinuous type transfer layer and cracks in it have been observed in these micrographs for all the loads investigated. The extent of wear track width and transfer layer has been found to increase with increasing applied load. The cracks in transfer layer for Ni-P coated and heat treated (HT₂-B) at 29.4 and 39.2 N are shown in Figs. 5.38 (a) and (b) respectively. The crack in the transfer layer is clearly seen in HT₂-B specimen even at the lowest load of 29.4 N, and marked by an arrow in Fig. 5.38 (a). Similar cracking has been observed at the highest load of 39.2 N as marked by an arrow in Fig. 5.38 (b).

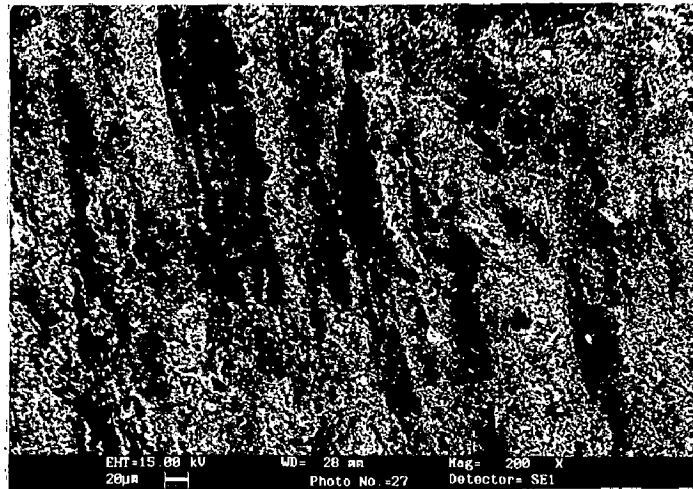
As the debris collected was very less in quantity, the wear debris generated during dry sliding of electroless Ni-P coatings on steel in as-coated (AC₂), heat treated at 400°C for 1 h (HT₁-B) and heat treated at 400°C for 1 h (HT₂-B) conditions was pooled together and its optical and SEM micrographs are shown in Figs. 5.39 (a) and (b) respectively. The finer oxide debris particle and a few agglomerates are observed in the debris collected during sliding of Ni-P coated steel. The fine oxide debris with irregular shape might have resulted due to flaking off of the transfer layer formed during the sliding of pin sample. A few bright irregular particles, as marked by an arrow, are also seen in Fig. 5.39 (a), which could be due to flaking off a part of coating layer from the substrate at localised area during dry sliding.

5.1.3 X-Ray Diffraction Analysis

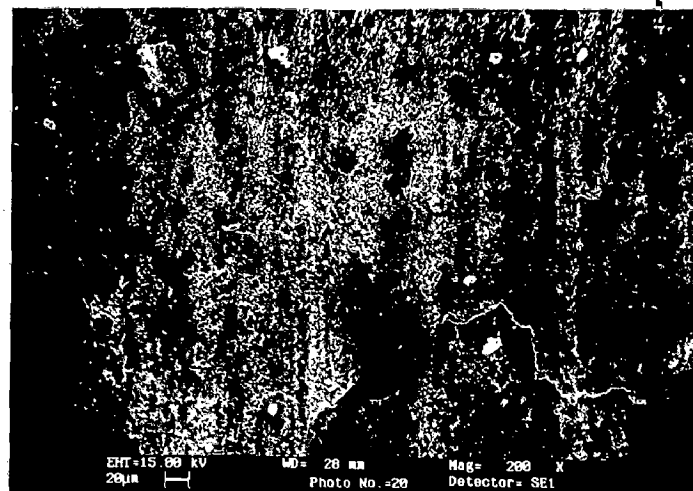
The X-ray diffraction analysis of wear debris has been carried out so as to get the information about the primary phase content in the debris which can be used to explain the nature of the wear mechanism operating in different types of pins used in this segment of the investigation. The amounts of debris collected for HT₁-A and HT₂-A types of pins were very less, therefore, those have been pooled together. The X-ray diffraction patterns obtained for the debris collected during sliding of different samples of steel substrate as such (NS), Ni-P-X coated steel (AC₁) and Ni-P-X coated and heat treated (HT₁-A and HT₂-A) are shown in Figs. 5.40 to 5.42 respectively. Figure 5.40 shows the X-ray



(a)



(b)



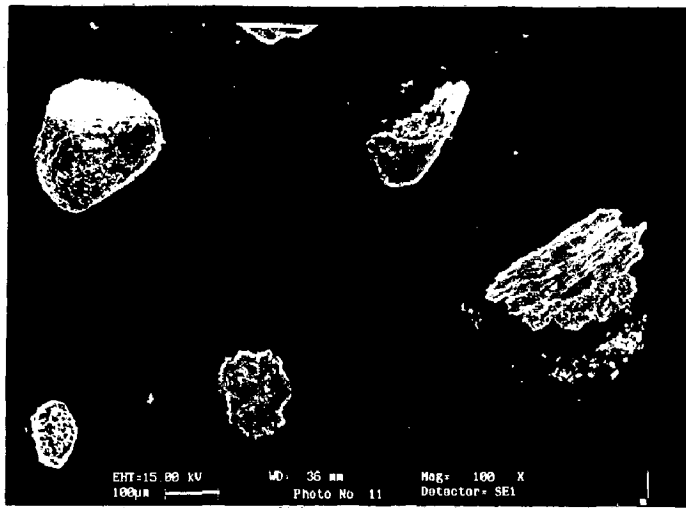
(c)

Fig. 5.33

Wear surfaces of the specimens of electroless Ni-P-X coated and heat treated at 400°C for 2 h specimens (HT₂-A) after sliding through (a) 600 m at 29.4 N, (b) 300 m at 34.3 N and (c) 150 m at 39.2 N.

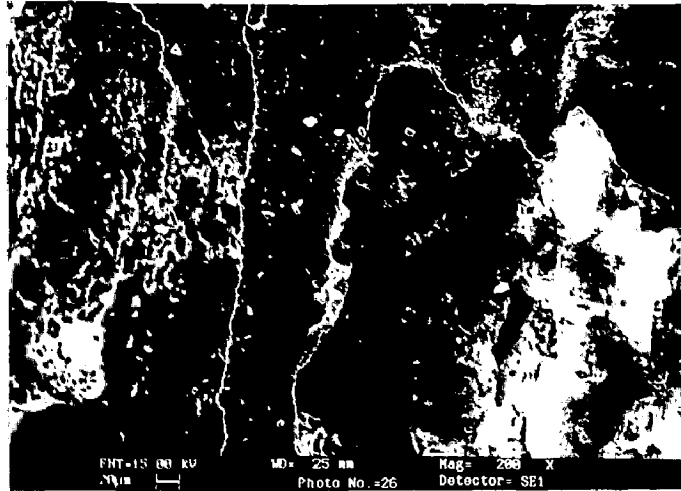


(a)

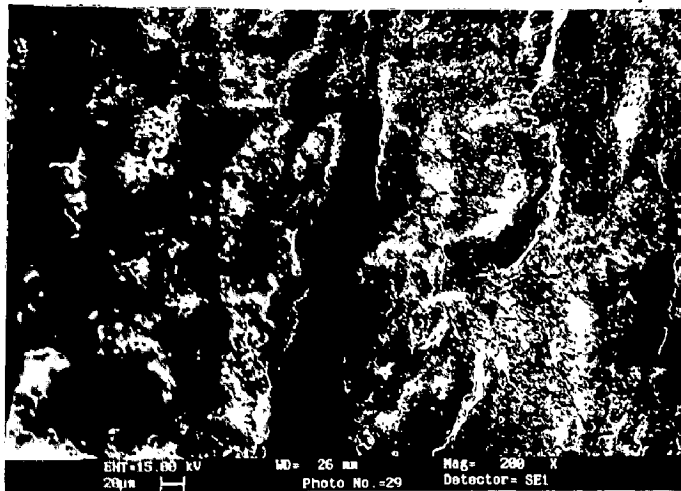


(b)

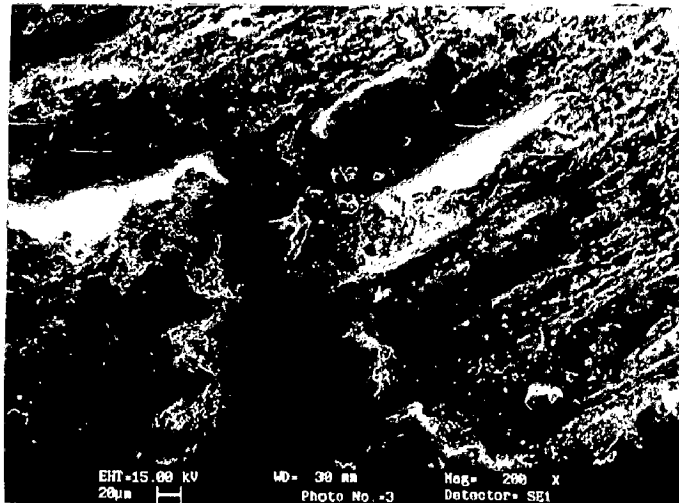
Fig. 5.34 Wear debris of electroless Ni-P-X coated and heat treated at 400°C for 2 h specimens (HT₂-A) after spreading on white paper (a) optical micrograph at magnification of × 25 and (b) SEM micrograph.



(a)

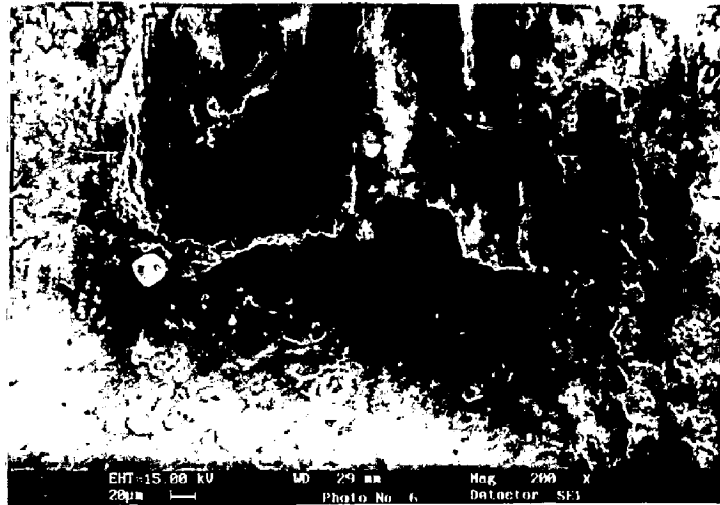


(b)

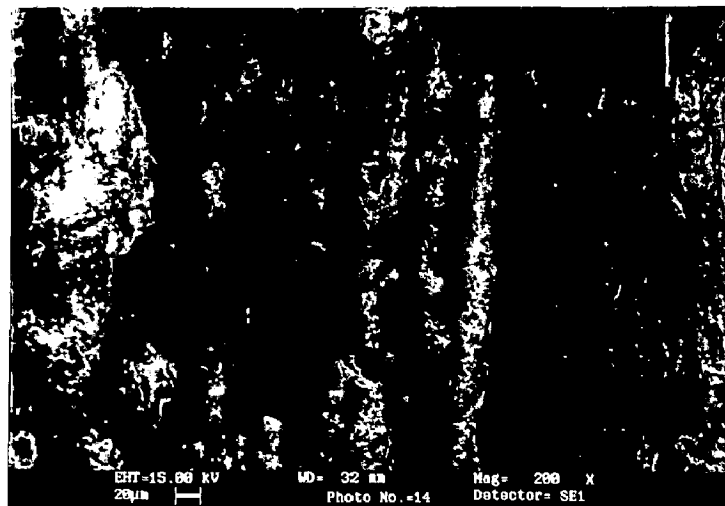


(c)

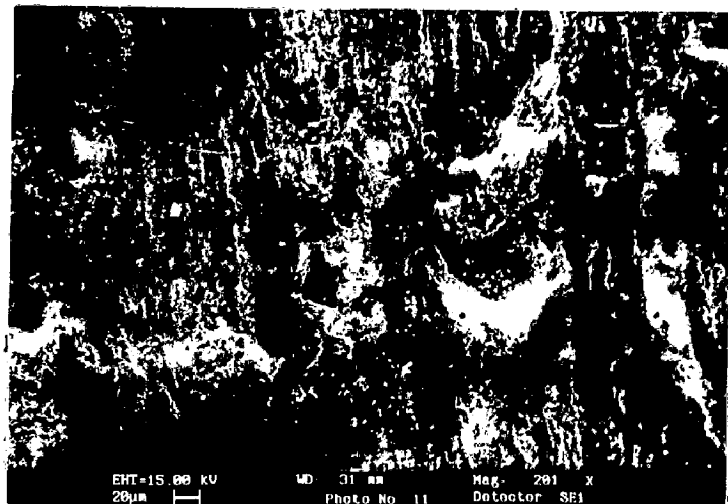
Fig. 5.35 Wear surfaces of the specimens of electroless Ni-P as-coated steel (AC_2) after sliding through (a) 240 *m* at 29.4 *N*, (b) 240 *m* at 34.3 *N* and (c) 150 *m* at 39.2 *N*.



(a)

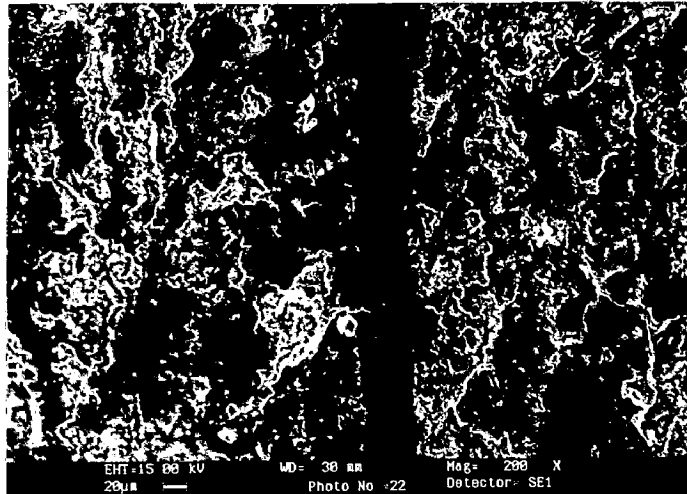


(b)

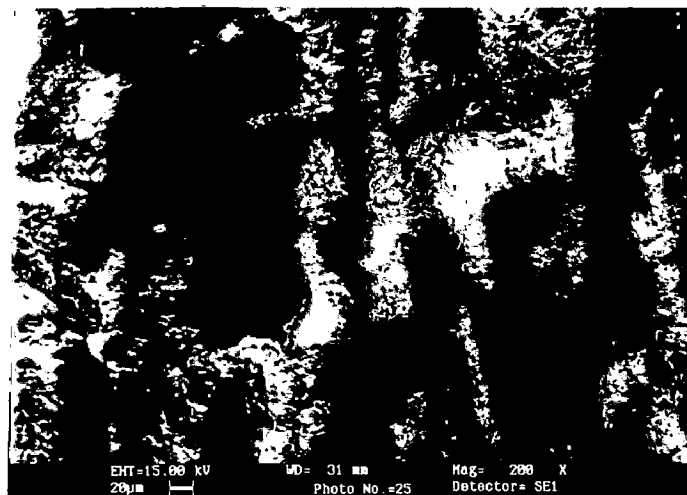


(c)

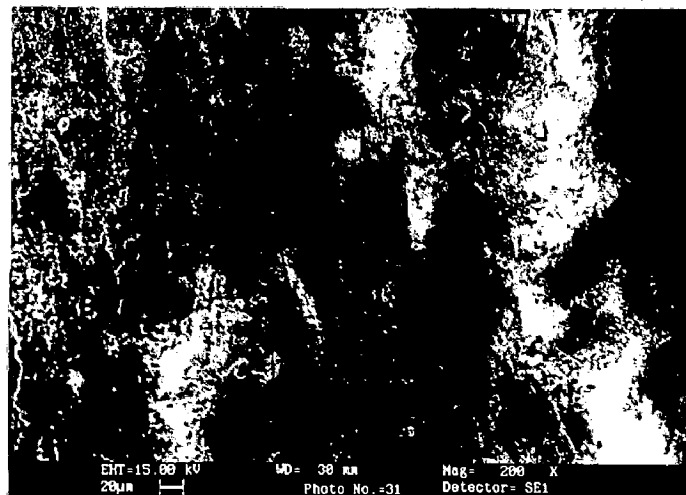
Fig. 5.36 Wear surfaces of the specimens of electroless Ni-P coated and heat treated at 400°C for 1 h specimens (HT₁-B) after sliding through (a) 540 m at 29.4 N, (b) 420 m at 34.3 N and (c) 300 m at 39.2 N.



(a)

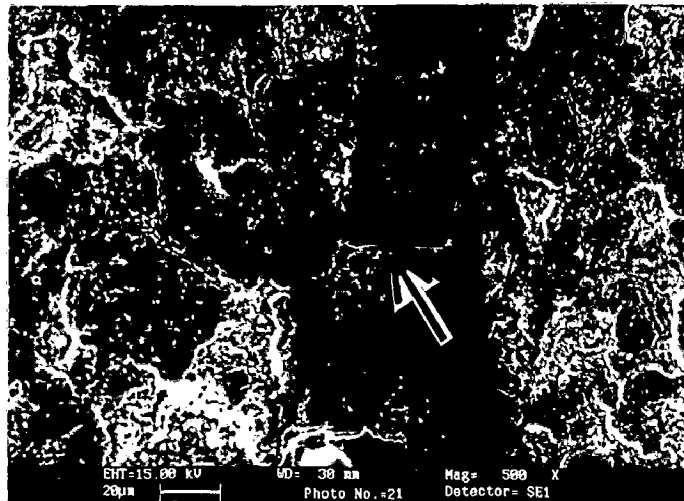


(b)

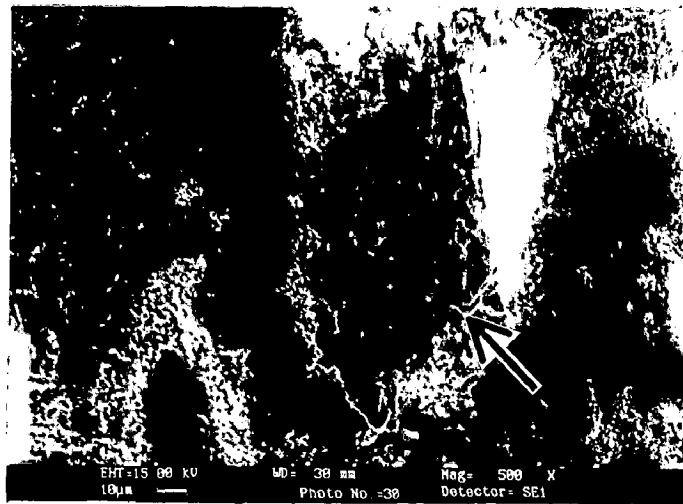


(c)

Fig. 5.37 Wear surfaces of the specimens of electroless Ni-P coated and heat treated at 400°C for 2 h specimens (HT₂-B) after sliding through (a) 420 m at 29.4 N, (b) 420 m at 34.3 N and (c) 150 m at 39.2 N.



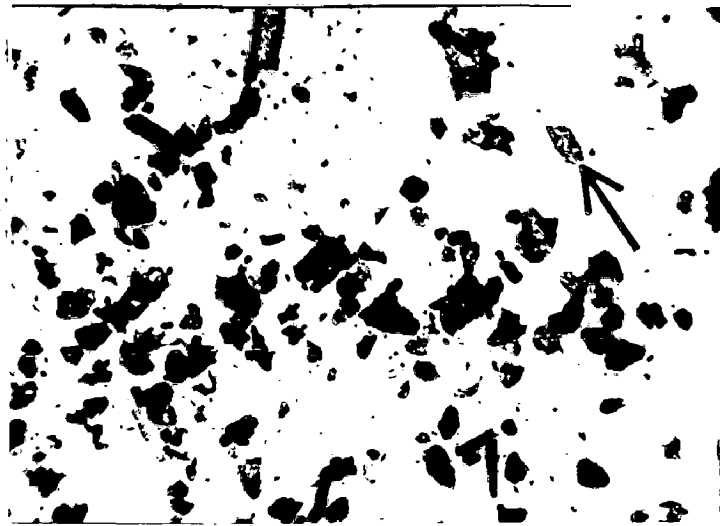
(a)



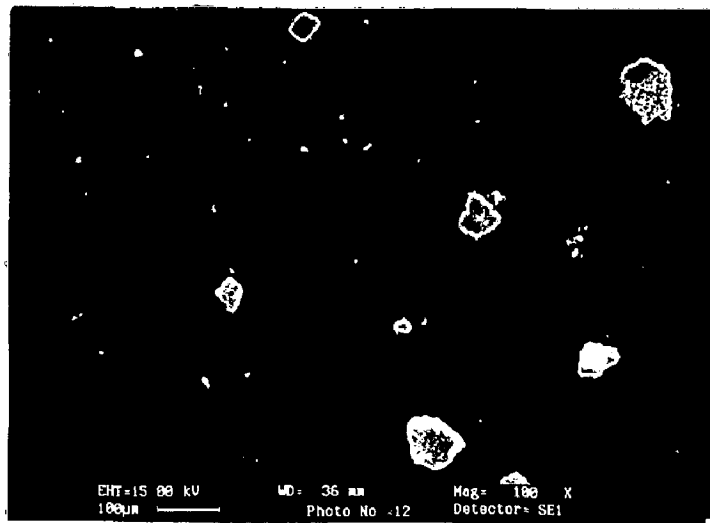
(b)

Fig. 5.38

The cracks in the transfer layer in electroless Ni-P coated and heat treated at 400°C for 2 h specimens (HT₂-B) after sliding through (a) 420 m at 29.4 N and (b) 150 m at 39.2 N.



(a)



(b)

Fig. 5.39

Wear debris of Ni-P coated steel by pooling together for different conditions (i.e., AC₂, HT₁-B and HT₂-B) after spreading on white paper for all the three normal loads, i.e., 29.4 N, 34.3 N and 39.2 N (a) optical micrograph at magnification of $\times 25$ and (b) SEM micrograph.

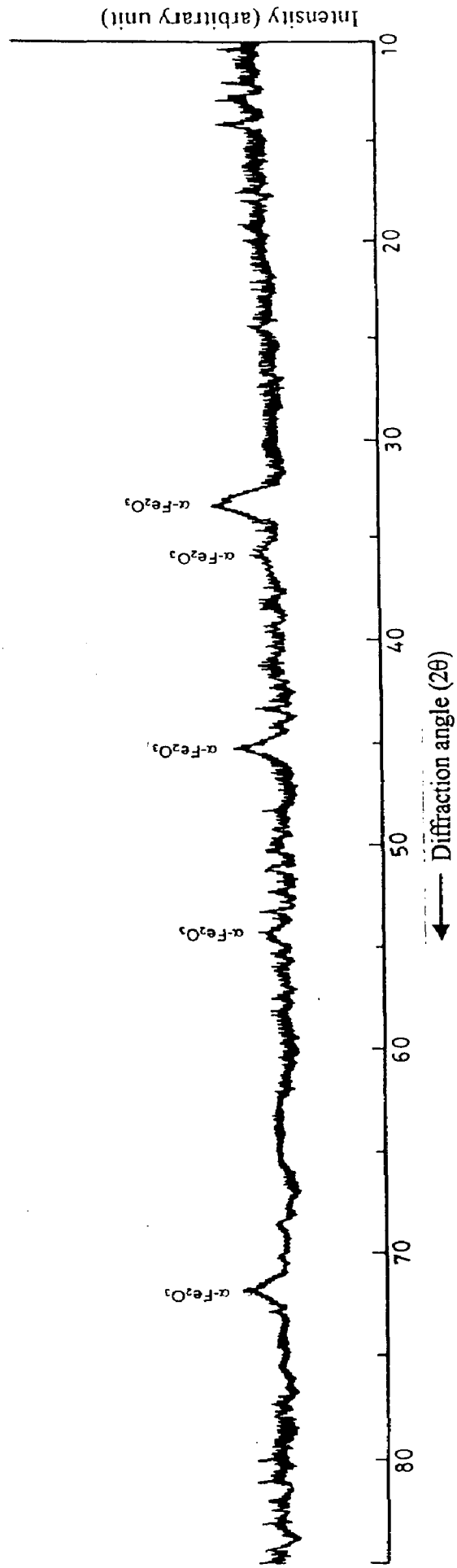


Fig. 5.40 X-ray diffraction pattern of the wear debris of normalised steel (NS) generated at all the three, i.e., 29.4 N, 34.3 N and 39.2 N normal loads and collected from the disc counterface.

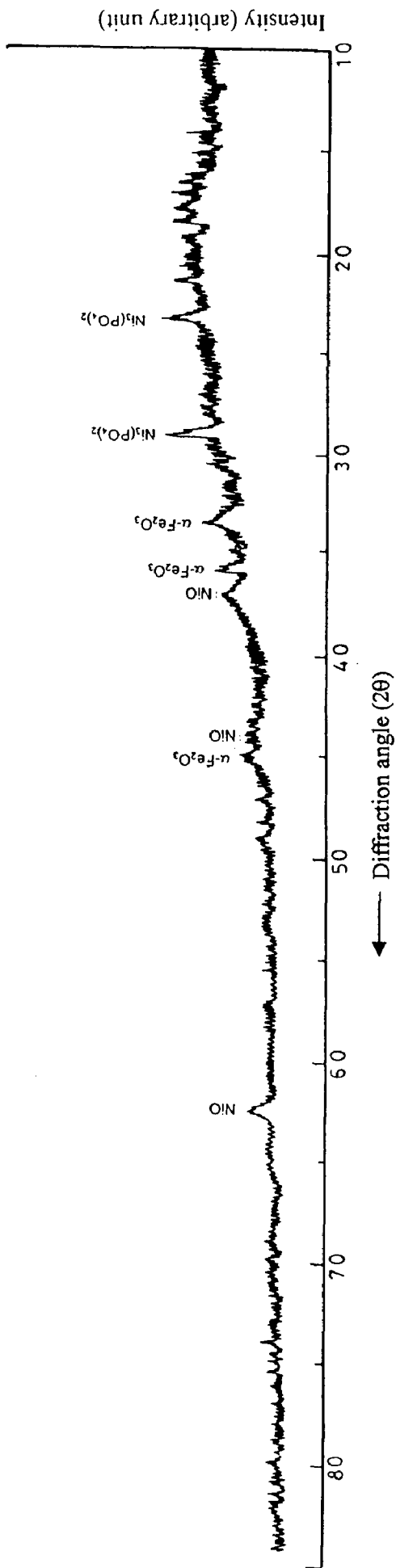


Fig. 5.41 X-ray diffraction pattern of the wear debris of Ni-P-X as-coated steel specimens (AC₁) generated at all the three, i.e., 29.4 N, 34.3 N and 39.2 N normal loads and collected from the disc counterface.

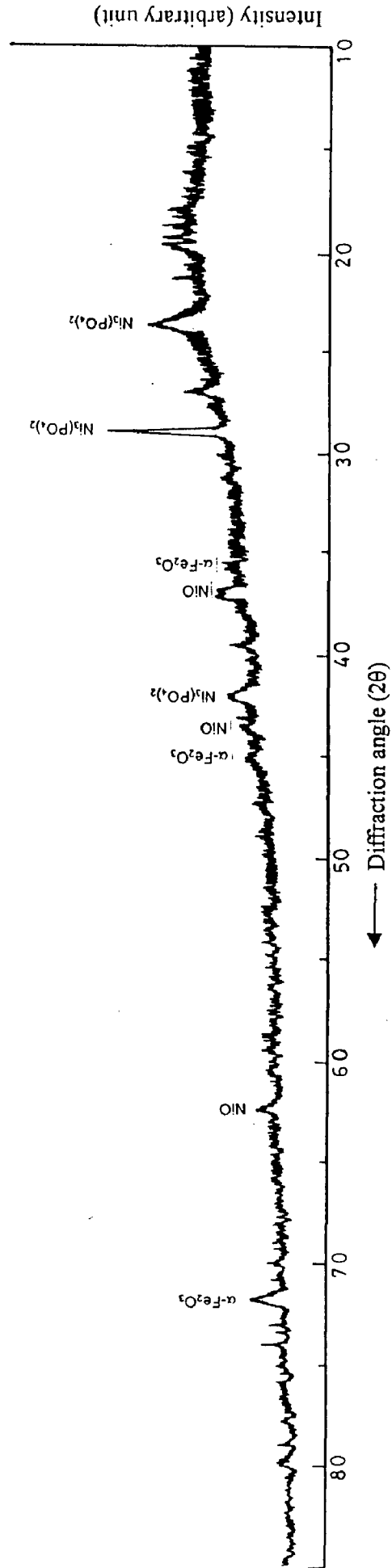
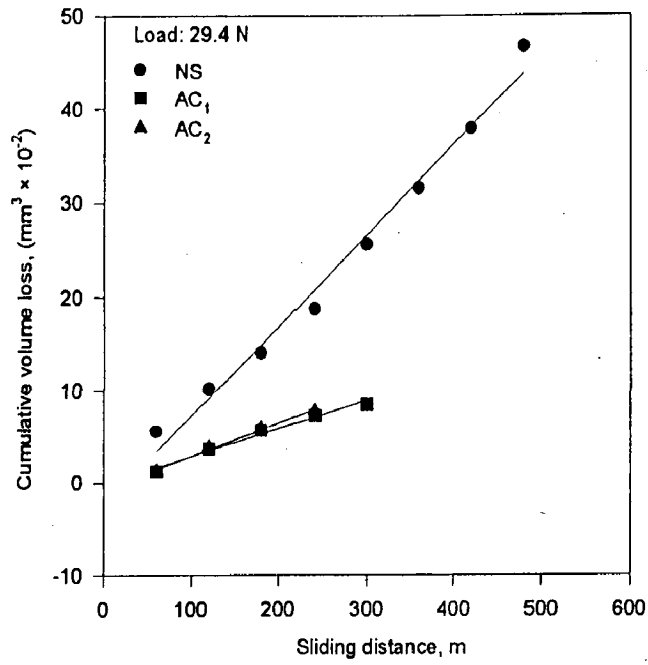


Fig. 5.42 X-ray diffraction pattern of the wear debris of Ni-P-X coated and heat treated at 400 °C for 1 h, (HT_{1-A}) and heat treated at 400 °C for 2 h, (HT_{2-A}) generated at all the three, i.e., 29.4 N, 34.3 N and 39.2 N normal loads and collected from the disc counterface.

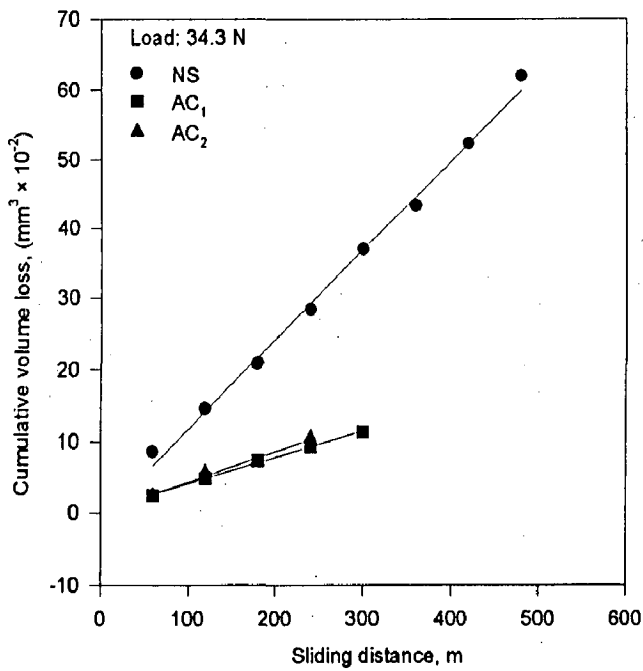
diffraction pattern obtained for the wear debris for NS samples, indicating all the three broad peaks correspond to α -Fe₂O₃ as observed by comparing the JCPDS ASTM data cards. The X-ray diffraction patterns obtained for the AC₁ and heat treated (HT₁-A + HT₂-A) are respectively shown in Figs. 5.41 and 5.42. The peaks indexed for the nickel oxide (NiO) and nickel orthophosphate octahydrate, Ni₃(PO₄)₂.8H₂O, have been observed to be primarily existing in the debris for both as-coated and heat treated samples. Apart from this at a few places, broad peaks corresponding to α -Fe₂O₃ are also observed. The characteristics of the phase constituents present in the wear debris for the Ni-P-X coating on steel (AC₁) and Ni-P-X coated and heat treated (HT₁-A + HT₂-A) are reported in Table A.15 given in appendix.

5.2 DISCUSSION

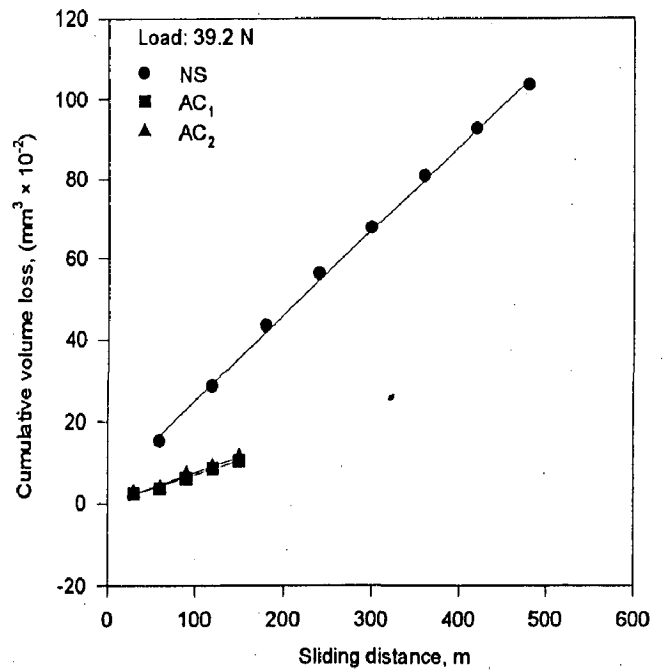
When normalised steel (NS) is coated either with a thin layer of Ni-P-X or Ni-P, the chemical nature of surface changes without any significant effect on macrohardness as shown in Table A.13. Since the real area of contact is inversely proportional to the hardness of the softer one of the two mating surfaces, it is expected that coating the steel with both the Ni-P-X and Ni-P form more or less the same extent of real area of contact on an average at a given load. This argument may not hold since asperity interaction involves micro level indentation and microhardness may be more relevant parameter for determining real area of contact. Cumulative volume loss in NS, AC₁ and AC₂ increases linearly with the sliding distance at a given load as evident from Figs. 5.3, 5.4 and 5.7 respectively. But a comparison of volume losses are shown in Figs. 5.43 (a) to (c) at three different loads and the figures clearly reveal that the cumulative volume losses decrease significantly on coating but there is only a little difference between the cumulative volume losses for Ni-P-X and Ni-P coatings. The Higher volume losses at all the loads in NS samples as observed, may be attributed to its chemical compatibility with the steel counterface disc. The substantially lower volume losses in AC₁ and AC₂ samples than those in NS under similar dry sliding conditions are observed at all the three applied loads. Therefore, a relatively less real area of contact at the sliding interface in electroless nickel coated steel-hardened steel tribosystem may explain lower volumetric wear losses in the load range of 29.4-39.2 N.



(a)



(b)



(c)

Fig. 5.43 Comparison of cumulative volume losses in NS, AC₁ and AC₂ type of wear pin samples with sliding distance at (a) 29.4 N, (b) 34.3 N and (c) 39.2 N.

During the sliding contact, even at the moderate sliding speeds the asperity temperature in most metals becomes high enough to cause significant surface oxidation (Huchings, 1992). Under the light loads wear scar tend to exhibit a smooth, glassy-like appearance and under these conditions low wear rates and finer wear particles of metallic oxides are expected (Bayer, 1994). Quinn (1983) has proposed a mechanism of oxidative wear extending the theory of sliding wear proposed by Archard (1961) to a situation involving oxidation. The form of the equation for wear rate (w) derived by both the investigators is as given below:

$$w = K_f A_r \quad (5.1)$$

where A_r is the real area of contact between sliding surfaces and K_f is the wear coefficient. K_f is sensitive to the chemical nature of the surface, thermal properties of the material, and asperity conditions, i.e., load, speed and environment (Bayer, 1994). In the study of Archard (1961), K_f is related to the probability of producing a wear particle during asperity encounter. Quinn (1971) also has assumed that on an average $1/K_A$ asperity encounters are necessary for a critical oxide film of thickness (ξ) to be built up before it becomes detached to form a wear particle, where K_A denotes the K_f for Archard's model. In oxidative wear each encounter adds to oxide thickness at a given asperity and Quinn (1971) has proposed the wear coefficient, $K_f = K_Q$, under these circumstances as:

$$K_Q = \frac{l_1 k_p}{\nu \rho_o^2 \xi^2 f_m^2} \quad (5.2)$$

where, k_p is the oxidation rate constant, l_1 is the sliding distance for a single encounter, ρ_o is density of oxide, f_m is the mass fraction of oxygen in oxide, ν is the sliding speed and ξ is the critical thickness of oxide film.

The metal surface is not virgin and is covered with absorbed gases and thin layers of oxide. During sliding, frictional heating at the asperity contacts results in temperature high enough for oxidising the region near contact as it has been mentioned earlier. This oxide

layer thickens to the critical thickness and gets removed during sliding generating wear debris. These wear debris of oxide particles gets trapped in between the sliding surfaces and get compacted into a layer called transfer layer, attached primarily to the softer one of the two sliding surfaces. This compacted layer often cracks and flakes off during sliding resulting into relatively larger sized wear debris (Tyagi *et al.*, 2001). The wear debris observed during dry sliding of normalised steel (NS), Ni-P-X coated steel (AC₁) and Ni-P coated steel (AC₂) are nonshining aggregates of finer oxide particles as shown in Figs. 5.28, 5.30 and 5.39. The X-ray diffraction analysis of the wear debris clearly reveals only diffraction peaks of Fe₂O₃ for NS sample (Fig. 5.40) and primarily NiO, Ni₃(PO₄)₂ for Ni-P-X coated steel (AC₁) as seen from Fig. 5.41. A small amount of Fe₂O₃ has also been observed in the latter sample. Thus, it is clearly established that the dry sliding wear under the conditions carried out in the present study is primarily oxidative.

It is well known that nickel has higher resistance to oxidation than steel, the latter is therefore, having relatively higher k_p than the former one. In the context of Eqs. (5.1) and (5.2), since hardness is more or less similar in NS and the coated samples AC₁ and AC₂, higher K_Q for NS due to relatively higher k_p may be responsible for the higher wear rates in NS compared to those in AC₁ and AC₂, under the given loads and sliding speed. The increase in wear rate with load may, however, be attributed to higher real area of contact due to softening caused by higher frictional heating even though there may not be any substantial change in K_Q . Such a situation could lead to more or less linear increase in wear rate with increasing load. However, in the samples NS, AC₁ and AC₂ at higher loads, the wear rate increases sharply at higher loads showing a nonlinear behaviour as given in Figs. 5.11, 5.12 and 5.13. Thus, the assumption of K_Q remaining more or less the same is not tenable for these materials. At higher load, k_p may increase at higher stress and temperature due to increasing diffusion constant. There could also be nonlinear increase in contact area with load; but in coated samples where high temperature at the asperities locally may induce phase transformation and diffusion of nickel into the underlying substrate, which may increase the hardness and counteract softening of the matrix.

Therefore, the extent of increase in wear rate with load is significantly lower at higher loads in coated samples compared to that observed for NS samples. But the present experiments are not designed to identify the exact cause of nonlinear increase in wear rate with load.

The coefficient of friction in uncoated (NS) samples of steel and those coated with Ni-P-X (AC_1) and with Ni-P (AC_2) is observed to fluctuate about the mean over the sliding distance at all the loads employed in this investigation and this can be seen from Figs. 5.16, 5.17 and 5.21. The fluctuation may be indicative of dynamic situation involving continuous formation and breaking of the transfer layer. The friction coefficient averaged over the sliding distance is found to decrease linearly with normal load as seen from Figs. 5.20 and 5.24 for both the steel samples (NS) and those coated with Ni-P-X and Ni-P (AC_1 and AC_2). However, for both the coated samples the average coefficient of friction is relatively lower than that observed for uncoated steel samples. This may again be attributed to relatively lower chemical compatibility between the coated layer and the counterface compared to that of steel and the counterface. The better compaction of the wear debris into the wear track and formation of well adhering transfer layer due to higher load may contribute to decreasing friction at higher loads. The work of Husheng *et al.* (1991) also reveals that the coefficient of friction of low and medium strength steels is reduced by Ni-P coatings.

Cumulative volume loss in the samples heat treated after Ni-P-X coating (HT_1 -A, and HT_2 -A) and the samples heat treated after Ni-P coating (HT_1 -B and HT_2 -B) increases linearly with sliding distance at a given load as evident from Figs. 5.5, 5.6 5.8 and 5.9 respectively. The substantially lower volume losses in Ni-P-X and Ni-P coated samples after heat treatment have been observed when compared to as-coated (AC_1 and AC_2) samples under similar dry sliding conditions. This may be attributed to enhancement in hardness due to heat treatment as a result of phase transformation as given in Table A.13. The lower chemical compatibility of nickel phosphide formed due to heat treatment is expected to result in less real area of contact at the interface, which may help in lowering the volumetric losses further in heat treated (HT_1 -A, HT_2 -A, HT_1 -B and HT_2 -B) samples.

As explained earlier, the continued sliding results in formation of transfer layer and cracking of this layer leads to flaked off agglomerates of oxides in the wear debris. The wear debris obtained during dry sliding of heat treated samples of HT₁-A, HT₂-A, HT₁-B and HT₂-B shows a few fine particles and primarily larger agglomerates, as given in Figs. 5.32, 5.34 and 5.39. There is no significant difference in wear debris generated during dry sliding of heat treated and as-coated samples. The X-ray diffraction pattern of the wear debris as given in Fig. 5.42 also reveals diffraction peaks of primarily NiO, Ni₃(PO₄)₂ for heat treated samples coated with Ni-P-X similarly as it was observed for as-coated samples. A small amount of Fe₂O₃ has also been observed in these heat treated samples. Thus, the dry sliding wear under the conditions employed in the present study, is also oxidative for Ni-P-X and Ni-P coated samples even after heat treatment.

Figures 5.11, 5.12 and 5.13 show relatively lower wear rates in HT₁-A, HT₂-A, HT₁-B and HT₂-B samples as compared to those observed in NS, AC₁ and AC₂. This may be ascribed to higher hardness resulting due to heat treatment. Enhanced hardness of Ni-P-X and Ni-P coating after the heat treatment may decrease the real area of contact, thereby decreasing the wear rates. The heat treatments at 400°C for 1 h and relatively longer period of 2 h resulted in more or less similar hardness in Ni-P-X coated steel pins (HT₁-A and HT₂-A) and therefore, it is not surprising that the results of wear rate at different loads are more or less identical for both these samples as shown in Fig. 5.11. Similarly, hardness of Ni-P coated samples after heat treatment (HT₁-B and HT₂-B) is almost the same after 1 h and 2 h of annealing at 400°C as given in Table A.13. Therefore, the results of wear rate at different loads are identical for both these duration of heat treatment as shown in Fig. 5.12. Saka *et al.*, (1977) have claimed that a harder substrate is able to hold a thicker transfer layer of oxide more firmly as compared to a softer one. The observed lower wear rates of HT₁-A and HT₁-B specimens may be due to their slightly higher hardness which results in a slightly higher ξ in Eq. (5.2).

Fluctuations in coefficient of friction in samples heat treated after Ni-P-X and Ni-P coated HT₁-A, HT₂-A, HT₁-B and HT₂-B samples are shown respectively in Figs. 5.18,

5.19, 5.22 and 5.23. A linearly decreasing trend in average coefficient of friction of these samples is observed similar to that observed in AC₁ and AC₂ samples as can be seen from Fig. 5.25. The asperity interactions taking place may involve oxide contact that primarily will need less energy for shearing during sliding and therefore, result in a lower coefficient of friction. Further, a surface with higher hardness has relatively lower contact area and therefore, shows a lower average coefficient of friction when compared to softer surfaces. Tyagi *et al.*, (2001) have similarly observed lower coefficient of friction for the harder material. Therefore, heat treated samples, which possess relatively higher hardness showed lower average coefficient of friction compared to those observed for as-coated samples. The linear decrease in average coefficient of friction with increasing hardness for Ni-P-X and Ni-P coated steel is evident from Fig. 5.26. As mentioned earlier, Ni-P-X and Ni-P coated steel pins after heat treatment at 400°C for 1 h (HT₁-A and HT₁-B) and those heat treated at the same temperature for relatively longer period of 2 h (HT₂-A and HT₂-B) have resulted in more or less similar hardness. The presence of X, hard ceramic oxides may result in enhanced scoring and ploughing, which may be responsible for higher friction in Ni-P-X compared to that in Ni-P coatings. The extent of oxide cover is observed to be relatively more in harder pins as compared to pins having lower hardness in the present study as seen in Figs. 5.27, 5.29, 5.31, 5.33, 5.35 to 5.38. The higher coefficient of friction in electroless composite coatings of Ni-P-B₄C compared to that observed in Ni-P alloy coatings has also been reported by Bozzini *et al.* (1999). Thus, heat treated Ni-P and Ni-P-X coatings result in relatively lower coefficient of friction compared to as-coated Ni-P and Ni-P-X coatings on steel although Ni-P-X has relatively higher hardness compared to Ni-P coating under similar treatment of either as-coated or the heat treated ones as it has been observed in this study.

The increase in wear rate with increasing load is almost linear for samples heat treated after coating. This may be attributed to stable structure in coating/substrate system. Presence of substantial amount of Ni₃P may have counteracted the tendency to softening with frictional heating. The oxidation of Ni₃P may also be slower than nickel and so the wear rate and cumulative volume loss in heat treated samples are lower than those observed

in as-coated samples. The coefficient of friction also attains a lower value on heat treatment of either Ni-P or Ni-P-X coating. The cumulative volume loss and wear rate of Ni-P and Ni-P-X coated samples are more in as-coated condition compared to those after heat treatment. It should be remembered that the amount of X is very low and it could be more effective in imparting wear resistance in relatively softer as-coated samples compared to those where substantial amount of hard Ni₃P, is primarily responsible for preventing wear. However, as stated earlier, the presence of hard ceramic particles may have contributed to scoring or ploughing during dry sliding and it may be responsible for higher coefficient of friction in Ni-P-X coatings compared to that in Ni-P coatings.

It is evident from the study reported above that substantial wear resistance could be imparted along with lower average coefficient of friction in the regime of oxidative wear by heat treating both the Ni-P and the Ni-P-X coatings on steel. Incorporating ceramic particles like X in Ni-P coating has the potential of further enhancing wear resistance if it could be incorporated in a relatively larger amounts but the coefficient of friction may increase.

FRICITION AND WEAR BEHAVIOUR OF ELECTROLESS Ni-P-X COATINGS ON ALUMINIUM

Electroless Ni-P-X ($X = \text{ZrO}_2\text{-Al}_2\text{O}_3\text{-Al}_3\text{Zr}$) coatings on commercial aluminium substrate have been heat treated at 400°C for 1 *h* and at 250°C for 12 *h* in order to arrive at the desirable heat treatment schedule for achieving better tribological properties under dry sliding friction and wear against the counterface of case hardened steel. The commercial aluminium specimens as-coated with Ni-P-X, heat treated after coating at 400°C for 1 *h* and heat treated after coating at 250°C for 12 *h* are designated as AC₃, HT₁-C and HT₂-C respectively. The aluminium pins as such without any coating have also been investigated for comparison and are designated as AL. The primary objective of this segment of investigation is to understand the effect of the Ni-P-X coating and its heat treatment on the dry sliding friction and wear behaviour of coated aluminium pins. The results have been discussed to develop a coherent understanding of the tribological behaviour of coated aluminium in terms of the composition of the coating, the changes taking place during heat treatment and their consequence on tribological properties in the context of changes observed in the hardness.

6.1 RESULTS

6.1.1 Dry Sliding Friction and Wear Behaviour

Dry sliding wear tests are carried out against hardened steel counterface at the constant sliding speed of 0.5 *m/s* under different normal loads of 4.9, 7.4, 9.8 and 12.3 *N*, by using pin-on-disc wear testing machine as described in chapter 3. The pin shaped aluminium samples coated with electroless Ni-P-X and those heat treated after coating at 400°C for 1 *h* have been tested for cumulative wear volume, wear rate, wear coefficient and coefficient of friction under the specified loads and the sliding velocity. In addition,

aluminium samples coated with Ni-P-X have been heat treated at 250°C for 12 *h* and tested for the same properties under similar dry sliding conditions. The results obtained are compared with those observed for aluminium (AL) pin samples that are used as the substrate material for coating, in this section of study. In order to confine the wear within the coating, dry sliding distances under a given load for different Ni-P-X coated pin wear samples of steel have been limited on the basis of preliminary studies in respect of volume loss behaviour and micrographic observations as described in chapter 5. The same study has been extended for this segment of investigation for Ni-P-X coating on aluminium samples by considering the weight loss data observed in Ni-P-X coating on aluminium such that the wear is primarily confined within the coatings. The limiting sliding distance selected on the basis of the above study for different types of wear pin samples at loads of 4.9, 7.4, 9.8 and 12.3 *N* are given in Table 6.1.

Table 6.1 The Sliding Distances Selected for Different Types of Wear Pins (AL, AC₃, HT₁-C and HT₂-C) for the Tests under Different Loads.

Sl. No.	Designation of the Wear Sample	Sliding Distance (<i>m</i>) as Selected for the Load (<i>N</i>)			
		4.9	7.4	9.8	12.3
1.	AL	600	600	600	600
2.	AC ₃	600	600	480	420
3.	HT ₁ -C	600	600	480	420
4.	HT ₂ -C	600	600	600	600

a) Wear behaviour

The cumulative volume losses observed with increasing sliding distance are plotted against sliding distance at different normal loads, i.e., 4.9, 7.4, 9.8 and 12.3 *N* for different types of pin samples tested under dry sliding wear. The variation of cumulative volume loss with sliding distance has been represented by linear least square fit lines so as to remain within the framework of Archard's law as extended by Quinn (1971) for oxidative wear.

Variation of cumulative volume loss with sliding distance for aluminium (AL) pin samples during dry sliding wear against the counterface of hardened steel is shown in Fig. 6.1. The cumulative volume loss increases linearly with sliding distance. At the given load of 4.9 *N*, the cumulative volume loss increases linearly from $1.22 \times 10^{-2} \text{ mm}^3$ to $34.3 \times 10^{-2} \text{ mm}^3$ when the sliding distance increases from 60 *m* to 600 *m*. Similarly, a linear increase in cumulative volume loss has also been observed for other loads. At a given sliding distance, the cumulative volume losses increase with increasing load, as shown in Fig. 6.1.

Figure 6.2 shows the variation of cumulative volume loss during dry sliding in aluminium pin samples coated with Ni-P-X (AC₃). A linearly increasing cumulative volume loss with sliding distance has been commonly observed for all the three different loads used for the present investigation. The cumulative volume loss is observed to increase with increasing applied normal load. The cumulative volume losses of AC₃ at 4.9 and 7.4 *N* loads have been observed to be $11.0 \times 10^{-2} \text{ mm}^3$ and $12.2 \times 10^{-2} \text{ mm}^3$ respectively after 420 *m* sliding and those at the loads of 9.8 and 12.3 *N* are observed to be $14.23 \times 10^{-2} \text{ mm}^3$ and $18.3 \times 10^{-2} \text{ mm}^3$ after sliding through the same distance. The corresponding cumulative volume losses have been observed to be substantially lower than those observed in AL type of pins, which were found to be 23.3×10^{-2} , 27.0×10^{-2} , 34.3×10^{-2} and $35.3 \times 10^{-2} \text{ mm}^3$ respectively for the loads of 4.9, 7.4, 9.8 and 12.3 *N* after 420 *m* of sliding.

Variation of cumulative volume loss with sliding distance in Ni-P-X coated pin samples of aluminium and those heat treated at 400°C for 1 *h* (HT₁-C) during dry sliding is shown in Fig. 6.3. The cumulative volume loss of HT₁-C, while dry sliding against the hardened steel counterface at load of 4.9 *N* increases linearly with the sliding distance. Similar trends of linearly increasing cumulative volume loss with sliding distance are also observed for other loads of 7.4, 9.8 and 12.3 *N* as shown in Fig. 6.3. The cumulative wear volume loss is found to be 3.66×10^{-2} , 8.54×10^{-2} , 11.4×10^{-2} and $16.3 \times 10^{-2} \text{ mm}^3$ after sliding through a distance of 420 *m* at normal loads of 4.9, 7.4, 9.8 and 12.3 *N*

respectively. These wear volumes are significantly less than those observed for both the AL and the AC₃ types of pin wear samples as mentioned in the previous paragraph. The cumulative volume loss in Ni-P-X coating heat treated at 400°C for 1 h (HT₁-C) is less than that observed in the substrate as such (AL) as well as in the samples coated with Ni-P-X (AC₃), at any sliding distance under the different loads employed in the investigation.

Variation of cumulative volume loss with sliding distance during dry sliding of Ni-P-X coated pin samples of aluminium heat treated at lower temperature of 250°C for a longer time of 12 h (HT₂-C) is shown in Fig. 6.4. The linearly increasing cumulative volume loss in wear with sliding distance has been observed under the different loads employed in this investigation as seen from Fig. 6.4. The volume loss in wear increases with increasing applied load for the entire range of sliding distance covered as seen in Fig. 6.4. Cumulative volume loss of 3.25×10^{-2} , 6.1×10^{-2} , 9.76×10^{-2} and $11.0 \times 10^{-2} \text{ mm}^3$ have been observed for different loads of 4.9, 7.4, 9.8 and 12.3 N respectively, for the same sliding distance of 420 m. At the lower load of 4.9 N, the cumulative wear volume in HT₁-C was found to be $3.66 \times 10^{-2} \text{ mm}^3$ after sliding through 420 m, which is relatively higher than that observed in HT₂-C pin. At the highest load of 12.3 N applied on the samples, HT₁-C showed $16.3 \times 10^{-2} \text{ mm}^3$ wear volume after sliding of 420 m, whereas the corresponding volume loss observed in HT₂-C pin has been found to be $11.0 \times 10^{-2} \text{ mm}^3$. HT₂-C type of pins show a relatively lower volume loss than HT₁-C type of pin samples particularly at the higher loads and sliding distance at the fixed sliding speed of 0.5 m/s. The HT₂-C type of pins also show significantly lower volume loss in wear when compared with AC₃ and AL types of pins.

As explained earlier in chapter 5, the slope of the variation of cumulative volume loss with increasing sliding distance has been used to determine the wear rate. The primary objective of this segment of study is to determine the wear rate of Ni-P-X coating on aluminium pin samples with and without heat treatment, i.e., AC₃, HT₁-C and HT₂-C, during dry sliding wear against hardened steel counterface at constant sliding speed of

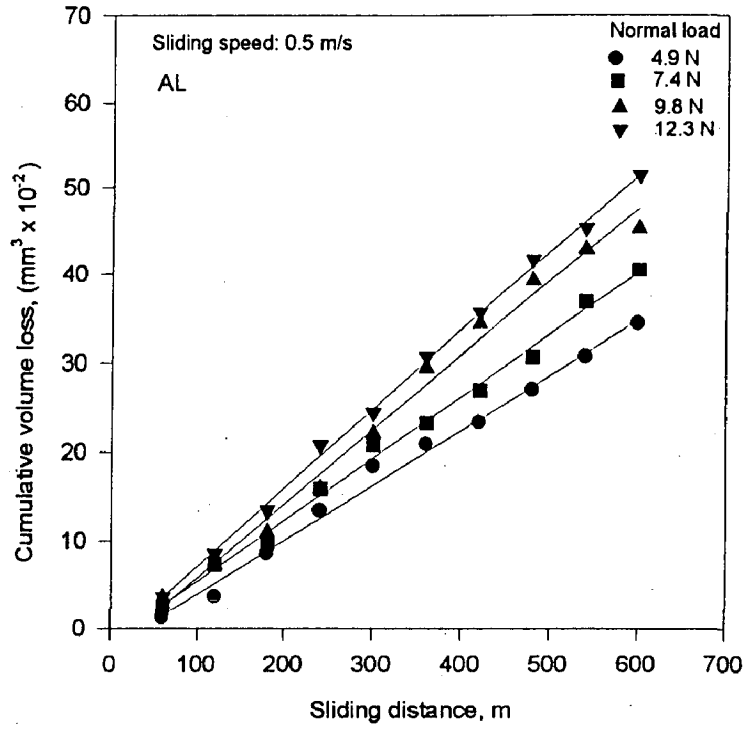


Fig. 6.1 Cumulative wear volume with sliding distance at different loads in commercial aluminium (AL).

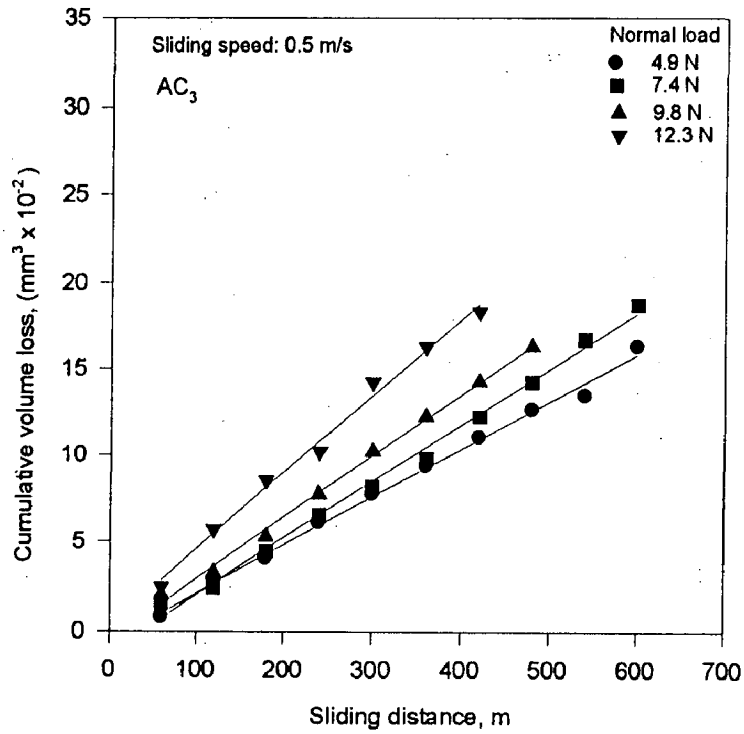


Fig. 6.2 Cumulative wear volume with sliding distance at different loads in electroless Ni-P-X as-coated aluminium (AC₃).

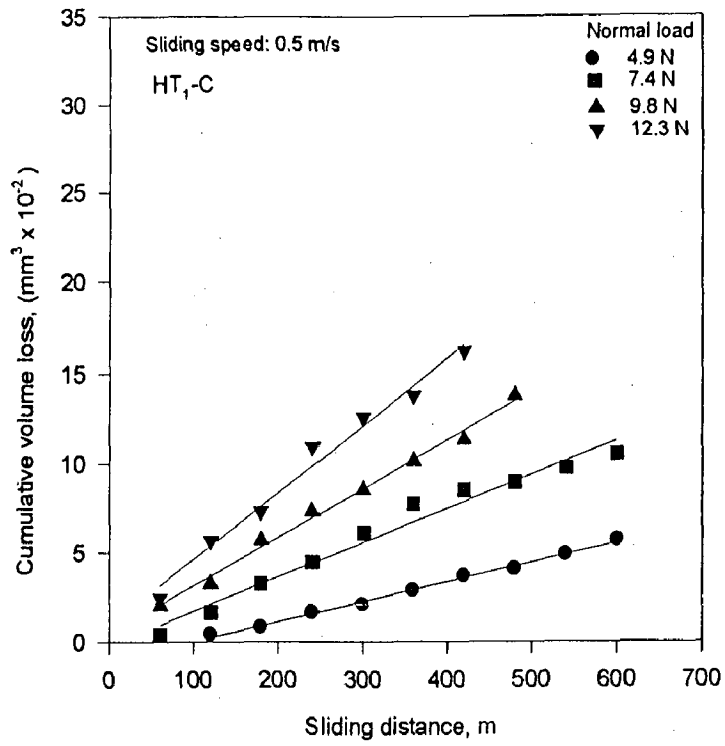


Fig. 6.3 Cumulative wear volume with sliding distance at different loads in electroless Ni-P-X coated and heat treated at 400°C for 1 h specimens (HT₁-C).

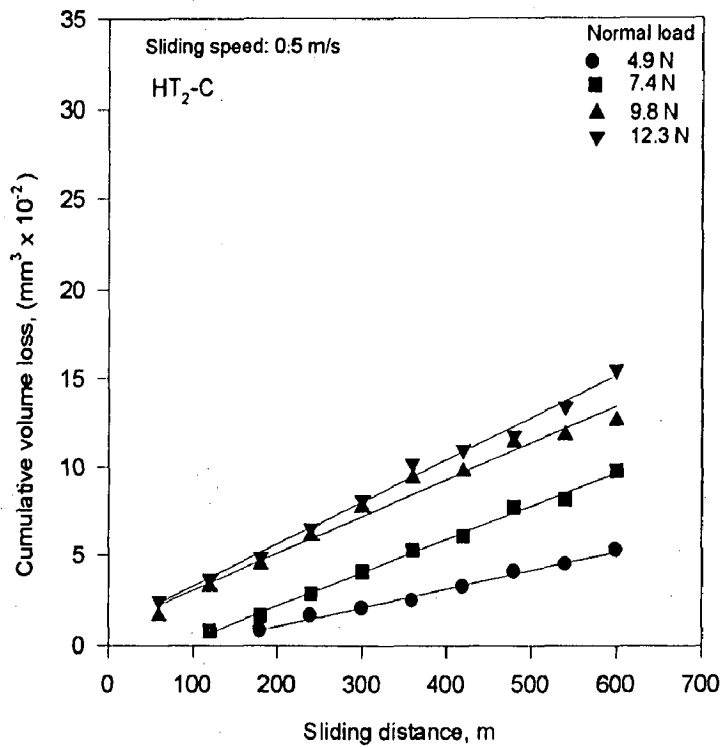


Fig. 6.4 Cumulative wear volume with sliding distance at different loads in electroless Ni-P-X coated and heat treated at 250°C for 12 h specimens (HT₂-C).

0.5 *m/s* under the applied normal loads of 4.9, 7.4, 9.8 and 12.3 *N*. In order to understand the capability of Ni-P-X coating in improving the resistance to wear of aluminium substrate. This study also includes the determination of the wear rate in aluminium pin samples under similar conditions for the purpose of comparison.

The variation of wear rate with applied normal load in different types of wear pins during dry sliding wear has been shown in Fig. 6.5. Wear rate is found to increase more or less linearly with load for different wear pins. Wear rate for the substrate aluminium (AL) has been observed to be the highest when compared to any of the Ni-P-X coating on aluminium in either as-coated or heat treated conditions. The wear rate of Ni-P-X coated aluminium (AC₃) type of pins has been observed to be substantially lower than that of substrate aluminium (AL), and it decreases further on heat treatment. Decreasing the heat treatment temperature from 400°C to 250°C and at the same time increasing heat treatment time from 1 *h* to 12 *h*, decreases the wear rate as observed from the wear rates of HT₁-C and HT₂-C samples at the loads of 4.9, 7.4, 9.8 and 12.3 *N*. At higher load of 12.3 *N*, the wear rate of HT₁-C is relatively larger compared to that in HT₂-C indicating enhancement in wear resistance with longer heat treatment at relatively lower temperature. Ni-P-X coated and heat treated aluminium pin at 400°C for 1 *h* (HT₁-C) samples are observed to possess lower wear rate than those observed for both the AC₃ and AL type of samples at the similar loads. However, as the load is increased the wear rate of HT₁-C samples approaches the wear rate observed in as-coated aluminium (AC₃) samples.

Figure 6.6 shows the variation of wear rate with macrohardness for the different wear pins, viz., AL, AC₃, HT₁-C and HT₂-C under different normal loads of 4.9, 7.4, 9.8 and 12.3 *N*. It is observed that the wear rate decreases as the Vickers macrohardness of the pin increases. The substrate aluminium having a relatively lower hardness value of 23 *VHN* has shown the maximum wear rates, i.e., 6.16×10^{-4} , 6.94×10^{-4} , 8.36×10^{-4} and 8.88×10^{-4} *mm*³/*m* for the applied normal loads of 4.9, 7.4, 9.8 and 12.3 *N* respectively. At the hardness of 31 *VHN* achieved after heat treating the Ni-P-X coating on aluminium at 250°C for 12 *h* (HT₂-C), the wear rate has been found to be the minimum, i.e.,

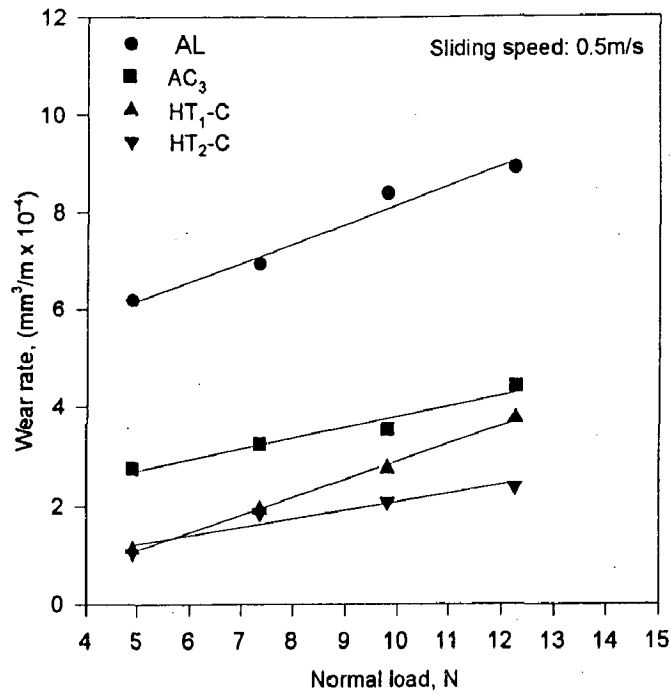


Fig. 6.5 Variation of wear rate with normal load in commercial aluminium (AL), electroless Ni-P-X as-coated aluminium (AC₃), electroless Ni-P-X coated and heat treated at 400°C for 1 h specimens (HT₁-C) and electroless Ni-P-X coated and heat treated at 250°C for 12 h specimens (HT₂-C).

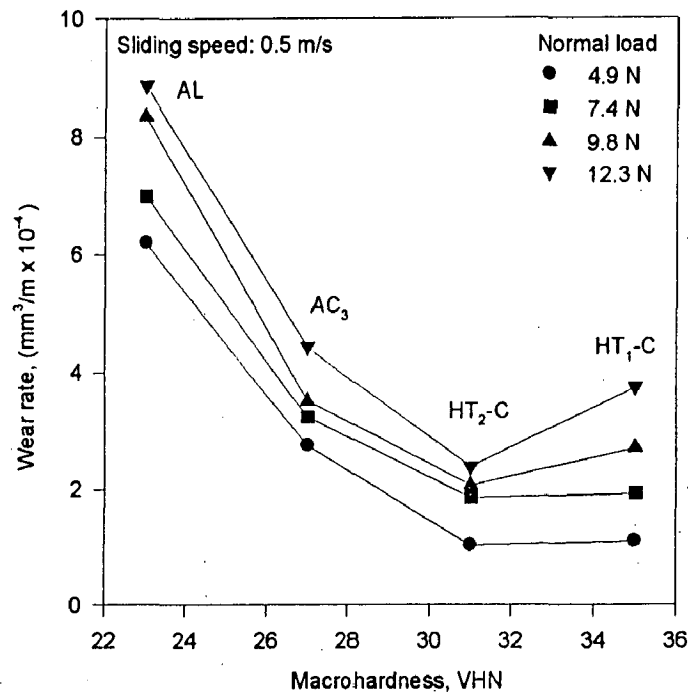


Fig. 6.6 Variation of wear rate with macrohardness of the wear pin specimen in commercial aluminium (AL), electroless Ni-P-X as-coated aluminium (AC₃), electroless Ni-P-X coated and heat treated at 400°C for 1 h specimens (HT₁-C) and electroless Ni-P-X coated and heat treated at 250°C for 12 h specimens (HT₂-C) at different normal loads.

1.04×10^{-4} , 1.86×10^{-4} , 2.08×10^{-4} and $2.38 \times 10^{-4} \text{ mm}^3/\text{m}$ for the applied loads of 4.9, 7.4, 9.8 and 12.3 N respectively as seen from Fig. 6.6. The Ni-P-X coated samples heat treated at higher temperature of 400°C for only 1 h (HT₁-C) demonstrates relatively higher wear rates than those observed for HT₂-C samples as seen in Fig. 6.6 even though the former has a relatively higher hardness of 35 VHN . The wear rates for AC₃ and HT₁-C samples are observed to be in between those observed for AL and HT₂-C samples at all the loads employed in the present work.

In order to understand the effect of decrease in aluminium substrate hardness due to heat treatment at 400°C for 1 h , the variation in wear rate for AC₃, HT₁-C and HT₂-C samples having different hardness, for coating as well as for the substrate beneath it, has been plotted for $(H_{\text{coating}} \times H_{\text{substrate}})^{1/2}$ and shown in Fig. 6.7. The wear rate is observed to decrease commonly for all the loads so long as the substrate hardness does not change significantly as in cases of AC₃ and HT₂-C samples. When the aluminium substrate has relatively lower hardness due to heat treatment at relatively higher temperature of 400°C for only 1 h duration, the wear rate at lower loads of 4.9 and 7.4 N is observed to almost saturate and when the load is increased further to 7.4 N , the wear rate is found to increase as seen in Fig. 6.7.

The wear coefficients for the different wear pin samples with and without coating on aluminium substrate have been determined by multiplying the slope of the variation of wear rate with load by corresponding hardness in N/mm^2 as mentioned earlier in context of samples with steel substrates in chapter 5. The wear coefficients calculated are given in Table 6.2.

Table 6.2 Wear Coefficients for Different Types of Wear Pin Samples (AL, AC₃, HT₁-C and HT₂-C) during Dry Sliding.

Sl. No.	Wear Pin Type	Wear Coefficient Calculated by Linear Regression, $k \times 10^{-5}$
1.	AL	0.87
2.	AC ₃	0.57
3.	HT ₁ -C	1.22
4.	HT ₂ -C	0.52

(b) Friction behaviour

Measurement of frictional force has been carried at definite interval of time (2 min) without interrupting the test. The coefficient of friction has been computed by dividing the frictional force by applied normal load as mentioned earlier in chapter 5. The variations of coefficient of friction with sliding distance have been determined to understand the friction behaviour in aluminium substrate (AL), Ni-P-X coated aluminium (AC₃), Ni-P-X coated aluminium heat treated at 400°C for 1 h (HT₁-C) and that heat treated at relatively lower temperature of 250°C for longer duration of 12 h after Ni-P-X coating on aluminium (HT₂-C).

The variation of coefficient of friction with sliding distance during dry sliding wear of aluminium substrate (AL) for 4.9, 7.4, 9.8 and 12.3 N is shown in Fig. 6.8. For all the four loads, the coefficient of friction is found to fluctuate around a mean level and the ranges of fluctuation of the coefficient of friction for the applied normal loads of 4.9, 7.4, 9.8 and 12.3 N are 0.89-1.02, 0.70-0.92, 0.69-0.77 and 0.68-0.78 respectively during sliding through a distance of 600 m as shown in Table 6.3. The ranges of fluctuation of coefficient of friction in different types of samples investigated in the present study at the specified load and sliding distance are also given in Table 6.3.

The variation of coefficient of friction with sliding distance for Ni-P-X coated aluminium pins (AC₁) is demonstrated in Fig. 6.9 for different loads of 4.9, 7.4, 9.8 and 12.3 N. The coefficient of friction for AC₃ samples has been observed to fluctuate in relatively higher range of values as compared to those for aluminium substrate (AL) for similar loads as shown in Fig. 6.9 and given in Table 6.3.

The variation in coefficient of friction observed during dry sliding of aluminium pins heat treated at 400°C for 1 h after coating with Ni-P-X (HT₁-C), is shown in Fig. 6.10 under different normal loads of 4.9, 7.4, 9.8 and 12.3 N employed during sliding. At the load of 29.4 N, the value of coefficient of friction is found to fluctuate between 0.87-1.10 over 600 m of sliding distance covered, which is relatively lower than that observed for the AC₃ but higher than those for AL samples. Similar variations in coefficient of friction

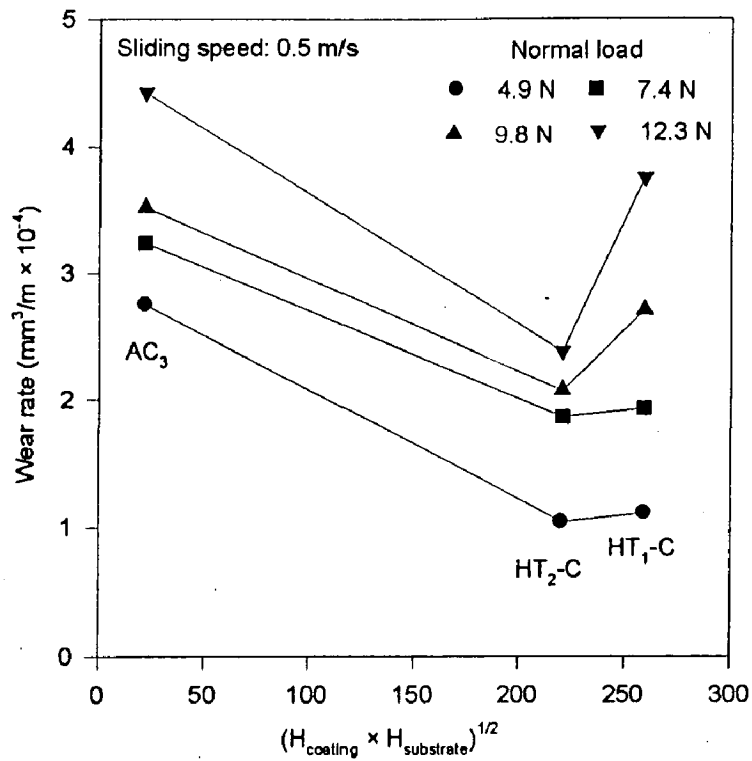


Fig. 6.7

Wear rate vs. $(H_{\text{coating}} \times H_{\text{substrate}})^{1/2}$ in commercial aluminium (AL), electroless Ni-P-X as-coated aluminium (AC₃), electroless Ni-P-X coated and heat treated at 400°C for 1 h specimens (HT₁-C) and electroless Ni-P-X coated and heat treated at 250°C for 12 h specimens (HT₂-C) at different normal loads.

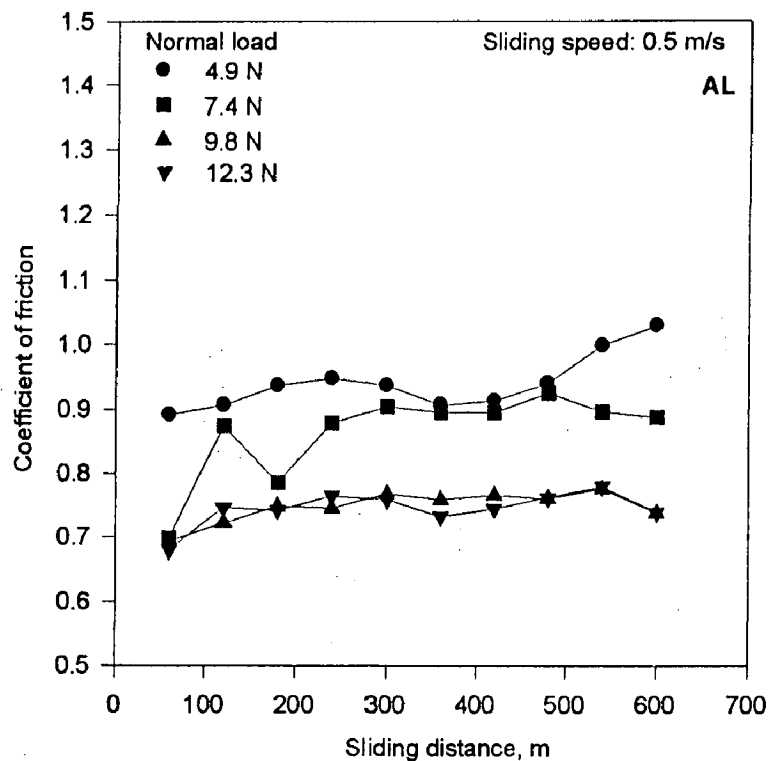


Fig. 6.8

Variation of sliding friction coefficient with sliding distance at different loads in commercial aluminium (AL).

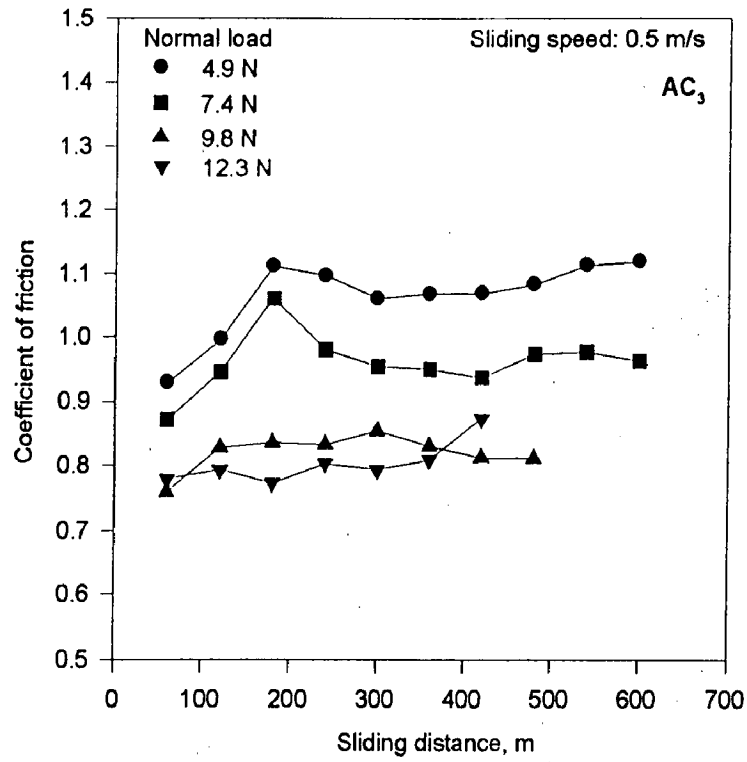


Fig. 6.9 Variation of sliding friction coefficient with distance at different loads in electroless Ni-P-X as-coated aluminium (AC₃).

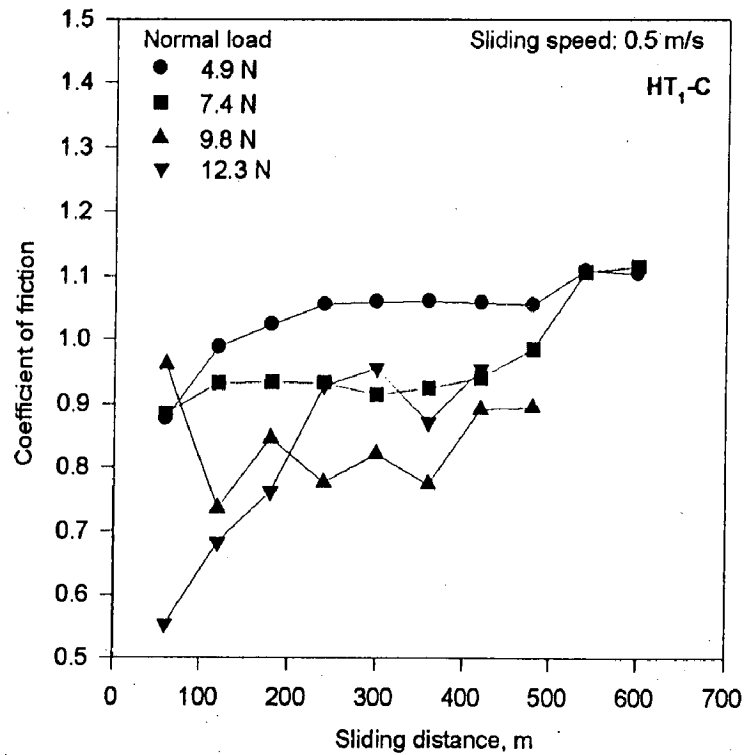


Fig. 6.10 Variation of sliding friction coefficient with distance at different loads in electroless Ni-P-X coated and heat treated at 400°C for 1 h specimens (HT₁-C).

between the ranges are observed at higher loads of 7.4, 9.8 and 12.3 *N*, which are mentioned in Table 6.3. The coefficient of friction for HT₁-C pin samples have been observed to fluctuate over a relatively higher range of values as compared to those for both the aluminium substrate (AL) and the Ni-P-X coated aluminium (AC₃), especially at higher loads of 9.8 and 12.3 *N* as seen in Figs. 6.8 –6.10.

Table 6.3 Ranges of Fluctuation of Coefficient of Friction (μ) in Different Types of Pin Samples (AL, AC₃, HT₁-C and HT₂-C) at Specified Loads.

Sl. No.	Sample Coating	Heat Treatment	Load, <i>N</i>	Range of μ Values
1.	AL	--	4.9	0.89-1.02
			7.4	0.70-0.92
			9.8	0.69-0.77
			12.3	0.68-0.78
2.	AC ₃	--	4.9	0.92-1.12
			7.4	0.87-1.05
			9.8	0.75-0.85
			12.3	0.77-0.87
3.	HT ₁ -C	At 400°C for 1 <i>h</i>	4.9	0.87-1.10
			7.4	0.88-1.11
			9.8	0.55-0.95
			12.3	0.69-0.89
4.	HT ₂ -C	At 250°C for 12 <i>h</i>	4.9	0.91-1.16
			7.4	0.92-1.12
			9.8	0.86-0.91
			12.3	0.66-0.90

Note: -- indicates that the heat treatment is not applicable in the particular type of sample.

The variations in coefficient of friction with sliding distance for Ni-P-X coated samples after heat treatment at relatively lower temperature of 250°C for a longer period of 12 *h* aluminium (HT₂-C) is shown in Fig. 6.11 at different loads of 4.9, 7.4, 9.8 and 12.3 *N*. For all the four loads, the coefficient of friction is found to fluctuate around mean level and the ranges of coefficient of friction observed for the applied normal loads employed and the corresponding sliding distances covered are given in Table 6.3. The values of coefficient of friction for HT₂-C pin samples have been observed to fluctuate more or less in similar range as compared to those for HT₁-C samples.

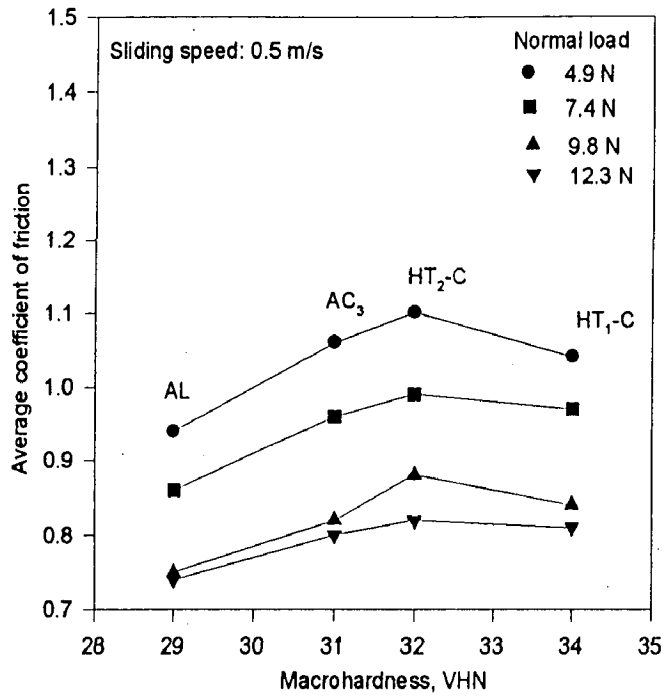


Fig. 6.13 Variation of average coefficient of friction with hardness during wear in commercial aluminium (AL), electroless Ni-P-X as-coated aluminium (AC₃), electroless Ni-P-X coated and heat treated at 400°C for 1 h specimens (HT₁-C) and electroless Ni-P-X coated and heat treated at 250°C for 12 h specimens (HT₂-C).

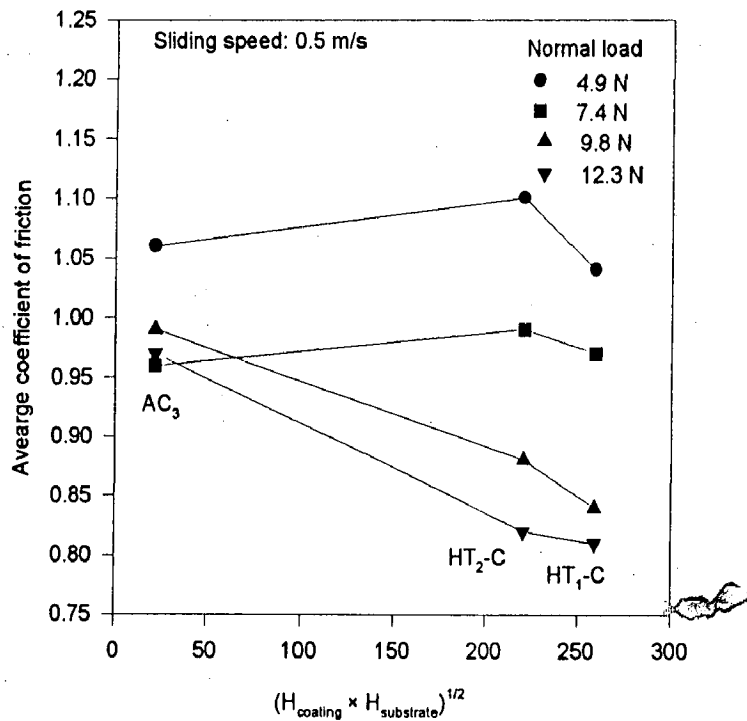
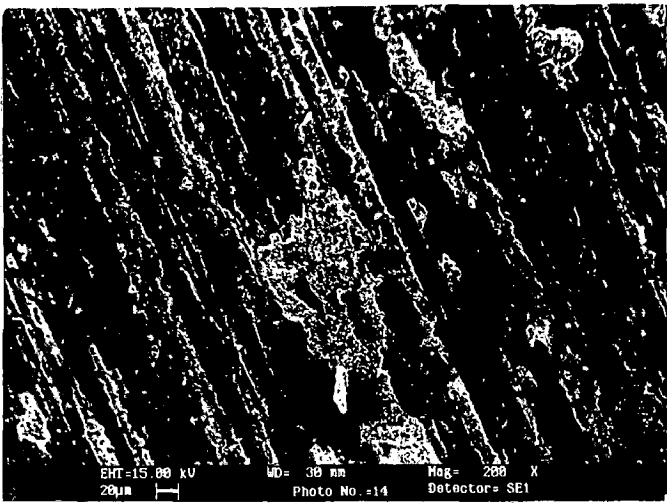
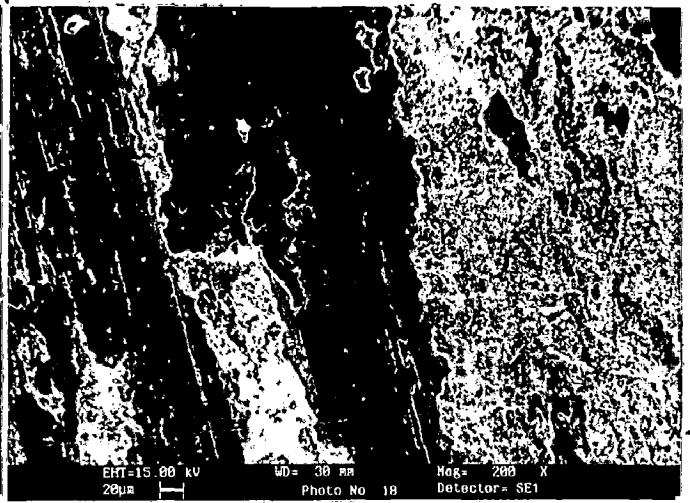


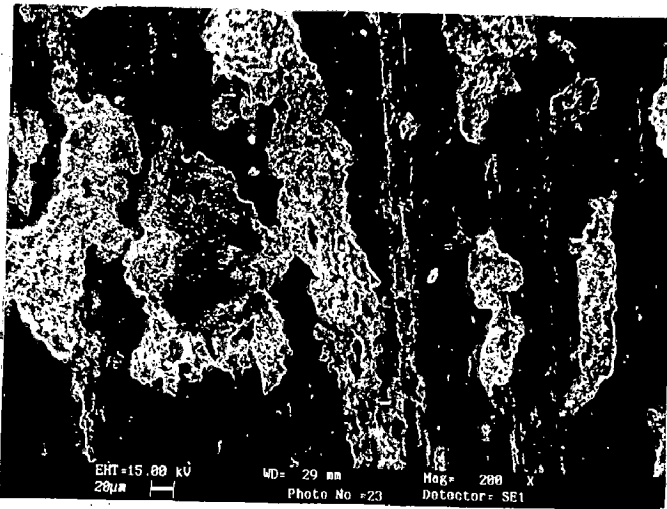
Fig. 6.14 Average coefficient of friction vs. $(H_{\text{coating}} \times H_{\text{substrate}})^{1/2}$ in commercial aluminium (AL), electroless Ni-P-X as-coated aluminium (AC₃), electroless Ni-P-X coated and heat treated at 400°C for 1 h specimens (HT₁-C) and electroless Ni-P-X coated and heat treated at 250°C for 12 h specimens (HT₂-C) at different normal loads.



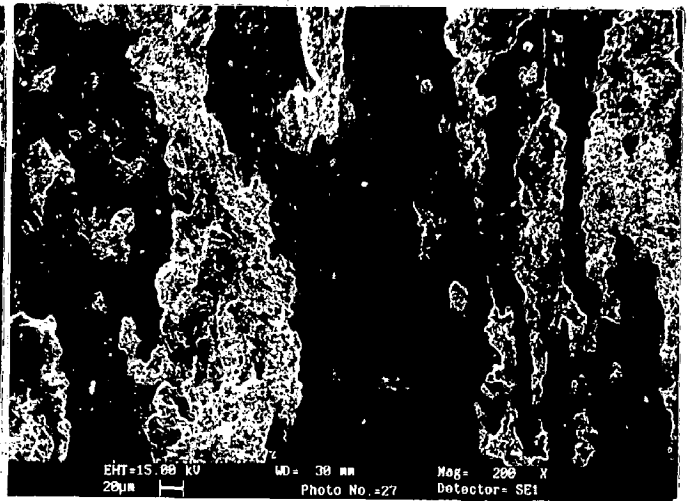
(a)



(b)



(c)

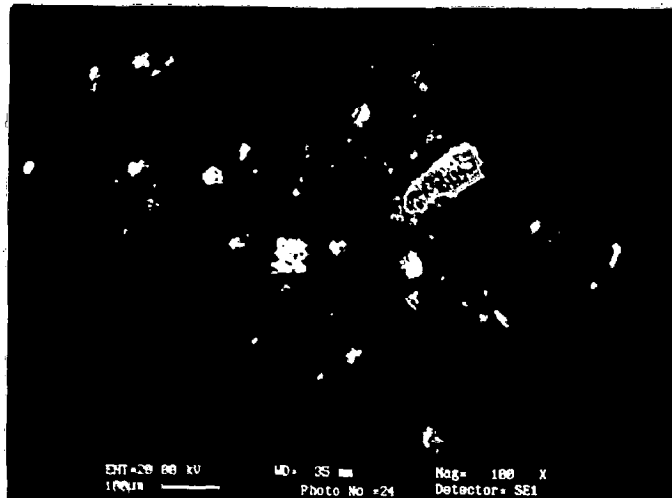


(d)

Fig. 6.15 Wear surfaces of the specimens of aluminium (AL) after sliding through a distance of 600 m at the normal load of (a) 4.9 N, (b) 7.4 N, (c) 9.8 N and (d) 12.3 N.



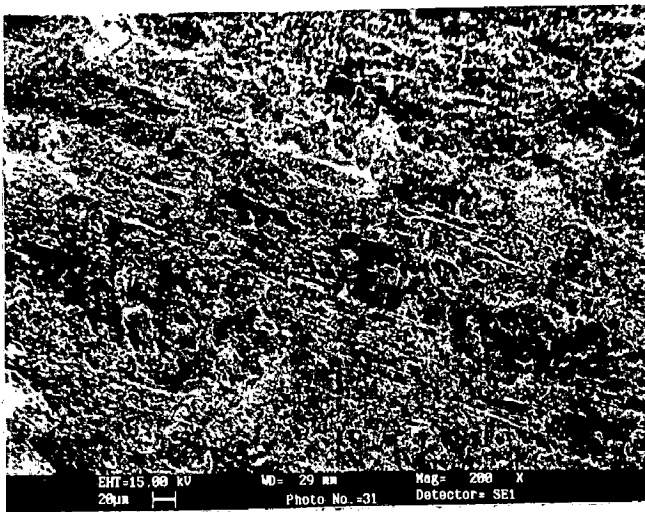
(a)



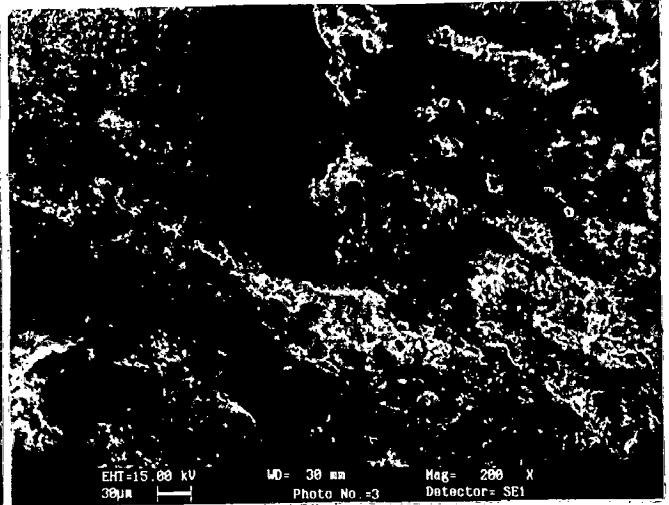
(b)

Fig. 6.16

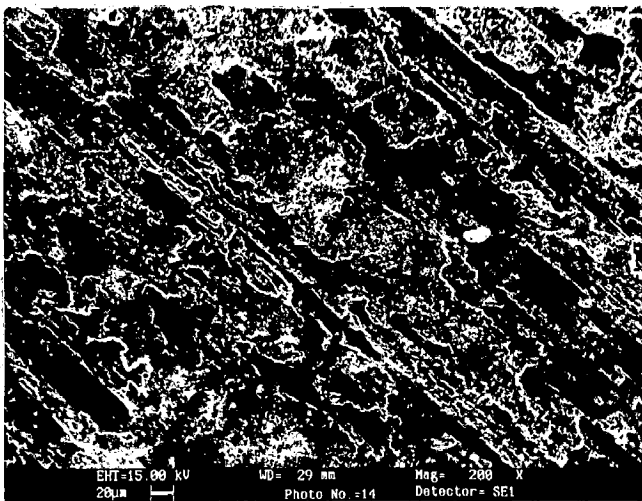
Wear debris of aluminium substrate (AL) after spreading on white paper
(a) optical micrograph at magnification of $\times 25$ and (b) SEM micrograph.



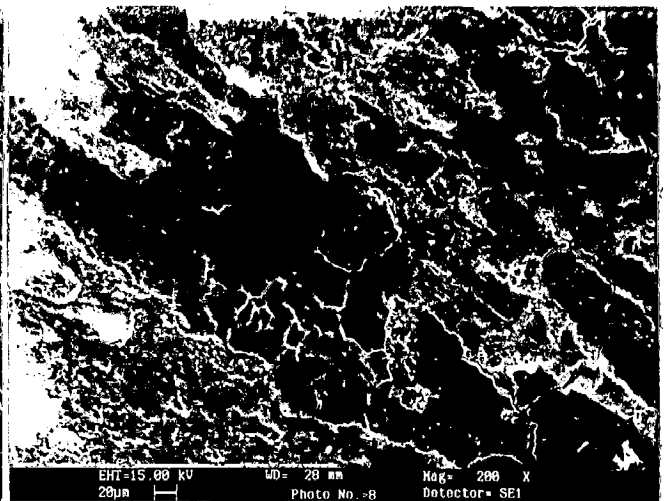
(a)



(b)

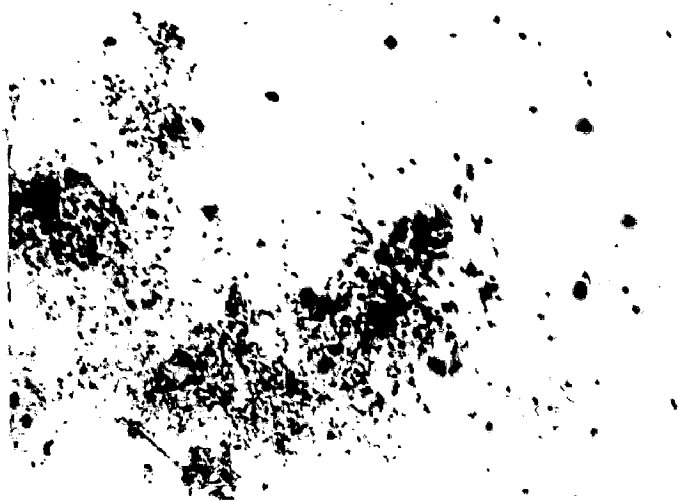


(c)

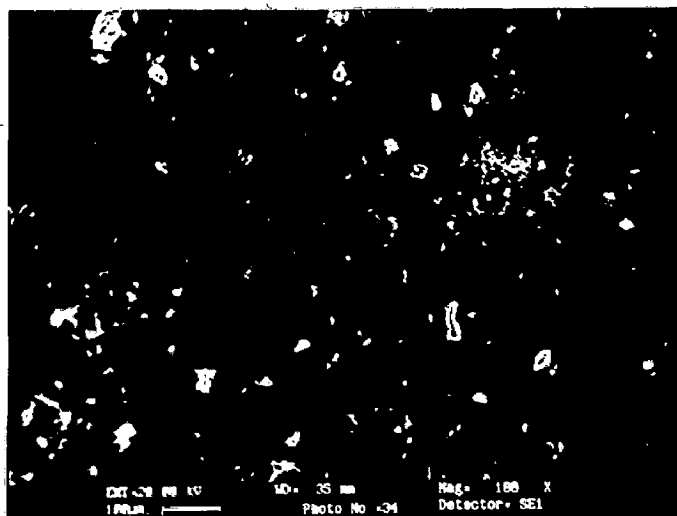


(d)

Fig. 6.17 Wear surfaces of the specimens of electroless Ni-P-X as-coated aluminium (AC₃) after sliding through (a) 600 *m* at 4.9 *N*, (b) 600 *m* at 7.4 *N*, (c) 480 *m* at 9.8 *N* and (d) 420 *m* at 12.3 *N*.



(a)



(b)

Fig. 6.18 Wear debris of electroless Ni-P-X as-coated aluminium (AC_3) after spreading on white paper (a) optical micrograph at magnification of $\times 25$ and (b) SEM micrograph.

can be seen in Figs. 6.19 (a) to (d). The cracks in the transfer layer are observed at relatively higher loads and appropriate arrows in Figs. 6.19 (c) and (d) indicate the cracks.

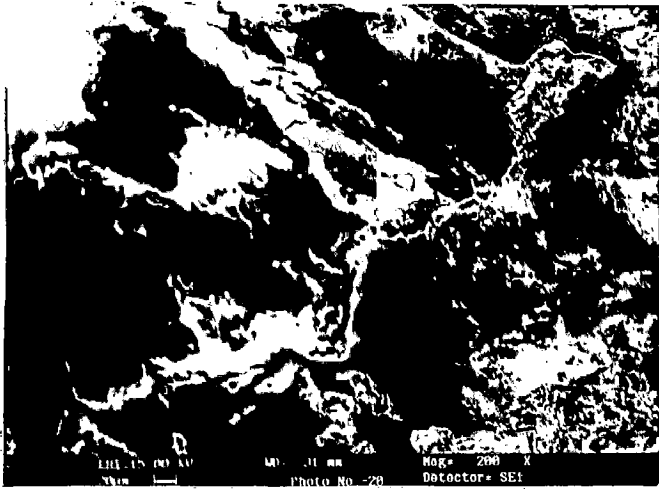
The wear debris collected during dry sliding of Ni-P-X coated aluminium samples heat treated at 400° C for 1 h (HT₁-C) type of wear pin specimens under optical microscope and SEM are shown in Figs. 6.20 (a) and (b) respectively. Coarser flaky debris and agglomerates of fine oxide particles are observed in above micrographs. The flaked off laminae from the transfer layer of relatively larger size are more predominantly observed in these micrographs.

The SEM micrographs of the wear surface for Ni-P-X coated aluminium samples heat treated at relatively lower temperature of 250°C for a longer time of 12 h (HT₂-C) after sliding through 600 m at different loads of 4.9, 7.4, 9.8 and 12.3 N are shown in Figs. 6.21 (a), (b), (c) and (d) respectively. These figures reveal compacted transfer layers and wear tracks similar to those observed in HT₁-C type of samples.

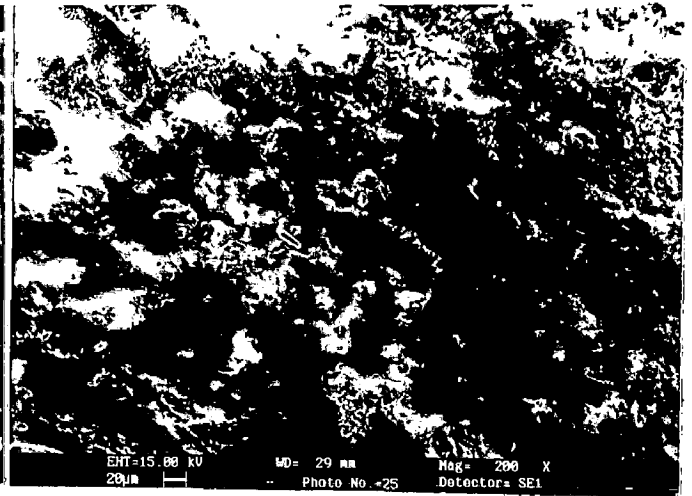
Figures 6.22 (a) and (b) respectively show the optical and SEM micrographs of wear debris collected during dry sliding of HT₂-C types of wear pin specimens. Coarser flaky debris of compacted oxide is commonly observed in above micrographs. A few finer oxide particles are also observed in the above mentioned figures.

6.1.3 X-Ray Diffraction Analysis

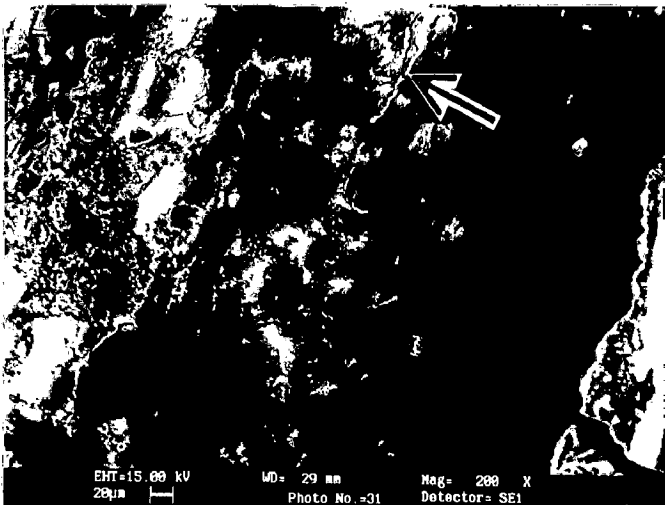
The primary phase constituents present in the debris confirms the operative wear mechanism involved in the testing, therefore, X-ray diffraction analysis of wear debris has been carried for debris collected during different types of pins used in this segment of the investigation. The amount of debris collected was very less, therefore, that for HT₁-C and HT₂-C types of pins has been pooled together for X-ray analysis. The X-ray diffraction patterns obtained for the debris collected during sliding of samples of Ni-P-X coated aluminium (AC₃) and Ni-P-X coated and heat treated (HT₁-C and HT₂-C) samples are shown in Figs. 6.23 and 6.24 respectively. The peaks indexed for the nickel oxide (NiO) and nickel orthophosphate octahydrate, Ni₃(PO₄)₂, have been observed to be primarily



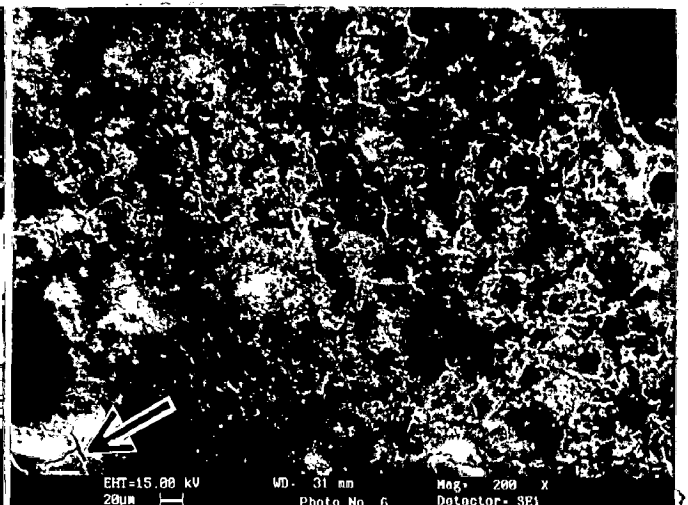
(a)



(b)



(c)



(d)

Fig. 6.19 Wear surfaces of the aluminium specimens heat treated at 400°C for 1 h after Ni-P-X coating (HT₁-A) after sliding through (a) 600 m at 4.9 N, (b) 600 m at 7.4 N, (c) 480 m at 9.8 N and (d) 420 m at 12.3 N.

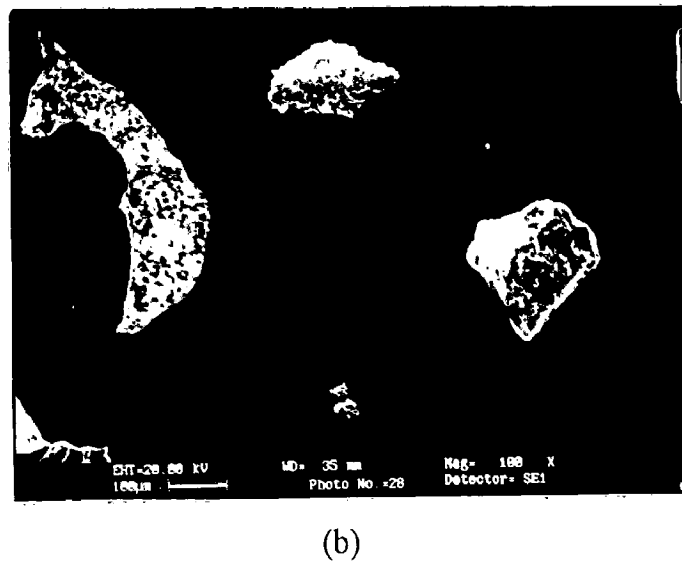
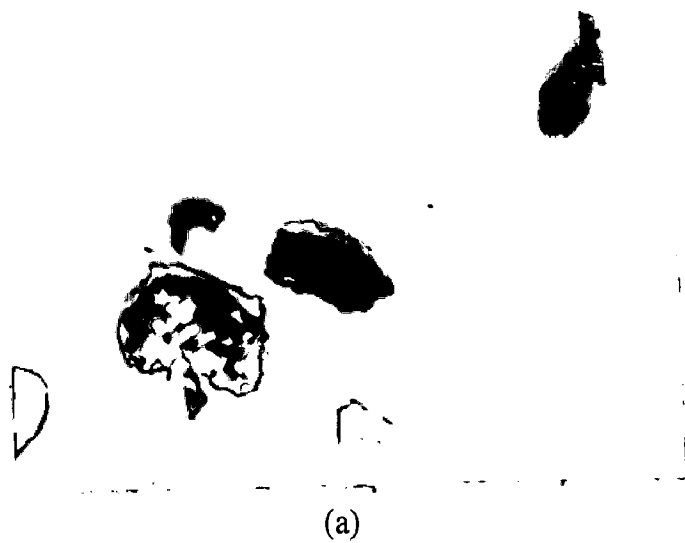


Fig. 6.20 Wear debris of specimens heat treated at 400°C for 1 *h* after Ni-P-X coating (HT₁-A) by spreading on white paper (a) optical micrograph at magnification of × 25 and (b) SEM micrograph.

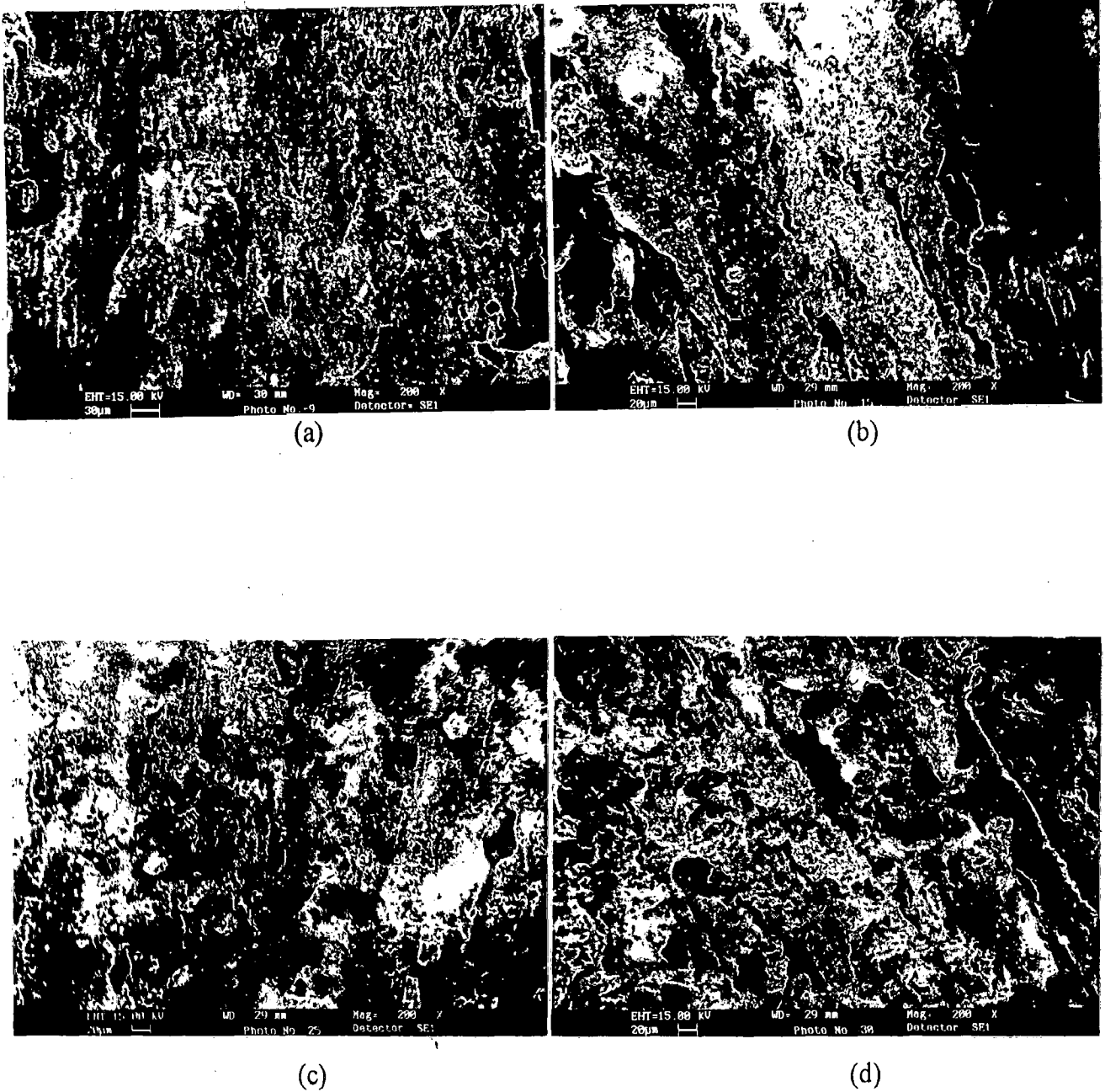
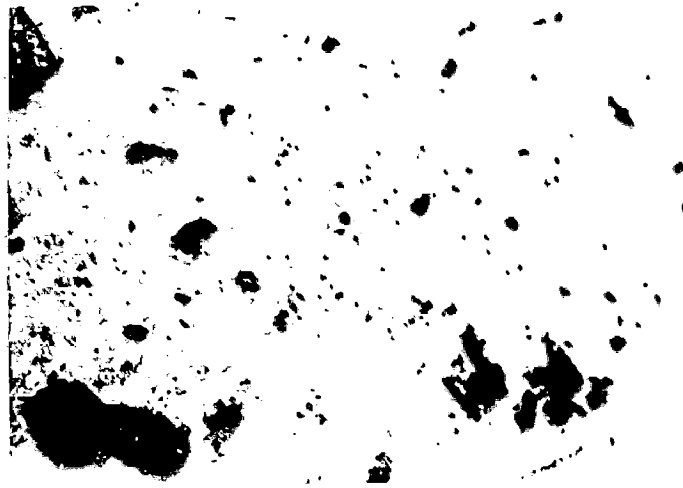
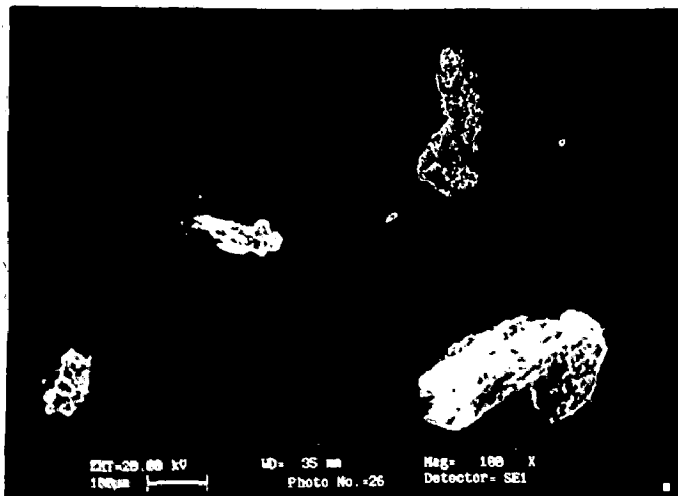


Fig. 6.21 Wear surfaces of the aluminium specimens heat treated at 250°C for 12 h after Ni-P-X coating (HT₂-A) after sliding through 600 m at given normal load of (a) 4.9 N, (b) 7.4 N, (c) 9.8 N and (d) 12.3 N.



(a)



(b)

Fig. 6.22 Wear debris of specimens heat treated at 250°C for 12 h after Ni-P-X coating (HT₂-A) by spreading on white paper (a) optical micrograph at magnification of $\times 25$ and (b) SEM micrograph.

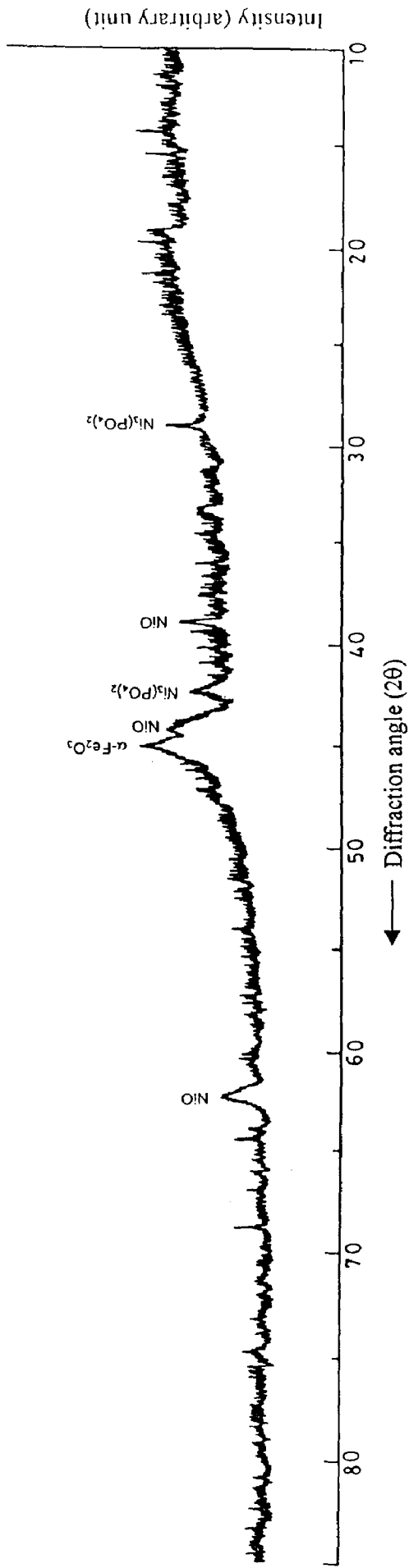


Fig. 6.23 X-ray diffraction pattern of the wear debris of Ni-P-X as-coated aluminum specimens (AC₃) generated at all the four loads applied and collected from the disc counterface.

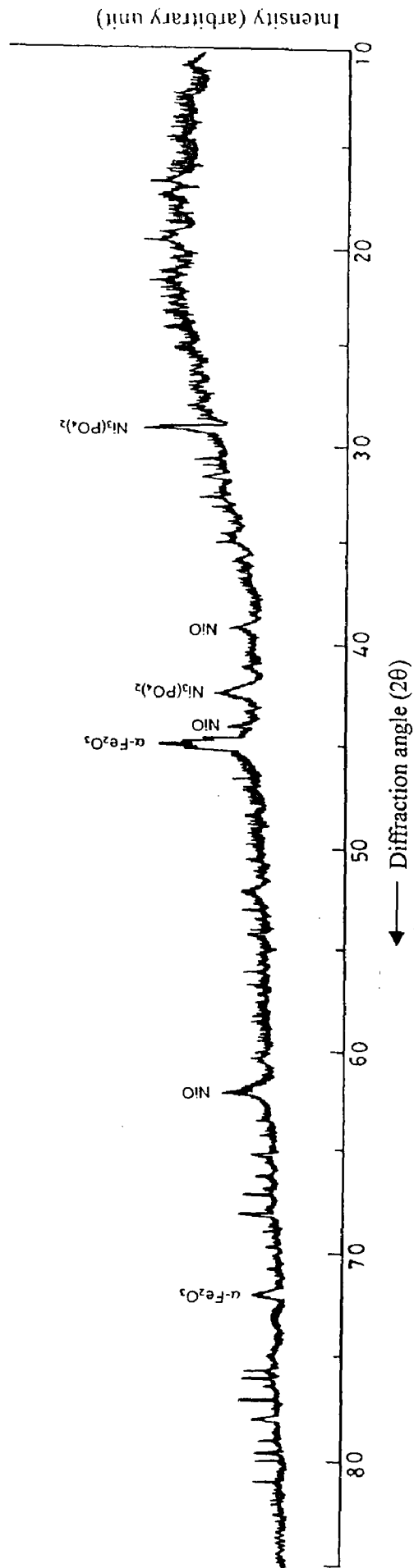


Fig. 6.24 X-ray diffraction pattern of the wear debris of Ni-P-X coated and heat treated at 400 °C for 1 h, (HT₁-C) and heat treated at 250 °C for 12 h, (HT₂-C) generated at all the four loads and collected from the disc counterface.

existing in the debris for both as-coated and heat treated samples. Apart from this at a few places, broad peaks corresponding to α -Fe₂O₃ are also observed by comparing the JCPDS ASTM data cards. The characteristics of the phase constituents present in the wear debris for the Ni-P-X coating on aluminium (AC₃) and Ni-P-X coated and heat treated (HT₁-C + HT₂-C) are reported in Table A.15 given in appendix.

6.2 DISCUSSION

When aluminium (AL) slides against the counterface of hardened steel, formation of junctions at the sliding interface occurs and the difference in hardness between aluminium and the counterface of hardened steel is significantly more than that for steel-hardened steel combination as discussed in chapter 5. When aluminium is coated with a thin layer of Ni-P-X, the chemical nature of surface changes from that of aluminium to that of coating without any significant effect on the macrohardness on the surface as shown in Table A.13 given in appendix. Since the real area of contact is inversely proportional to the hardness of the softer one of the two mating surfaces, it is expected that coating the aluminium with the Ni-P-X may result in more or less the same real area of contact at the sliding interface on the average at a given load. Cumulative volume loss in AL, AC₁, HT₁-C and HT₂-C increases linearly with the sliding distance at a given load as evident from Figs. 6.1, 6.2, 6.3 and 6.4 respectively. A comparison of volume losses in these samples is shown in Figs. 6.25 (a) to (d) at four different loads and the figures clearly reveal that the cumulative volume losses decrease significantly on Ni-P-X coating under conditions of dry sliding employed in this study.

The wear debris observed during dry sliding of aluminium (AL), Ni-P-X coated aluminium (AC₃) and samples heat treated after Ni-P-X coating (HT₁-C, and HT₂-C) are aggregates of finer oxide particles as respectively shown in Figs. 6.16 (a)-(b), 6.18 (a)-(b), 6.20 (a)-(b) and 6.22 (a)-(b). The X-ray diffraction analysis of the wear debris clearly reveals diffraction peaks of primarily NiO, Ni₃(PO₄)₂ for Ni-P-X coated aluminium (AC₃) samples (Fig. 6.24). Similar peaks are observed in aluminium samples heat treated after

Ni-P-X coating (HT₁-C and HT₂-C) as seen in Fig. 6.24. A small amount of Fe₂O₃ has also been observed in these samples. Thus, the dry sliding wear under the conditions carried out in the present study is oxidative for Ni-P-X coated aluminium samples in both the as-coated and the heat treated conditions at given loads and sliding speed. During sliding, frictional heating at the asperity interactions results in temperature high enough for oxidising the region near contact as it has been mentioned earlier in chapter 5 for the coatings on steel substrate. Therefore, the oxidative wear for the aluminium samples and Ni-P-X coated aluminium can be explained on similar grounds. Thus, Eqs. (5.1) and (5.2) as proposed respectively by Archard (1961) and extended for oxidative wear by Quinn (1971) are expected to be helpful for discussion of the results presented in this segment of investigation. After thickening of oxide layer to the critical thickness it gets removed during sliding generating wear debris. These wear debris of oxide particles get trapped in between the sliding surfaces and get compacted into a layer called transfer layer, attached primarily to the softer one of the two sliding surfaces as explained earlier.

In the context of Eqs. (5.1) and (5.2), since hardness is more or less similar in AL, coated samples AC₃ and those heat treated (HT₁-C and HT₂-C), higher K_Q for AL may have resulted from relatively higher k_p since aluminium readily forms impervious layer of oxide on its surface. Saka *et al.*, (1977) have claimed that a harder substrate is able to hold a thicker transfer layer of oxide more firmly as compared to a softer one and thus, softer material will have lower critical thickness, ξ , before it is removed. Thus, K_Q which is inversely proportional to ξ , will be relatively higher in relatively softer aluminium. The increase in wear rate with load may, however, be attributed to higher real area of contact due to softening caused by higher frictional heating even for the same K_Q . Such a situation could lead to more or less linear increase in wear rate with increasing load when varied over a limited range as seen in Fig. 6.5. The heat treatment causes increase in the microhardness of Ni-P-X coatings as such although macrohardness of the specimen does not change significantly. Also, the hardness of the underlying substrate of aluminium in HT₂-C samples remains the same since it is heat treated at relatively lower temperature of

250°C; but the hardness of the underlying substrate in HT₁-C samples decreases considerably during heat treatment at 400°C. Since both the HT₁-C and the HT₂-C have attained almost equilibrium structure of Ni + Ni₃P after heat treatment, the hardness of the underlying substrate will be the determining factor for the wear rate. Since HT₂-C has higher substrate hardness it may have higher ξ as observed by Saka *et al.* (1977) and thus, K_Q is relatively lower for this heat treatment compared to that given in HT₁-C. But this distinction could manifest with increasing load and at lower loads, both the HT₁-C and the HT₂-C have shown similar wear rates as shown in Fig. 6.7. Since the asperity interaction during sliding takes place over micron scale, the increase in microhardness due to heat treatment may decrease the real area of contact in the specimens heat treated after coating with Ni-P-X as compared to those observed in either as-coated samples or aluminium.

The coefficient of friction in uncoated (AL) samples of aluminium and those coated with Ni-P-X (AC₃) is observed to fluctuate about the mean over the sliding distance at all the loads under this investigation and this can be seen respectively from Figs. 6.8 and 6.9. The fluctuation may be indicative of forming, breaking and reforming of the transfer layer under dynamic situation as mentioned earlier in a similar context. The fluctuations in samples heat treated after Ni-P-X coated HT₁-C and HT₂-C samples are shown respectively in Figs. 6.10 and 6.11. For aluminium substrate (AL), the samples as-coated with Ni-P-X (AC₃) and those heat treated after coating (HT₁-C and HT₂-C) the friction coefficient averaged over the sliding distance is found to decrease more or less linearly with normal load applied as seen from Fig. 6.12. However, for both the as-coated (AC₃) and the heat treated samples (HT₁-C and HT₂-C) the average coefficient of friction is relatively higher than that observed for uncoated aluminium (AL) samples. Relatively higher area of contact may result in larger coverage of sliding surface by oxide although their thickness may be relatively less. It may contribute to lower values of coefficient of friction in aluminium samples, decreasing with increasing loads, as seen in Fig. 6.12. Presence of X, hard ceramic oxides may result in enhanced scoring and ploughing as it has been inferred in the case of Ni-P-X coated steel samples, and it may be responsible for higher friction in samples with Ni-P-X coating. The coefficient of friction as observed in

HT₁-C is relatively lower than that of HT₂-C, particularly at lower load as shown in Fig. 6.14. The soft underlying substrate in HT₁-C due to heat treatment at 400°C may have formed compacted transfer layer more extensively due to larger area of contact than that formed on HT₂-C due to its relatively harder underlying substrate. The formation of compacted layer could be clearly observed in Figs. 6.15, 6.17, 6.19 and 6.21.

The stable structure in coating/substrate system is expected to result in linearly increasing wear rate with load. The Ni-P-X coated aluminium samples in as-coated and heat treated conditions possess better resistance to sliding wear than uncoated aluminium, which could be explained in the similar way as it has been done for the steel substrate in chapter 5. Heat treatment of Ni-P-X coatings results in substantial amount of Ni₃P, which may have counteracted the tendency to softening with frictional heating. Since asperity interaction is confined to micron scale the transformation leading to increasing hardness in the coated layer may make significant difference to the real area of contact. The oxidation of Ni₃P may also be slower than nickel and so, the wear rate and cumulative volume loss in heat treated samples are lower than those observed in as-coated samples. The coefficient of friction also attains a lower value on heat treatment of Ni-P-X coating as the load is increased. The difference in cumulative volume loss and wear rate between as-coated and heat treated samples are relatively more at higher loads than those at lower loads as seen in Figs. 6.1-6.5 and 6.26 (a) to (d). It should be remembered that the amount of X is very low and possibly, it could be more effective in imparting wear resistance in relatively softer as-coated samples if present in larger amounts. The heat treated samples where hard Ni₃P is present in significant amount, the presence of X may not contribute that effectively in preventing wear. However, the presence of hard ceramic particles may contribute to scoring or ploughing during dry sliding and it may be responsible for higher coefficient of friction in Ni-P-X coatings. It is interesting to note that the relatively softer underlying substrate may result in relatively higher wear volume particularly at higher loads when indentation becomes deeper and the wear rate increases relatively more with increasing load even though the hardness of the coating is higher. It is evident from the study reported above that substantial wear resistance could be imparted in the regime of

oxidative wear by heat treating the Ni-P-X coating on aluminium and the wear resistance becomes still better if the substrate hardness could be retained during heat treatment. A relatively higher average coefficient of friction may result due to presence of X during dry sliding at a given load and sliding speed.

ELECTROLESS COATED CARBON FABRIC : A CASE STUDY

The primary objective of this segment of investigation is to apply electroless Ni-P-X ($X = \text{ZrO}_2\text{-Al}_2\text{O}_3\text{-Al}_3\text{Zr}$) and Ni-P coatings by the use of specified bath composition and their characterisation in terms of uniformity, composition and phase constituents present. The characteristics of the coated fabric discussed in this chapter have been compared with those of the coatings on metallic substrates, i.e., aluminium and steel, as explained in chapter 4. The tensile behaviour of carbon fabric samples has been studied for different conditions of the samples, viz., uncoated fabric, Ni-P-X as-coated, heat treated at 400°C for 1 h after Ni-P-X coating the fabric, Ni-P as-coated and heat treated at 400°C for 1 h after Ni-P coating. Carbon fibers/fabrics play an indispensable role in the manufacture of reinforcement for metal matrix composite (MMC) and these coatings can facilitate its better usage in reinforcement into aluminium alloys, therefore, an attempt is made to study the feasibility of reinforcement of Ni-P based coated carbon fabric into aluminium matrix.

7.1 RESULTS

In the present segment of investigation, electroless Ni-P-X and Ni-P coatings were applied on woven carbon fabric samples for 5 min coating time. The primary focus of this study is to understand the role of electroless coating on tensile behaviour and feasibility of reinforcement in aluminium melt as mentioned earlier. The coatings are especially characterised in terms of uniformity, qualitative analysis and element/phase constituents present in it. The as-coated and heat treated at 400°C for 1 h specimens of Ni-P-X and Ni-P deposited fabric have been subjected to tensile testing and fractography. Feasibility of the coated fabric reinforcement into molten aluminium has been studied by conventional casting such that the fabric remains surrounded by the matrix. SEM, X-ray diffraction and tensile testing were used as tools for different analyses. The results have been discussed to develop

a coherent understanding of electroless coating on carbon fiber in terms of coating composition, tensile behaviour and reinforcement feasibility into aluminium.

7.1.1 Specifications of Carbon Fabric

The detailed specifications of the carbon fabric used in the present investigation is given in the Table 7.1.

Table 7.1 Specifications of the Carbon Fabric*

Particulars	Description
Carbon	94 %
Ash contents	1% max
Na	500 ppm
Specific gravity	1.7-1.9 gm/cc
Breaking strength:	
Warp	9.1 kg/iN ²
Fill	6.8 kg/iN ²
Weight	225-325 gm/m ²
Thickness	0.4-0.5 mm
Surface resistivity	0.4 -1.0 ohm/iN ²
Weaving type-1	8 H.S.
pH value	7.1
Width	820-1100 mm

* As provided by Regional Research Laboratory (CSIR), Thiruvananthapuram (India).

7.1.2 Coatings on Carbon Fabric

The carbon fabric samples have been coated successfully with electroless Ni-P-X composite and Ni-P alloy deposits and the reproducibility of the same has been experimentally confirmed. Detailed procedure for these coatings and the bath composition used has already been explained in chapter 3. Figure 7.1 shows photographs of the typical samples of uncoated, as-coated Ni-P and as-coated Ni-P-X carbon fabric as marked by labels A, B and C respectively. It has been visually observed that both the Ni-P-X and the Ni-P types of coatings are uniformly deposited on fibers of the carbon fabric with the marked colour difference in-between them. Semi-bright and dull appearance of Ni-P-X and bright appearance of Ni-P coated fabric has been observed by visual examination of Fig. 7.1. The Ni-P-X coated carbon fabric under SEM is shown in Fig. 7.2, in which

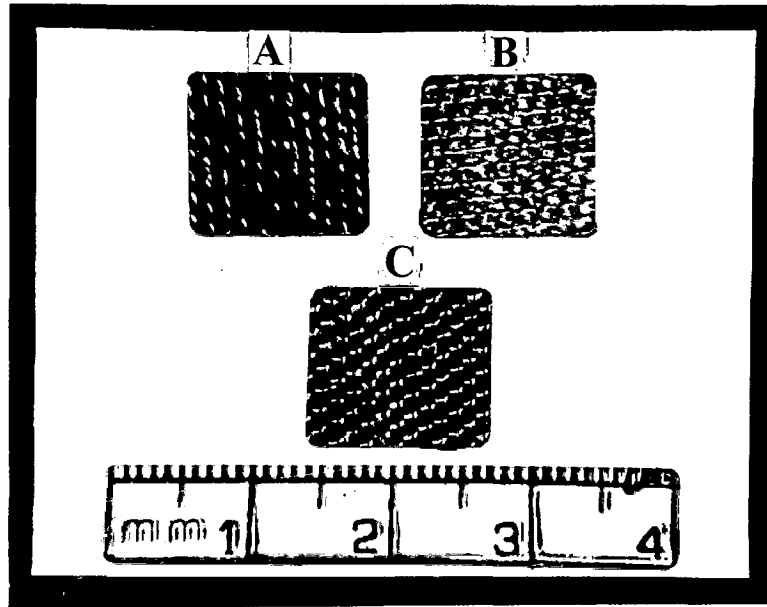


Fig. 7.1 Photographs of the carbon fabric specimen (A) uncoated , (B) electroless Ni-P as-coated and (C) electroless Ni-P-X as-coated.

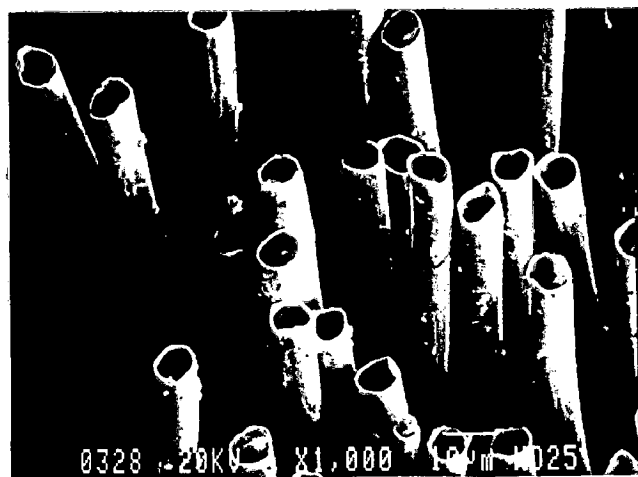


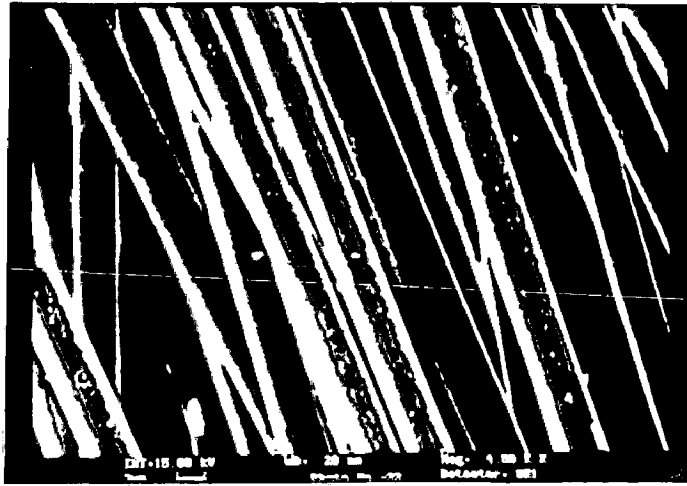
Fig. 7.2 SEM micrograph of electroless Ni-P-X coated carbon fabric showing the fibers with uniform coating.

uniform coating around all the fibers of the fabric is clearly observed. It is also observed that the coating and fiber are clearly distinguished at their interface. A few particles are also observed over the lateral surface of the coating and the uniform distribution of cluster like particles are also seen over almost all fibers of the fabric.

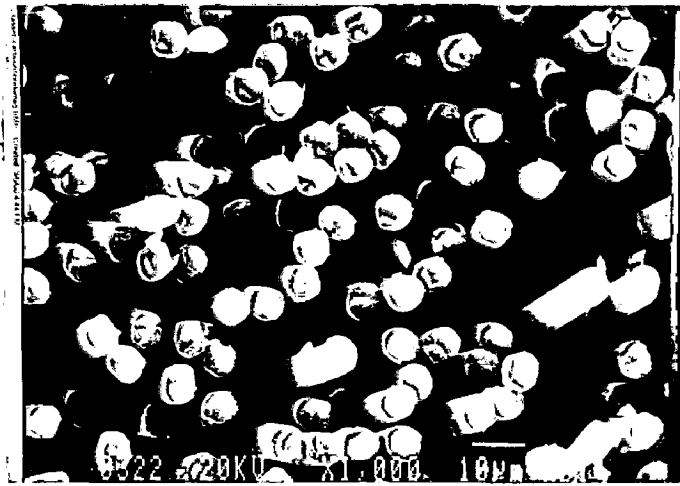
7.1.3 Examination of Carbon Fabric under SEM

The uncoated carbon fabric substrate as used in the present work, after cleaning by acetone, is shown in Figs. 7.3 (a) and (b), which represent its longitudinal and cross sectional views respectively. The SEM micrographs of as-coated Ni-P-X carbon fabric specimens in longitudinal and cross-sectional views are presented in Figs. 7.4 (a) and (b) respectively. The globule like coating on the fibers of the fabric has been observed in Fig. 7.4 (a) and uniform coating thickness (t_c) of about $0.8 \mu\text{m}$ is seen around the fibers as seen in Fig. 7.4 (b). The coating thickness has been determined from Fig. 7.4 (b) and the schematic view for the same is shown in Fig. 7.4 (c). The area fraction of the coating as determined by knowing the diameter of the uncoated fiber, d_f and diameter of the coated fiber, d_c is found to be around 0.40 as illustrated in Fig. 7.4 (c). Figures 7.5 (a) and (b) show the SEM micrographs of Ni-P as-coated carbon fabric in longitudinal and cross-sectional view respectively. In the longitudinal view the globules of coating developed are evident whereas the coating covering the fibers is observed in Fig. 7.5 (b). The electroless coating on the carbon fabric develops in form of a layer as seen from Figs. 7.4 (b) and 7.5 (b), which is similar to coating layer developed on aluminium and steel substrates that has already been explained in chapter 4.

In view of assessing the qualitative analysis of the coated carbon fabric the SEM-EDX for a typical point has been carried out and the spectrograph obtained for the same is shown in Fig. 7.6. From the above figure the peaks corresponding to Ni, P, Zr and Al are observed to be relatively more clear but those for O (oxygen) and C (carbon) are found to be insignificant. Figure 7.6 depicts the peaks corresponding to Ni, and P as the common elements present in the coating and the presence of Al, Zr along with O peaks as less common elements.

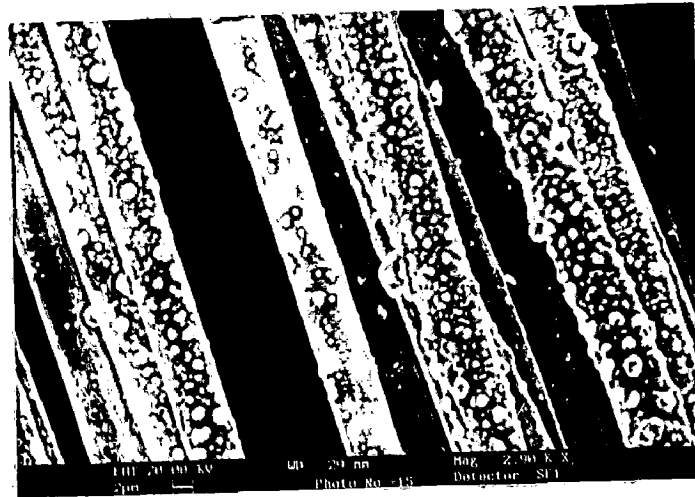


(a)

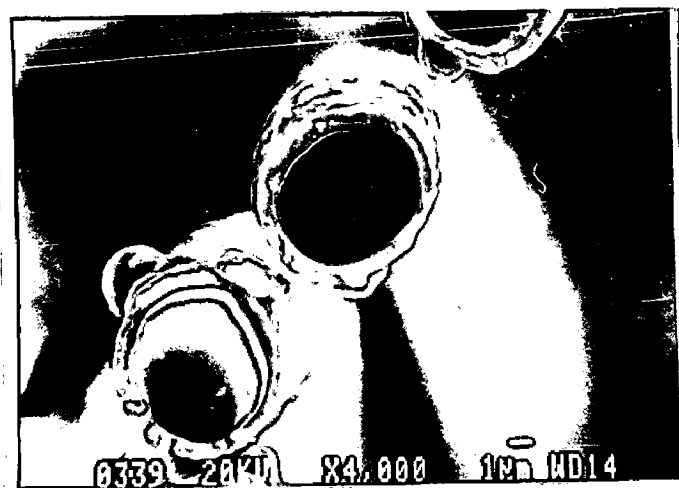


(b)

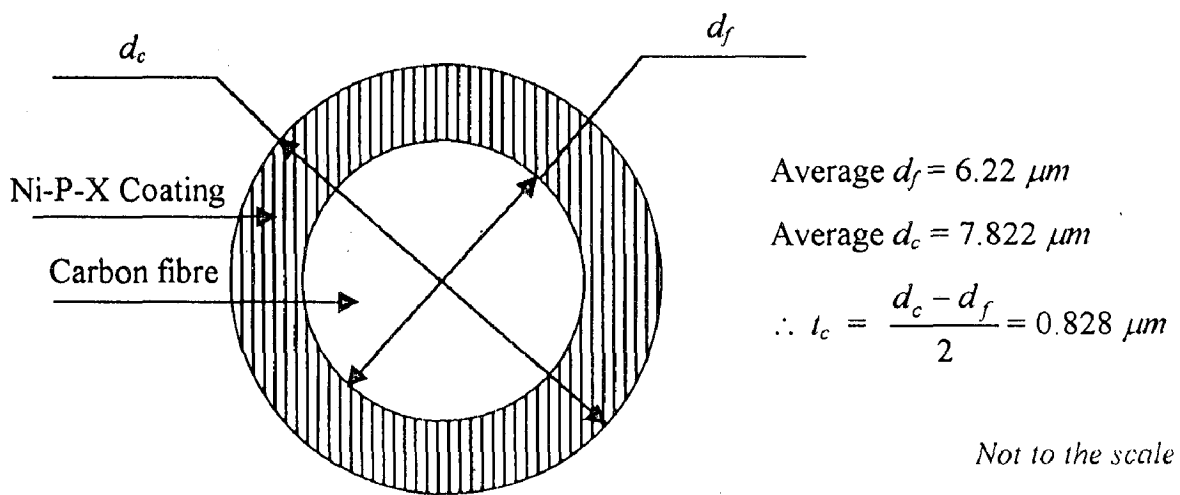
Fig. 7.3 SEM micrographs of the uncoated carbon fabric in (a) longitudinal view and (b) cross sectional view.



(a)



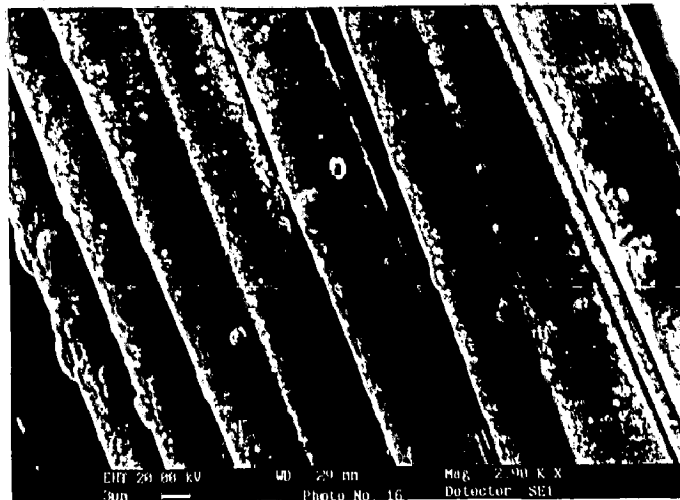
(b)



Not to the scale

(c)

Fig. 7.4 SEM micrographs of the electroless Ni-P-X as-coated carbon fabric in (a) longitudinal view, (b) cross sectional view and (c) schematic diagram of coated fiber.



(a)



(b)

Fig. 7.5 SEM micrographs of the electroless Ni-P as-coated carbon fabric in (a) longitudinal view and (b) cross sectional view.

7.1.4 Phase Analysis

The compositions in terms of phase constituents present in the uncoated, as-coated and heat treated samples have been determined by X-ray diffraction analysis. Figure 7.7 shows the X-ray diffraction pattern for uncoated carbon fabric sample in which all the peaks of carbon have been evidenced and the characteristics of carbon observed in this pattern are presented in Table A.16 given in appendix. Figures 7.8 (a) and (b) show the X-ray diffraction patterns obtained for Ni-P-X coated carbon fabric in as-coated and heat treated at 400°C for 1 h conditions respectively. A single broad peak primarily corresponding to amorphous nickel has been observed. A few other phases like Ni₁₂P₅, Ni₅P₂ etc. (Ni_xP_y) in amorphous phase are also present in the as-coated condition along with Al₃Zr as seen in Fig. 7.8 (a). The heat treatment at 400°C for 1 h results in crystallisation of different Ni_xP_y to Ni₃P phase, indicating the small peaks emerging out as observed from Fig. 7.8(b). The peaks for the other nickel phosphite phases observed were found to be similar to those explained earlier for X-ray analysis for both the Ni-P-X and the Ni-P film as given in chapter 4. The peaks for the less common phases such as Al₂O₃ and ZrO₂ have not been observed in the above figures. The X-ray diffraction patterns for Ni-P as-coated carbon fabric and that heat treated, after coating at 400°C for 1 h conditions are shown in Figs. 7.9 (a) and (b) respectively. A single broad peak in as-coated condition has been observed and due to heat treatment, different Ni_xP_y phases transform into Ni₃P. The different phase constituents present in Ni-P-X and Ni-P coated carbon fabric in both the as-coated and the heat treated conditions along with their characteristics are reported in Table A.17 given in appendix. It is found that in as-coated condition, for both the types of coating, the Ni-P-X and the Ni-P, microcrystalline Ni constitutes the common phase. The less common phases like Al₃Zr, Ni₅P₂ and Ni₁₂P₅ are also observed in as-coated condition. After heat treatment of these coated samples at 400°C for 1 h, it is noticed that Ni and Ni₃P appear as common phases whereas Al₃Zr, Ni₅P₂ and Ni₁₂P₅ are also observed as less common phases as evident from Figs. 7.8 (b) and 7.9 (b). A relatively larger peaks in Ni-P coated and heat treated samples are observed than in Ni-P-X coated and heat treated

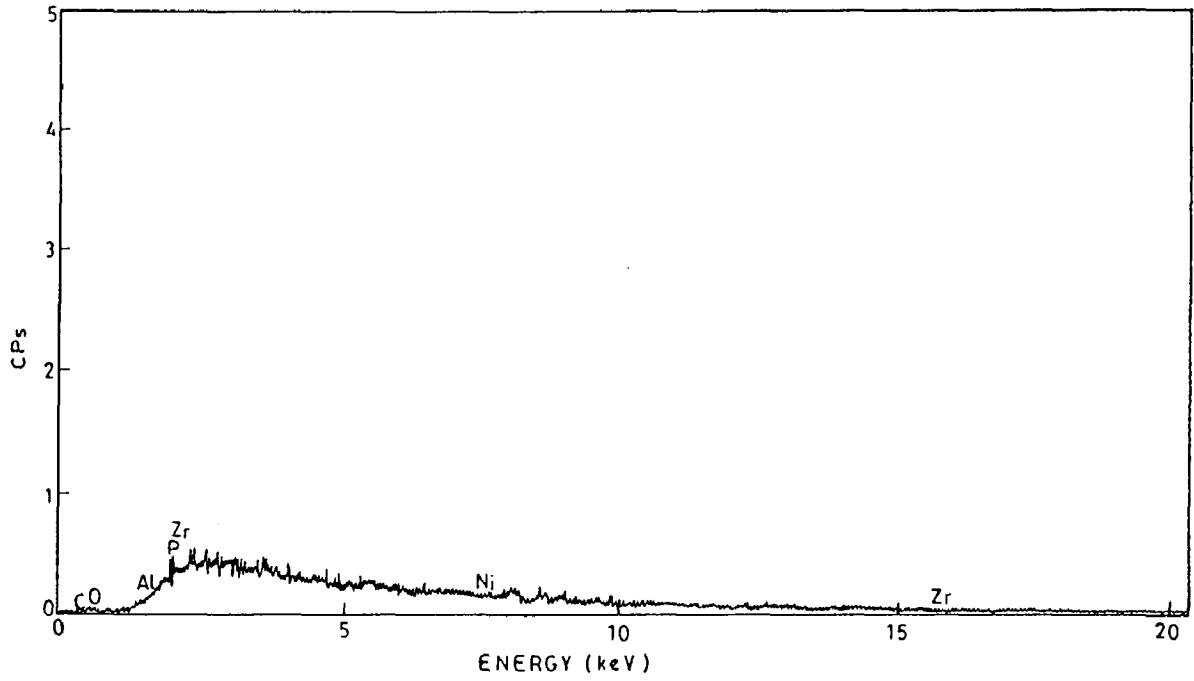


Fig. 7.6 SEM-EDAX for a typical point on the electroless Ni-P-X as-coated carbon fabric showing the presence of different elements in the composite coating.

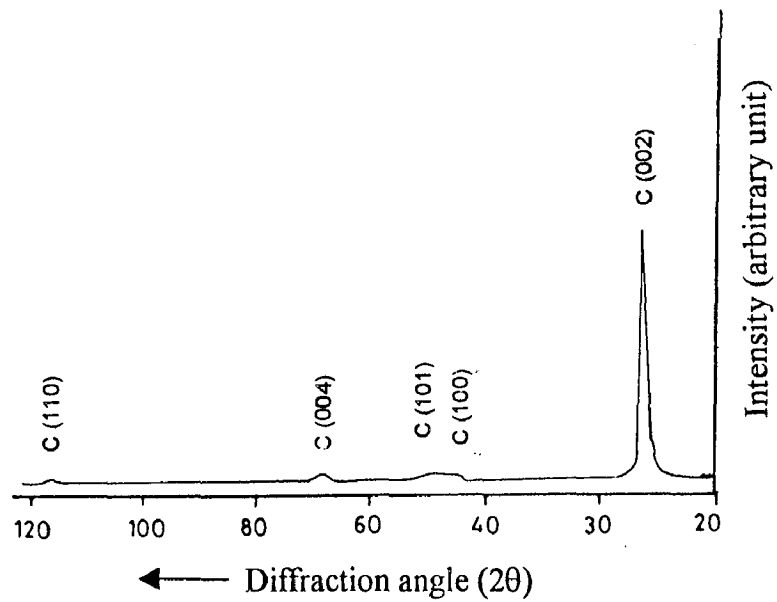


Fig. 7.7 X-ray diffraction pattern of uncoated carbon fabric substrate.

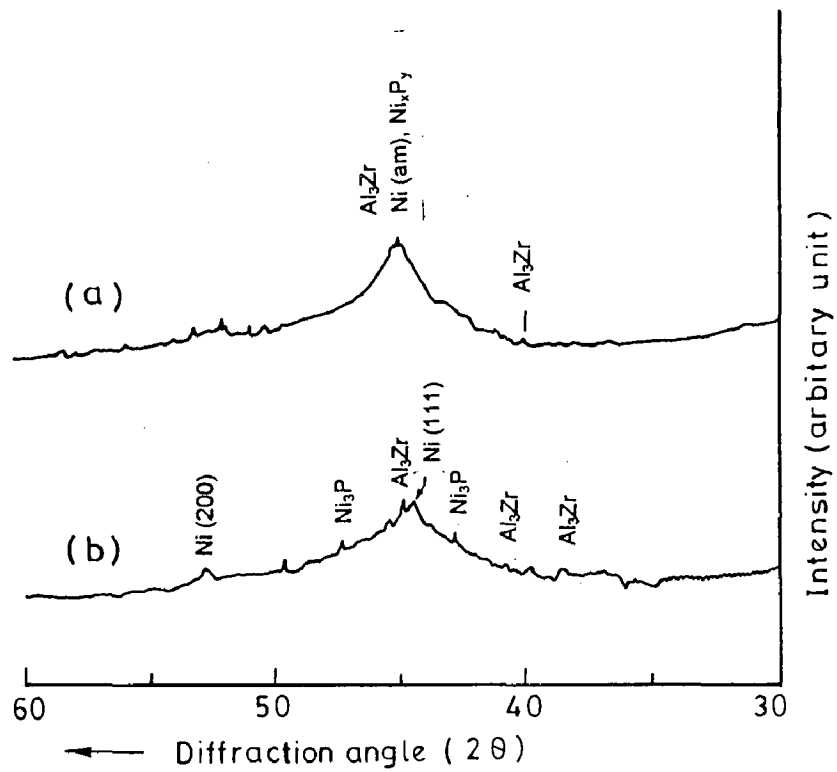


Fig. 7.8 X-ray diffraction pattern of electroless Ni-P-X coated carbon fabric sample in (a) as-coated and (b) heat treated at 400°C for 1 h conditions.

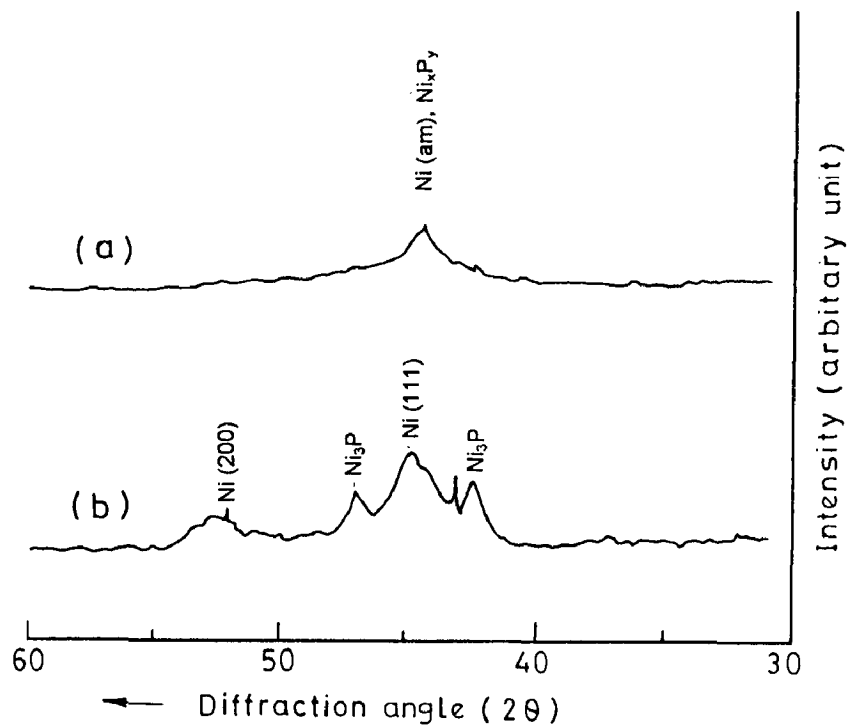


Fig. 7.9 X-ray diffraction pattern of electroless Ni-P coated carbon fabric sample in (a) as-coated and (b) heat treated at 400°C for 1 h conditions.

conditions as observed from Figs. 7.8 (b) and 7.9 (b). However, the peaks for Al_2O_3 and ZrO_2 could not be observed in the X-ray diffraction patterns for Ni-P-X coated fabric samples in both the as-coated and the heat treated conditions. The amounts present for these phases may be beyond the detection limit of X-ray diffraction.

7.1.5 Tensile Testing and Fractography

The carbon fabric samples were cut to the size of $25 \text{ mm} \times 80 \text{ mm}$ and have been coated with Ni-P-X and Ni-P deposits as explained earlier in chapter 3. The tensile tests were carried out on different types of fabric samples viz., uncoated, as-coated and those after heat treated at 400°C for 1 h . The results of representative tensile tests carried out for different fabric specimens, i.e., uncoated, as-coated Ni-P-X, heat treated Ni-P-X, as-coated Ni-P and heat treated Ni-P are shown in Figs. 7.10 (a) to (e) respectively. From the above load vs. extension curves, it is observed that the Ni-P-X coated and heat treated sample failed under tension at a load of 136 N and Ni-P coated and heat treated is found to fail at 126 N . The tensile failure loads for Ni-P-X as-coated, Ni-P as-coated and uncoated fabric samples were noticed to be 71 , 67 and 41 N respectively. The insignificant amount of extension is observed during the tensile tests of the fabric and is found to ^{be} insensitive to the type of coating on the fabric used in the present study. The ultimate failure of the fabric is observed after about 5 mm of extension as seen from Figs. 7.10 (a) to (e). In order to know the effect of coating composition and heat treatment in terms of tensile behaviour, the ultimate tensile strength (UTS) of the carbon fabric specimens have been determined and shown in Fig. 7.11. The UTS of the fabric samples was determined by considering the 50% packing density, i.e., by assuming 25 strands along 25 mm width of the sample, as can be calculated on the basis of specifications (8 H. S. two way woven type and 0.48 mm thickness) as given in Table 7.1. The UTS of Ni-P-X and Ni-P as-coated carbon fabric so calculated have been found to be 12.7 N/mm^2 and 12 N/mm^2 respectively while after heat treatment at 400°C for 1 h , the corresponding values for Ni-P-X and Ni-P coated fabric are observed to be 24.7 N/mm^2 and 22.5 N/mm^2 as seen in Fig. 7.11. The UTS for uncoated carbon fabric has been observed to be 7.3 N/mm^2 . The UTS of carbon fabric increases by

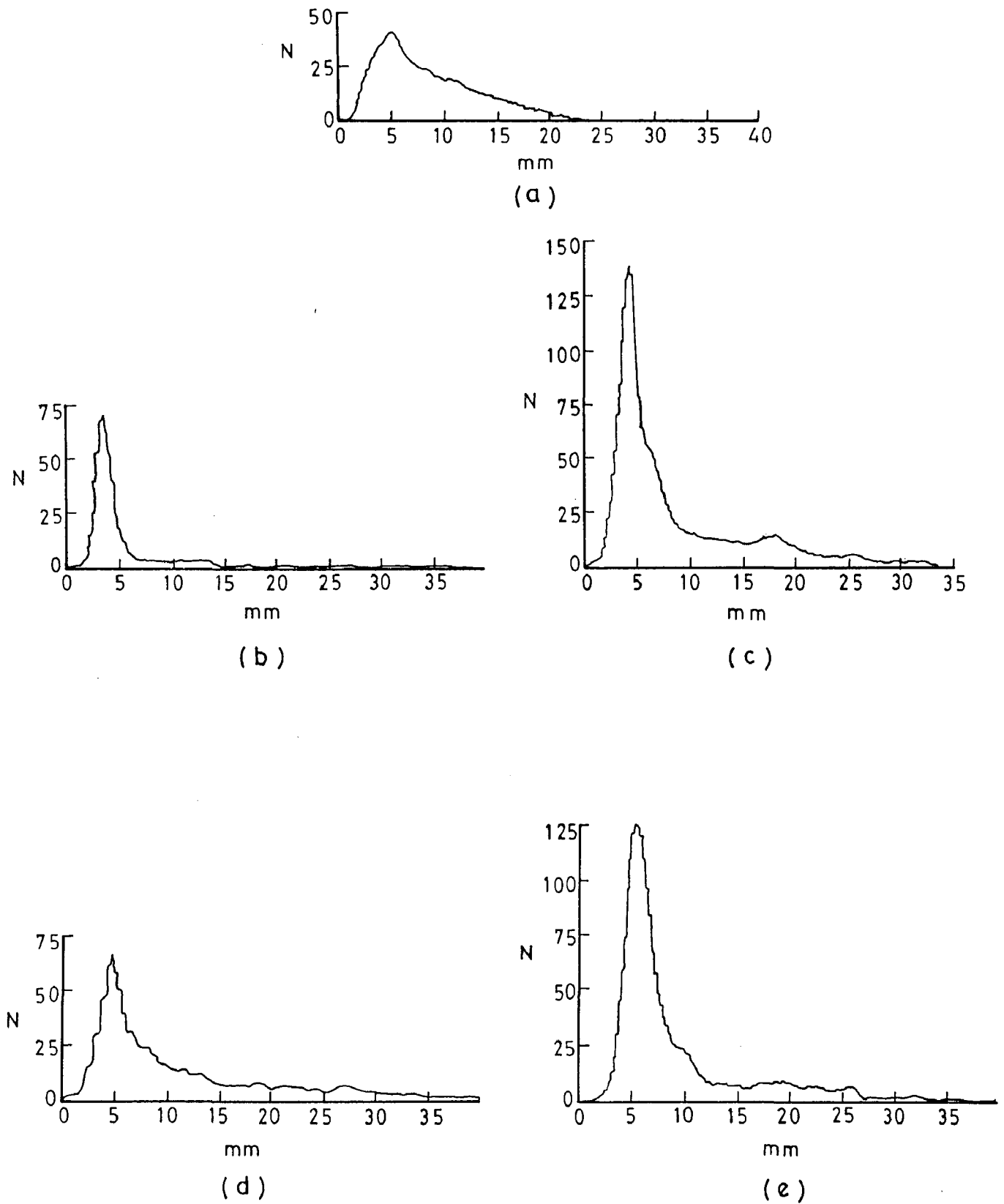


Fig. 7.10 Tensile failure loads for different carbon fabric specimens (a) uncoated, (b) Ni-P-X as-coated, (c) Ni-P-X coated and heat treated at 400°C for 1 h, (d) Ni-P as-coated and (e) Ni-P coated and heat treated at 400°C for 1 h.

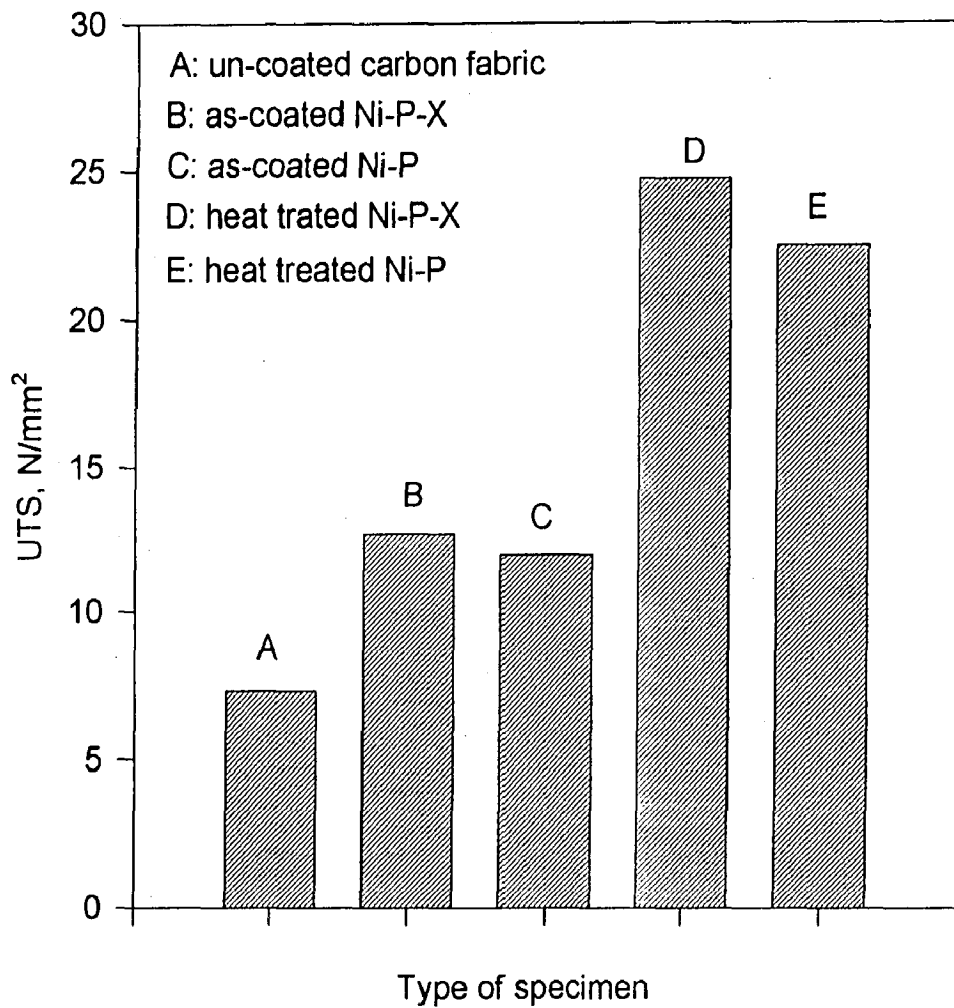


Fig. 7.11 UTS values for carbon fabric samples in uncoated, Ni-P-X as-coated, Ni-P-X coated and heat treated, Ni-P as-coated and Ni-P coated and heat treated conditions.

about 1.7 times by electroless coating and the same after heat treatment further increase by about 3.25 time higher than uncoated fabric as seen from Fig. 7.11.

The SEM fractographs of carbon fabric samples in uncoated, as-coated Ni-P, as-coated Ni-P-X, heat treated Ni-P and heat treated Ni-P-X coatings are shown in Figs. 7.12 (a) to (e) respectively. The fracture of uncoated carbon fabric has been observed without any thinning of the fiber strands near fractured region as seen in Fig. 7.12 (a). The wavy nature of the broken fabric strands along the lateral surface and almost cleaved surface at the fiber core has been observed in the fractographs of electroless Ni-P and Ni-P-X as-coated fabric specimens as shown by appropriate arrows in Figs. 7.12 (b) and (d). Such irregular edge has been seen only along the lateral surface but the core of the fiber is observed to fail under tension in the similar way as for the uncoated fabric sample. More wavy nature of the fabric strands has been observed in the fractographs of heat treated after Ni-P/Ni-P-X coated fabric specimens at the edge as observed from Figs. 7.12 (c) and (e) at a few places where the arrows are pointed.

7.1.6 Reinforcement Feasibility into Metal Matrix

In view of assessing the feasibility of reinforcement of carbon fabric with and without electroless Ni based coating into aluminium melt the fabric pieces of $25\text{ mm} \times 80\text{ mm}$ were reinforced by casting without applying external pressure. The carbon fabric zone into aluminium matrix and has been observed by reinforcement of uncoated carbon fabric and as-coated Ni-P-X carbon fabric. The transversely cut and polished samples from reinforced fabric castings have been subjected to SEM and EPMA examinations and corresponding micrographs are explained with the help of Figs. 7.13 to 7.16 in the subsequent part of this subsection.

(a) Examination of fabric zone into aluminium matrix

The fabric zone of uncoated carbon fabric into the matrix at two different magnifications, i.e., $\times 500$ and $\times 1000$ are shown in Figs. 7.13 (a) and (b) respectively.

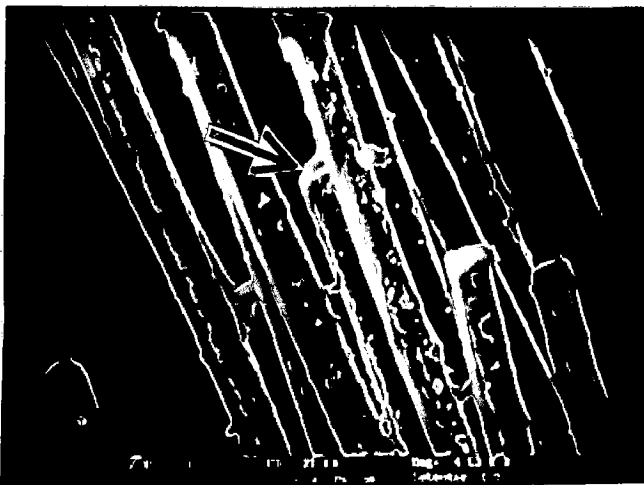
Similarly, Figs. 7.14 (a) and (b) show the similar zone for as-coated Ni-P-X fabric at two different magnifications of $\times 500$ and $\times 1000$ respectively. The uncoated fabric strands without any significant reaction at the interface are visible in Figs. 7.13 (a) and (b). The reaction zone can be observed at the similar interface with as-coated Ni-P-X fabric as seen in Figs. 7.14 (a) and (b). The reaction zone in-between coating on fabric and aluminium matrix has been indicated by an arrow in Fig. 7.14 (a) while an arrow in Fig. 7.14 (b) indicates fiber-coating interface, in which no reaction between fiber and nickel coating has been observed. The coated fabric has been observed as relatively compressed after the reinforcement than uncoated fabric. The width of the fabric zone in uncoated sample is seen to be about 40-50 μm whereas that with the coated fabric has been observed to be 25-30 μm as observed respectively from Figs. 7.13 (b) and 7.14 (b).

(b) X-ray mapping

As mentioned earlier, the assessment of reinforcement feasibility has been studied by subjecting the fabric zone in the specimen to X-ray mapping under EPMA, which provides the qualitative distribution of the different elements. Figure 7.15 shows the area covering the uncoated fabric zone into the matrix, which has been scanned for aluminium and the similar zone with the Ni-P-X coated fabric is shown in Fig. 7.16 (a). Infiltration of aluminium into the uncoated carbon fabric has not been observed, however, a bright spot within the fabric zone may indicate locally entrapped aluminium during polishing of the sample as seen from Fig. 7.15. The distribution of different elements along the interface between the coating and aluminium matrix can be distinguished clearly. The elemental nickel, phosphorus and aluminium scans for the Ni-P-X coated fabric reinforced specimen are shown in Figs. 7.16 (b) to (d) respectively. The uniform distribution of nickel and phosphorous over the interface line is observed from these figures. In Fig. 7.16 (d), the bright areas corresponding to aluminium within the fabric boundary have been observed.



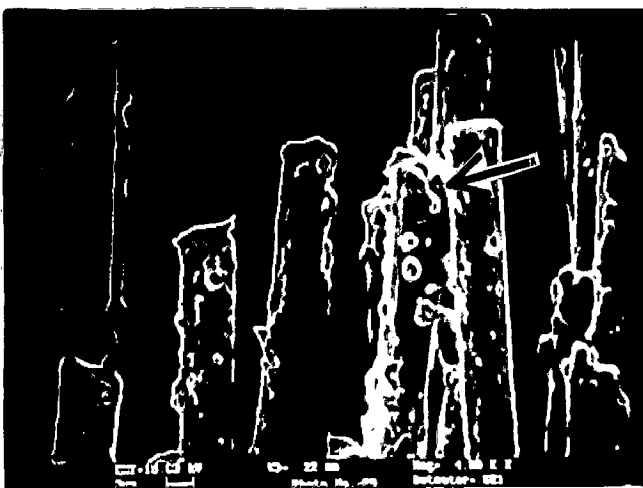
(a)



(b)



(c)



(d)



(e)

Fig. 7.12 Fractographs of the carbon fabric specimens under SEM (a) uncoated, (b) Ni-P-X as-coated and (c) Ni-P-X coated and heat treated at 400°C for 1 h (d) Ni-P as-coated, (e) Ni-P coated and heat treated at 400°C for 1 h.

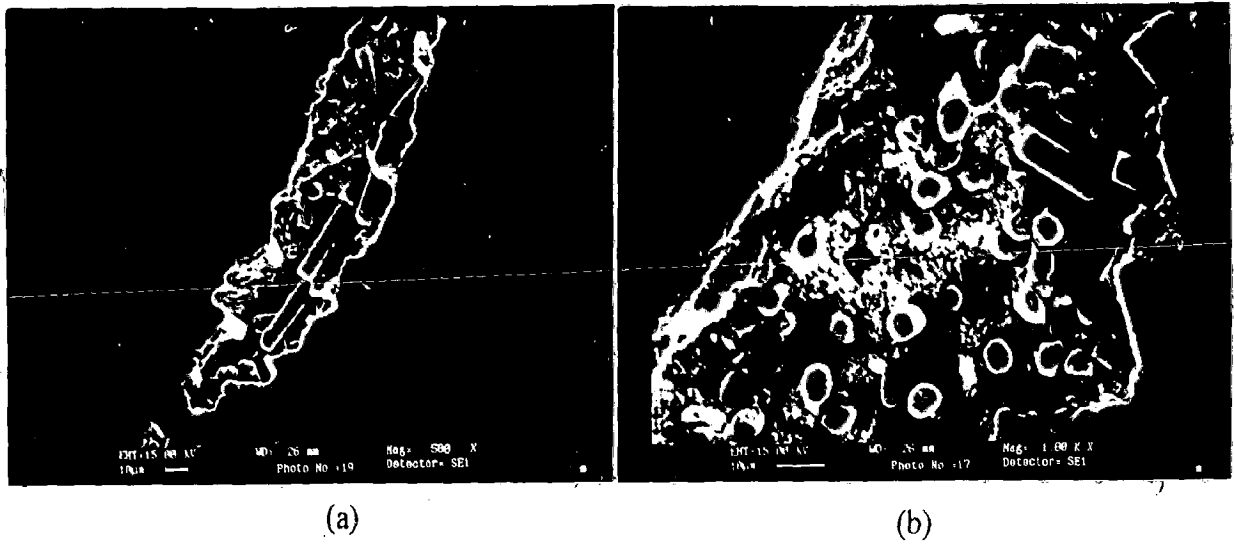


Fig. 7.13 SEM micrographs showing the uncoated carbon fabric zone into aluminium matrix (a) $\times 500$ and (b) $\times 1000$.

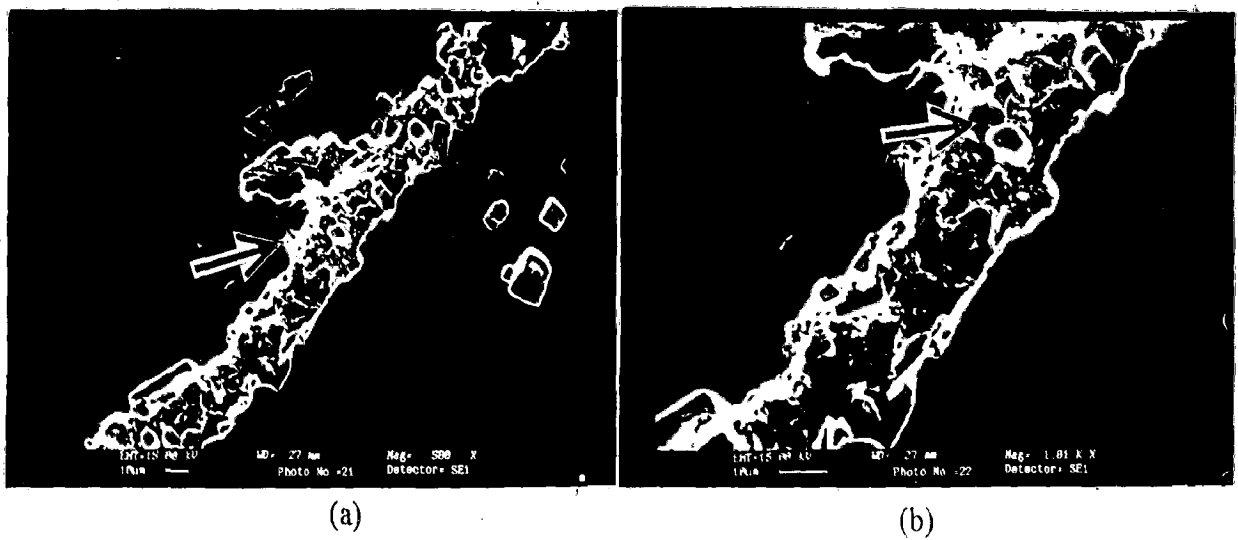
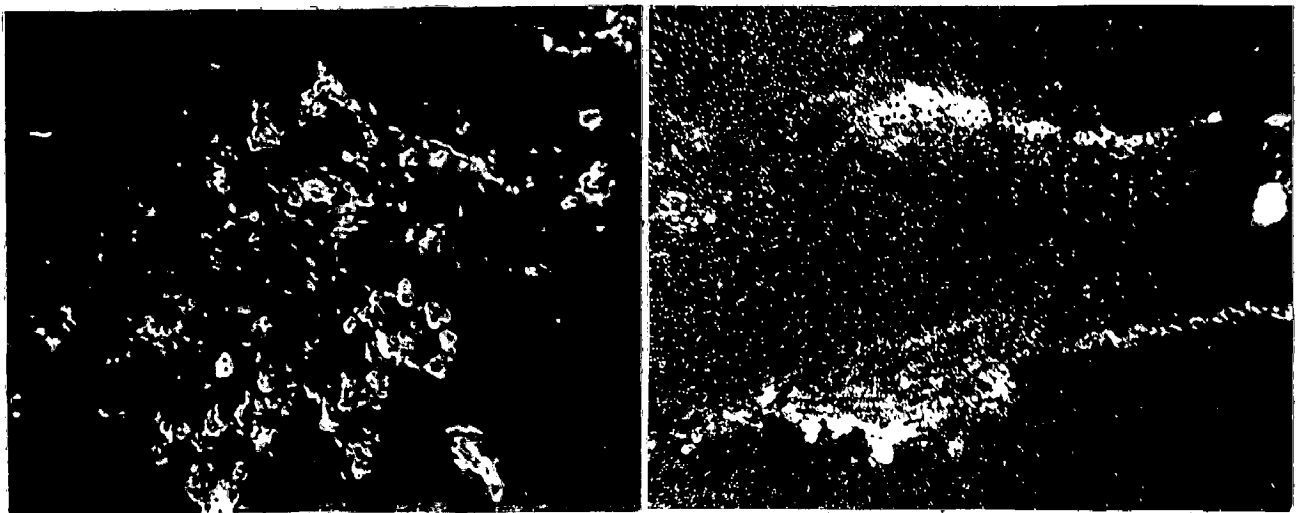


Fig. 7.14 SEM micrographs showing the electroless Ni-P-X coated carbon fabric zone into aluminium matrix (a) $\times 500$ and (b) $\times 1000$.

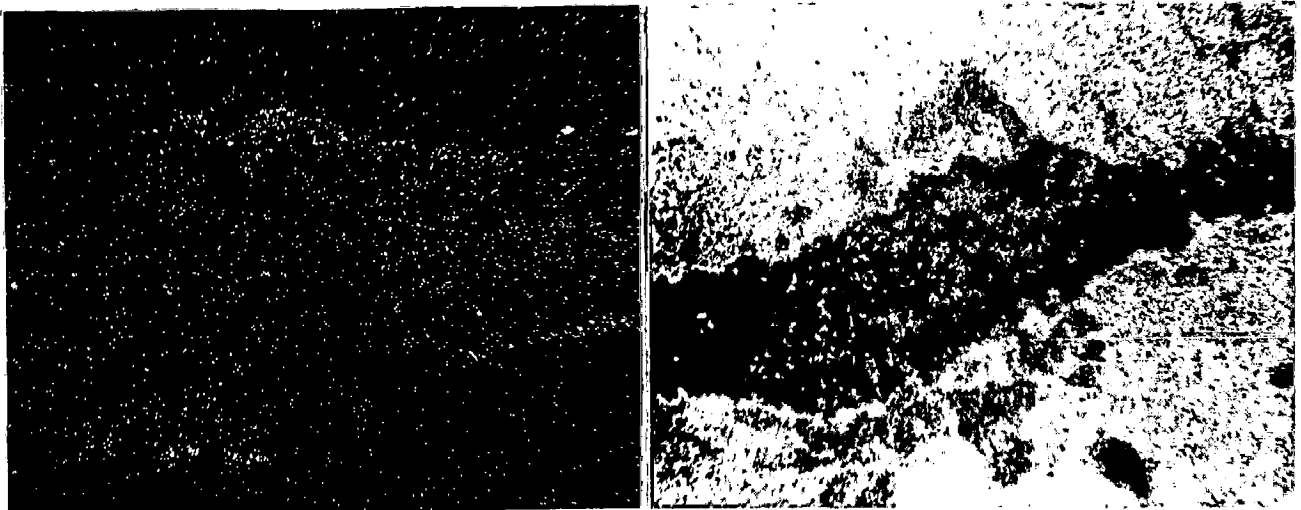


Fig. 7.15 Uncoated carbon fabric zone into aluminium matrix under EPMA when subjected to X-ray mapping for aluminium.



(a)

(b)



(c)

(d)

Fig. 7.16 Electroless Ni-P-X coated carbon fabric zone into aluminium matrix under EPMA when subjected to X-ray mapping (a) area selected for mapping, (b) distribution of nickel, (c) distribution of phosphorus and (d) distribution of aluminium.

7.2 DISCUSSION

Graphite in the form of fibers or particulate, has long been recognised as high strength low density material and, therefore, graphite fiber reinforced metal matrix composites are receiving profuse attention as the properties mentioned above and stiffness in fibers can be retained even at elevated temperatures (Ip *et al.*, 1998; Himbeault *et al.*, 1988). The major problems encountered in the development of carbon fiber-metal matrix composite are the reactivity of carbon with many metals and the poor wetting characteristics of carbon by liquid metals, which introduce many difficulties in the fabrication and limit the high temperature applications of these composites (Himbeault *et al.*, 1989/1 and 1989/2). One of the solutions to these problems is the application of a suitable coating or diffusion barrier to the carbon fiber. The unique properties of graphite fibers have also attracted a lot of attention in the area of metal matrix composites, especially with aluminium alloys (Ip *et al.*, 1998). Aluminium does not have wettability with carbon/carbon fibers, therefore, it is difficult to reinforce into molten aluminium alloy to produce the reinforced ingots. In some cases, either the preforms are prepared or the pressure is applied for reinforcement of graphite fibers/particles in molten aluminium alloy by casting process.

Uniform and continuous deposition of electroless Ni-P-X composite and Ni-P alloy coatings on the carbon fabric has been successfully consummated. The coating on fabric can be markedly seen from Fig. 7.1. Visual examination of this figure reveals that brightness is one of the obvious differences in Ni-P and Ni-P-X coatings, when compared with that of the uncoated sample. The Ni-P coating possesses relatively more brightness than the Ni-P-X coating, which may be due to scattering of light because of roughness in Ni-P-X coatings. The mechanism of coating seems to be similar to that observed for other substrates of aluminium and steel as explained in chapter 4. The deposition of Ni-P alloy results due to the formation of several nucleation sites to start with and grows to form a coating layer in both the lateral and the vertical directions. As the coating grows, entrapment of the co-precipitated particles within the deposit occurs resulting in the formation of composite coating. This is an indication that the in-situ co-precipitation within

the electroless bath has behaved in a similar way as was observed in aluminium and steel substrates, therefore, its behaviour appears to be insensitive to substrate material used. The Ni-P-X coating globules develop as seen from Fig. 7.4 (a) and the vertical growth of them results in the uniform coating around all the fibers of the fabric as seen from Figs. 7.2, 7.4 (a) and 7.5 (a). This mechanism can be attributed to the synergetic effect of infinite number of nucleation sites formed by initialisation of the coating during the pretreatment which makes the fabric strands catalytic and the newer nuclei generate and follow the sustained coating process. Similar mechanism of coating has been revealed from Fig. 7.5 (a) and (b) for electroless Ni-P alloy coatings. However, the reaction between carbon fiber and nickel has not been observed and the coating seems to have mechanical bonding with the fiber that can be observed from the interface between coating and fiber as marked by arrow in Fig. 7.14 (b). The semi-bright appearance with the spread of California gold (dull golden spread) colour appears in Ni-P-X coatings, as seen in Fig. 7.1-label (C), which may be due to the presence of zirconia along with other phases like Ni_xP_y and Al_2O_3 that has been confirmed by SEM-EDAX as shown in Fig. 7.6. Therefore, relatively less bright Ni-P-X coating on carbon fabric can be attributed to the co-deposition of composite in Ni-P alloy that can be revealed by visual examination of the photographs of the coatings as mentioned earlier. The X-ray diffraction patterns shown in Figs. 7.7 to 7.9 demonstrate the phases present in uncoated carbon fabric, Ni-P-X coated fabric and Ni-P coated fabric respectively. As the peaks correspond to carbon are not present in Figs. 7.8 and 7.9, it can be inferred that electroless coatings of both the Ni-P and the Ni-P-X could be continuous and pore free on the carbon fabric substrate. Such uniform coating of electroless Ni-P on carbon fibers has also been reported by Abraham (1997).

The SEM-EDAX result as seen from Fig. 7.6 reveals the presence of nickel and phosphorus along with traces of Al, Zr and O (oxygen) in the Ni-P-X coated fabric specimen. These contents can be ascribed to the presence of Al_2O_3 , and $Al_3Zr + ZrO_2$ in the composite coating as similar coatings on other substrates that have also shown the presence of these phases, which is explained earlier in chapter 4. When phosphorus atoms go into

lattice of *fcc* nickel, distortion of the *fcc* lattice occurs and results in a small and broad peak for nickel exists in the X-ray diffraction pattern of as-coated carbon fabric as seen in Figs. 7.8 (a) and 7.9 (a). The X-ray diffraction patterns reveal that the coating on carbon fabric is microcrystalline in nature similar to those observed in other substrates of aluminium and steel. Ni-P and Ni-P-X depositions in as-coated condition have experienced a transformation to crystalline nature containing Ni and Ni₃P, which is revealed from Figs. 7.8 (b) and 7.9 (b). During crystallisation due to heat treatment, different nickel phosphite phases (Ni_xP_y) observed undergo transformation into several metastable phases followed by the complete crystallisation in Ni and Ni₃P phases (Hur, *et al.*, 1990; Agarwala, 1987). Similar crystallisation sequence is observed with Ni-P-X coated specimens but the crystallisation growth compared to that of Ni-P coated specimen has been found to be hindered. This may be due to faster nucleation of Ni₃P phase in Ni-P coated sample than that in Ni-P-X coated fabric. The retarded growth of Ni₃P in Ni-P-X coated sample at 400°C for 1 h may be ascribed to compositional difference in the coating. The peaks in the X-ray diffraction patterns corresponding to less common phases, i.e., Al₂O₃, and ZrO₂, could not be noticed possibly because of smaller amounts contained in the Ni-P-X coating, but they act as grain refiner.

From Figs. 7.10 (a) to (e), it is inferred that failure load during tensile test for the uncoated carbon fabric is minimum, as it has failed at 41N load and that for the Ni-P-X coated and heat treated at 400°C for 1 h is maximum with the value of 136 N. The carbon fabric in as-coated Ni-P-X and Ni-P coated and heat treated at 400°C for 1 h are observed to have substantially higher tensile failure loads of 71 N and 126 N respectively. Therefore, commonly observed trend of improving the strength by electroless coatings on the carbon fabric can be seen. The electroless coatings of both the Ni-P and the Ni-P-X result in substantially improved tensile strength of carbon fabric. The ultimate tensile strength (UTS) for different types of the samples in the present study has been represented in Fig. 7.11. The tensile strengths of Ni-P alloy coated and Ni-P-X composite coated carbon fabric are observed to vacillate in the range of 12-12.7 N/mm² and UTS for the as-coated fabric has

lattice of *fcc* nickel, distortion of the *fcc* lattice occurs and results in a small and broad peak for nickel exists in the X-ray diffraction pattern of as-coated carbon fabric as seen in Figs. 7.8 (a) and 7.9 (a). The X-ray diffraction patterns reveal that the coating on carbon fabric is microcrystalline in nature similar to those observed in other substrates of aluminium and steel. Ni-P and Ni-P-X depositions in as-coated condition have experienced a transformation to crystalline nature containing Ni and Ni₃P, which is revealed from Figs. 7.8 (b) and 7.9 (b). During crystallisation due to heat treatment, different nickel phosphite phases (Ni_xP_y) observed undergo transformation into several metastable phases followed by the complete crystallisation in Ni and Ni₃P phases (Hur, *et al.*, 1990; Agarwala, 1987). Similar crystallisation sequence is observed with Ni-P-X coated specimens but the crystallisation growth compared to that of Ni-P coated specimen has been found to be hindered. This may be due to faster nucleation of Ni₃P phase in Ni-P coated sample than that in Ni-P-X coated fabric. The retarded growth of Ni₃P in Ni-P-X coated sample at 400°C for 1 *h* may be ascribed to compositional difference in the coating. The peaks in the X-ray diffraction patterns corresponding to less common phases, i.e., Al₂O₃, and ZrO₂, could not be noticed possibly because of smaller amounts contained in the Ni-P-X coating, but they act as grain refiner.

From Figs. 7.10 (a) to (e), it is inferred that failure load during tensile test for the uncoated carbon fabric is minimum, as it has failed at 41*N* load and that for the Ni-P-X coated and heat treated at 400°C for 1 *h* is maximum with the value of 136 *N*. The carbon fabric in as-coated Ni-P-X and Ni-P coated and heat treated at 400°C for 1 *h* are observed to have substantially higher tensile failure loads of 71 *N* and 126 *N* respectively. Therefore, commonly observed trend of improving the strength by electroless coatings on the carbon fabric can be seen. The electroless coatings of both the Ni-P and the Ni-P-X result in substantially improved tensile strength of carbon fabric. The ultimate tensile strength (UTS) for different types of the samples in the present study has been represented in Fig. 7.11. The tensile strengths of Ni-P alloy coated and Ni-P-X composite coated carbon fabric are observed to vacillate in the range of 12-12.7 *N/mm*² and UTS for the as-coated fabric has

been found to be about 1.7 times more than that of uncoated fabric. Due to heat treatment, the UTS of Ni-P and Ni-P-X coated and heat treated samples has been found to be further increased by about 1.8 time as compared to UTS of Ni-P-X as-coated fabric samples. This improvement could be attributed to the formation of hard Ni_3P phase as a result of heat treatment. When finer particles are closely spread, a fine particulate distribution effectively increases the distortion to bend and bypass. The stresses from the dislocation loops tend to elastically strain the non-deforming particles to conform to the plastically deforming matrix, which results in a high tensile strength as compared to the yield strength (Raghavan, 1984).

The fractographs shown in Figs. 7.12 (a) to (e) respectively, for carbon fabric samples in uncoated, as-coated Ni-P-X, heat treated Ni-P-X, as-coated Ni-P and heat treated Ni-P coatings show the similar nature of fracture. The above figures did not mark the thinning effect due to the strain and dimples over the broken section. This could be ascribed to brittle fracture of carbon fibers. The coatings along the strands seem to be defect free as seen in Figs. 7.4 (a)-(b) and 7.5 (a)-(b) and it gives more strength to the fiber. The higher strength due to such defect free electroless nickel coating has also been reported by Abraham *et al.* (1990). Relatively higher hardness of coating in both the as-coated and the heat treated conditions may be responsible for the loss of ductility and the presence of wavy edge at the fractured surface as seen in Figs. 7.12 (b to c). The Ni-P-X coating for about 5 *min* coating time resulted in about 40 % area fraction of the coating, which surrounds carbon fiber that contains about 60 % area fraction of the carbon as seen from Fig. 7.4 (b) and (c). Thus, nature of the fracture remained brittle even after nickel based coatings on the carbon fabric is applied, as commonly observed in Fig. 7.12 (b) to (e), which may be due to relatively lower area fraction of the brittle fibers of the fabric. The brittle fracture of uncoated carbon fiber and the electroless nickel coated fibers as observed in this investigation is in good agreement with the work of Abraham *et al.* (1990).

Reinforcement of carbon fabric in the metal depends on the wettability characteristic of the fabric. As explained earlier, due to the lower wettability of carbon with aluminium metal it is difficult to make carbon fiber reinforced metal matrix composite. As

nickel has better wettability with aluminium, therefore, the wettability of carbon fibres with aluminium is expected to improve by providing an intermediate layer of nickel between aluminium and carbon. The sequential events that occur when the aluminium drop comes into contact with the nickel are: (i) dissolution of nickel into the drop, (ii) local saturation of nickel and formation of Al_3Ni precipitates at the nickel/aluminium interface, (iii) Al_3Ni intermetallic reacts with nickel to form Al_3Ni_2 layer; (iv) diffusion of nickel through Al_3Ni_2 layer causes Al_3Ni to form continuously and (v) the thickness of Al_3Ni_2 layer increases while Al_3Ni layer maintains an equilibrium thickness (Ip, *et al.*, 1998). This proposed mechanism of reaction formation could be analogous to the features observed in Figs. 7.15 and 7.16. The width of the coated fabric zone into the aluminium matrix decreases after reinforcement when compared to that of uncoated fabric as seen in Figs. 7.13 and 7.14, which may be due to better wettability of nickel coated fabric. Similarly the aluminium infiltration into the fabric zone as seen in Fig. 7.16 (d) can be ascribed to better wetting behaviour of nickel coated carbon. A detailed study of wettability of carbon fabric has not been conducted in this investigation, therefore, the quantitative data of wettability of graphite by aluminium is not reported here. The presence of nickel, phosphorus and aluminium in the same zone for coated fabric can be observed from Figs. 7.16 (b) to (d) which indicates the possibility of reaction between Ni-P-X and aluminium at the interface of carbon fiber. Thus, nickel base coating layer on carbon fabric changes the interface and is expected to increase the feasibility of reinforcement into aluminium matrix.

The present investigation on the synthesis and characterisation of Electroless Ni-P-X coatings may be concluded in two sections corresponding to two major segments covered in this study: (i) synthesis and characterisation of electroless Ni-P-X coatings on steel, aluminium and carbon fabric, and (ii) tribological behaviour of Ni-P-X coatings on steel and aluminium substrates.

8.1 Synthesis and Characterisation of Coatings

1. Electroless nickel bath with in-situ co-precipitation reaction can be successfully used for Ni-P-X ($X = \text{ZrO}_2\text{-Al}_2\text{O}_3\text{-Al}_3\text{Zr}$) composite coatings. The studies carried by obtaining in-situ co-precipitation reaction within electroless Ni bath indicate that the alkaline bath considered for the study is suitable for both the Ni-P-X composite and the Ni-P alloy coatings.
2. The presence of NH_4Cl as one of the bath constituents and also as a byproduct of co-precipitation reaction acts as a buffer in the solution. Hence, it helps in maintaining the pH of the bath for relatively longer time and results in better uniformity of composition of the coating.
3. The in-situ co-precipitation reaction in electroless bath gives rise to Al_2O_3 and ZrO_2 as the products of reaction and the fine particles from these get incorporated into the growing Ni-P matrix resulting in a composite coating. At the catalytic island, when three atoms of Al and one atom of Zr come in the vicinity of each other, they form an intermetallic compound, Al_3Zr , which also gets embedded into Ni-P matrix along with the co-precipitated powder. Thus, in-situ co-precipitation reaction along with electroless Ni-P coating results in Ni-P-X composite coating.

4. In the electroless coating, several globules nucleate at isolated sites and grow laterally and vertically to cover the entire surface of the substrate. The deposition of hemispherical islands grows gradually to cover the substrate area by repeated nucleation and lateral growth. This mechanism can be observed for both the Ni-P alloy and the Ni-P-X composite coatings for different substrate materials used in this investigation.
5. By electroless technique, uniform and continuous coatings of Ni-P alloy and Ni-P-X composite could be successfully achieved on almost all the strands of carbon fabric and the mechanism of coating on carbon fabric samples remain the same as that for steel and aluminium substrates.
6. The particles co-deposited in electroless Ni-P-X composite coating by using an in-situ co-precipitation reaction appear to be uniformly distributed and these particles are in the range from sub micron to nano size.
7. As the cluster forming ability of ZrO_2 is more than that in the coating with co-deposited Al_2O_3 , formation of clusters results in a few Zr rich islands in Ni-P-X coated specimens, which may be locally coagulated in the different regions of the coating. Such Zr rich clusters may be due to presence of compounds of zirconium in hydrated form in the co-precipitated powder.
8. During co-deposition of Al_2O_3 , ZrO_2 and X ($X = ZrO_2-Al_2O_3-Al_3Zr$), these particles do not take part in the reaction but they get entrapped into growing Ni-P film. The distribution of co-deposited Al_2O_3 in Ni-P matrix appears to be more uniform than that of ZrO_2 particles. But when ZrO_2 and Al_2O_3 are co-deposited simultaneously along with Al_3Zr , finer particles get distributed uniformly and cluster of particles also appear in a few areas, thus, resulting in non-uniform size distribution of co-deposited particles.
9. The globule size variations in case of electroless Ni-P and Ni-P-X coatings are found to follow more or less normal distribution, whereas in case of electroless Ni-P- Al_2O_3 and Ni-P- ZrO_2 co-deposited coatings, globule size distribution does not

follow normal distribution. The average size of globules in electroless Ni-P alloy coating is higher than that with the Ni-P based composite coatings with co-deposition of Al₂O₃, as these particles cause globule growth retardation in composite coatings.

10. Coating rate in composite coatings is commonly observed to be higher than that in Ni-P alloy coating. The investigation reveals that deposition rate for composite coating under consideration is about 1.5 to 1.75 times greater than that of Ni-P alloy coatings for similar operating conditions. This coating rate for composite coating is experimentally found to be optimum when about 60 cm²/l of bath loading factor is used for immersing into the electroless composite coating bath for 45 min.
11. The composite electroless bath used in the present study has an optimum concentration of co-precipitation reaction reagents. Similarly, 9.0±0.25 pH and 90±2 °C temperature are also observed to be optimum in the present study.
12. The as-coated electroless Ni-9.5wt.%P-X composite coatings possess microcrystalline nature with the pockets of amorphous region and its crystallisation temperature is around 375°C.
13. The presence of ZrO₂, Al₂O₃ and Al₃Zr particles, which are embedded in to Ni-P matrix contributes to hardness enhancement of Ni-P-X coatings.
14. The electroless Ni-P base coating attains an equilibrium structure of Ni + Ni₃P after heat treatment. The heat treatment applied to substrate along with coating at 400°C for 1h causes an increase in microhardness by about two folds primarily due to formation of Ni₃P phase.
15. The heat treatment results in flattening of coating globules and the variation in rate of transformation may result in formation of a void or crack near the globule boundary. This may be attributed to change in specific volumes of constituent phases during transformation of Ni_xP_y to Ni₃P.

16. The DSC study reveals that the lower activation energy for Ni-P alloy coatings results in faster phase transformation when compared to that in Ni-P-X composite coatings which has relatively higher activation energy. The presence of X in Ni-P coating not only results in higher activation energy but also decreases the order of reaction. Therefore, it is primarily responsible for slower phase transformation in Ni-P-X coatings.
17. Under tensile loads, the electroless Ni-P-X coated carbon fabric exhibits relatively higher ultimate tensile strength (UTS) than that in uncoated carbon fabric. Also, further increase in UTS can be obtained when either Ni-P or Ni-P-X coated carbon fabric samples are heat treated at 400^oC for 1*h*. The brittle fracture of uncoated carbon fabric is retained even after the coating on the fiber though the fracture at the coated region of the carbon fibers, in as-coated condition is ductile in nature.
18. The Ni-P based coating changes the interface from fiber-aluminium matrix to (Ni-P)-aluminium, which may be primarily responsible for the reaction in Ni-P to aluminium matrix, resulting in better reinforcement ability of carbon fiber into the aluminium melt. The Ni-P and Ni-P-X coatings enhance their wetting characteristic with molten aluminium that is primarily responsible in fabrication of carbon fiber reinforced metal matrix composites. The feasibility of reinforcement of Ni-P-X coated carbon fabric into aluminium matrix seems to be fair due to the higher possibility of chemical reaction at the coated fabric-molten aluminium interface.

8.2 Tribological Behaviour of Ni-P-X Coatings on Steel and Aluminium

19. The coefficient of friction during the wear tests of different types of pins, fluctuates about the mean value. These fluctuations may be ascribed to continuous formation and breaking of oxide layer. Better compaction of transfer layer of wear debris with increase in load results in decrease in average coefficient of friction as commonly observed with both the steel and the aluminium wear pin samples under both the uncoated and the electroless Ni-P/Ni-P-X coated conditions.

20. Presence of X, hard ceramic oxides, in Ni-P matrix may result in enhanced scoring and ploughing, which may be responsible for relatively higher coefficient of friction in Ni-P-X deposits compared to that in Ni-P coatings.
21. In case of as-coated sample or that heat treated after electroless coating, the wear tracks are relatively more discontinuous as compared to those for metallic samples of both the steel and the aluminium. Worn surfaces of specimens, as-coated and heat treated after coating, show extensive formation of the compacted transfer layer on the wear tracks. The extent of transfer layer seems to increase with increasing applied load. A few cracks in the transfer layer on the wear surfaces of heat treated samples could be observed, and these cracks may link up to result in flaking off particles of wear debris.
22. Wear debris collected during dry sliding of Ni-P and Ni-P-X coated samples consists of fine oxide particles and larger agglomerates. The samples heat treated after coating result in relatively more coarser debris than that for as-coated samples.
23. During dry sliding wear of steel, the wear debris are primarily α -Fe₂O₃ whereas during the wear of Ni-P-X coating on steel samples (in as-coated and heat treated conditions), the wear debris are primarily NiO + Ni₃(PO₄)₂. Similar oxide constituents appear in the wear debris of Ni-P coated steel and Ni-P-X coated aluminium. This indicates that oxidative wear is the primarily operating mechanism during dry sliding of electroless coatings of both the Ni-P and the Ni-P-X under the given range of applied load and at specified sliding speed.
24. Substantially lower cumulative volume losses and wear rates in electroless Ni-P-X coated samples may be primarily attributed to lower oxidation rate constant of Ni-P-X coatings, when compared to those for aluminium and steel.
25. The heat treatments significantly enhance the microhardness of the coatings due to phase transformation and result in counteracting the softening due to frictional heating. The heat treatment of Ni-P and Ni-P-X coated samples results in lower real area of contact apart from enhanced oxidation resistance of Ni-based phases.

Therefore, these samples show a further decrease in cumulative volume loss and wear rates compared to those observed in as-coated samples.

26. The wear performance of electroless Ni-P-X as-coated steel is better than that of aluminum, which may be attributed to the backing of relatively harder underlying steel substrate beneath the coating, decreasing the real area of contact.
27. The dry sliding wear of electroless Ni-P-X coatings on aluminium is influenced also by substrate hardness. Lower substrate hardness in Ni-P-X coated aluminium heat treated at 400°C for 1 *h* has shown relatively larger cumulative volume loss and wear rate as compared to those in Ni-P-X coated aluminium samples heat treated at 250°C for 12 *h*.
28. Incorporating ceramic particles like X in Ni-P coating has the potential of further enhancing wear resistance if it could be incorporated in a relatively larger amounts but the coefficient of friction may increase.

The in-situ co-precipitation reaction can be controlled by addition of suitable dispersants within the bath. Use of such dispersants is expected to form fine powder, which will not contain the coagulated particles. Therefore, uniform distribution of particles in the Ni-P matrix can be consummated. Similarly, variation of volume fraction of reinforced matter, i.e., X ($ZrO_2-Al_2O_3-Al_3Zr$) in the coating to form composite coatings may lead to tailored properties. The systematic studies on structural characterisation and thermal response could be conducted to establish the kinetics of transformation. The mechanical properties of the Ni-P-X composite coatings can be determined and structure-property correlation could be used for reckoning suitable composition. The friction and wear behaviour could be assessed for varying sliding speed and in different environments by the use of different wear testing geometries. Hence, further understanding of tribological responses in the Ni-P-X coating could be carried out. Thus, further data generated may be used to supplement knowledge regarding the capabilities for specific engineering applications. Coatings with higher volume fraction of X in Ni-P matrix also could be obtained for better exploitation of this new electroless Ni-P-X system.

APPENDIX

Table A.1 The Values of n_l and k_l for Different Bath Loading Factors.

Particulars	Bath Loading Factor, cm^2/l					
	32.5	40	50	62.5	75	112.5
n_l	0.746	0.768	0.76	0.734	0.709	0.65
$k_{\text{experimental}}$	3.17	4.40	5.18	6.69	8.10	10.59
$k_{\text{calculated}}$	3.55	4.34	5.384	6.664	7.955	11.72

Table A.2 Correlation Factors for Least Square Fit Lines for the $\ln(W)$ vs. $\ln(t)$ Plots for Different Bath Loading Factors.

Bath Loading Factor, cm^2/l	Correlation Factor Obtained from $\ln(W)$ vs. $\ln(t)$ Plots
32.5	0.98
40.0	0.99
50.0	0.99
62.5	0.98
75.0	0.98
112.5	0.98

Table A.3 X-Ray Diffraction Analysis for Co-precipitated Powder Showing Phase Constituents Present and Their Characteristics.

Sl. No.	d	hkl	Phase Constituent																						
			Na ₂ AlH ₆			(ZrO ₂) ₂ .7H			NiP ₂			Zr ₃ O _{7-x}			NiZrH ₃			Al ₂ O ₃			Zr ₅ P ₃				
			d	hkl	hkl	d	hkl	hkl	d	hkl	hkl	d	hkl	hkl	d	hkl	hkl	d	hkl	hkl	d	hkl	hkl		
1.	3.85	28	30																						
2.	2.809	16		2.815	50	(110)	2.808	7.5	(020)	2.815	80	(110)								2.80			8		
3.	2.72	100	100																						
4.	2.63	84					2.649	75	(112)								2.614	100	(111)						
5.	2.473	41		2.475	100	(111)	2.448	25	(002)	2.475	100	(113)					2.468	50	(130)				2.47	100	
6.	2.229	22															2.224	20	(041)						
7.	1.924	20	80	1.91	50	(112)	1.192	50	(311)																
8.	1.726	14	40	1.73	10	(211)	1.740	100	(112)																
9.	1.624	9		1.625	50	(300)	1.64	25	(223)	1.625	80	(300)					1.75	50	(200)				1.90	35	
10.	1.577	22	70	1.586	10	(215)				1.586	10	(215)					1.62	70	(132)	1.621	50	(422)	1.621	6	
			70														1.558	10	(221)	1.55	60	(313)			
11.	1.372	10	60	1.378	50	(302)				1.378	80	(306)					1.379	70	(241)	1.394	100	(352)			
				1.359	50	(221)				1.359	80	(223)													
12.	1.288	7								1.299	70	(0012)													
13.	1.226	10	30																	1.292	10	(602)			
																				1.281	20	(271)			
14.	1.165	4																		1.264	10	(513)			
																				1.216	20	(063)			
15.	1.036	8																		1.161	50	(172)			
																				1.030	10	(713)			

Note : --- indicates non-availability of the data in the ASTM cards used.

Table A.4 Results of XRF Analysis of Ni-P-X Coating Showing the Intensities and Position of Different Peaks.

Sl. No.	Element Detected	Intensity (KCps)	Position (2θ)
1	Ni	413.98	48.647
2	P	2.60	141.335
3	Zr	1.80	144.962
4	Al	0.96	22.516

Table A.5 X-Ray Diffraction Analysis for Ni-P-X As-coated Film Showing Phase Constituents Present and Their Characteristics.

Sl. No.	d	hkl	Phase Constituent																			
			Ni Cubic		Ni ₅ P ₂ Hexagonal		Ni _{2.58} P Hexagonal		Ni ₁₂ P ₅ Tetragonal		Al ₂ Zr Tetragonal		Al ₂ O ₃ Tetragonal		Al ₂ O ₃ Orthorhombic		ZrO ₂ Tetragonal		Ni ₃ P Tetragonal			
			d	hkl	d	hkl	d	hkl	d	hkl	d	hkl	d	hkl	d	hkl	d	hkl	d	hkl	d	hkl
1.	2.955	5																				
2.	2.54	5																				
3.	2.33	12																				
4.	2.16	8																				
5.	2.13	9																				
6.	2.09	12																				
7.	2.08	13																				
8.	2.071	14																				
9.	2.04	20																				
10.	2.026	100	2.034	100	(111)																	
11.	1.99	17																				
12.	1.90	10																				
13.	1.72	6	1.76	42	(200)																	
14.	1.60	5																				
15.	1.24	6	1.25	21	(220)	1.243	16	(322)														
16.	1.22	13																				
17.	1.215	8																				
18.	1.21	6																				
19.	1.20	5																				
20.	1.085	5																				

Table A.6 X-Ray Diffraction Analysis for Ni-P As-coated Film Showing Phase Constituents Present and Their Characteristics.

Sl. No.	d	I ₁	Phase Constituent																
			Ni Cubic			Ni ₁₂ P ₅ Tetragonal			Ni ₅ P ₂ Hexagonal			Ni _{2.58} P Hexagonal			NiP ₂ Monolitic				
			d	I ₁	hkl	d	I ₁	hkl	d	I ₁	hkl	d	I ₁	hkl	d	I ₁	hkl		
1.	2.558	26																	
2.	2.46	28																	
3.	2.23	33																	
4.	2.16	41				2.16	33	(040)				2.16	35	(420)			2.45	90	(210)
5.	2.08	87										2.10	20	(408)			2.23	90	(211)
						2.073	16	(505)				2.073	16	(2110)					
6.	2.03	100	2.034	100	(111)	2.04	20	(330)				2.05	08	(502)			2.041	60	(214)
7.	1.96	70										2.041	16	(424)					
												1.975	100	(409)			1.98	100	(1110)
8.	1.93	48				1.93	65	(240)									1.93	75	(220)
9.	1.91	48				1.859	100	(312)				1.91	100	(600)			1.908	100	(300)
10.	1.75	30	1.76	42	(200)							1.77	16	(428)					
11.	1.648	27				1.64	08	(051)									1.649	100	(311)
12.	1.51	24															1.52	35	320
13.	1.46	24															1.46	45	(323)
14.	1.36	23				1.37	16	(629)											
								(4410)											

Table A.7 Phases Identified by Indexing the SAD Patterns of Ni-P-X Electroless Composite Coatings.

<i>d</i> Value, Å	Phases Indexed from Fig. 4.33 (c)	Phases Indexed from Fig. 4.34 (c)
2.792	Al ₂ O ₃	--
2.584	ZrO ₂	--
2.46	Ni ₃ P	--
2.114	Ni ₅ P ₂	--
2.03	Ni	Ni
1.975	Ni ₅ P ₂	Ni ₅ P ₂
1.823	Ni ₅ P ₂	Ni ₅ P ₂
1.77	Ni ₅ P ₂	--
1.67	--	Ni ₅ P ₂
1.645	Ni ₁₂ P ₅	--
1.621	--	Al ₂ O ₃
1.514	Al ₂ O ₃	--
1.42	Al ₃ Zr	Al ₃ Zr
1.381	--	Ni ₁₂ P ₅
1.292	Al ₂ O ₃	--
1.276	--	Al ₂ O ₃
1.26	Al ₃ Zr	--
1.25	Al ₃ Zr	--
1.246	Ni	Ni
1.20	--	Ni ₁₂ P ₅
1.18	Al ₃ Zr	--
1.16	--	Ni ₁₂ P ₅
1.055	--	Al ₂ O ₃
1.01	--	Al ₃ Zr
1.005	Al ₂ O ₃	--
0.94	Al ₂ O ₃	--
0.926	Ni ₁₂ P ₅	--
0.9178	Al ₂ O ₃	--
0.889	--	ZrO ₂
0.875	Ni ₁₂ P ₅	Ni ₁₂ P ₅

Table A.8 X-Ray Diffraction Analysis for Ni-P-X Coated and Heat Treated at 400°C for 1 h Film Showing Phase Constituents Present and Their Characteristics.

Sl. No.	d	hkl	Phase Constituent																											
			Ni Cubic			Ni ₃ P Tetragonal			Al ₃ Zr Tetragonal			Al ₂ O ₃ Hexagonal			Al ₂ O ₃ Orthorhombic			ZrO ₂ Tetragonal			Ni ₃ P ₂ Hexagonal			Ni ₁₂ P ₅ Tetragonal						
			d	hkl	hkl	d	hkl	hkl	d	hkl	hkl	d	hkl	hkl	d	hkl	hkl	d	hkl	hkl	d	hkl	hkl	d	hkl	hkl				
1.	2.458	6		2.46	5	(301)																								
2.	2.336	19					2.37	100	(114)																					
3.	2.15	15		2.16	14	(231)	2.16	90	(008)													2.16	35	(420)						
4.	2.10	10		2.11	15	(330)																2.097	20	(408)						
5.	2.068	12		2.07	49	(112)																2.05	08	(502)						
6.	2.03	59	2.03	100	(111)																	2.041	16	(424)	2.04	20	(330)			
7.	2.01	100		2.00	3	(240)	2.00	100	(200)													2.001	16	(506)						
8.	1.961	8		1.97	12	(202)																1.947	25	(3110)	1.933	65	(240)			
9.	1.92	13																				1.91	100	(600)						
10.	1.87	6																				1.862	80	(003)						
11.	1.831	5																												
12.	1.82	5		1.80	32	(222)	1.82	50	(204)													1.80	100	(202)	1.803	8	(434)			
13.	1.79	7		1.80	32	(222)	1.78	50	(211)													1.77	16	(428)	1.756	4	(435)			
14.	1.761	13	1.76	42	(200)																									
15.	1.75	11																				1.74	45	(024)	1.746	35	(6110)			
16.	1.728	8		1.73	11	(132)	1.73	50	(109)																					
17.	1.601	5					1.59	50	(215)																					
18.	1.568	4		1.56	4	(402)																								
19.	1.533	5																												
20.	1.425	5		1.44	4	(103)	1.42	60	(220)																					
21.	1.31	5					1.31	50	(219)																					
22.	1.25	6	1.246	21	(220)		1.26	11	(323)																					
23.	1.218	16		1.21	9	(149)	1.22	19	(228)																					
24.	1.16	7					1.17	10	(1114)																					
25.	1.09	4		1.09	100	(004)																								

Table A.9 The Different Phase Constituents Present in Electroless Ni-P Based Coatings Under This Study.

Sl. No.	Coating System and its Condition	Common Phases	Less Common Phases	Remark
1.	Ni-P-X as-coated	Ni microcrystalline	Ni ₁₂ P ₅ , Ni ₅ P ₂ , Ni _{2.55} P, Ni ₃ P, Al ₃ Zr, Al ₂ O ₃ , ZrO ₂ , Ni(am)	Ni ₃ P identified may be in some localized areas
2.	Ni-P-X coated and heat treated at 400°C for 1 h	Ni ₃ P, Ni	Ni ₁₂ P ₅ , Ni ₅ P ₂ , Al ₃ Zr, Al ₂ O ₃ , ZrO ₂	-
3.	Ni-P-X coated and heat treated at 400°C for 2 h	Ni ₃ P, Ni	Ni ₁₂ P ₅ , Al ₃ Zr, Al ₂ O ₃ , ZrO ₂	-
4.	Ni-P-X coated and heat treated at 250°C for 12 h	Ni ₃ P, Ni	Ni ₁₂ P ₅ , Ni ₅ P ₂ , Al ₃ Zr, Al ₂ O ₃ , ZrO ₂	-
5.	Ni-P as-coated	Ni microcrystalline	Ni ₁₂ P ₅ , Ni ₅ P ₂ , Ni _{2.55} P, NiP ₂ , Ni(am)	-

Table A.10 Temperatures Observed for the Peak of DSC Curves for Electroless Ni-P-X and Ni-P Coatings.

Coating Type	Temperature ($^{\circ}\text{K}$) for the Peak, T_m at Different Heating Rates, β			
	10 $^{\circ}\text{C}/\text{min}$	15 $^{\circ}\text{C}/\text{min}$	20 $^{\circ}\text{C}/\text{min}$	25 $^{\circ}\text{C}/\text{min}$
Ni-P-X	668	672	675	683
Ni-P	615	625	629	651

Table A.11 Microhardness of Electroless Ni-P-X and Ni-P Coatings.

Coating Type	Microhardness, HV_{100}		
	As-coated	HT ₁	HT ₂
Ni-P-X on steel	620 (14.6)	1219 (44.8)	1048 (45.1)
Ni-P-X on aluminium	608 (28.9)	1080 (126.6)	1034 (68.4)
Ni-P on steel	510 (21.1)	1025 (25.49)	981 (28.4)

HT₁ : heat treated at 400 $^{\circ}\text{C}$ for 1 h

HT₂ : Heat treated at 400 $^{\circ}\text{C}$ for 2 h for steel and 250 $^{\circ}\text{C}$ for 12 h with aluminium.

The values in the parenthesis indicate the standard deviation observed in the corresponding reading(s).

Table A.12 Microhardness of Different Phases Present in Different Types of Sample Used in Wear Testing.

Particulars of Sample	Region	Phase(s) Identified	Average Microhardness in HV_{100} (GPa)
Normalised steel (NS)	White	Ferrite	212 (2.08)
	Dark	Pearlite	312 (3.06)
Ni-P-X as-coated Steel (AC ₁)	White	Ni, Ni _x P _y matrix	585 (7.3)
	Dark	Al ₂ O ₃ / ZrO ₂ /Al ₃ Zr	1584 (15.54), 1446 (14.2)
Ni-P-X heat treated at 400 $^{\circ}\text{C}$ for 1 h after coating (HT ₁ -A)	White	Ni, Ni ₃ P	1176 (12.5)
	Dark	Al ₂ O ₃ / ZrO ₂ /Al ₃ Zr	2250 (22.1), 1676 (16.44)
Ni-P-X heat treated at 400 $^{\circ}\text{C}$ for 2 h after coating (HT ₂ -A)	White	Ni, Ni ₃ P	1132 (11.4)
	Dark	Al ₂ O ₃ / ZrO ₂ /Al ₃ Zr	2284 (22.4), 1658 (16.3)

Table A.13 Macrohardness of Electroless Ni-P-X and Ni-P Coatings.

Coating Type	Macrohardness, <i>VHN</i>		
	As-coated	HT ₁	HT ₂
Ni-P-X on steel	125	159	138
Ni-P on steel	122	158	140
Ni-P-X on aluminium	27	35	31

HT₁ : heat treated at 400°C for 1 h

HT₂ : Heat treated at 400°C for 2 h for steel and 250°C for 12 h with aluminium.

Table A.14 Microhardness and Macrohardness of the Substrate Materials in Different Conditions.

Material	Microhardness, <i>HV</i> ₁₀₀			Macrohardness, <i>VHN</i>		
	As Received	HT ₁	HT ₂	As Received	HT ₁	HT ₂
Steel	131	131	131	113	113	113
Aluminium	69	45	65	23	18	22

HT₁ : heat treated at 400°C for 1 h

HT₂ : Heat treated at 400°C for 2 h for steel and 250°C for 12 h with aluminium.

Table A.15 X-Ray Diffraction Analysis for Wear Debris Showing the Characteristics of Phase Constituents Present in NS, AC₁, (HT₁-A + HT₂-A), AC₃ and (HT₁-C + HT₂-C) Samples.

Sl. No.	d	Phase Constituent										Sample in which the corresponding phase is present			
		Ni ₃ (PO ₄) ₂			α-Fe ₂ O ₃			NiO							
		d	l/l ₁	hkl	d	l/l ₁	hkl	d	l/l ₁	hkl					
1.	3.810	3.78	36	—	—	—	—	—	—	—	—	—	—	—	AC ₁ , (HT ₁ -A + HT ₂ -A)
2.	3.104	3.13	32	—	—	—	—	—	—	—	—	—	—	—	AC ₁ , (HT ₁ -A + HT ₂ -A), AC ₃ , (HT ₁ -C + HT ₂ -C)
3.	2.690						2.69	100	(104)						NS, AC ₁
4.	2.517						2.51	50	(110)						NS, AC ₁ , (HT ₁ -A + HT ₂ -A)
5.	2.420											2.412	60	(101)	AC ₁ , (HT ₁ -A + HT ₂ -A), AC ₃ , (HT ₁ -C + HT ₂ -C)
6.	2.190	2.18	20	—	—	—	—	—	—	—	—	—	—	—	(HT ₁ -A + HT ₂ -A), (HT ₁ -C + HT ₂ -C)
7.	2.110											2.09	100	(012)	AC ₁ , (HT ₁ -A + HT ₂ -A), (HT ₁ -C + HT ₂ -C)
8.	2.060						2.07	2	(202)						AC ₁ , (HT ₁ -A + HT ₂ -A), AC ₃ , (HT ₁ -C + HT ₂ -C)
9.	1.720						1.69	60	(116)						NS
10.	1.510											1.48	35	(110)	AC ₁ , (HT ₁ -C + HT ₂ -C)
11.	1.313						1.310	20	(1010)	(119)					NS, (HT ₁ -C + HT ₂ -C)

Note : --- indicates non-availability of the data in the ASTM cards used.

Table A.16 X-Ray Diffraction Analysis of Uncoated Carbon (C) Showing its Characteristics.

Sl. No.	<i>d</i> As Received	<i>I/I</i> ₁ HT ₁	C Hexagonal		
			<i>d</i>	<i>I/I</i> ₁	<i>hkl</i>
1	3.388	100	3.36	100	(002)
2	2.122	3	2.13	10	(100)
3	2.0578	4	2.036	50	(101)
4	1.689	5	1.68	80	(004)
5	1.233	4	1.232	30	(110)

Table A.17 The Different Phase Constituents Present in the Electroless Ni-P-X and Ni-P Coated Carbon Fabric Under this Study

Sl. No.	Coating System and its Condition	Common Phases	Less Common Phases	Remark
1	Ni-P-X as-coated	Ni microcrystalline	Ni ₁₂ P ₅ , Ni ₅ P ₅ , Ni _{-2.55} P, Al ₃ Zr, Ni(am)	Al ₂ O ₃ and ZrO ₂ may present even not detected
2	Ni-P-X coated and heat treated at 400°C for 1 h	Ni ₃ P, Ni	Ni ₁₂ P ₅ , Ni ₅ P ₂ , Al ₃ Zr	
3	Ni-P as-coated	Ni microcrystalline	Ni ₁₂ P ₅ , Ni ₅ P ₅ , Ni _{-2.55} P, Ni(am)	
4	Ni-P coated and heat treated at 400°C for 1 h	Ni ₃ P, Ni	Ni ₁₂ P ₅ , Ni ₅ P ₂	

REFERENCES

1. *Abraham, S.*, (1997), "Studies on the Morphology of Coatings and its Effect on Interfaces in Metal Matrix Composites", Ph.D. Thesis, University of Kerala, Thiruvananthapuram (India).
2. *Abraham, S.*, *Pai, B. C.*, *Satyanarayana, K. G.* and *Vaidyan, V. K.*, (1992), "Copper Coating on Carbon Fibers and their Composites with Aluminium Matrix", *J. of Materials Science*, **Vol. 27**, pp. 3479-3486.
3. *Abraham, S.*, *Pai, B. C.*, *Satyanarayana, K. G.* and *Vaidyan, V. K.*, (1990), "Studies on Nickel Coated Carbon Fibers and their Composites", *J. of Materials Science*, **Vol. 25**, pp. 2839-2845.
4. *Agarwala, R. C.* and *Ray, S.*, (1988), "Variation of Structure in Electroless Ni-P Films with Phosphorus Content", *Z. Metallkd.*, **Vol. 79**, pp. 472-475.
5. *Agarwala, R. C.* and *Ray, S.*, (1989), "TEM Investigation of the Transformation During Annealing in Electroless NI-P Films", *Z. Metallkd.*, **Vol. 80**, pp. 556-559.
6. *Agarwala, R. C.* and *Ray, S.*, (1992), "Crystallization Behaviour of Electroless Ni-P Films Part II: A Kinetics Study", *Z. Metallkd.*, **Vol. 83**, No. 3, pp. 203-207.
7. *Agarwala, R. C.*, (1987), "Structural Studies and Crystallization Behaviour of Electroless Ni-P Films", Ph.D. Thesis, University of Roorkee, Roorkee (India).
8. *Allen, R. M.*, and *VanderSande, J. B.*, (1982), "The Structure of Electroless Ni-P Films as a Function of Composition", *Scripta Metallurgica*, **Vol. 16**, pp. 1161-1164.
9. *Andre, M. T.*, *Putten V.* and *De Bakker J. W. G.*, (1993), "Geometrical Effects in the Electroless Metallization of Fine Metal Patterns", *J. of Electrochem. Soc.*, **Vol. 140**, No. 8, pp. 2221-2228.
10. *Apachitei, I.* and *Duszczyk J.*, (2000), "Autocatalytic Nickel Coating on Aluminium with Improved Abrasive Wear Resistance", *Surface and Coatings Technology*, **Vol. 132**, pp. 89-98.

11. *Apachitei*, I. and *Duszczuk*, J., (1999), "Hydrogen Evolution, Incorporation and Removal in Electroless Nickel Composite Coatings on Aluminium", *J. of Applied Electrochemistry*, Vol. 29, pp. 837-843.
12. *Apachitei*, I., *Duszczuk*, J., *Katgerman*, L. and *Overkamp*, P. J. B., (1998/1), "Electroless Ni-P Composite Coatings: The Effect of Heat Treatment on the Microhardness of Substrate and Coating", *Scripta Materialia*, Vol. 38, No. 9, pp. 1347-1353.
13. *Apachitei*, I., *Duszczuk*, J., *Katgerman*, L. and *Overkamp*, P. J. B., (1998/2), "Particles Co-deposition by Electroless Nickel", *Scripta Materialia*, Vol. 38, No. 9, pp. 1383-1389.
14. *Archard*, J. F., (1961), "Single Contacts and Multiple Encounters", *J. Appl. Phys.*, Vol. 32, No. 8, pp. 1420-1425.
15. *Asthana*, R. and *Sobczak*, N., (2000), "Wettability, Spreading and Interfacial Phenomena in High-Temperature Coatings", *J. of Metals*, Vol. 52, No. 1. Electronic Supplement.
16. *Bakonyi*, I., *Cziraki*, A., *Nagy*, I. and *Hosso*, M., (1986), "Crystallization Characteristics of Electrodeposited Amorphous Ni-P Alloys", *Z. Metallkd.*, Vol. 77, pp. 425-432.
17. *Balaraju*, J. N. and *Seshadri*, S. K., (1999), "Synthesis and Characterization of Electroless Nickel – High Phosphorus Coatings", *Metal Finishing*, Vol. 97, No. 7, pp. 8- 13.
18. *Bangwei*, Z., *Haowen*, X. and *Xiewen*, X., (1999), "Autocatalytic Deposition of Nickel-Tin-Copper-Phosphorus Amorphous Alloys", *Metal Finishing*, Vol. 97, No. 10, pp. 35-41.
19. *Baudrand*, D. (1999), "Electroless Nickel Applications Involving Heat Excursions", *Metal Finishing*, Vol. 97, No. 1, pp. 36-41.
20. *Baudrand*, D. W. (1994), "Electroless Nickel Plating", *ASM Handbook, Surface Engineering*, Vol. 5, pp. 290-310.

21. *Bayer, R. G.*, (1994), *Mechanical Wear Prediction and Prevention*, Marcel Dekker, Inc., New York, USA.
22. *Bedingfield, P. B.*, Lewis, D. B., Datta, P. K., Gray, J. S. and Wells, P. B., (1991), "Studies of Electroless Nickel-Boron Alloy Coatings", *Trans. Inst. Metal Finish.*, Vol. 70, No. 1, pp. 19-23.
23. *Bhushan, B.* and Gupta, B. K., (1991), *Handbook of Tribology*, McGraw Hill, Inc., USA, pp. 10.34 - 10.41 and 14.14 - 14.19.
24. *Bin-Sudin, M.*, Leyland, A., James, A. S., Matthew, A., Housden, J. and Garside, B., (1996), "Substrate Surface Finish Effects in Duplex Coatings of PAPVD TiN and CrN with Electroless Nickel-Phosphorus Interlayers", *Surface and Coatings Technology*, Vol. 81 No. 2-3, pp. 215-224.
25. *Blau, P. J.*, (1997), "Fifty Years of Research on the Wear of Metals", *Trib. Int.*, Vol. 30, No. 5, pp. 321-331.
26. *Bowden, F. P.* and Tabor, D., (1964), *The Friction and Lubrication of Solids*, Part II, Clarendon Press, Oxford.
27. *Bowden, F. P.* and Tabor, D., (1950), *Friction and Lubrication of Solids*, Clarendon Press, Oxford.
28. *Bozzini, B.* and Boniardi, M., (1997), "Fracture Toughness of Supported Ni-P Films Prepared by Autocatalytic Chemical Deposition", *Z. Metallkd.*, Vol. 88, No. 6, pp. 493-497.
29. *Bozzini, B.* and Cavallotti, P. L., (1997), "Evidence of Clustering in X-ray Amorphous Ni-P Prepared by Autocatalytic Chemical Deposition", *Scripta Materialia*, Vol. 36, No.11, pp.1245-1248.
30. *Bozzini, B.*, Martini, C., Cavallotti, P. L. and Lanzoni, E., (1999), "Relationships among Crystallographic Structure, Mechanical Properties and Tribological Behaviour of Electroless Ni-P (9%)/B₄C Films", *Wear*, Vol. 225-229, Part-2, pp. 806-813.

31. *Brenner, A. and Riddell, G., (1946), "Nickel Plating on Steel by Chemical Reduction", Res. Nat. U. S. Bur. Stand., Vol. 37, p. 31.*
32. *Brenner, A. and Riddell, G., (1947), "Nickel Plating on Steel by Chemical Reduction", Res. Nat. U. S. Bur. Stand., Vol. 39, p. 385.*
33. *Brenner, A., (1963), Electrodeposition of Alloys, Principle and practice, Vol II, Academic Press.*
34. *Bull, S. J., (1997), 'Tribological and Micro-Tribological Phenomena in Coatings', Material Science Forum, Vol. 246, pp. 105-152.*
35. *Caturla, F. Molina, F., Molina-Sabio, M., Rodriguez-Reinoso, F. and Esteban, A., (1995), "Electroless Plating of Graphite with Copper and Nickel", J. of Electrochem. Soc., Vol. 142, No. 12, pp. 4084-4090.*
36. *Chitty, J., Pertuz, A. Hintermann, H, Staia, M. H. and Puchi, E. S., (1997), "Influence of Electroless Ni-P Deposits on the Corrosion-Fatigue Properties of an AISI 1045 Steel", Thin Solid Films, Vol. 308-309, pp. 430-435.*
37. *Criado, J. M. and Ortega, A., (1987), "Non-isothermal Crystallization Kinetics of Metal Glasses: Simultaneous Determination of both the Activation Energy and the Exponent n of the JMA Kinetic Law", Acta Metall., Vol. 35, No. 7, pp.1715-1721.*
38. *Cziraki, A., Fogarassy, B., Bakonyi, I., Tompa, K. and Hegedus, Z., (1980), "Investigation of Chemically Deposited and Electrodeposited Amorphous Ni-P Alloys", J. De Physique, Collogue C8, Supplement au no. 8, Tome 41, aout C8-141.*
39. *Datta, P. K., Bedingfield, P. B., Lewis, D. B. and Wells, P. B., (1991), "Structure and Phase Changes Accompanying Heat Treatment of an Electroless Ni-B Alloy Coating", Conf. Proc., 2nd Int. Electroless Nickel Conference, Solihull, October, 1991, pp. 139-153.*
40. *Debsikdar, J. C., (1987), "Influence of Synthesis Chemistry on Alumina-Zirconia Powder Characteristics", J. of Materials Science, Vol. 22, pp. 2237-2247.*

41. *Dehoff*, R. T. and Rhines F. N., (1968), *Quantitative Microscopy*, Series in Materials Science and Engineering, McGraw-Hill Inc., New York, USA.
42. *Feldstein*, M. D., (1999), "Composite Coatings with Light-Emitting Properties", *Metal Finishing*, Vol. 97, No. 2, pp. 87-90.
43. *Feldstein*, N., (1983), "Electroless (Autocatalytic) Plating" and "Electroless Composite Plating", *Metal Finishing*, Vol. 82, 1A, pp. 408-416 and 417-420.
44. *Feldstein*, N., Lancsek, T., Lindsay, D. and Salerno, L., (1983), "Electroless Composite Plating", *Metal Finishing*, Vol. 81, No. 8, pp. 35-41.
45. *Gaurilow*, G. G., (1979), *Chemical (Electroless) Nickel Plating*, Porticullis Press, Redhill, England.
46. *Gawne*, D. T. and Ma, U., (1989), "Friction and Wear of Chromium and Nickel Coatings", *Wear*, Vol. 129, pp. 123-142.
47. *Gawne*, D. T., (1984), "Failure of Electrodeposited Chromium Coatings on Cast Iron Substrates", *Thin Solid Films*, Vol. 118, pp. 385-393.
48. *Gawne*, D.T. and Ma, U., (1987), "Wear Mechanisms in Electroless Nickel Coating", *Wear*, Vol. 120, pp. 125-149.
49. *Ge*, J-P, Che, R. X. and Wang, X. Z., (1998), "Structure and Properties of Electroless Ni-P-B₄C Composite Coatings", *Plating and Surface Finishing*, Vol. 85, No.10, pp. 69-73.
50. *Gee*, M. and Jennett, N. M., (1995), "High Resolution Characterisation of Tribochemical Films on Alumina", *Wear*, Vol. 193, pp. 133-145.
51. *Giampaolo Di*, A. R., Ordonez, J. G., Gugliemacci, J. M. and Lira, J., (1997), "Electroless Nickel-Boron Coatings on Metal Carbides", *Surface and Coatings Technology*, Vol. 89, pp. 127-131.
52. *Gill*, R.M., (1972), *Carbon Fibres in Composite Materials*, Published for the Plastics Institute, ILIFFE books, London.

53. **Gillespie, P.** (1996), "Electroless Nickel Coatings: Case Study", *Surface Engineering Casebook*, Edited by Burnell-Gray J. S. and Datta P. K., Woodhead Publishing limited, pp. 49-72.
54. **Glaeser, W. A.**, (1992), "Materials for Tribology", *Tribology Series*, 20, Elsevier, Amsterdam.
55. **Gorbunova, K. M.** and **Nikiforova, A. A.**, (1963), *Physicochemical Principles of Nickel Plating*, Translated from Russian, Published by Israel program for Scientific Translations, Jerusalem.
56. **Gorbunova, K. M.**, **Nikiforova, A. A.** and **Sadkov, G. A.**, (1966), *Modern Problems of Metal Deposition by Reduction with Hypophosphite*, *Electrochemistry* (ed.) Melnikova, M. M., p. 41.
57. **Graham, A. H.**, **Lindsay, R. W.** and **Read, H. J.**, (1962), "Structure of Electroless Nickel", Brief Communication, *J. of Electrochem. Soc.*, Vol. 109, No. 12, pp. 1200-1201.
58. **Graham, A. H.**, **Lindsay, R. W.** and **Read, H. J.**, (1965), "The Structure and Mechanical Properties of Electroless Nickel", *J. of Electrochem. Soc.*, Vol. 112, No. 4, pp. 401-413.
59. **Groshart, E. A.**, (1983), "Design for Finishing: Electroless Nickel Coating - its Use in Design", *Metals Finishing*, Vol. 81, No. 11, pp. 19-21.
60. **Grosjean, A.**, **Rezrazi, M.** and **Tachez, M.**, (1997), "Study of the Surface Charge of Silicon Carbide (SiC) Particles for Electroless Composite Deposits: Nickel-SiC", *Surface and Coatings Technology*, Vol. 96, No. 2-3, p. 300-304.
61. **Guntherodt, H. J.** and **Beck, H.**, (1981), *Topics in Applied Physics, Vol. 46: Glassy Metals I*, Springer Verlag, Berlin Heidelberg, Germany.
62. **Gutzeit, G.**, (1959), "Outline of the Chemistry Involved in the Process of Catalytic Nickel Deposition from Aqueous Solution", *Plating and Surface Finishing*, Vol. 46, pp. 1158, 1275 and 1377.

63. **Harris, S. J., Overs, M. P. and Gould, A. J., (1985), "The Use of Coatings to Control Fretting Wear at Ambient and Elevated Temperatures", *Wear*, Vol. 106, pp. 35-52.**
64. **Henry, J., (1985), "Electroless (Autocatalytic, Chemical) Plating", *Metal Finishing*, Vol. 83, pp. 372-387.**
65. **Himbeault, D. D., Varin, R. A. and Piekarski, K., (1988), "Coating of Graphite Fibers With Tungsten Carbide Using Solid and Liquid Copper as a Transfer Medium", *Metall. Trans., A*, Vol. 19A, pp.2109-2113.**
66. **Himbeault, D. D., Varin, R. A. and Piekarski, K., (1989/1), "Carbon Fibers Coated with Chromium Carbide Using the Liquid Metal Transfer Agent Technique", *Metall. Trans., A*, Vol. 20A, pp. 165-170.**
67. **Himbeault, D. D., Varin, R. A., Piekarski, K., (1989/2), "Carbon Fibers Coated with Titanium Carbide Using the Liquid Metal Transfer Agent Technique", *J. of Materials Science*, Vol. 24, pp. 2746-2750.**
68. **Hogmark, S., Hedenqvist, P. and Jacobson, S., (1997), "Tribological Properties of Thin Hard Coatings: Demand and Evaluation", *Surface and Coatings Technology*, Vol. 90, No. 3, pp. 247-257.**
69. **Holmberg, K., Mathews, A. and Ronkainen, H., (1998), "Coatings Tribology – Contact Mechanisms and Surface Design", *Trib. Int.*, Vol. 31, No. 1-3, pp. 107-120.**
70. **Hong, J. S., De la Torre, S. D., Miyamoto, K., Miyamoto, H. and Gao, L., (1998), "Crystallization of Al₂O₃/ZrO₂ Solid Solution Powders Prepared by Co-precipitation", *Materials Letters*, Vol. 37, No. 1-2, pp. 6-9.**
71. **Horowitz, H and Metzger, G., (1963), "A New Analysis of Thermogravimetric Traces", *Analyt. Chem.*, Vol. 35, pp. 1464-1468.**
72. **Huchings, I. M., (1992), *Tribology: Friction and Wear of Engineering Materials*, Edward Arnold Publication, London.**

73. **Hur**, K-H, Jeong, J-H and Lee, D. N., (1990), "Microstructures and Crystallization of Electroless Ni-P Deposits", *J. of Materials Science*, Vol. 25, pp. 2573-2584.
74. **Husheng**, G., Haicheng, G. and Huijiu, Z., (1991), "Sliding Wear and Fretting Fatigue Resistance of Amorphous Ni-P Coatings", *Wear*, Vol. 142, pp.291-301.
75. **Ip**, S. W., Sridhar, R., Toguri, J. M., Stephenson, T. F. and Warner A. E. M., (1998), "Wettability of Nickel Coated Graphite by Aluminium", *Materials Sc. and Engg.*, Vol. A244, pp. 31-38.
76. **Kim**, D-H, Aoki, K. and Takano, O., (1995), "Soft Magnetic Films by Electroless Ni-Co-P Plating", *J. of Electrochem. Soc.*, Vol. 142, No. 11, pp. 3763-3767.
77. **Lanzoni**, E. and Martini, C., (2000), "Microstructure and Tribological Behaviour of ACD Ni-P Matrix Composite Coatings", *Proc. of AIMETA International Tribology Conf.*, Sept. 20-22, L' Aquila, Italy, pp. 776-782.
78. **Lanzoni**, E., Martini, C., Ruggeri, O., Bertoncetto, R. and Glisenti, A., (1997), "Structure and Corrosion Behaviour of Electroless Ni Coatings Deposited from Differently Stabilised Baths", Published for European Federation of Corrosion, No. 20, *The Institute of Materials*, Edited by Fedrizzi, L. and Bonora, P. L., pp. 232-243.
79. **Levy**, D. J., (1963), "Thin Nickel Films by Hydrazine Autocatalytic Reduction", *Electrochem. Tech.*, Vol. 1, p. 38.
80. **Li**, J., Hu, X. and Wang, D., (1996), "Effects of Codeposited Tungsten on the Properties of Low-Phosphorus Electroless Nickel Coatings", *Plating and Surface Finishing*, Vol. 83, No. 8, pp. 62-64.
81. **Li**, Y., (1997), "Investigation of Electroless Ni-P-SiC Composite Coatings", *Plating and Surface Finishing*, Vol. 84, No. 11, pp. 77-81.
82. **Mahoney**, M. W. and Dynes P. J., (1985), "The Effects of Thermal History and Phosphorus Level on the Crystallization Behavior of Electroless Nickel", *Scripta Metallurgica*, Vol. 19, pp. 539-542.

83. *Mai, Q. X., Daniels, R. D. and Harpalani, H. B., (1988), "Structural Changes Induced by Heating in Electroless Nickel-phosphorus Alloys", Thin Solid Films, Vol. 166, pp. 235-247.*
84. *Makhsos, E. V., Thomas, E. L. and Toth, L. E., (1978), "Electron Microscopy of Crystalline and Amorphous Ni-P Electrodeposited Films: In-Situ Crystallization of an Amorphous Solid", Metall. Trans., Vol. 9A, pp. 1449-1460.*
85. *Mallory, G. O., (1974), "Influence of the Electroless Plating Bath on the Corrosion Resistance of the Deposit", Reprinted Courtesy Allied-Kellite Products Division, The Richardson Company, Des Plaines, Illinois 60018. Originally presented at the 61st Annual Technical Conference, June 18, 1974, American Electroplater's Society, Chicago, Illinois.*
86. *Mallory, G.O., (1979), "The Electroless Nickel Plating Bath", Reprinted Courtesy Allied-Kellite Products Division, The Richardson Company, Des Plaines, Illinois 60018. Originally presented at Electroless Nickel Conference, Nov. 1979, Cincinnati, Ohio.*
87. *Mallory, G.O., (1980), "Electroless Nickel-Myths and Facts", Reprinted Courtesy Allied-Kellite Products Division, The Richardson Company, Des Plaines, Illinois 60018. Originally presented at Electroless Nickel Conference II, 1980, Cincinnati, Ohio.*
88. *Masumoto, T. and Maddin, R., (1975), "Structural Stability and Mechanical Properties of Amorphous Metals", Materials Sc. and Engg., Vol. 19, p. 1.*
89. *Moonir-Vaghefi, S. M., Saatchi, A. and Hedjazi, J., (1997), "Tribological Behaviour of Electroless Ni-P-MoS₂ Composite Coatings", Z. Metallkd., Vol. 88, No. 6, pp. 498-501*
90. *Narayan, R. and Pandey, A. (1997), "Electroless Ni-PTFE Composite Coatings", Proc. of 12th National Convention of Metallurgists and Material Scientists and Proc. of National Seminar on Surface Engineering, at Institute of Engineers (India), Jaipur, India, pp. 98-106.*

91. *Odekerken*, (1966), *Brit. Pat.* 1,041,753, U. S. Pat. 3,644,183 and *DDR Pat.* Vol. 41, p. 406.
92. *Okado*, J., Shima, M., McColl, I. R., Waterhouse, R. B., Hasegawa, T. and Kasaya, M., (1999), "Ni-P and Mo: An Excellent Fretting Wear Resistant Combination", *Wear*, Vol. 225-229, Part 2, pp. 749-757.
93. *Park*, S. H. and Lee, D. N., (1988), "A Study on the Microstructure and Phase Transformation of Electroless Nickel Deposits", *J. of Materials Science*, Vol. 23, pp. 1643-1654.
94. *Pearlstein*, F., Weightman, R. F. and Wick, R., (1963), "Nickel-Tungsten Electroless Deposition: A Preliminary Report", *Metal Finishing*, Vol. 61, p. 77.
95. *Pearson*, W. B., (1967), *Handbook of Lattice Spacing and Structures of Metals*, Vol. I, Pergamon Press Ltd., Headington Hill Hall, Oxford OX3 0BW, England.
96. *Pedraza*, A. J. and Godbole, M. J., (1990), "Recrystallization and Mechanical Properties of Electroless Copper", *Scripta Metallurgica*, Vol. 24, pp. 1185-1189.
97. *Pena-Munoz*, E., Bercot, P., Grosjean, A., Rezrazi, M. and Pagetti, J., (1998), "Electrolytic and Electroless Coatings of Ni-PTFE Composites. Study of Some Characteristics", *Surface and Coatings Technology*, Vol. 107, pp. 85-93.
98. *Puchi*, E. S., Staia, M. H., Hintermann, H, Pertuz, A. and Chitty, J., (1997), "Influence of Ni-P Electroless Coating on the Fatigue Behavior of Plain Carbon Steels", *Thin Solid Films*, Vol. 290-291, pp. 370-375.
99. *Quinn*, T. F. J., (1971), "Oxidational Wear", *Wear*, Vol. 18, pp. 413-419.
100. *Quinn*, T. F. J., (1983), "Review of Oxidational Wear Part I: The Origin of Oxidational Wear", *Trib. Int.*, Vol. 16, No. 5, pp. 257-271.
101. *Rabinowicz*, E., (1965), *Friction and Wear of Metals*, John Wiley and Sons, Inc., New York, USA.
102. *Rabinowicz*, E., (1977), "The Formation of Spherical Wear particles" *Wear*, Vol. 41-43, pp. 149-156.

103. **Raghavan, V.** (1984), *Physical Metallurgy - Principles and Practice*, Prentice-Hall of India, New Delhi.
104. **Ramasubramanian, M., Popov, B. N., White, R. E. and Chen, K. S.,** (1999), "A Mathematical Model for Electroless Copper Deposition on Planar Substrates", *J. of Electrochem. Soc.*, Vol. 146, No. 1, pp. 111-116.
105. **Razavizadeh, K. and Eyre, T. S.,** (1982), "Oxidative Wear of Aluminium Alloys: Part I", *Wear*, Vol. 79, pp. 325-333.
106. **Razavizadeh, K. and Eyre, T. S.,** (1983), "Oxidative Wear of Aluminium Alloys: Part II", *Wear*, Vol. 87, pp. 261-271.
107. **Reddy, V. V. N., Ramamoorthy, B. and Kesavan Nair, P.,** (1998), "Studies on Electroless Ni-P/diamond Composite Coatings", *Proc. of 18th AIMTDR Conference* held at IIT, Kharagpur, Dec. 21 – 23, 1998, pp. 440-444.
108. **Rigney, D. A.,** (1997), "Comments on the Sliding Wear of Metals", *Trib. Int.*, Vol. 30, No.5, pp. 361-367.
109. **Rigney, D. A., Chen, L. H. and Naylor, M. G. S.,** (1984), "Wear Processes in Sliding Systems", *Wear*, Vol. 100, pp. 195-219.
110. **Roy, R. K.,** (1990), *A Primer on Taguchi Method*, Van Nostrand Reinhold, New York, USA.
111. **Saka, N., Pamies-Teixeira, J. J., and Suh, N. P.,** (1977), "Wear of Two Phase metals", *Wear*, Vol. 44, pp. 77-86.
112. **Satyanarayana, K. G., Agarwala, R. C., Agarwala, V. and Sharma, S. B.,** (2001), "Ni-P-Al₂O₃-Al₃Zr-ZrO₂: Co-precipitation of Alumina-Zirconia followed by Co-deposition", *Filed for Indian Patent through CSIR, India*, No. 100/Del/2001, appeared in the Gazette of India, part III – Sec. 2, May 19, 2001.
113. **Scott, M. G.,** (1978), "The Crystallization Kinetics of Fe-Ni based Metallic glasses", *J. of Materials science*, Vol. 13, pp. 291-296.

114. *Shi, Z.*, Wang, X. and Ding, Z., (1999), "The Study of Electroless Deposition of Nickel on Graphite Fibers", *Applied Surface Science*, Vol. 140, No. 1-2, pp. 106-110.
115. *Srivastava, A.*, Mohan, S., Agarwala V. and Agarwala, R.C., (1992), "Factors Influencing the Deposition Rate of Ni-B Electroless Films", and "On the Crystallization Behaviour of an Amorphous Ni-17.8 at.% B Electroless Deposit", *Z. Metallkd.*, Vol. 83, No. 4, pp. 254-257, and 251-253.
116. *Staia, M. H.*, Castillo, E. J., Puchi, E. S., Lewis, B., Hintermann, H. E., (1996), "Wear Performance and Mechanism of Electroless Ni-P Coating", *Surface and Coatings Technology*, Vol. 86-87, pp. 598-602.
117. *Staia, M. H.*; Enriquez, C. and Puchi, E. S., (1997), "Influence of the Heat Treatment on the Abrasive Wear Resistance of Electroless Ni-P", *Surface and Coatings Technology*, Vol. 94-95, pp. 543-548.
118. *Strafford, K. N.*, Datta, P. K. and Gray, J. S. (1990), "Applications and Performance of Coatings: Some Perspectives and Prospects", *Surface Engineering Practice*, Ellis Horwood Publishers, U.K., pp. 397-419.
119. *Suh, N. P.*, (1973), "The Delamination Theory of Wear", *Wear*, Vol. 25, pp. 111-124.
120. *Suh, N. P.*, (1977), "An Overview of the Delamination Theory of Wear", *Wear*, Vol. 44, pp. 1-16.
121. *Suh, N. P.*, (1986), *Tribophysics*, Prentice – Hall, Inc., Englewood Cliffs, New Jersey, USA.
122. *Tottle, C. R.*, (1984), *An Encyclopaedia of Metallurgy and Materials*, Macdonald and Evan Ltd., pp. 11-18.
123. *Tromans, B.*, Probet, D. and Essex, F., (1982), *The Canning Handbook – Surface Finishing Technology*, Published by W. Canning Plc., Birmingham in association with E. and F. N. Spon Ltd., London, pp. 423-429.

124. **Tyagi, R., Nath S. K. and Ray S.,** (2001), "Dry Sliding Friction and Wear in Plain Carbon Dual Phase Steel", *Metall and Mater. Trans., A*, **Vol. 32A**, pp. 359-367.
125. **Vasudevan, R., Narayanan, S. and Karthik, P. R.,** (1998), "Some Investigations on the Effect of Ultrasonic Agitation on the Properties of Nickel-Phosphorous and Nickel-Boron Electroless Deposits", *Trans. Indian Inst. Met.*, **Vol. 51**, No. 5, pp. 445-448.
126. **Wang, L., Zhao, L., Zhang, B. Liao, S., Ou Yang, Y. and Hu, W.,** (1997), "On Structure and Crystallization of Amorphous Fe-Mo-W-B Alloys Obtained by Electroless Plating", *Z. Metallkd.*, **Vol. 88**, No. 12, pp. 945-948.
127. **Wang, L.,Zhau, L., Zhang, B., Hu, W., Shu, X. and Sheng, X.,** (1999), "Magnetic Properties of Fe-TM-B (TM=Sn,W,Mo-W) Alloys Prepared by Electroless Plating", *Z. Metallkd.*, **Vol. 90**, No. 5, pp. 338-341.
128. **Wang, Y-Q. and Zhou, B-L.,** (1996), "Behaviour of Coatings on Reinforcements in Some Metal Matrix Composites", *Copmosites, part A*, **Vol. 27A**, pp. 1139-1145.
129. **Yugang, L. and Tondon, K. N.,** (1996), "Effect of Temperature on the Wear of an Electroless Nickel Coating under lubricated Reciprocating Sliding Conditions", *Tribology Letters*, **Vol. 2**, No. 3, pp. 263-272.
130. **Zang, X. H., Liu, J. J. and Zhu, B. L.,** (1992), "The Tribological Performance of Ni/MoS₂ Composite Brush Plating Layer in Vacuum", *Wear*, **Vol. 157**, pp. 381-387.
131. **Zhang, Y. Z, Wu, Y.Y., and Yao, M.,** (1998/1), "Characterization of Electroless Nickel with Low Phosphorus", *J. of Material Science Letters*, **Vol. 17**, No. 1, pp. 37-40.
132. **Zhang, Y. Z, Wu, Y.Y., Sun, K. N. and Yao, M.,** (1998/2), "Characterization of Electroless Ni-P-PTFE Composite Deposits", *J. of Material Science Letters*, **Vol. 17**, No. 2, pp. 119-122.